Title
Assembly of and Ion Transport Through Porous Nanocrystal Thin Films

Author
Ong, Gary Kah Ping

Publication Date
2018

Peer reviewed|Thesis/dissertation

Assembly of and Ion Transport Through Porous Nanocrystal Thin Films

by

Gary Kah Ping Ong

A dissertation submitted in partial satisfaction of the

requirement for the degree of

Doctor of Philosophy

in

Engineering – Materials Science and Engineering

in the

Graduate Division

of the

University of California, Berkeley

Committee in charge:

Professor Fiona M. Doyle, Co-chair
Professor Delia J. Milliron, University of Texas at Austin, Co-chair
Professor Ting Xu
Professor Bryan D. McCloskey

Summer 2018

Abstract

Assembly of and Ion Transport through Porous Nanocrystal Thin Films

by

Gary Kah Ping Ong

Doctor of Philosophy in Engineering – Materials Science and Engineering

University of California, Berkeley

Professor Fiona M. Doyle, Co-chair

Professor Delia J. Milliron, University of Texas at Austin, Co-chair

Of all the defining characteristics of a material, there are probably none more important than structure. Through a simple change in structure, materials can exhibit vastly different properties due to its influence at length scales from atomic crystal structure to microstructure. In fact, structure is so important in the study of materials science that it is given one of the four coveted spots on the materials science tetrahedron.

From advances in colloidal nanocrystals, materials with well-defined intrinsic characteristics such as composition and phase can now be synthesized reproducibly. However, these materials are often orders of magnitude smaller than actual device length scales. This disparity in length scales, however, is a fertile opportunity space where structural control can be used both to augment the intrinsic properties of nanocrystals and to bridge the length scales between nanocrystal building blocks and that of an actual device. More specifically, it may actually allow independent imposition of a structural motif separate from other parameters like composition and phase: an almost impossible feat from the standpoint of bulk materials processing.

Recent developments in nanocrystal surface chemistry have generated a sub-class of nanocrystals, called ligand-stripped nanocrystals, which are colloidally stable even in the absence of stabilizing ligands. This advancement opens both opportunities to access properties that require access to the nanocrystal surface, and new avenues for assembly that capitalizes on interactions with the nanocrystal surface. In assembly, it opens the question of how one might direct the arrangement of these nanocrystals through the use of a structure-directing agent such as a block copolymer. Initial work in 2012 demonstrated the first assembly of these nanocrystals using an artisanal polystyrene-b-polydimethylacrylamide (PS-PDMA) block copolymer of which the latter block is hypothesized to interact strongly with the nanocrystal surface. Chapter 2 expounds this discovery by investigating the assembly of ligand stripped nanocrystals using PS-PDMA micelles with emphasis on the influence of nanocrystal size and volume fraction on the overall ordering of the assembled structures. Grazing incidence small angle x-ray scattering is employed to quantitatively characterize ordering both at the block copolymer and nanocrystal

length scale. The nanocrystal size dependence of ordering is shown such that ordering decreased dramatically for nanocrystal sizes bigger than the PDMA domain size. Similarly, nanocrystal ordering also decreased for nanocrystal volume fractions exceeding the volume fraction of PDMA in the system. Finally, the extreme limits of assembly using PS-PDMA micelles is demonstrated whereby single nanocrystal networks or networks with two length scales of ordering can be generated either at low volume fractions of large nanocrystals or at high volume fractions of small nanocrystals.

Chapter 3 extends the assembly of ligand stripped nanocrystals into block copolymer microphase-separated morphologies using PS-PDMA. Here, the phase separation behavior of PS-PDMA with and without nanocrystals is shown alongside methods used to achieve the final morphologies. Both volume fraction and size studies mirroring the studies in Chapter 2 is conducted to arrive at the maximal nanocrystal size and volume fractions after which assembly is kinetically arrested. Morphological control to access the hexagonal and lamellae phases is demonstrated with either a change in relative block copolymer block lengths or through a co-swelling approach using mixed solvents. Then, the compositional diversity of this assembly paradigm is demonstrated with the successful assembly of different metal oxide, metal chalcogenide, and gold nanocrystals. The nature of this diversity is expanded upon with a Fourier Transform Infrared Spectroscopy (FTIR) study that ultimately suggests that the nature of the interaction between PDMA and the nanocrystal surface is based upon hydrogen bonding. Finally, Chapter 4 discusses future work based on the co-assembly of nanocrystal mixtures, the control of PS-PDMA morphology in solution, and the use of block copolymers beyond PS-PDMA for the directed assembly of ligand stripped nanocrystals.

Moving beyond the context of assembly towards the arena of ion transport properties, ligand free nanocrystal thin films are applied as model systems to investigate the phenomena of intermediate temperature proton conduction between 250 °C and 100 °C: an anomalous phenomenon where porous metal oxide structures exhibit significant protonic conductivity that are traditionally absent in their bulk counterpart. Chapter 5 explores this phenomenon using porous nanocrystal thin films of cerium oxide or titanium oxide. The study establishes the viability of nanocrystals as model systems by demonstrating the influence of nanocrystal size on protonic conductivity for cerium oxide holding other variables such as porosity comparable. Then, capillary condensation is ruled out as the cause of the phenomenon, and an alternate hypothesis built upon metal oxide surface defect chemistry is proposed. This influence of defect chemistry is preliminary studied with emphasis on the oxygen partial pressure dependence of intermediate temperature protonic conductivity. The observed non-dependence of conductivity on oxygen partial pressure for cerium oxide is consistent with prior observations of the poor dependence of cerium oxide surface defect chemistry on oxygen partial pressure. This is in contrast with the clear oxygen partial pressure dependence observed for titanium dioxide. Holding porosity constant, the higher proton conductivity observed for 4 nm cerium oxide compared to that of 9 nm cerium oxide is rationalized by an enrichment of Ce^{3+} on the surface and corresponding oxygen vacancies for ultra small cerium oxide nanocrystals. Similarly, the higher proton conductivity observed for cerium oxide compared to titanium dioxide is rationalized by the lower enthalpy of formation of oxygen vacancies for cerium oxide. Then, the link between surface defect chemistry and protonic

conductivity is proposed: dissociate water adsorption in surface oxygen vacancies may be responsible for the generation of mobile protons on the surface of the metal oxide.

Chapter 6 continues the investigation of intermediate temperature proton conductivity but addresses the stability of the phenomena. Here, time dependent conductivities at all temperatures is presented where a general decrease in conductivity under humidified conditions at temperatures lower than 200 °C is observed. Extended time dependent conductivity measurements at 100 °C show a gradual decrease in conductivity over 2 orders of magnitude over 48 hours for cerium oxide. Detailed FTIR studies reveal the nature of the decrease as passivation of the metal oxide surface due to the formation of cerium hydroxycarbonate consistent with the characteristic instability of rare-earth oxides under ambient or humidified conditions. Thermodynamic analysis further reveal a transition point of 575 °C after which the formation of cerium hydroxycarbonate becomes thermodynamically unfavorable. A reaction for the formation of cerium hydroxycarbonate from cerium oxide, CO_2 and H_2O is proposed and tested with a time, temperature and oxygen partial pressure dependent conductivity measurement. The results show that the rate of decrease in conductivity is significantly slower for pure oxygen environments. Gallium doping of cerium oxide to reduce the surface affinity toward hydroxycarbonate formation was tested but was found to have little efficacy in enhancing the stability. Thus, an alternate materials selection criteria based upon mineralogy that ultimately suggest titanium dioxide as a stable material under humidified conditions is tested. While the absolute conductivity of porous titanium dioxide nanocrystal systems start lower than that of cerium oxide nanocrystal systems, titanium dioxide appears stable over the tested 48-hour period thus showing the merit of using titanium dioxide over cerium oxide in actual applications due to gains in system stability. The study for titanium dioxide is completed with another detailed FTIR study that shows the formation of bicarbonate species on the surface of titanium dioxide under humidified conditions though the species do not hinder protonic conductivity. The stability of the phenomena for titanium dioxide under pure oxygen environments is also demonstrated. Finally, Chapter 7 discusses future work utilizing *in situ* FTIR studies to identify the spectroscopic signatures of acidic protons on the oxide surface that result from the aforementioned dissociative water adsorption on surface oxygen vacancies, and tuning of conductivity through manipulation of surface defect concentrations either by acceptor doping or tuning of surface facet termination.

"The things you learn can only compliment who you are, and in my book, who you are counts for a whole lot."

Richard Branson

"Wait long enough and people will surprise and impress you. It might take even years, but people will show you their good side. Just keep waiting."

Randy Pausch

"Shall we educate ourselves in what is known, and then casting away all we have acquired, turn to ignorance for aid to guide us among the unknown?"

Michael Faraday

Table of Contents

List of Figures

List of Tables

Acknowledgements

I must confess that for every book I have read, I have skipped the acknowledgements page, eager to dive deep into the content. For this reason, I am now dreading the idea that my readers will also skip the following pages, just as I did. Despite my dearth of karmic currency, I would still like to humbly ask of you, my dear reader, to bottle your eagerness to read the ensuing one hundred and forty pages for just a few minutes to allow me the privilege to express my gratitude for the people that have made this dissertation possible.

First and foremost, I would like to thank none other than myself. Good job on completing the dissertation. On a more serious note, I would like to start by thanking my two advisors, Professor Delia Milliron and Professor Fiona Doyle. Delia, you have helped me become the scientist I am today. And for that, I am eternally grateful. My skills as a scientist today is but a reflection of your belief in my ability to execute – be it starting projects, writing proposals, or building equipment – even when I had no prior history doing them. Thank you for creating a safe environment in the group where failure is all right and ignorance is not condemned. I will never forget the time I was presenting new data in group meeting in my second year; you stopped me and said, "You clearly don't understand what you're talking about right now. So, go back, read up, and try again next week." I think this statement best exemplifies what I admire most about your mentorship: you gave me the space to try, fail, try again, grow and succeed on my own. And, you did it without judgment, trusting that I was capable of figuring everything out. You showed faith in me long before I had faith in myself. If I am considered a good scientist today, it's because of you. Fiona, thank you for showing me the mentorship ideal. If I ever was a good mentor in graduate school, it was probably because I was channeling you and your beliefs. There is nothing I can say here that can sufficiently express the depth of my gratitude for what you have shown me over the last six years through your dedication and actions as my co-advisor. Thank you for challenging me to be precise and meticulous in all my scientific discussions with you. Thank you for showing me how mentorship can be both compassionate and strict. Thank you for always having my back and for providing the panacea to all the difficult existential moments in graduate school. I remember the time I came to you anxious about not publishing enough when you said, "Gary, a successful PhD program is not about the papers. It's about the candidate. My job is to make sure you become a good scientist." I really think that every PhD candidate should hear that. It helped me place things into perspective, and I hope others reading it here will find it helpful too.

To my post-doctoral mentors, Natacha, Ajay, and Raffa, thank you for teaching me much of what I know, and more importantly, for showing me how science should be done. Natacha, thank you for making beam time so enjoyable and for teaching me electrochemistry when I first started in the group. Ajay, thank you for teaching me nanocrystal assembly and how to plan and think through nanocrystal synthesis. Also, thank you for teaching me how to properly cook lentils, chicken curry, and goat curry. Raffa, thank you for the email of encouragement when my first paper was rejected and for the scientific discussions about synthesis, Thank you very much for that one conversation in my first year when you told me that you will not give me nanocrystals,

but that you will teach me nanocrystal synthesis. It was a pivotal change in perspective that helped me develop my various skills as a scientist today. Jongwook, Amita, Yang, and Yizheng, thank you for teaching me about everything from Korean cuisine and electrochromics to Hindi and how to properly take FTIR spectra.

To members of my qualifying exam committee, Mark, Andy, Bryan and Ting, thank you for the extensive feedback during the qualifiers. I probably would not have ventured into the realm of ion transport if it were not for your feedback. Thank you for passing me in my qualifiers despite the hiccups and hurdles, and thank you for having faith in my ability to succeed, to do good work, and hit a higher standard than even that which I had set for myself. To the staff of the Materials Science and Engineering department at Berkeley, and especially to Catalina and Ariana, thank you for facilitating my PhD journey despite my prolonged physical absence from the department. The two of you have truly made MSE feel like a big family. Chris, thank you for your positive attitude and always being welcoming whenever you saw me in the building.

To my collaborators Brett and Teresa, thank you for making the polymers that made half of this dissertation possible. To staff members at the Molecular Foundry, Tracy and Alyssa specifically, thank you for teaching me how to do science safely and practice proper lab etiquette. To members of the ALS beamline 7.3.3, specifically Eric and Chenhui, thank you for giving me all the beam time that made the assembly projects possible, and thank you for always being supportive of my experiments no matter how difficult. Eric, thank you for always showing faith in my scientific abilities and me. To staff members at the Texas Materials Institute, Hugo, Andrei and Karalee specifically, thank you for teaching me tons about XPS, TOF-SIMS, and TEM; thank you for tolerating all my sudden request for instrument time and my incessant questioning during the sessions. To Shallaco, thank you for helping me with both the design and construction of the ion transport stage. Chapters 5 and 6 would not have been possible without your help.

To all the graduate students I have had the pleasure to work and interact with, thank you for making the last six years of graduate school truly enjoyable and arguably the best times of my life so far. Amy, thank you for introducing me to Delia's group, for being a great ACG hood mate, for tolerating me calling you 'Ames' all the time, and for allowing me to treat you like the big sister I've always wanted. Evan, thank you for introducing me to ion transport, for saving me from disaster many times in lab and at beam time, and for teaching me how to finally serve pasta truly al dente. You are indeed my guardian angel (I finally got injured in lab after you left), a true friend, and one I would consider an older brother without hesitation. Camila, thank you for tolerating all the shenanigans, for embracing all the jokes that were often at your expense, the tea times, and general support across the six years. Lauren, thank you also for taking the time to join tea time, always trying to cheer me up whenever I seemed down and all the awesome Game of Throne viewing parties. Shin, you have been a wonderful office neighbor that never failed to keep things interesting. Thank you for teaching me so much about geology and mineralogy. Corey, I could always count on you to tell me the truth no matter how harsh it was. Thank you for the pep talks and quit-complaining interrupts. It was painful at times, but the patient needed it. Sungyeon, thank you for bearing the enormous responsibilities that keep the lab running smoothly. Nothing else garners more respect from me than this. Clay, thank you for making

Fresh House a wonderful place to live in. Your endless optimism, laidback personality and general coolness serves as a constant reminder for me to slow down and smell the roses. To the members of (Just) Fam, Ankit and Dainah, thank you for turning one of my hardest years in graduate school into my most enjoyable and happiest year. One could not ask for better company both in and outside of lab. Ankit, thank you for serving as my intellectual sounding board and for providing me with much needed advice whenever the circumstances called for it. I knew I could always count on you to be the voice of reason even in the direst situations. Thank you for tolerating all the outburst and mood swings during the toughest times in graduate school. Dainah, Chapter 3 of this dissertation probably would not exist if it were not for your relentless dedication to the project, patience, and willingness to stick with me through the first six months when nothing worked. I know that Ankit and I joke all the time that you would do wonderful work in graduate school. But truthfully, I know you will do spectacular work wherever you are, and I am honored to have had the pleasure of mentoring and working with you.

To my family, who have been more than understanding throughout the whole PhD endeavor, thank you for hearing me out and always remaining supportive. Dad, if you had not brought me to the US, I probably would not have attended Berkeley for my undergraduate studies. I probably would not have attended graduate school, and I probably would not be where I am today. I know I don't say this nearly enough, but thank you for all your sacrifices throughout the years. Most of my peers today often point out my vehement insistence on doing things the right way and strict adherence to ethics. In truth, I am pretty sure I got those two things from you, and I cannot thank you enough for them. Mom, thank you for making the sacrifices, taking care of Baron and me, and serving the physical role of mom and dad while dad was in the US laying the foundation for our arrival. Thank you for tolerating all the arguments, for enduring my absence throughout the years, and for always supporting my decisions and choices no matter how bizarre they seem. Baron, one could not have asked for a better brother. Thank you for the leather shoes you sent me after you heard about the hole that formed on my canvas shoes after a drop of acid landed on it. Thank you for all the vacations you arranged to keep me sane, for shouldering the responsibilities of taking care of mom and dad for both of us, and for going into the work force soon after undergrad so that I may have the freedom to do the PhD and pursue my dreams. Thank you also for the smiley face mug, bullshit button, happy face calendar you sent when I seriously wanted to quit graduate school. I really could not have done it without you.

Finally, to Dai, the one who makes me strive everyday to be a better man, have faith in human nature, and try to make this world better if for nothing else than for you. Every time I think of you, I cannot help but think that Mencius got it right: human nature is good. You are the kindest, gentlest, most considerate, caring, and good person I know. Everyday, I thank my lucky stars for bringing us together. Thank you for being my support whenever I was down, for having faith in me when I doubted myself, and for cheering me on every single day. Thank you for indulging my obsessions with dim sum and fried chicken, and for listening to my blabbering all the time. Thank you for letting me vent about life, research, science, and work and smiling at the end to make everything better. Thank you for the hugs, kisses, snuggles and cuddles. I love you so much, now, always and forever.

Chapter 1

Introduction

1.1 Prologue: the prevalence of structure

If we had to pick one defining characteristic of materials science that distinguishes this field apart from its brethren in physics, chemistry, and all other branches of engineering, a strong contender is likely the field's emphasis on structure. More specifically, it may be the field's obsession with microstructure. On the materials science tetrahedron, structure is given one of the coveted corners, because it is justifiably important given its implications on the processing, properties and performance of materials.

Within the context of advanced materials, structure is important because it is one of two distinct approaches to manipulate the properties of materials with the other being composition. For the approach of compositional control commonly used in modern engineering, material properties are tuned with emphasis on elemental composition, and structure is examined as a consequence. In contrast, for the approach of structural control commonly used in nature, elemental composition is fixed and material properties are tuned with the precise control of structure. Both approaches have yielded extraordinary results. Using mechanical materials as an example, on one end of the spectrum, we have advanced metal alloys with compositions in excess of five elements such as the nickel superalloys and metallic glasses, while on the other end of the spectrum, nature has the mineralized skeleton of the Euplectella species of the marine sponge that is composed of silica glass with seven levels of intricate microstructure. This level of microstructural control bestows the skeleton with optical properties rivaling modern optical fibers combined with exceptional flexibility and toughness. The questions that remains, therefore, is can we potentially achieve independent control of composition and structure to realize advance material properties.

A clue towards the independent control of composition and structure can be gleaned from the aforementioned example of the mineralized skeletal system of the Eupleectella species of marine sponge. To construct the seven levels of structure present, the marine sponge utilizes silica nanoparticles as the basic building block. Starting the structural description of the seven starting at the highest level, we have a macroscopic cylindrical structure (a); a cage arrangement of spicules that form a rectangular lattice (b,c); bundles of spicules that make up a major spicule (d), concentric lamellar layers of silica and organic matter in the 200 nm lengh scale that make up a single spicule (g,h); and finally the basic building block of silica nanoparticles that underpin the whole skeletal system (l). This hierarchical structure is shown in Figure 1.1

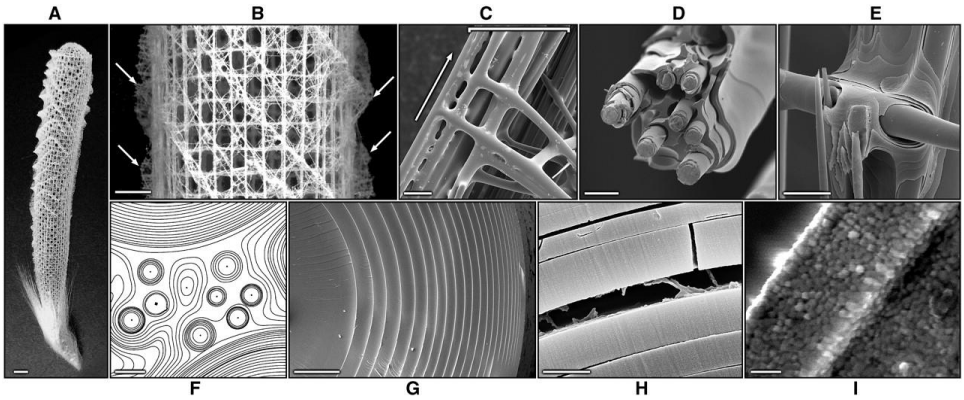

Figure 1.1: Mineralized skeletal system of Euplectella sp. marine sponge demonstrating multiple length scales of structure. Scale bar of 1 cm (A), 5 mm (B), 100 μm (C), 20 μm (D), 25 μm (E), 10 μm (F), 5 μm (G), 1 μm (H), 500 nm (I). (A) Photograph of the entire skeleton, showing cylindrical glass cage. Scale bar, 1 cm. (B) Fragment of the cage structure showing the square-grid lattice of vertical and horizontal struts with diagonal elements arranged in a chessboard manner. Orthogonal ridges on the cylinder surface are indicated by arrows. Scale bar, 5 mm. (C) Scanning electron micrograph (SEM) showing that each strut (enclosed by a bracket) is composed of bundled multiple spicules (the arrow indicates the long axis of the skeletal lattice). Scale bar, 100 μm. (D) SEM of a fractured and partially HF-etched single beam revealing its ceramic fiber-composite structure. Scale bar, 20 μm. (E) SEM of the HF-etched junction area showing that the lattice is cemented with laminated silica layers. Scale bar, 25 μm. (F) Contrast-enhanced SEM image of a cross section through one of the spicular struts, revealing that they are composed of a wide range of different-sized spicules surrounded by a laminated silica matrix. Scale bar, 10 μm. (G) SEM of a cross section through a typical spicule in a strut, showing its characteristic laminated architecture. Scale bar, 5 μm. (H) SEM of a fractured spicule, revealing an organic interlayer. Scale bar, 1 μm. (I) Bleaching of biosilica surface revealing its consolidated nanoparticulate nature. Scale bar, 500 nm. Reproduced verbatim from reference 1.

Of the levels of structural control portrayed, modern additive manufacturing techniques from 3-D printing to robocasting using ultra-small nozzle sizes have enabled precise structural control down to the one micrometer length scale. Advances in synthetic methods have also allowed us to make nanoparticles like that of the silica nanoparticle building block mentioned above. The final piece of the puzzle, therefore, is to investigate how we can control structure in the length scale between the nanoparticle building blocks (usually from 1 to 50 nm) to the micrometer length scale. The promise of understanding structural control at this intermediate length scale (10 nm to 1000 nm) is that we can eventually independently manipulate composition and structure to achieve the material properties we desire: to dictate the composition of the material with the choice of nanoparticle and to impose structure by directing their arrangement in space.

1.2 Technological motivation

There are significant advantages in understanding the assembly of nanoscopic building blocks into more complex structures from the bottom up. Limiting our discussion of advantages imparted by nanostructure design to systems where it is already accepted that the presence of structure enhances or alters properties, we are naturally led to discuss properties that are either

dictated by interfaces (a solid-liquid or solid-air interface such as a pore in most cases) or influenced by nearest neighbor coordination, as in the case of optics. In the case of the former, porosity may be a good example of why structural control at this intermediate length scale (10 nm to 1000 nm) is important. Seminal studies in fields of catalysis and ion transport have demonstrated that proper control of structure to impart useful porosity – porosity that results in a significant increase in solid-gas interface – can significantly decrease the need for overall catalyst loading in the case of catalysis or lead to new interface mediated properties in the case of ion transport.

One particular interface mediated property that will be discussed and studied further in part II of this dissertation is an anomalous phenomenon exhibited by porous metal oxide networks. Here, with the introduction of porosity, metal oxides such as cerium oxide, zirconium oxide, and titanium oxide – oxides that are traditionally poor proton conductors – exhibit significant proton conductivity under humidified conditions at temperatures above 100 °C . This property has garnered significant interest due to current limitations in proton exchange membranes that limit fuel cell operation at elevated temperatures. Nafion, the workhorse material currently deployed in this role for instance, dehydrates above 100 °C, resulting in a significant loss in proton conductivity. A host of materials are currently being developed to circumvent this limitation because there is significant interest in operating proton exchange membrane fuel cells at mild elevated temperatures between 100 °C and 300 °C. At these mild elevated temperatures, there may be efficiency gains in electrochemical kinetics that may reduce our dependence on expensive platinum catalysts and increase the resistance of fuel cells to poisoning. For an extended discussion on this phenomenon, the reader is referred to Chapter 5. However, before pursuing studies on porosity enabled ion transport, we must first consider how one might introduce and tailor structure, and in turn porosity, at the nanoscale.

1.3 Controlling structure at the nanoscale

There are many ways to control structure at the nanometer scale. The simplest method is to control the kinetics of agglomeration. For instance, when particles are frozen and kinetically trapped, they tend to adopt fractal networks, as has been demonstrated in many studies on aerosolized particle networks. On the opposite side of the spectrum, when a system of particles is allowed to equilibrate to their desired equilibrium configuration, they tend to form close packed structures that obey simple geometric rules and are reminiscent of atomic crystal structure configurations such as hexagonal close packed spheres for single component systems or binary crystal structures (CsCl, ZnS, etc.) for multicomponent systems as shown in Figure 1.2.

The latter is often preferred because these configurations can be predicted by thermodynamics and are less susceptible to experimental variations that prevent scale-up or reproducibility. However, how can we access structures that are not close packed without relying on control of kinetic parameters? For instance, how can we arrange particles into more complicated networks such as lamellae or hexagonally packed porous networks?

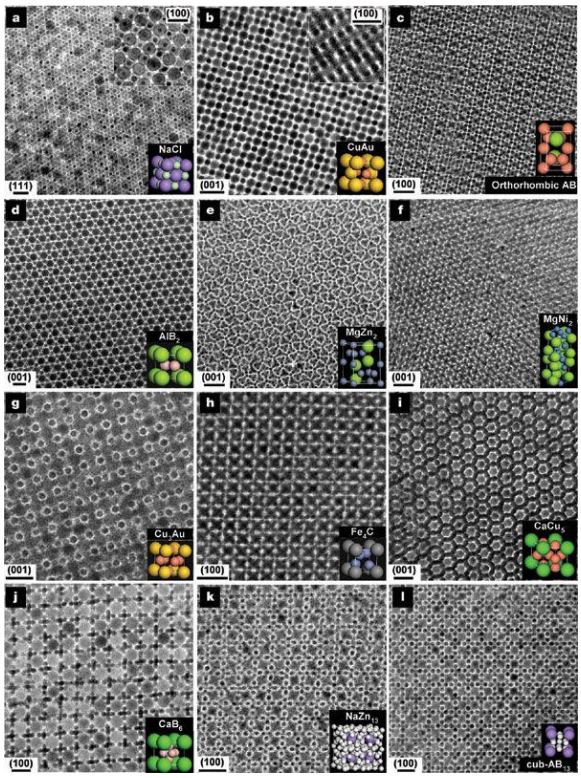

Figure 1.2: Superlattice of nanoparticles of various size ratios exhibiting close pack arrangements reminiscent of atomic crystal structures. Reproduced from reference 2**.**

1.3.1 Controlling structure with a structure-directing agent

1.3.1.1 Utilizing block-copolymer phase separation

One of the most promising methods to direct the arrangement of particles in space is through the use of a structure-directing agent, for example, block copolymers. These agents are known to reconfigure into various thermodynamically stable arrangements such as cubic close pack spheres, hexagonally close pack cylinders, gyroids and lamellae for binary linear block copolymers. The driving force for this rearrangement is the minimization of free energy, specifically that of the interface between the two dissimilar blocks in the case of a block copolymer. The degree of dissimilarly can be qualitatively appreciated by considering how the two blocks are different chemically but can be quantitatively represented by the Flory Huggins interaction parameter, χ_{AB}, defined as

$$\chi_{AB} = \left(\frac{z}{k_B T}\right)(\epsilon_{AB} - \frac{1}{2}(\epsilon_{AA} + \epsilon_{BB}) \qquad \text{Equation 1.1}$$

where z is the number of nearest neighbors per repeat unit in the polymer, k_BT is the thermal energy represented by multiplication of the Boltzman constant with temperature, and ϵ_{AA}, ϵ_{BB}, ϵ_{AB} are the interaction energies per repeat unit for A-A, B-B and A-B interactions. Borrowing from solution thermodynamics, we can understand χ as a parameter proportional to the energy of

mixing between segments normalized by thermal energy and ultimately scales the free energy of mixing for the system.

For a binary block copolymer, the theoretical phase diagram can be drawn with χN (N being the number of monomeric units in the block copolymer chain) with the block copolymer block fractions as the floating parameter. The resulting general phase diagram is presented in Figure 1.3, and the various morphologies that can be obtained are depicted in Figure 1.4. This result is obviously highly simplified as we see that the actual experimental phase diagram of a block copolymer such as polyisoprene-b-polyethylene oxide shown in Figure 1.5 deviates significantly from the theoretical phase diagram presented. However, the salient features such as the dependence of morphology on block fraction and the importance of χN are apparent. For a full exploration of the phase separation of block copolymers, the reader is referred to excellent papers by Edward Kramer, Craig Hawker, Thomas Russell, Mark Matsen and seminal work by Frank Bates.[3–5]

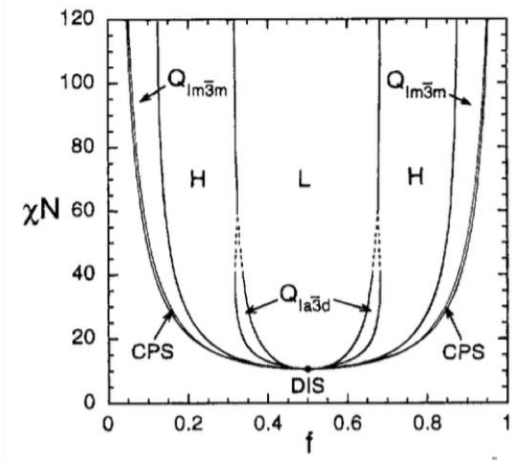

Figure 1.3: Mean field phase diagram for conformationally symmetric diblock copolymer melts. Phases indicated include lamellar (L), hexagonal cylinders (H), bicontinuous (Q_{Ia3d}), body centered cubic spheres (Q_{Im3m}), close-packed spheres (CPS), and disordered (DIS). Reproduced from reference 3**.**

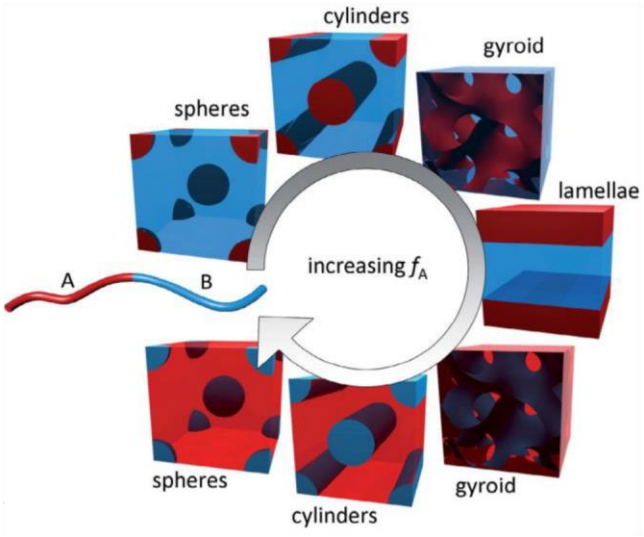

Figure 1.4: Pictorial depictions of the polymer phases that can be obtained with increasing length of block A relative to block B. Reproduced from reference 6.

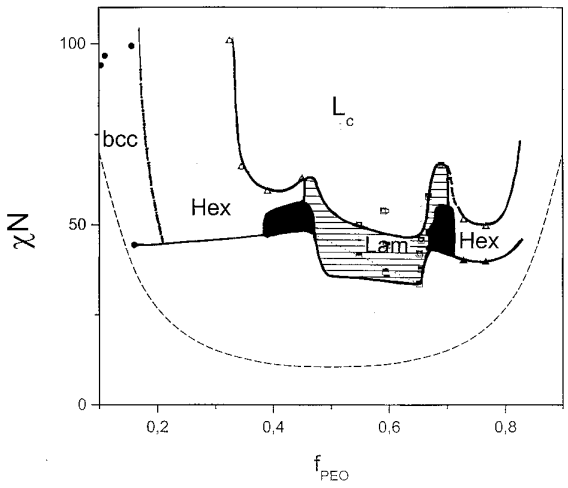

Figure 1.5: Experimental phase diagram for PI-PEO determined using small angle x-ray scattering and rheology. Reproduced from reference 7.

1.3.1.2 Utilizing block copolymer surfactant behavior

In the previous discussion on block copolymer phase separation and their tendency to form ordered structures after relaxation to their thermodynamically preferred state, we have omitted the discussion of solvents that are often used in the casting and deposition of these polymers. However, beyond facilitating casting and processing, introduction of the solvent actually introduces an additional parameter that can be used to control the morphology of the block copolymer in solution. The presence of stable morphologically distinct phases in solution should come as no surprise given the presence of distinct surfactant phases in solution that are classically understood by considering the balance in interaction between the polar headgroup, non-polar chain and the solvent. In the case of a block copolymer, the equivalent consideration

would be the interaction between the solvents or inorganic components with block A and block B of the A-B block copolymer. An example of the complexity and possibility space that this introduces is presented in Figure 1.6 where the space was mapped experimentally for polyisoprene-b-polyethylene oxide in the presence of (3-glycidyloxypropyl)trimethoxysilane and aluminum (III) sec-butoxide.

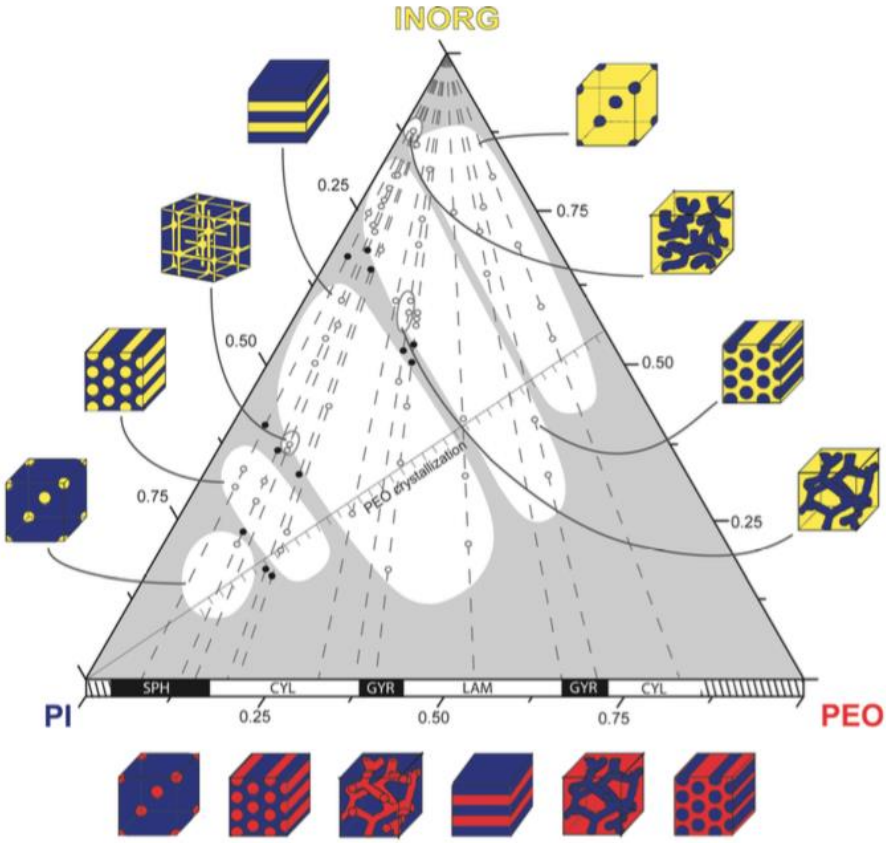

Figure 1.6: Ternary phase diagram mapping out the morphological space for PI-PEO in the presence of aluminosilicate sol nanoparticles derived from (3-glycidyloxypropyl)trimethoxysilane and aluminum (III) sec-butoxide. The bottom of the diagram shows the phase diagram of the PI-PEO block copolymer. The yellow regions in the schematic represent the PEO-aluminosilicate rich domains. Reproduced from reference 8.

1.3.2 Introducing an inorganic phase into an organic phase

Prior works on templating inorganic materials have relied primarily on introducing the inorganic component into a block copolymer template as a molecular precursor that is subsequently cross-linked using sol-gel chemistries. This approach has yielded good results for single component oxides such as titanium oxide[9,10], silicon oxide[11], vanadium oxide[12] and niobium oxide[9] to name a few. Other approaches have also utilized reduction of metal salts that are preferentially sequestered into a particular block copolymer domain to synthesize noble metal particles in a particular block copolymer domain. While both approaches can be used reliably to introduce an inorganic phase into a block copolymer domain, the primary shortcoming of the former is poor

crystallinity, necessitating further high temperature processing, while the primary shortcoming of the latter is an uneven distribution of nanoparticles and low inorganic loading in the polymer domain. Regardless, this early method of incorporating an inorganic component into the polymer was adopted because molecular precursors do not significantly perturb the polymer chain configuration. Therefore, their presence in the domain does not cause a significant entropic penalty in the system. This, however, is not the case for preformed inorganic particles.

Prior to a discussion of incorporating preformed particles, we should first consider potential benefits of starting with preformed inorganic material as opposed to what is essentially *in situ* synthesis of the material in the polymer domain after incorporation of the inorganic precursor. The benefits of using preformed particles include better control of particle size, shape, and composition. More importantly, it leverages synthetic advances in inorganic chemistry over the past two decades that have enabled the synthesis of functional inorganic materials such as quantum dots, plasmonic nanoparticles, doped oxides, magnetic materials, and upconverting nanoparticles.[13,14,15,16] The properties of these functional inorganic building blocks (photoluminescence, plasmonics, magnetism, for instance) have been shown to be highly dependent on nearest neighbor configuration of the particles thus providing further motivation for proper control of their arrangement in space for full utilization of their properties. However, incorporation of preformed particles into a polymer domain is difficult because it can significantly perturb the polymer chain often resulting in segregation of the particles out of the system. Put simply, the entropic penalty of incorporating particles into the system must be offset by an enthalpic gain from a preferred interaction between particle and polymer.

Prior work on block copolymer directed assembly of nanoparticles has relied mainly on van der Waals attractions because colloidally synthesized nanoparticles tend to be ligand capped with long chain alkyl ligands. Even so, there has been success in incorporating nanoparticles into a block copolymer domain up to about 10 vol % of particles in the system after which macrophase separation of nanoparticles out of the system is observed. This phenomenon is particularly prevalent in the case of thin film block copolymer directed assembly of nanoparticles due to the near proximity of free surfaces (film-air or film-substrate) where nanoparticles can be segregated in order to reduce the entropic penalty in the system. In order to introduce a stronger interaction between polymer and nanoparticle, we can rely on stronger molecular interactions such as hydrogen bonding and electrostatic or ionic interactions. Using noble metal particles grafted with specialty ligands that exhibit either hydrogen bonding or ionic interactions along with complementary polymer side chains, Kramer and Weisner have shown that i nanoparticles can be incorporated up to a high volume fraction of about 50 vol % in the case of bulk block copolymer nanoparticle systems.[17–19]

More recently, a new class of inorganic nanoparticles characterized by their absence of surface capping ligands were developed utilizing novel ligand stripping chemistries. This advancement has had significant implications for functional properties that rely on access to the bare nanocrystal surface. But more importantly, access to the nanocrystal surface allows access to adsorption interactions between a polymer and the nanocrystal surface thus potentially opening a new avenue for assembly. Work on these new systems is scarce but preliminary studies by

Milliron and coworkers have shown that these ligand stripped nanocrystals can be templated using specific polymers that demonstrate an affinity for the nanocrystal surface.[20–24] Specifically, block copolymers containing the polydimethylacrylamide block appear to have a significant negative enthalpic interaction with ligand stripped metal oxide nanocrystals while block copolymers containing the polydimethylacrylamide block codoped with polyacrylic acid segments have an affinity for ligand stripped metal chalcogenide nanocrystals. Assembly of these nanocrystals has been shown in micellar configuration whereby preformed block copolymer micelles that are mixed with a colloidal suspension of nanoparticles yields nanocrystal decorated micelles that can be subsequently casted into films. Interestingly, this assembly paradigm appears to be applicable to a wide variety of nanocrystal compositions.

1.4 Selected Methodology

1.4.1 Nanocrystal synthesis

The synthetic methodology employed for material synthesis in this dissertation is a highly controllable form of solution-based synthesis that is referred to generally as high temperature colloidal nanocrystal synthesis. Different from other methods for generating nanoscale objects such as the simple reduction of metal salts to yield metallic nanoparticles or the use of an acid or base to drive a condensation reaction and yield a metal oxide sol-gel, colloidal nanocrystal synthesis usually employs the decomposition of a metal salt in the presence of ligands in a high boiling point solvent under a controlled inert atmosphere. This modification affords advantages such as i) the ability to yield crystalline as-synthesized product that is size, shape and phase controlled, ii) ultra-stable colloidal dispersions, and iii) composition versatility allowing the synthesis of metal, metal chalcogenide, metal nitride, metal fluoride, and metal oxide nanocrystals.[13,15,16,25]

Typical colloidal nanocrystal synthesis involves three components, namely the metal salt, ligand, and solvent. The metal salts employed are often metal carboxylates, nitrates, and halides. Ligands consist of traditional cationic or anionic ligands such as oleic acid, oleylamine, and trioctylphosphine, and solvents include long chain hydrocarbons such as octadecene and squalene or ethers such as dioctyl ether. In synthesis, all three components are either simultaneously heated up to decompose the precursors and form nanocrystals or specific reactive metal salts such as metal chlorides or nucleophilic agents such as the alkyl amine or alkyl alcohols can be injected later at high temperature to initiate a nucleophillic attack and create a burst of nanocrystal nucleation. The former approach was primarily employed to generate all nanocrystals used in this dissertation and will be elaborated upon further below.

Traditionally, colloidal synthesis is understood by extrapolating from the model first proposed by La Mer and Dinegar in their study of the precipitation of a sulfur sol from a reaction of acid and thiosulfate. This model differentiates the growth of colloids in solution into three stages, namely monomeric buildup, nucleation and particle growth. These three stages are shown in the classical

La Mer diagram. An original figure by La Mer used to describe the nucleation and growth of a monodisperse sulfur sol is reproduced below.

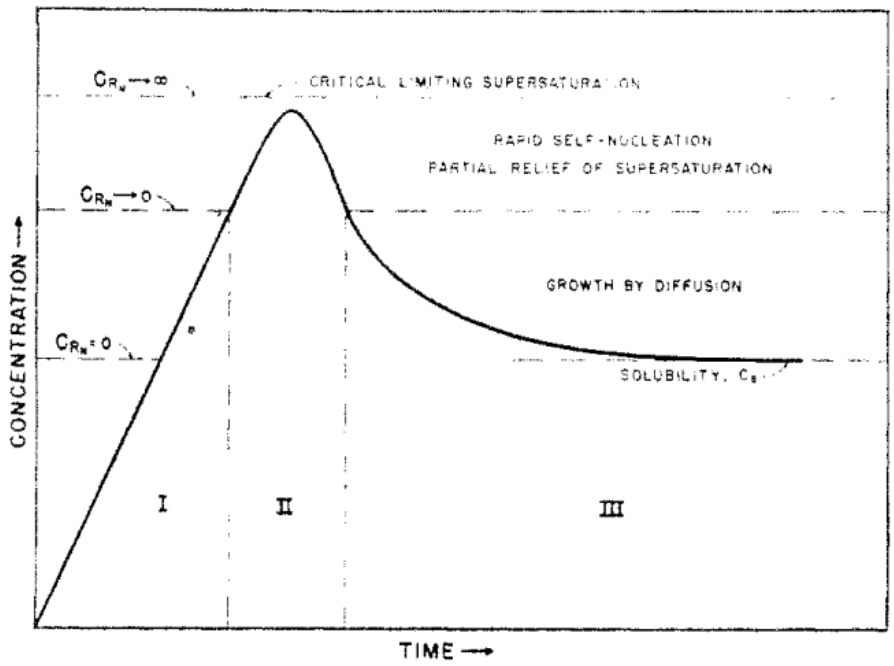

Figure 1.7: La Mer diagram describing the three phases describing the buildup, nucleation and growth of a monodisperse sulfur sol through the reaction of an acid and thiosulfate. Reproduced from reference 26.

Applied to describe nanocrystal synthesis, phase I involves gradual decomposition of metal salt precursors in solution (a metal acetate for instance) as temperature increases to initiate the buildup of active metal precursors in solution, phase II involves nucleation of nanocrystal seeds from a supersaturated monomer solution, and phase III involves growth of the nanocrystals that depletes the remaining monomers in solution. Despite its widespread use as a qualitative framework, the application of the La Mer model should be cautiously applied within this context because the model was first proposed for the homogeneous nucleation of a single component system thus limiting its use for binary, ternary, and even quaternary systems of metal oxides and metal chalcogenides commonly synthesized in the field of colloidal nanocrystals. Though, recent studies have shown qualitative mapping of viable models for both heat-up and hot-injection synthesis onto the classical La Mer model.

In the case of the heat-up synthesis of a metal oxide utilizing a metal carboxylate such as a metal oleate in the presence of a ligand (oleic acid) and a solvent (octadecene), one of the most well studied prototypical systems is the decomposition of iron oleate to form monodisperse iron oxide nanocrystals. This synthesis was employed to generate all iron oxide nanocrystals used in this dissertation, and synthetic concepts discussed here broadly apply to that of the synthesis of cerium oxide nanocrystals used in this dissertation as well. Unlike hot-injection synthesis where a reactive precursor is injected at high temperatures to induce almost immediate supersaturation of monomer to induce homogenous nucleation, the method to achieve homogeneous burst

nucleation in the heat up synthesis of nanoparticles is less direct and warrants further explanation.

Mentioned previously, the synthesis of iron oxide nanocrystals from iron oleate is the prototypical model system to study the heat-up synthesis of nanocrystal and is particularly instructive for the development of heat-up synthesis that can generate monodisperse nanocrystals. In this synthesis, the formation of nanocrystals is composed of two distinct steps: i) the thermal decomposition of iron-oleate to form monomers, and ii) the nucleation and growth of iron oxide nanocrystal. From this understanding, simple solutions that describe the nucleation and growth process of nanocrystals can be derived. Starting with nucleation, we can arrive at a nucleation rate by assuming that the free energy change upon nucleation is equal to the free energy change from nucleating a particle at a critical radius r_c, From classical nucleation theory, we know that the free energy change for nucleation of a condensed phase takes the form

$$\Delta G(r) = \frac{4}{3}\pi r^3 \Delta G_v + 4\pi r^2 \gamma \qquad \text{Equation 1.2}$$

where γ is the surface energy, r is the radius of the particle, and ΔG_v is the free energy change resulting from the change in phase (a negative number). These relative contributions are shown graphically below.

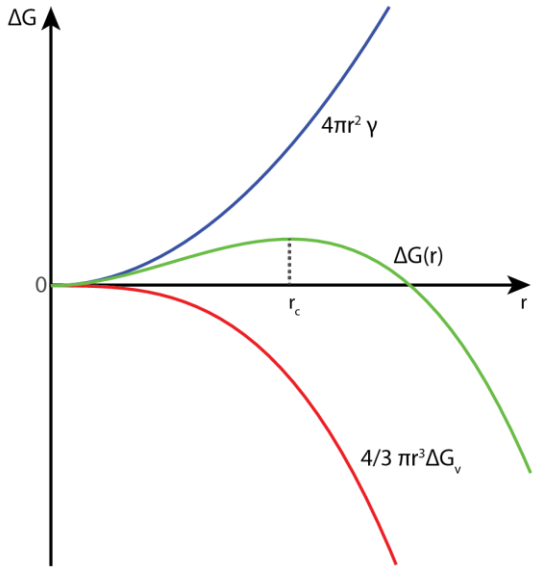

Figure 1.8: Illustration of the respective contributions of the volumetric free energy contribution and interfacial energy contribution to the total free energy change

From this, we can readily appreciate the existence of a critical nucleus of radius r_c after which nucleation becomes preferable. Specifically, one can solve for r_c by assuming $d\Delta G/dr\ (r = r_c) = 0$. Furthermore, with the temperature dependence of ΔG_v discussed shortly, as temperature increases, the critical nucleus size decreases.

$$r_c = -\frac{2\gamma}{\Delta G_v} \qquad \text{Equation 1.3}$$

For an estimation of ΔG_v, if we use a simplified picture of nucleation of a crystallized monomer solid from a solution consisting of the same monomers, we can express this change in free energy as

$$\Delta G(n) = -nkT \ln S_s \qquad \text{Equation 1.4}$$

where S_s is the supersaturation ratio given by the ratio of monomer concentration c, and the equilibrium monomer concentration c_e. For consistency, we can express this volumetrically by scaling with the molar volume V_m

$$\Delta G_v = -\frac{1}{V_m} RT \ln S_s \qquad \text{Equation 1.5}$$

From this, we can now express a nucleation rate assuming an Arrhenius relation as

$$\frac{\mathrm{dN_{nuc}}}{\mathrm{dt}} = A \exp\left(-\frac{\Delta G(r=r_C)}{k_B T}\right) \qquad \text{Equation 1.6}$$

where N_{nuc} is the number of nuclei in the system. Plugging in the results for ΔG_r at r_c expressed in terms of the supersaturation ratio, we get

$$\frac{dN_{nuc}}{dt} = A \exp\left(-\frac{16\pi\gamma^3 V_m^2}{3k_B^3 T^3 N_A^2 (\ln S_s)^2}\right) \qquad \text{Equation 1.7}$$

Here, despite the multiple simplifications and assumptions, we can still arrive at two instructive results, namely an increase in nucleation rate with an increase in temperature or an increase in supersaturation.

As a first approximation for the growth of the particles, we can combine Fick's laws of diffusion and the Gibbs-Thompson relation for a spherical particle to arrive at the following expression. The full derivation is covered in reference [13] but in short, the growth rate of particles in the system can be expressed in terms of reduced variables r* and τ that map to the particle radius, r, and reaction time, t.

$$\frac{dr^*}{d\tau} = \frac{S - \exp\left(\frac{1}{r^*}\right)}{r^* + K} \qquad \text{Equation 1.8}$$

$$r^* = \frac{RT}{2\gamma V_m} r \qquad \text{Equation 1.9}$$

$$\tau = \frac{R^2 T^2 D[M]_o}{4\gamma^2 V_m} t \qquad \text{Equation 1.10}$$

$$K = \frac{RT}{2\gamma V_m} \frac{D}{k} \qquad \text{Equation 1.11}$$

where D is the diffusion constant, k the reaction rate, and $[M]_o$ a scaling concentration for paramerization with the Gibbs-Thompson relation. The most important value here is K because it contains the first term that describes the influence of surface energy thus dictating how size would ultimately affect the chemical potential of an atom on the surface, and the second term (the ratio of D and k) that describes the competing influences of diffusion limited or reaction

limited kinetics. In the case where D ≫ *k*, the system is not impeded by monomer diffusion and growth is limited by reaction of the monomer on the surface of the particle. Conversely, with *k* ≫ D, growth is limited by the rate of diffusion of monomers to the particle surface. When S_s, the degree of supersaturation is large, naturally the system would suffer less from diffusion limitations so ultimately, systems that nucleate and then subsequently grow under sufficiently high supersaturation would expectedly be reaction limited. These trends are shown graphically below.

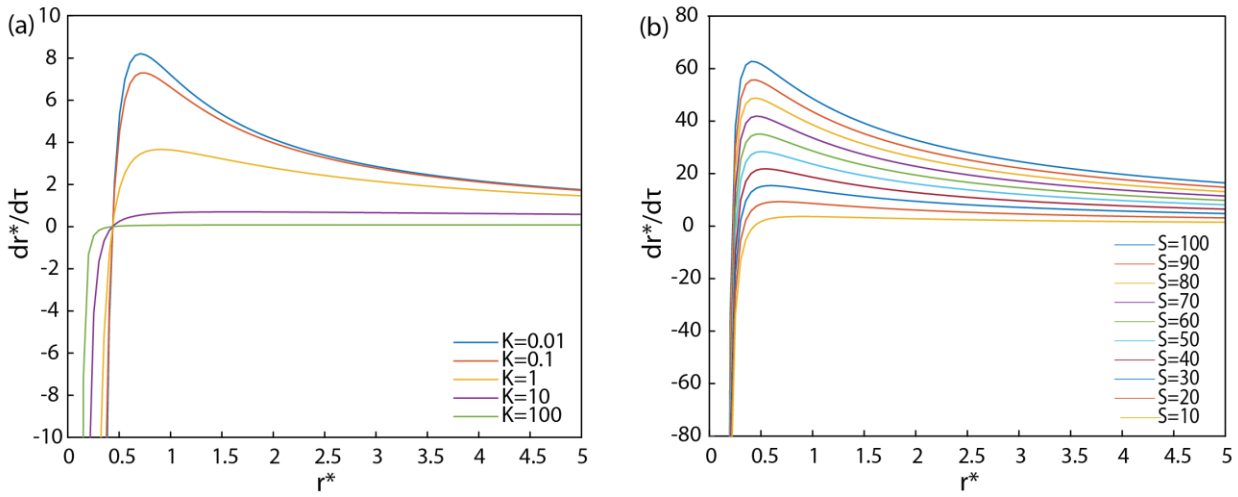

Figure 1.9: (a) The influence of increasing K on the growth rate of a particle with S=10, and (b) the influence of increasing S_s on the growth rate of the particle with K=1.

Last, on the applicability of such simplified models on actual nanocrystal systems where nucleation and growth involves two or more elements, a seminal study using iron oxide has in fact shown that nucleation and growth appears to have La Mer form. Shown below, we see that the number of nanocrystals and nanocrystal size as a function of time takes a shape close to that of the La Mer model, and that nucleation and growth can be distinguished as two separate stages in the synthesis.

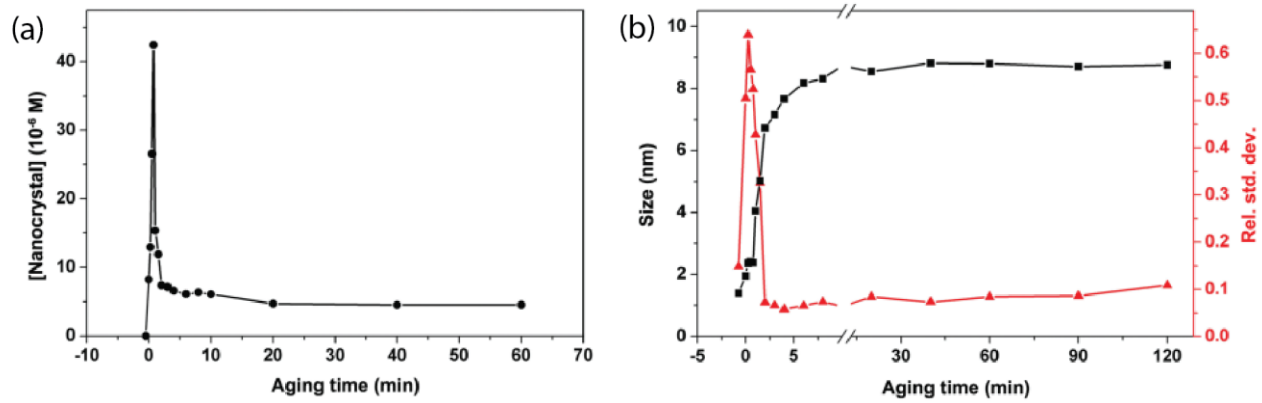

Figure 1.10: (a) Change in nanocrystal concentration as a function of time, and (b) change in nanocrystal size as a function of time. Time zero is set at the time when the reaction reached the desired reaction temperature of 320 °C for the thermal decomposition of iron oleate. Reproduced from reference 13.

1.4.2 Ellingham diagrams, reducibility, and stability

In the latter sections of this dissertation, we will be exploring the stability of intermediate temperature proton conduction, and as part of that investigation, we will have to consider material stability as a function of temperature, oxygen partial pressure, and water partial pressure. This can be qualitatively achieved by examining the Ellingham diagram for a material. Such as diagram is a simple plot of $\Delta G = \Delta H - T\Delta S$ where ΔH is the enthalpy change and y-intercept while $-\Delta S$ is the entropy change and slope. Assuming that the contribution to ΔS is largely configurational and therefore not temperature dependent, we would expect a constant slope with temperature. A traditional Ellingham diagram illustrates the oxidation of a pure metal into its oxide counterpart. However, for a system with the same cationic component, we can also plot the curve for the transformation between two phases of the oxide as shown in the diagrams below for cerium oxide.

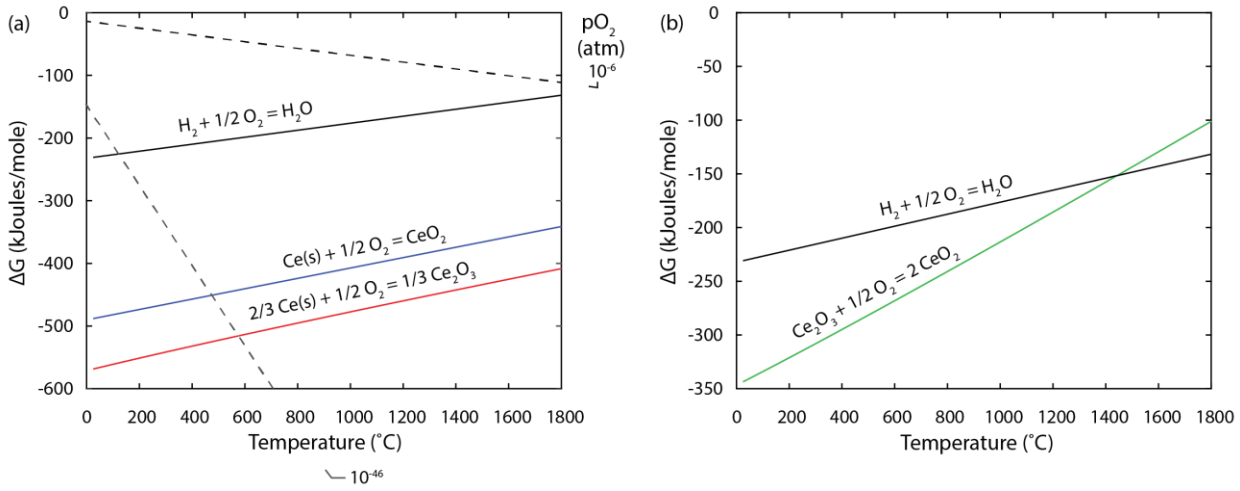

Figure 1.11: (a) Ellingham diagram for cerium oxide and water with an oxygen partial pressure outer axis. The dotted lines show the Ellingham construction for the two partial pressures of 10^{-6} atm and 10^{-46} atm. (b) A modified Ellingham diagram for the oxidation of Ce_2O_3 to CeO_2.

From this Ellingham diagram, we can immediately arrive at a few preliminary hypotheses for the system. First, for the partial pressure of oxygen investigated in this dissertation (pO_2 > 1e-6 ppm), cerium (IV) oxide is not expected to undergo any oxidation from CeO_2 to Ce_2O_3. Second, from the qualitative location of cerium oxide on the Ellingham diagram relative to that of the formation of water from H_2 and O_2, the phenomenon of intermediate temperature proton conduction is expected whereby cerium (III) oxide in the presence of water would readily dissociate water to form hydrogen gas and a higher cerium (IV) oxide below the temperature at which both curves intersect.

1.4.3 Defect chemistry

From the second law of thermodynamics, we can conclude that that even a 'perfect' single crystal has an equilibrium defect concentration due to the gains in mixing entropy in the dilute regime. In the case of metal oxides, defect reactions and defect chemistry is particularly intriguing because the chemical potential of oxygen in the lattice can ideally be controlled with the partial pressure of oxygen in the surrounding environment. Before discussing defects further however, it is imperative to first note the three criteria that defect reactions must obey, namely i) mass balance, ii) conservation of lattice sites, and iii) electroneutrality, and introduce suitable notation to facilitate the discussion, namely the Kroger-Vink notation below.

$$M_S^C$$

In this notation, M is the identity of the defect, S is the defect site, and C is the charge of the defect (X for no charge difference, $'$ for a negative charge and $^\bullet$ for a positive charge). Using a prototypical example of cerium in its native site where there is no charge difference, the notation would be expressed as Ce_{Ce}^X.

Using this formalism, we can now express the formation of the most common point defect in metal oxides, namely the oxygen vacancy and see its direct dependence on the partial pressure of oxygen.

$$M_M^X + \mathrm{O_O^X} \rightarrow M_M^X + V_O^{\cdot\cdot} + 2\,e'' + \frac{1}{2}O_2(g) \qquad \text{Equation 1.12}$$

$$2\,M_M^X + O_O^X \rightarrow 2\,M_M' + V_O^{\cdot\cdot} + \frac{1}{2}O_2(g) \qquad \text{Equation 1.13}$$

In the first case, charge is compensated by free electrons that reside in the conduction band of the system and provide intrinsic n-type conductivity. In the second case, charge is compensated by a reduction in the formal charge of the metal center and can be understood as an electron that is localized at the metal site, formally called a small polaron. Other intrinsic defect mechanisms include Schottky defects and Frenkel defects where the former involves stoichiometric removal of both the cation and anion to generate a cation and an anion vacancy, while the latter involves migration of either the cation or anion into an interstitial site and accompanying electronic charge compensation. Examples of both assuming a MO system such as ZnO are shown below.

$$Schottky\ defect: M_M^X + O_O^X \rightarrow V_M'' + V_O^{\cdot\cdot} \qquad \text{Equation 1.14}$$

$$Cation\ Frenkel\ defect: M_M^X \rightarrow M_i^{\cdot\cdot} + V_M'' \qquad \text{Equation 1.15}$$

$$Anion\ Frenkel\ defect: O_O^X \rightarrow O_i'' + V_O^{\cdot\cdot} \qquad \text{Equation 1.16}$$

$$Intrinsic\ electronic\ neutrality: null \rightarrow e' + h^{\cdot} \qquad \text{Equation 1.17}$$

Beyond intrinsic defects, one can also controllably introduce defects in a system (extrinsic defects) in attempts to tune the properties of a material. For instance, aliovalent doping of metal oxides using a donor dopant is a known method to increase the free carrier concentration in a

material. This has been used to augment the properties of indium oxide using tin oxide as the substitutional aliovalent dopant. This reaction is shown below.

$$2\ \mathrm{SnO_2} \xrightarrow[In_2O_3]{} 2\ Sn_{In}^{\cdot} + 3\ \mathrm{O_O^X} + 2\ e' + \frac{1}{2} O_2\ (g) \qquad \text{Equation 1.18}$$

Conversely, acceptor doping also used to tune the properties of metal oxides, and is commonly used as in the case of cerium oxide where a trivalent ion (gadolinium, samarium, etc.) is used to pin the oxygen vacancy concentration in the system. This reaction is shown below alongside the intrinsic formation of Ce^{3+} often observed in cerium oxide systems for comparison.

$$2\ Ce_{Ce}^{X} + 4\ O_O^X \rightarrow 2\ Ce_{Ce}' + V_O^{\cdot\cdot} + 3\ O_O^X + \frac{1}{2} O_2(g) \qquad \text{Equation 1.19}$$

$$\mathrm{Gd_2O_3} \xrightarrow[CeO_2]{} 2\ Gd_{Ce}' + 3\ \mathrm{O_O^X} + V_O^{\cdot\cdot} \qquad \text{Equation 1.20}$$

These mechanisms will play a significant role in determining the ultimate behavior of materials in the latter portions of this dissertation where we discuss the influence of defect chemistry on the intermediate temperature proton transport in materials.

1.4.4 Impedance spectroscopy

AC impedance spectroscopy is a frequency dependent characterization method used to characterize the frequency dependent resistance or impedance of a system. Unlike traditional DC conductivity measurements where a single voltage or current is applied for a measurement of a corresponding current or voltage with resistance calculated with V=IR, impedance spectroscopy is conducted by applying a small sinusoidal voltage under the assumption of linearity within this small voltage window. Then, the sinusoidal current response is measured providing us with both the scalar magnitude as well as its phase in relation to the input voltage. Expressed with Euler's formula, we can write

$$V(t) = V_o + V_a \exp(j\omega t) \qquad \text{Equation 1.21}$$

and a corresponding current response

$$I(t) = I_o + I_a \exp(j\omega t + \phi) \qquad \text{Equation 1.22}$$

To quantify a system's response to an AC perturbation, under the assumption of linearity within the perturbation window, the relationship between V and I can be predicted by constructing a transfer function that converts an AC voltage input into an AC current output or vice versa. Expressed generally, this transfer function $Z(j\omega)$, is the characteristic impedance of the system.

$$Z(j\omega) = \frac{V(j\omega)}{I(j\omega)} \qquad \text{Equation 1.23}$$

The transfer functions for various common circuit elements are reproduced below. Once expressed as follows, the impedance of a circuit containing multiple elements can be expressed by treating each element like that of a resistor

Table 1.1: Table of transfer functions for various common circuit elements.

Resistor	$Z_{resistor} = R$	R is the resistance of the system
Capacitor	$Z_{capacitor} = \frac{1}{j\omega C}$	C is the capacitance of the system
Inductor	$Z_{inductor} = j\omega L$	L is the inductance of the system
Constant phase element (non-ideal capacitor)	$Z_{CPE} = \frac{1}{Q(j\omega)^{\alpha}}$	Q is the qualitative equivalence of capacitance and α is term to account for non ideality that takes on values usually between 0.9 and 1.
Warburg element (solution to an infinite length one dimensional diffusion from a flat surface)	$Z_W = \frac{A_w}{\sqrt{j\omega}}$ $A_w = k_B T \frac{1}{n^2 F^2 A C_o \sqrt{D}}$	k_B : Boltzmann constant T : temperature n : charge of the mobile species F : Faraday's constant A : surface area C_0: surface concentration D : diffusion constant

As an AC measurement, the technique is inherently sensitive to differences in the system in the time domain. Therefore, in applications for measuring conductivity, on top of measuring total conductivity in the system, the technique also allows one to potentially decouple various contributions to conductivity such as from mobile ions or electrons, or from conductivity arising from a bulk or an interface assuming that each contribution has a sufficiently different relaxation time constant to be resolved. When applied to materials characterization, the technique does not however provide information about the source of the difference. In other words, the impedance response of a system may not be unique and physical intuition about the system must be used to both propose a viable equivalent circuit and interpret the results of the fit.

1.4.5 Small angle x-ray scattering (SAXS)

SAXS is a popular technique for the characterization of structure on the 1-200 nm length scale and has been extensively applied for characterization of porous structure, gel networks, block copolymer assemblies, colloids, and more generally of materials that exhibit nanoscale heterogeneity. As a scattering technique, it is useful for its capacity to probe multiple length scales of structure and to incorporate information from a representative sample volume, especially when used in conjunction with microscopy techniques for real space structural correlation. However, as it is not a direct recording of structure in real space, wherein the structural data is encoded in reciprocal space as a function of the scattering vector or momentum transfer vector (**q,** whose magnitude has units of inverse distance, $Å^{-1}$), interpretation of the results in terms of real space structure (size, shape, spacing, *etc.*) requires varying levels of

sophistication in data analysis depending on the complexity of the sample and the information required to address a given research question.

The raw SAXS data is often a 2-D data map of intensity in two perpendicular directions. If the pattern is anisotropic, for example due to preferential orientation of block copolymer domains or symmetry breaking due to substrate effects, the pattern can be analyzed in its 2-D form to obtain information such as domain orientations, or directionally dependent strains. Often, most samples such as nanoparticles or macromolecules in solution scatter isotropically. Hence, the data can be reduced to a 1-D scattering pattern by circular averaging without loss of information.

Generally, results from scattering experiments can be qualitatively understood as a multiplicative contribution from three components: i) a difference in electron density between the scatterer and its environment that provide x-ray contrast, ii) the form factor of a primary scatterer that is a function of the material's electron density distribution in space, and iii) the structure factor that is a function of the spatial arrangement of the primary scatterer. Specifically, the contribution of all three components to the final scattered intensity is as follows

$$I(q) = I_0\, \Delta\rho^2 V^2 N_p\, P(q) S(q) \qquad \text{Equation 1.24}$$

where I_0 is the incident x-ray intensity accounting for sample transmittance, Δρ is the difference in electron density, V is the volume of the primary scatterer, N_p is the number of scatterers, P(q) is the form factor, and S(q) is the structure factor. The form factor contains information about properties inherent to the primary scatterer such as size, shape, and conformation while the structure factor contains information about collective structural properties such as interparticle spacing, domain size and arrangement symmetry.

To obtain these pieces of information, first order analysis of the 1-D scattering data utilizes standard plots that accentuate specific features pertinent to the system under study. When the data is plotted simply as **I**(q) versus **q**, intensity increase at any q corresponds to scattering from features present at that particular real space length scale, d = 2π/q . For instance, a powder sample with three distinct crystallite sizes will show distinct "humps" at three different **q** values. For strongly scattering periodic structures, such as lithographically defined nanostructures, block copolymer phase separated morphologies, and mesoporous metal oxides, these "humps" manifest as peaks due to scattering being dominated by the structure factor, and the value of **q** at the peak is proportional to the characteristic spacing in the material. Examples of standard plots include the Guinier plot ln(**I**(q)) versus $\mathbf{q}^2$, Krattky plot **I**(q) $\mathbf{q}^2$ versus **q**, Zimm plot 1/**I**(q) versus $\mathbf{q}^2$, and Porod plot **I**(q) $\mathbf{q}^4$ versus $\mathbf{q}^4$. Each plot is meant to accentuate specific intensity scalings with q that will become evident in the case for the generalized Guinier shapes as follows.

Table 1.2: Table of Guinier solutions for the radius of gyration for the spheroid, rod and sheet.

Shape	Solution
Spheroid *Radius of gyration, R_g*	$I(q) = A \exp(-\frac{R_g^2 q^2}{3})$
Rod *Radius of gyration, R_g* *Length, $L = \sqrt{2}\, R$*	$I(q) = \frac{\pi}{q} A \exp(-\frac{R_g^2 q^2}{2})$

Sheet *Radius of gyration, R_g* *Thickness, $t=\sqrt{12}\,R$*	$$I(q) = \frac{2\pi}{q^2} A \exp(-R_g^2 q^2)$$
Generalized formula	$$I(q) = \begin{pmatrix} 1 & for\ \alpha = 0 \\ \alpha\pi q^{-\alpha} & for\ \alpha = 1,2 \end{pmatrix} A \exp\left(-\frac{R_\alpha^2 q^2}{3-\alpha}\right)$$ $$\alpha = 0\,, spheroid$$ $$\alpha = 1\,, rod$$ $$\alpha = 2\,, sheet$$

For samples with no regular architecture where S(q)=1, the form factor of the scatterer (each protein or nanocrystal in an assembly, for example) would be the dominant contribution. If the shape of the primary scatterer were not perfectly geometric such as that of a protein, we can start with a generalized approach such as one formulated by Guinier. This Guinier formulation for three shapes is shown in Figure 1.12 for contrast with the actual form factor solutions provided shortly.

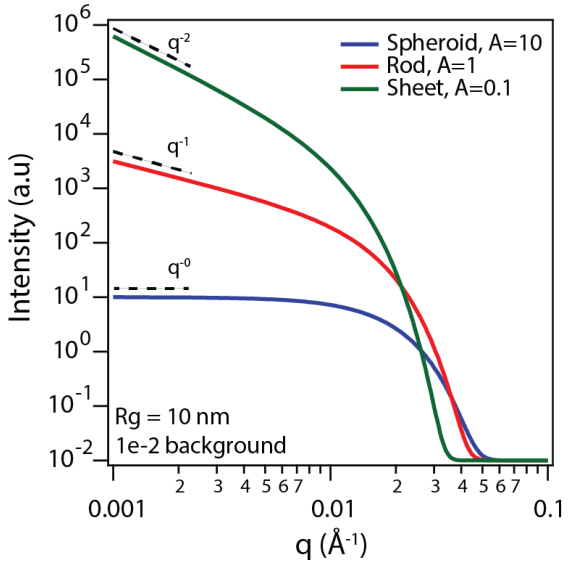

Figure 1.12: Generalized Guinier form factors for three shapes showing the difference in intensity scaling with q. I(q) was plotted with a background intensity of 1e-2 to enhance clarity.

To obtain more quantitative information, a second level analysis can be performed by fitting the data with empirical models such as different nanoparticle form factors, specific structure factor models that assume particular structural arrangements, or generalized treatments for aperiodic structures. In the case of nanoparticle form factors, the closed form of I(q) can be obtained by Fourier transform of the real-space shape function. This allows accurate sizing of inorganic materials with statistical significance even for ultra-small particles that are difficult to size in microscopy, and non-destructive *in situ* evaluation of morphological changes such as particle growth, elongation, etc. Alternately, the form factor can be removed to allow assessment of the pure structure factor to obtain information about particle spatial distribution or interparticle

forces. The analytical solutions for common geometries such as spheres, core-shell, cylinders, and sheets are reproduced below. The solutions for more complicated geometries are conveniently available in a compilation by Joachim Kohlbrecher and Ingo Bressler in the guide for the SAXS software package SASfit.[27]

Table 1.3: Table containing the analytical solution to the form factor for four common geometries: sphere, core-shell, cylinder, and thin disc sheet.

Shape	Solution
Sphere *Radius, R*	$I(q,R) = \left[\frac{4}{3}\pi R^3 \Delta\eta^3 \ \frac{(\sin(qR) - \cos(qR))}{qR^3}\right]^2$
Core-shell *Inner radius R2,* *Outer radius, R1*	$I(q,R1,R2,\Delta\eta,\mu) = [K(q,R1,\Delta\eta) - K(q,R2,\Delta\eta(1-\mu))]^2$ $K(q,R,\Delta\eta) = \frac{\frac{4}{3}\pi R^3 \Delta\eta \ 3(\sin qR - qR cos\ qR)}{(qR)^3}$ $Core\ scattering\ contrast: \mu\Delta\eta$ $Shell\ scattering\ contrast: \Delta\eta$
Cylinder *Radius, R* *Length, L*	$I\ = 16\ (\pi R^2 L^2)\Delta\eta^2 \int_0^1 \frac{J_1\left(qR\sqrt{1-x^2}\right) \sin\left(\frac{qLx}{2}\right)}{q^2 R\sqrt{(1-x^2)}Lx}\ dx$ J denotes the Bessel function of the first kind
Sheet *Thickness, L* *Disc radius, R*	$P_{planar}(q) = \frac{\pi^2 R^4 \eta^2 2}{(qR)^2}\ (1 - \frac{1}{qR} J_1 2qR)$ $P_{cross-section}(q) = \left(\eta L \frac{\sin\left(\frac{qL}{2}\right)}{\frac{qL}{2}}\right)^2$ $I(q) = P_{planar}(q) P_{cross-section}\ (q)$ Two-part factorization of the form factor applied to solve for the form factor for very anisotropic particles

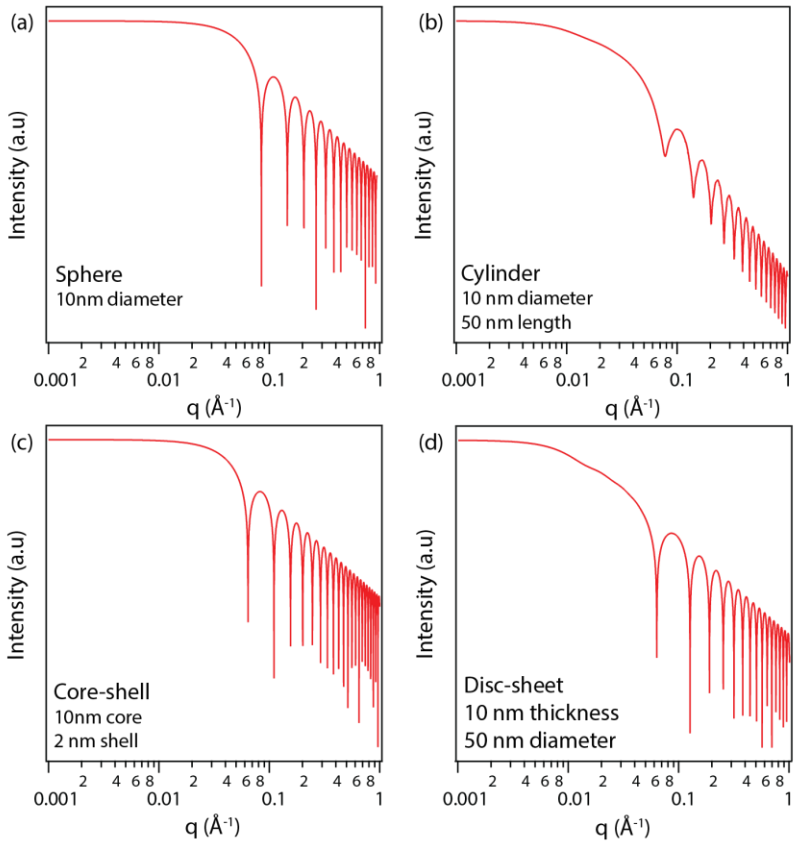

Figure 1.13: Monodisperse form factors for four shapes: sphere, cylinder, core-shell sphere, and thin-sheet disc.

As alluded to previously, when particles interact to form assemblies, a structure factor that describes the extended arrangement of particles in the system tends to emerge. In this case, for simple packing of particles under clear geometric arrangements, the structure factor consist of peaks where higher order peaks are related to the primary scattering peak by a characteristic multiplier. These multipliers are similar to ones calculated for various crystal structures. In fact, for single crystals patterns, assignment of peaks in SAXS in both a 1-D structure factor as well as in 2-D patterns follows the same basic principles used to index standard x-ray diffraction and electron diffraction patterns. The ratios for three common geometries are given below.

$$Lamellar\ symmetry: 1, 2, 3, 4, 5, \ldots$$

$$Cubic\ symmetry: 1, \sqrt{2}, \sqrt{3}, 2, \sqrt{5}, \ldots$$

$$Hexagonal\ symmetry: 1, \sqrt{3}, 2, \sqrt{7}, 3, \ldots$$

As the assembly becomes more disordered, one would have to examine the structure factor as-is or fit it to known empirical models that solve for the structure factor solution in SAXS. Before discussing the various structure factors, we must first discuss how the structure can be combined with the form factor to yield the final scattering spectra. We have asserted previously that I(q) should be simply proportional to F(q) S(q) where F(q) is the form factor and S(q) is the structure

factor. However, this simple formulation actually only applies to monodisperse systems and is termed the monodisperse approximation. Other than this, two well-accepted approximations for the total intensity for a non-monodisperse sample are the decoupling approach and the local monodisperse approximation. In the decoupling approach, we assume that particle size and orientation are uncorrelated with the position of the particles so a particle has equal probability of interacting with another particle in the system regardless of properties of the polydispersity. This allows simplification using an average form factor weighted by the distribution in particle size, and ultimately manifest as a correction factor to the structure factor. This correction factor is a ratio of the average form factor and the monodisperse form factor that suppresses the structure factor (its value decreases) as the average form factor deviates from the monodisperse form with increasing polydispersity. On the other extreme, the local monodisperse approximation assumes that particles of a particular size are always surrounded by particles of the same size. Therefore, scattering from an ensemble of particles can be represented by multiple populations of sub-systems each with a form factor and structure factor that is then recombined and weighted by the size distribution. An illustration of these three approximations is shown below using the classic hard-sphere structure factor with the Percus-Yevick closure relation (this closure relation will be discussed shortly).

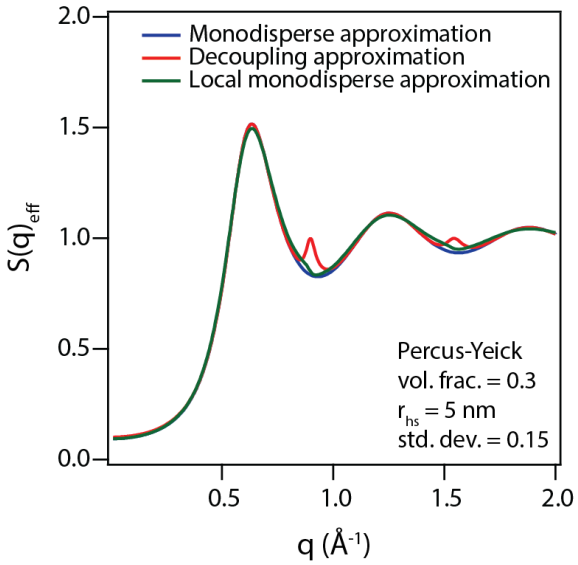

Figure 1.14: The influence of the three approximations on the predicted effective structure factor for a Percus-Yevick hard sphere model with a 5 nm hard sphere radius, and 15% standard deviation in a Gaussian size distribution.

Having discussed how the structure factor can be decoupled from the form factor, we can now consider how we can arrive at the structure factors themselves. The derivation of a non-lattice structure factor often starts with a closure relation in order to compute the radial distribution function of which the structure factor is the Fourier transform. A radial distribution function g(r) for a pair of particles can be computed if we knew how particles interact directly and indirectly (through another particle) with one another. This is the Ornstein-Zernike construction that decomposes the total correlation function that describes total influence between a pair of

particles in the system into a direct correlation function c(r) and an indirect component expressed in integral form involving c(r).

$$h(r) = g(r) - 1 \qquad \text{Equation 1.25}$$

$$h(r) = c(r) + N \int dr\, c(r - r')h(r) \qquad \text{Equation 1.26}$$

Note that we are trying to solve the second equation, but it contains both $h(r)$ and $c(r)$ as unknowns. Therefore, we need one more independent expression in order to solve for the two unknowns. This additional expression is termed a closure relation. Two common assumed closure relations are presented below.

Table 1.4: Table containing the two main closure relations used to solve for the structure factor, namely the Percus-Yevick closure relation and the mean spherical approximation.

Closure relation	Assumption
Percus-Yevick closure relation	$c(r) = g(r)\left[1 - \exp\left(-\frac{U(r)}{k_B T}\right)\right]$ where $U(r)$ is some interaction potential in the system
Mean spherical approximation	$c(r) = -\beta U(r), r > D$ $h(r) = -1, \quad r < D$ $\beta = \frac{1}{k_B T}, D\ is\ the\ diameter\ of\ the\ particle$ where $U(r)$ is some interaction potential in the system

Building upon the closure relation, specifically the Percus-Yevick closure, we can arrive at a structure factor after assuming some interaction potential $U(r)$. The structure factors for the hard-sphere, and sticky hard-sphere (Baxter model) are presented below as examples. The reader is referred to reference [27] for the full derivation and analytical solution for the models.

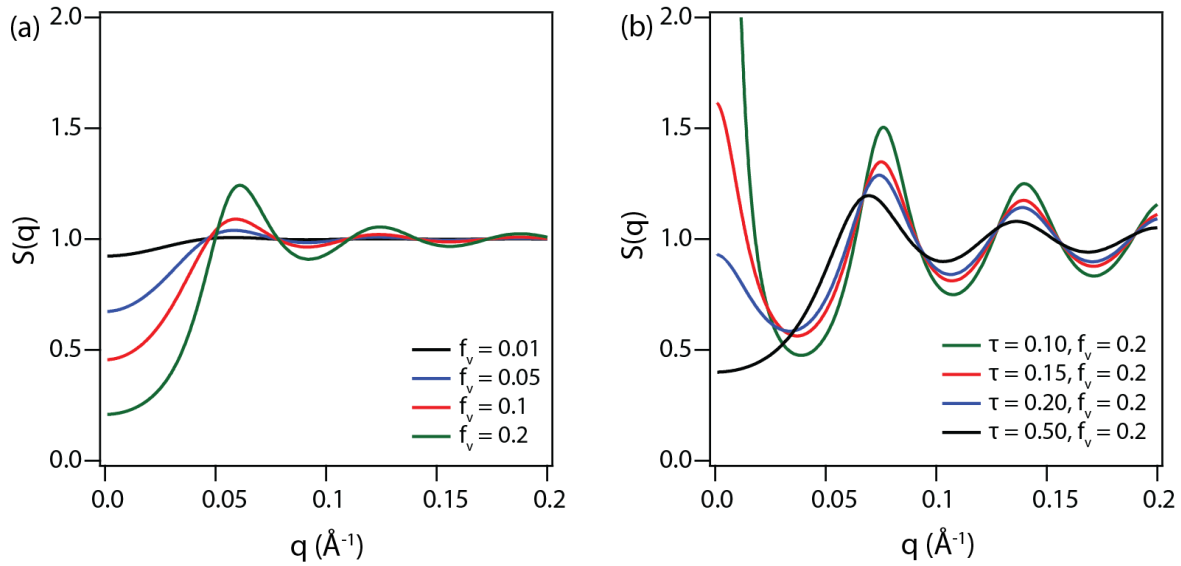

Figure 1.15: (a) Hard-sphere structure factor and (b) sticky hard sphere structure factor solved using the Percus-Yevick closure relation. f_v denotes the colloid volume fraction, and τ is the 'stickiness' parameter where lower values imply more 'stickiness.'

Finally, for structures that are almost disordered such as that of gels or fractals, where the scattering profiles may no longer appear particulate and bear more resemblance to a general two phase system, we can adopt approaches previously derived for randomly distributed two phase inhomogeneous systems. Classic examples of these approaches include the Ornstein-Zernike formulation with a Lorentzian profile $I(q)=[1+q^2\xi^2]^{-1}$, and the Debye-Anderson Brumberger form factor $I(q)=[1+q^2\xi^2]^{-2}$. Ultimately, these profiles assume no shape factor and no structure factor and involve only a general correlation length ξ and a functional form that can properly fit the observed peak shape in SAXS at the location ξ.

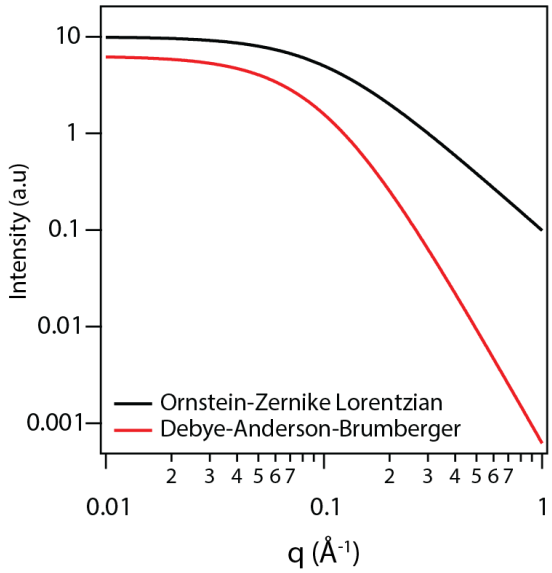

Figure 1.16: (a) Ornstein Zernike solution using a Lorentzian, and (b) Debye-Anderson-Brumberger form factor as general models for fitting single correlation peaks

The methods above apply generally to SAXS techniques, but the methods used in this dissertation involve SAXS conducted in both transmission geometry where all the points noted above apply, and in grazing incidence geometry where modifications to the theory must be made prior to application.

In grazing incidence small-angle x-ray scattering (GISAXS), the sample is exposed to the x-ray beam at an angle of grazing incidence to increase the amount of material seen by the beam. This technique allows us to probe structure in thin films or on thick substrates where x-ray penetration in transmission geometry would be impossible. The technique is usually done at an angle below the critical angle of the substrate so that all x-rays are reflected from the substrate, but at an angle that is either above or below the critical angle of the film. In the case of the former where the incidence angle is lower than the critical angle of the film, x-ray penetration is minimized and the resulting scattering pattern arises from the evanescent wave right below the film-air interface with penetration depth on the order of 1-10 nm depending on the material. For an incident angle above the critical angle, it is assumed that the whole thickness of the film is probed and sampling is only limited by x-ray absorption in the material. The critical angle of a film can be determined experimentally by x-ray reflectivity, or calculated for simple materials if the scattering length density or similarly the x-ray n and k values, where n is the refractive index and k is the extinction coefficient of a material, are known. It is important to note that all these values are dependent upon the x-ray energy. The relevant equations for the calculation of critical angle and penetration depth are included below along with the critical angle and penetration depth for a few materials calculated using the material's scattering length density at 10 keV ($\lambda = 0.124$ nm) and 8.05 keV ($\lambda = 0.154$, Cu Kα) x-ray energy.

$$SLD = \frac{(r_e \Sigma f_i)}{V_m} \qquad \text{Equation 1.27}$$

$$q_c = \sqrt{16\pi SLD} \qquad \text{Equation 1.28}$$

$$\theta_{critical} = \arcsin\left(\frac{\lambda q_c}{4\pi}\right) \qquad \text{Equation 1.29}$$

$$z_{1/e} \sim \frac{1}{q_c} \qquad \text{Equation 1.30}$$

Table 1.5: Critical angles and x-ray penetration depths for select materials at two different x-ray energies.

	α_c (critical angle) (degrees)						
λ (nm)	Polystyrene	Polydimethylacrylamide	Fe_2O_3	CeO_2	In_2O_3	Au	Si
0.124	0.12	0.13	0.26	0.29	0.29	0.46	0.18
0.154	0.15	0.16	0.32	0.36	0.36	0.57	0.22
Penetration depth (nm) (below α_c)	4.7	4.4	2.1	1.9	1.9	1.2	3.2

where r_e is the classical electron radius, f_i is the atomic form factor of element i, V_m is the unit cell volume, SLD is the scattering length density, λ is the x-ray wavelength, and $z_{1/e}$ is the depth at which the evanescent wave decays to a scale of 1/e beneath the surface.

Shown below is this influence of critical angle on the scattering observed. The data is a simulation of the 2-D GISAXS data for 20 nm diameter Au nanoparticles embedded in a carbon matrix with a 5 nm carbon top layer under the Distorted Wave Born Approximation (discussed shortly) using the BornAgain software package.[28] We see that when we are below the critical angle (1/2 α_c) of the matrix (ca. 0.12 degrees), the scattering is significantly diminished but not extinguished. Conversely, the scattering is much more pronounced above the critical angle of the film.

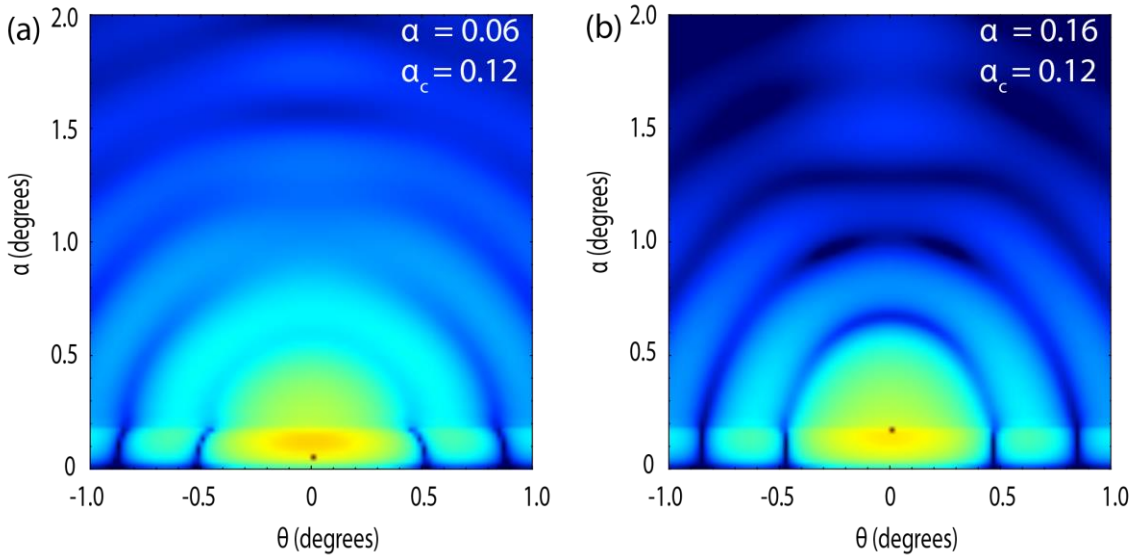

Figure 1.17: GISAXS simulation at two incident angles for a bilayer stack on silicon. The bottom layer consists of 20 nm diameter Au particles embedded in a carbon matrix, the top layer consists of a 5nm carbon film. The simulation was computed for x-ray energy of 10 keV, so the associated critical angle for carbon is approximately 0.12 degrees.

One should note that the data shown is presented in angles rather than the typical momentum transfer vector representation, **q**. This representation in angles is actually equivalent to a representation in **q** per the transform below. For the simulations, the geometry adopted is that of Figure 1.18 (a). Data shown in both representations of **q** and θ is presented in Figure 1.20 for comparison.

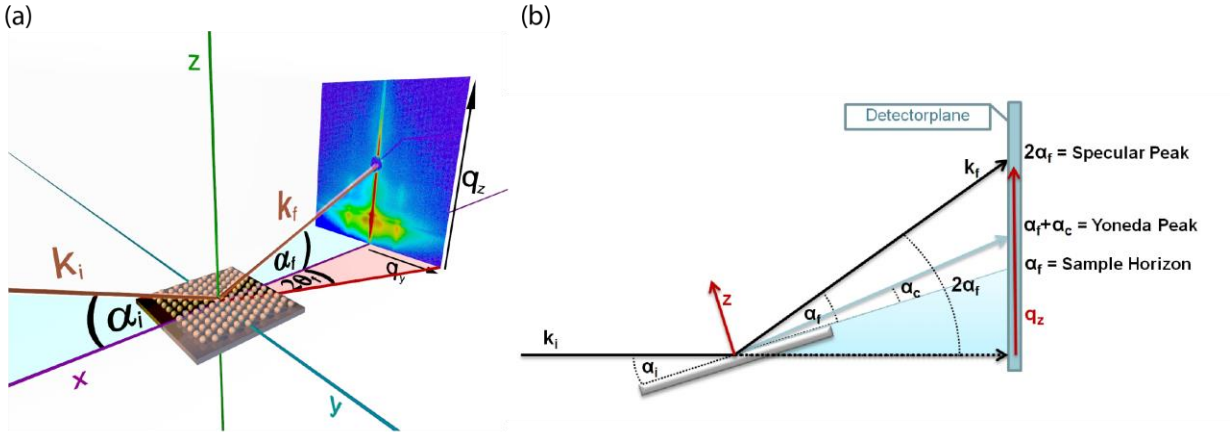

Figure 1.18: The two geometries of grazing incidence small angle x-ray scattering and the corresponding angles for the coordinate transform provided below. Reproduced from reference 29.

$$q_{x,y,z} = \frac{2\pi}{\lambda}\begin{bmatrix}\cos(\alpha_f)\cos(2\theta_f) - \cos(\alpha_i)\\ \cos(\alpha_f)\sin(2\theta_f)\\ \sin(\alpha_f) + \sin(\alpha_i)\end{bmatrix} \qquad \text{Equation 1.31}$$

Similar to SAXS, GISAXS data analysis can also be done either on the 2-D data or once again on data that is reduced to 1-D. For the latter, this is usually done with a simple line cut in plane and parallel to the substrate surface around the horizon of the specular reflected beam. Since influences of the grazing incidence geometry only manifest in the features that are above this horizon, these line cuts can be analyzed simply as standard SAXS patterns with no grazing incidence modification. Significant complication arises when the pattern is analyzed out-of-plane or as a 2-D pattern because corrections have to be made to account for both reflection and refraction effects arising from the grazing incidence geometry. This is usually done with the Distorted-Born Wave Approximation, which decomposes the scattering into four different scattering events and by weighing their relative contributions by corresponding Fresnel reflection coefficients depending on whether reflection from the substrate is involved in the event. This is shown pictorially in the schematic below.

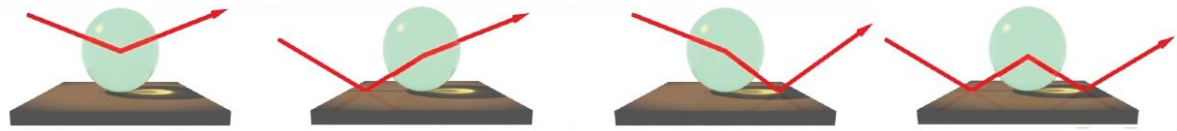

Figure 1.19: The four distinct possibilities involving reflection and refraction of the incident beam addressed using the Distorted-Born Wave Approximation. Reproduced from reference 29.

To obtain the 2-D pattern in GISAXS, similar to SAXS, the pattern is a result of a combination of both the structure factor and the form factor contributions. The primary difference is the DWBA approximation applied to both the form factor and the structure factor. When applied to the form factor, it causes a distortion out of plane such that a GISAXS pattern of spheres on a substrate will not have a truly radially isotropic pattern. Illustration of this effect is shown below

for a simulation of 20 nm diameter gold spheres in air on silicon. This figure also shows how, similar to transmission SAXS, the combination of a form factor and structure factor gives rise to the overall scattering pattern.

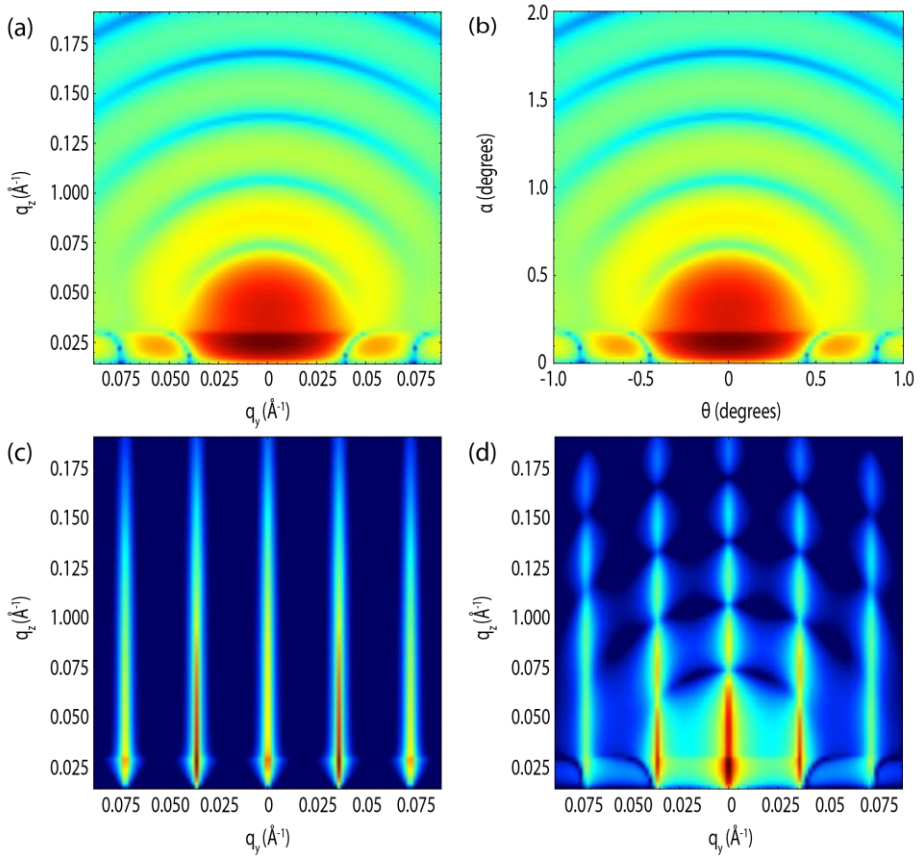

Figure 1.20: GISAXS simulation of 20 nm diameter gold nanoparticles in air on a silicon substrate at an x-ray incident angle of 0.16. (a) and (b) are equivalent representations in terms of the momentum transfer vector or in angle. (c) Structure factor for a hypothetical 2-D hexagonal lattice with 20 nm lattice spacing. (d) Scattering pattern of the 20 nm gold nanoparticles arranged on the 20 nm lattice. All simulations were performed with the Distorted Wave Born Approximation using the BornAgain software package.[28]

Last, since we are only considering a 2D in-plane structure factor in Figure 1.20, distortions from the GISAXS geometry on the structure factor may not be as apparent. Therefore, simulations of this distortion on a single crystal obeying 35Cmm2 symmetry are shown below. Here, we clearly see the distinct splitting of the peaks due to the reflection and refraction effects when we are above the critical angle of the film and assuming perfect reflection by the substrate. This effect goes away once we are below the critical angle of the film where there is no longer a contribution from reflection from the substrate.

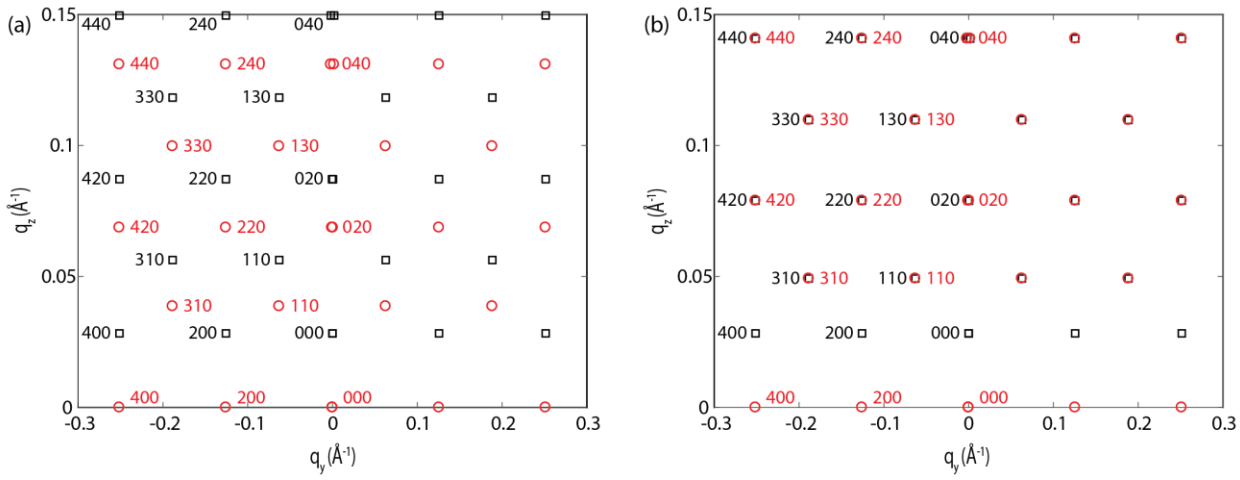

Figure 1.21: Simulation of a single crystal diffraction in GISAXS configuration for a crystal with a=10 nm and b = 20 nm obeying 35Cmm2 symmetry. The red circles are the diffraction spots from the film while the black squares correspond to the reflection contributions from the substrate. The incident angle was fixed at 0.16 degrees but the critical angle of the film was set at 0.12 for (a) and 0.18 for (b). Simulations were performed using GIXGUI.[30]

1.5 Dissertation Outline

In the first half of this dissertation, we will begin by investigating the aforementioned assembly of ligand stripped nanocrystals using polystyrene-b-polydimethylacrylamide. First, we consider the assembly using preformed micelles and address the influence of nanocrystal size and volume fraction for this assembly paradigm. Then, we proceed to realize assembly of ligand stripped nanocrystals into equilibrium morphologies dictated by the block copolymer phase diagram by relaxing the structures using solvent annealing. This is followed by a study of size, volume fraction, composition, and phase control cumulating in an investigation of the nature of the interaction between polydimethylacryalmide and ligand stripped nanocrystals. Finally, we end the first portion of the dissertation with a discussion of potential future directions such as the coassembly of mixtures of ligand stripped nanocrystals, phase tuning in solution using different solvent mixtures, and assembly of ligand stripped nanocrystals using a different more conventional polymer.

In the second half of this dissertation, we will begin with a proof of concept demonstrating the utility of colloidal nanocrystals as an avenue towards making structures suitable for the study of intermediate temperature proton conduction. Then, we show that capillary condensation is not responsible for the phenomenon of intermediate temperature proton conduction unlike previous claims in the field and allude to the possible influence of defect chemistry instead on the phenomena. Then, we address the influence of surface chemistry and stability on this phenomenon discussing its potential implications on materials selection for choosing appropriate stable metal oxides that demonstrate this phenomenon. We end this second portion of the dissertation with a discussion of potential future directions involving in-depth studies to prove the underlying mechanisms that form the basis for intermediate temperature proton conduction,

and potential studies involving defect concentration tuning either by doping or by changes in nanocrystal surface termination.

Chapter 2

Ordering in Polymer Micelle-Directed Assemblies of Colloidal Nanocrystals

2.1 Introduction

Colloidal nanocrystals have been proposed as functional building blocks for constructing mesostructured materials,[24] and sophisticated control has been garnered over the organization of ligand-capped nanocrystals into close-packed superlattices.[32] Design rules for coassembly of two or even three nanocrystal components into ordered architectures have been gleaned by evaluating assembly outcomes while systematically varying the nanocrystal sizes and relative volume fractions. Meanwhile, block copolymers (BCPs) have been used to direct the assembly of preformed nanocrystals into more open structures.[21,33–35] In the dilute limit, such assemblies follow principles established for thermodynamically driven BCP self- assembly, with the low volume fraction of nanocrystals acting as a perturbation. However, these design rules fail at high nanocrystal volume fractions, where in fact the realization of thermodynamically directed ordering may be rendered kinetically infeasible.[36] Nonetheless, such highly loaded composites offer a pathway to porous nanocrystal frameworks and can be functional materials in their own right by virtue of the continuous nanocrystal pathways they contain. As such, the development of clear principles to predict the emergence of ordering in nanocrystal-BCP coassemblies at high loading fraction is needed.

Typically, entropic penalties that arise from mixing polymers with nanocrystals drive macrophase separation at high nanocrystal volume fractions. By deliberately introducing favorable enthalpic interactions between polymer and nanocrystal components in the form of ionic interactions,[19,37] hydrogen bonding,[17,18,38,39] or specific adsorption interactions with bare nanocrystal surfaces,[20,22,23] macrophase separation can be mitigated to create coassemblies that have sufficiently high inorganic volume fraction that they retain their structure as mesoporous frameworks after removing the polymer template.

To circumvent prohibitively slow kinetics of using BCP phase separation to direct nanocrystal

assembly within composite thin films, an alternate approach utilizes BCPs in micellar configuration with assembly occurring both in solution and during solvent evaporation. Specifically, kinetically trapped polymer micelles[40–42] are formed in solution and assembled together with the inorganic component.[43] This approach has been extensively employed with sol-gel chemistries[44–51] but has only recently been applied to presynthesized nanocrystals.[20,22–24,52–54] Although the ability to template nanocrystals in this way opens up new opportunities for fabricating functional materials from the vast library of already-developed colloidal nanocrystals, the loss of configurational entropy upon mixing nanocrystals with polymers makes it challenging to assemble nanocrystals whose diameter, d, may be comparable to the mean end-to-end distance, R_0, of the polymer segments. [55]

We sought to understand how nanocrystal size and volume fraction impact the potential to create ordered mesostructured composite architectures by micelle-directed assembly of nanocrystals. Our model system consists of monodisperse colloidally synthesized iron oxide nanocrystals[56,57] between 3 and 16 nm in diameter and 60 000−10 000 Da polystyrene− b-poly(N,N-dimethylacrylamide) (PS−PDMA) micelles.[20] Favorable enthalpic interactions between PDMA and bare iron oxide nanocrystals that have been stripped of their native organic ligands[58] allow micelles and nanocrystals to associate, promoting assembly. Thin films (100 nm) that result after spin coating from a single dispersion containing these two components consist of nanocrystals incorporated between close packed micelles.

2.2 Experimental methods

2.2.1 Nanocrystal synthesis

Iron oxide synthesis was done using the decomposition of iron oleate, following a literature procedure.[56,57] The initial iron oleate complex was synthesized using 5.4 g iron chloride ($FeCl_36H_2O$, 20 mmol, Aldrich 98%) and 18.25 g of sodium oleate (60 mmol, TCI 95%) dissolved in a mixture of 40 mL ethanol, 30 mL deionized water, and 70 mL hexane. The solution was then heated to reflux at approximately 66 °C under a nitrogen atmosphere for 4 hours. After cooling to room temperature, the organic layer containing iron oleate was poured into a separatory funnel and washed 5 times using 70 mL of water per wash. After that, hexane was evaporated off using a rotovap leaving a viscous iron oleate complex.

In a typical synthesis of iron oxide nanocrystals larger than 5 nm (7 nm for instance), 2.7 g (3 mmol) of the iron oleate complex and 0.4275 g oleic acid (1.5 mmol, Aldrich 90%) is dissolved in 15 mL dioctyl ether (Aldrich 99%) at room temperature. Then, the solution is degassed under vacuum for 30 minutes at 110 °C, heated at a constant ramp rate of 3.3 °C/min to reflux under nitrogen (ca. 295 °C for dioctyl ether), and left to react for 30 minutes. After the reaction was completed, the solution was cooled rapidly with air until ca. 80 °C when 5 mL of toluene (Aldrich ≥ 99.5%) is added into the solution followed by 20 mL of reagent alcohol (Aldrich) to precipitate the nanocrystals. The nanocrystals were washed three times post synthesis with a

toluene/reagent alcohol combination for suspension and precipitation via centrifugation, filtered using a 0.5 μm PTFE filter, and stored.

In a typical synthesis of iron oxide nanocrystals smaller than 5 nm, 1.8 g (2 mmol) of the iron oleate complex, 1.61 g oleyl alcohol (6 mmol, Aldrich 85%) and 0.57 g oleic acid (2 mmol, Aldrich 90%) is dissolved in 10 g of diphenyl ether (Aldrich >99%) at ca. 50 °C. Then, the mixture was degassed at 90 °C for 30 minutes, heated at a constant ramp rate of 10 °C/min to reflux under nitrogen (ca. 260 °C), and left to react for 30 minutes. After the reaction was completed, the solution was cooled rapidly with air until ca. 80 °C when 5 mL of toluene is added into the solution followed by 20 ml of reagent alcohol to precipitate the nanocrystals. The nanocrystals were washed three times post synthesis with a toluene/reagent alcohol combination for suspension and precipitation, filtered using a 0.5 μm PTFE filter, and stored.

2.2.2 Ligand exchange

In a typical ligand stripping[58] of a batch of nanocrystals, nanocrystals were precipitated from toluene with reagent alcohol, and re- suspended in hexane (Aldrich >95% n-hexanes) and added into an equivalent volume of N,N-dimethylformamide (DMF) (Aldrich ≥ 99%) to form a two phase mixture. The nanocrystal concentration was controlled to be ca. 20 mg/mL for efficient ligand stripping, and a typical ligand stripping is done with 1 mL of hexane and 1 mL of DMF. Then, nitrosyl tetrafluoroborate (Aldrich 95%) equivalent to half the approximated weight of nanocrystal in solution is added into the mixture, and the mixture was agitated to promote ligand stripping. A phase transfer from hexane to DMF, usually within ten minutes, indicates successful ligand stripping. Then, the nanocrystals in DMF are washed six times using a DMF/toluene combination for suspension and precipitation, filtered using a 0.5 μm PTFE filter, and stored.

2.2.3 Micelle and assembly colloid preparation

In a typical preparation of block copolymer micelles, 10 mg of PS-PDMA block copolymer is dissolved in 100 μL of DMF and added dropwise into 800 μL of ethanol (EtOH) (Aldrich, 200 proof, anhydrous, ≥ 99.5%) under constant stirring at 350 rpm. The final solution appears opalescent and is left stirring overnight. Then, 180 μL of the micelle solution is transferred to a separate vial where 20 μL of DMF containing the desired amount of nanocrystals is added into the solution. For a typical assembly consisting of 1:1.5 polymer to nanocrystal weight ratio, this corresponds to 2 mg of polymer and 3mg of nanocrystals in 200 μL of final solution consisting of 40 μL DMF and 160 μL EtOH. The solution is left stirring to equilibrate overnight. Preparation of PS-PDMA polymer is reported in the supporting information of our previous work.[20]

2.2.4 Thin-film deposition

Silicon wafers (University Wafers, 0-100 ohm-cm P type) were cleaved to 1 cm by 1 cm

substrates and cleaned using stepwise sonication for 10 minutes in chloroform (Aldrich ≥ 99.5%), acetone (Aldrich ≥ 99.9%), and isopropanol (Aldrich ≥ 99.7), and cleaned by UV ozone for 10 minutes. Assembled films were spin casted at 1250 rpm with a 1 second ramp using 15 μL of solution per coating and using 2-3 coatings.

2.2.5 Transmission Electron Microscopy

Transmission electron microscopy (TEM) was performed on a Zeiss Libra 120 TEM at 120 kV or JOEL 2010F TEM at 200 kV accelerating voltage. Samples for nanocrystal TEM images were prepared by dropcasting a dilute nanocrystal solution in toluene on carbon Type- A (Ted Pella, 01821, 300 mesh) or ultrathin carbon film on holey carbon (Ted Pella, 01824, 400 mesh) TEM grids. The TEM sample for micelles and assemblies were prepared by spincoating an assembly solution at 1⁄2 concentration onto the TEM grid by first placing the TEM grid at the center of a silicon substrate followed by spin coating at 2000 rpm with 15 μL of solution once.

2.2.6 Scanning electron microscopy

Scanning electron microscopy was performed on a Zeiss Gemini Supra 55 VP-SEM at 3.00kV accelerating voltage. Film thickness was determined by cross-section imaging.

2.2.7 Small angle x-ray scattering

Small angle x-ray scattering (SAXS) was carried out at the Lawrence Berkeley National Laboratory Advance Light Source beamline 7.3.3 at either 1.8m or 3.6m sample-detector distances. Calibration was done using a silver behenate standard.

Solution phase SAXS was performed on nanocrystal dispersions in toluene or PS-PDMA micelle solutions in DMF:EtOH 20:80 v/v enclosed in glass capillaries (Charles-Supper Company, Boron Rich, 1.5 mm diameter, 0.01 mm wall thickness) in transmission geometry. Control samples containing neat solvent were used for background subtraction.

Grazing incidence small angle x-ray scattering was performed on thin films assembled on silicon at an incident angle of 0.14 degrees. Multiple incident angles were sampled from 0.12 to 0.2 degrees to determine the angle that provides the maximum signal per collection time, and 0.14 degrees was determined as the optimum angle for data collection. Book matching of the grazing incidence data left and right of the beam stop was used to ensure horizontal alignment of the sample and reduce uncertainties in q values that might occur due to stage tilt. Control sample of a clean silicon substrate was used for background subtraction.

Data extraction and fitting was performed using the Nika and Irena tool suite for modeling and analysis of small angle x-ray scattering data.[59,60] Specifically, the Modeling II module was used to fit the nanocrystal and block copolymer micelle form factors, and structure factor components

of the data. Gaussian peak fitting was done using the multi-peak fitting tool in IgorPro.

2.3 Results and discussion

2.3.1 Evaluating nanocrystal size, micelle coronal width and PDMA radius of gyration

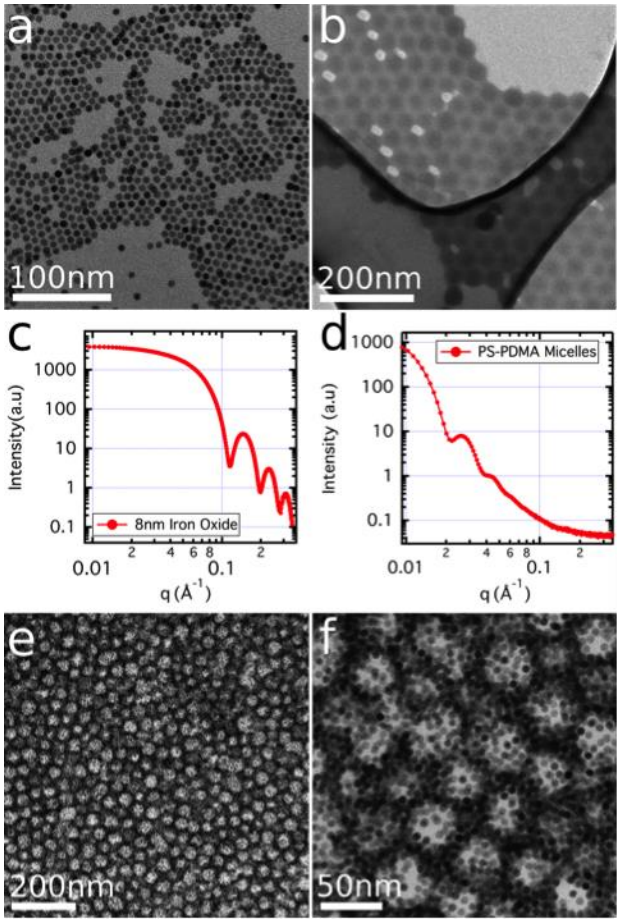

Figure 2.1: (a) TEM of 8 nm diameter iron oxide nanocrystals and (b) PS-PDMA micelles. (c,d) Solution phase SAXS of the same building blocks. (e,f) TEM of the resulting micelle-iron oxide assembly at two magnifications.

To evaluate the influence of nanocrystal size on mesoscale ordering, building blocks with highly uniform size and shape were synthesized and characterized by transmission electron microscopy (TEM) and small-angle X-ray scattering (SAXS) (Figure 2.1 a−d). In the SAXS data, the form factors of both nanocrystals and micelles exhibit periodic undulations characteristic of monodisperse, uniform particles with different distinctive sizes. Because the PDMA corona adsorbs to the nanocrystal surfaces during assembly, we hypothesized that the relative sizes of the nanocrystals and PDMA corona would significantly influence assembly outcomes.

The coronal width was assessed by fitting the block copolymer micelle SAXS form factor with a core−shell model. The fit results indicate a micelle with a 23.6 nm diameter core and 8.7 nm shell (Figure 2.2). The coronal width was also estimated by using SAXS to determine R_0 for PDMA homopolymer in the same solvent system (see Appendix A , Figure A.1), which was 6.9 nm. Thus, the coronal width, l_0, is around 7 to 9 nm and our nanocrystal diameters range from about 0.5 to 2 times this dimension.

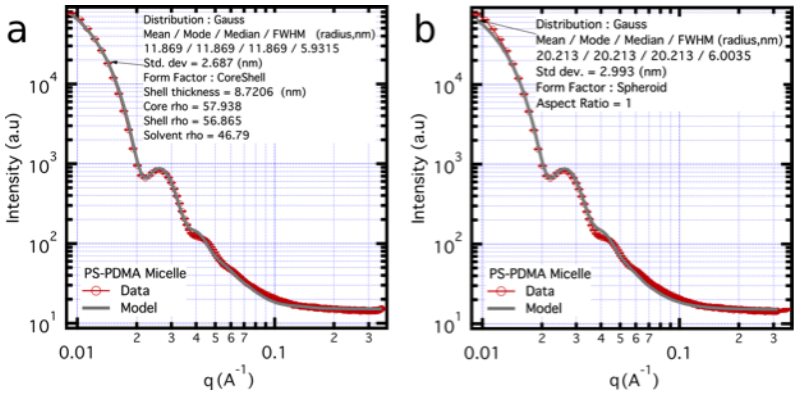

Figure 2.2: PS-PDMA micelle form factor fitted to core-shell model (a) indicating a 23.74nm diameter core and 8.72nm shell, or a regular spheroid (b) with 40.42nm diameter

2.3.2 The influence of nanocrystal size on ordering

The degree of ordering in nanocrystal−BCP composite films was evaluated using grazing incidence SAXS (GISAXS), interpreting the data in the context of local structure observed by electron microscopy. TEM of the composite films (Figure 2.1e,f) typically revealed structures with hexatic ordering on the mesoscale: local close-packing of nanocrystal-covered micelles without long-range translational order. GISAXS patterns were collected on a two-dimensional area detector; however these 100 nm thick films are only about two micelles in thickness and do not exhibit out of plane ordering, so one-dimensional line- cuts across the horizon were analyzed. A typical line-cut exhibits two sets of peaks: the first three peaks at low q, 0.01 $Å^{-1}$ < q < 0.05 $Å^{-1}$, are characteristic of local structure among micelles, whereas additional peaks at q > 0.05 $Å^{-1}$ are characteristic of order on the nanocrystal length scale, for example close-packing of nanocrystals in the interstitial spaces between micelles (Figure 2.3a).

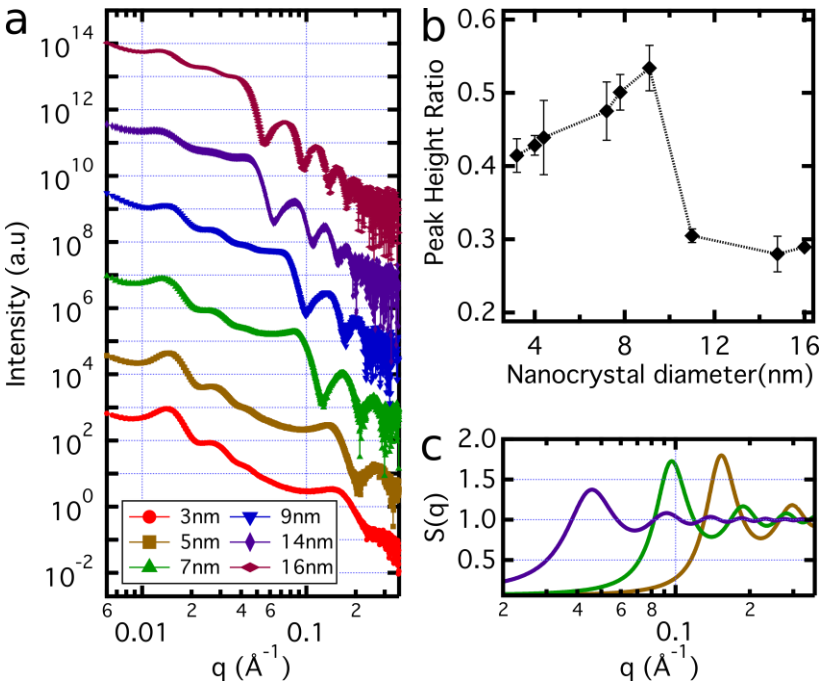

Figure 2.3: (a) One-dimensional GISAXS line-cuts of micelle-nanocrystal assemblies with different nanocrystal size at 1:1.5 w/w BCP:nanocrystal loading. The data have been vertically offset for clarity. (b) Ratio of low q GISAXS peak heights as a function of nanocrystal size. (c) Fits to the GISAXS structure factor in the higher q range for three nanocrystal sizes. The legend applies to (a) and (c). S(q) plot for all six nanocrystal sizes is available in Figure 2.4.

We examined the influence of nanocrystal size on assembly by varying the nanocrystal diameter, d, hypothesizing that the assembled structure should exhibit marked degradation of order for $d > l_0$, the micelle coronal width. We used a polymer to nanocrystal weight ratio of 1:1.5, an empirically determined lower limit of nanocrystal content that yields a freestanding structure when the polymer is removed by thermal depolymerization following assembly. This weight ratio corresponds to around 25 vol % of iron oxide, assuming bulk densities (Table A.2). Nanocrystal sizes determined by SAXS (Figure A.2 and Figure A.3 for TEM images) are shown in Figure 2.3a rounded to the closest nanometer for clarity, and a tabulation of the nanocrystal diameters and dispersities is provided in the Supporting Information (Table A.3). Ordering at the length scale of the micelles can be qualitatively determined by observing changes of peak width and peak height of the primary peak at $q = 0.015$ Å^{-1} as nanocrystal diameter is varied (Figure 2.3a). As a quantitative measure of structural order, we calculated the peak height ratio of the primary (lowest q) and secondary SAXS peaks after removal of the form factor background using a log-cubic fit (described fully in SI Figure A.4). Ordering is apparent for the smallest nanocrystals and improved slightly with increasing nanocrystal size up to $d \simeq l_0$ after which marked degradation of order occurred (Figure 2.3b).

Poorer mesoscale ordering for larger (>8 nm diameter) nanocrystals is consistent with expectations based on theoretical models that consider the entropic cost of incorporating nanocrystals within the coronal region. Previous studies that contemplated BCP−nanoparticle

assembly in the dilute limit highlight the constraint on polymer chain configuration imposed by nanoparticles with increasing diameters, approaching and exceeding R_0.[33,55,61] The associated increase in free energy tends to exclude nanoparticles or confine them at the block center with polymer chains demixing from the nanoparticle domain. Through the inclusion of favorable enthalpy of polymer adsorption, we avoid such segregation effects; nonetheless, the entropic penalty remains and can explain the poorer ordering we observe for larger nanocrystals. We also see somewhat reduced ordering below an optimum nanocrystal size of ~8 nm (similar to l_0), which may be associated with the extensive interaction between PDMA and the large surface area of these small nanocrystals.

Analysis of the scattering vectors, that is, q values for the peaks, suggests that these same considerations of size- dependent enthalpic and entropic terms cause nanocrystals of different diameters to locate at variable distances from the micelle cores. Specifically, the intermicelle spacing decreases with diminishing nanocrystal size (Figure 2.4), suggesting a more compact assembly in which small nanocrystals are well embedded in the corona. Conversely, larger nanocrystals remain at the micelle's periphery, thus moderating the entropic cost of assembly. Segregation of smaller nanocrystals toward a BCP interface has similarly been observed in low-loading assemblies of nanoparticles with BCPs driven by equilibrium microphase separation.[61,62]

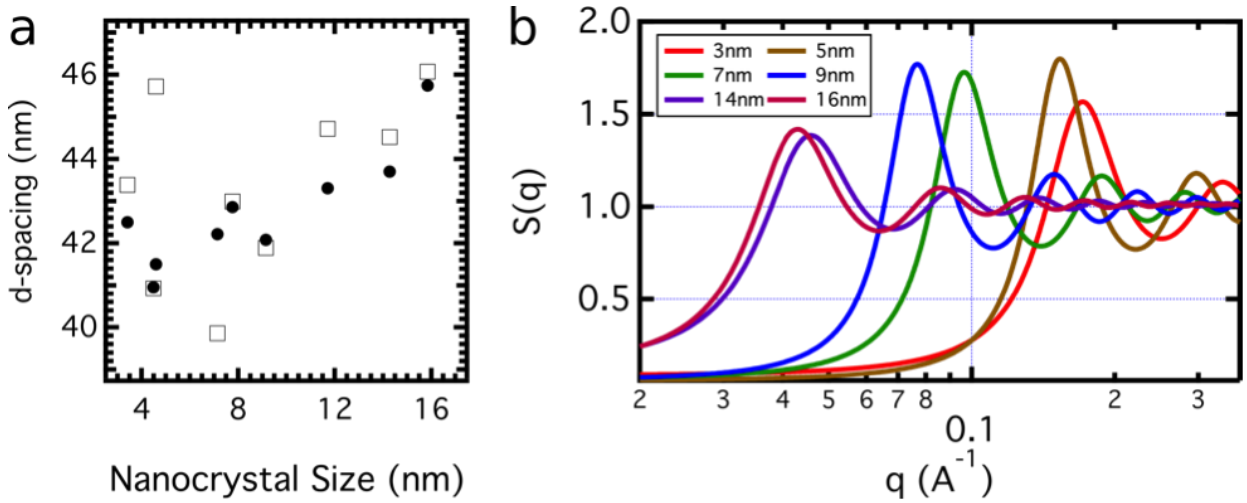

Figure 2.4: (a) Compilation of the change in d-spacing between micelles derived from the q value of the primary scattering peak, converted using $d = \frac{2\pi}{q}$ and plotted against the nanocrystal diameter, demonstrating an increase in intermicelle spacing with nanocrystal size. The filled and unfilled points are from two separate independent sets of samples. (b) Compilation of the structure factor for all 6 sizes of nanocrystal used in the size series data presented in figure 2 of the main text. The three other nanocrystal size structure factors used in the volume series studies are presented in Figure 3 in the main text and Figure S8. The decrease in nanocrystal-nanocrystal ordering for the smallest nanocrystal sample is likely due to the slightly more polydisperse nature of the nanocrystal sample.

Besides influencing structural ordering at the micellar length scale, nanocrystal size impacts the structural ordering at the nanocrystal scale. Most of the composites exhibited a second length scale of ordering attributed to ordering within the nanocrystal domains. This phenomenon is

qualitatively observable in GISAXS as the appearance of interference peaks at the shoulder of the nanocrystal form factors, with higher order peaks convoluted with form factor oscillations at higher q. To extract the structure factor representative of ordering at the nanocrystal length scale, the scattering data were fit using a combination of the nanocrystal form factor and a simple Percus−Yevick structure factor[59,60,63] (Figure A.5 for fitting procedure). The structure factor was pronounced for nanocrystals with $d < l_0$ indicating regular nanocrystal packing (Figure 2.3c). The intensity of the structure factor is significantly diminished for nanocrystals $d > l_0$.

2.3.3 The influence of nanocrystal volume fraction on ordering

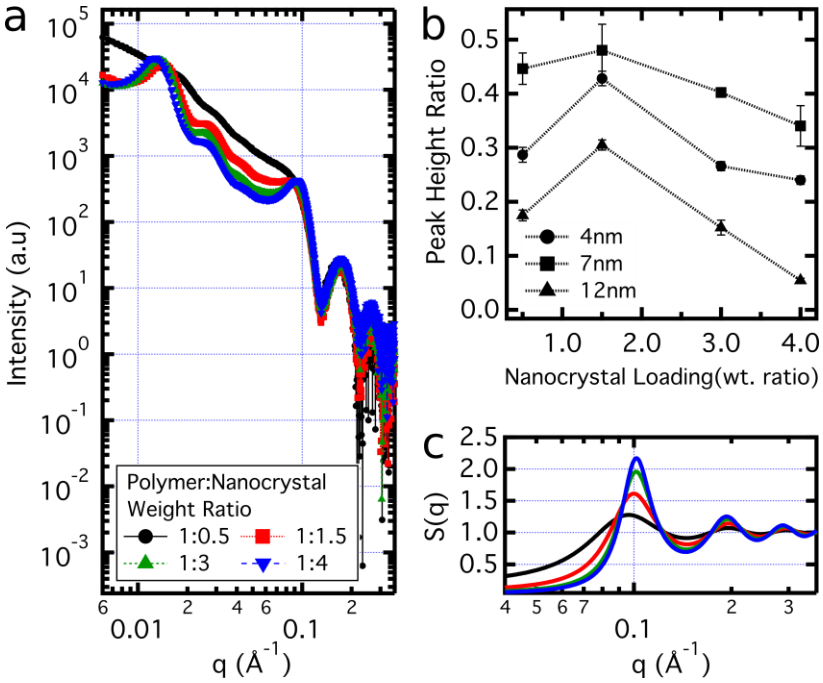

Figure 2.5: (a) One-dimensional GISAXS line-cuts of micelle-nanocrystal assemblies with different loading of 7 nm iron oxide nanocrystals expressed in weight ratio. (b) Peak height ratio of low q scattering peaks as a function of nanocrystal loading for three nanocrystal diameters. (c) Structure factors, extracted by fitting, in the range of q corresponding to the nanocrystal length scale at different loading of 7 nm nanocrystals. The legend applies to (a) and (c). GISAXS spectra for 4nm and 12nm series are available in Figure 2.6.

For larger ($d > l_0$) nanocrystals, we hypothesized that ordering at the nanocrystal length scale might be improved at sufficiently high loading. It has been observed in theoretical simulations that nanocrystal ordering becomes more pronounced at higher nanocrystal volume fractions[64,65] and our structure factor data for 7 nm nanocrystals shows the same trend (Figure 2.5c). As the loading of 7 nm diameter nanocrystals is increased, the structure expands to accommodate well-packed domains of nanocrystals between the micelles, as seen by the systematic shift of the primary micellar scattering peak at $q = 0.015$ Å^{-1} toward lower q indicating increasing intermicelle spacing (Figure 2.5a and Figure 2.7). However, nanocrystals larger than l_0 fail to incorporate homogeneously at higher loading. Though we observe the enhancement of

nanocrystal order in the structure factor (Figure 2.6), intermicelle spacing stops increasing with further nanocrystal addition (Figure 2.7). Hence, these larger nanocrystals tend to phase segregate at high volume fractions (Figure A.6 l).

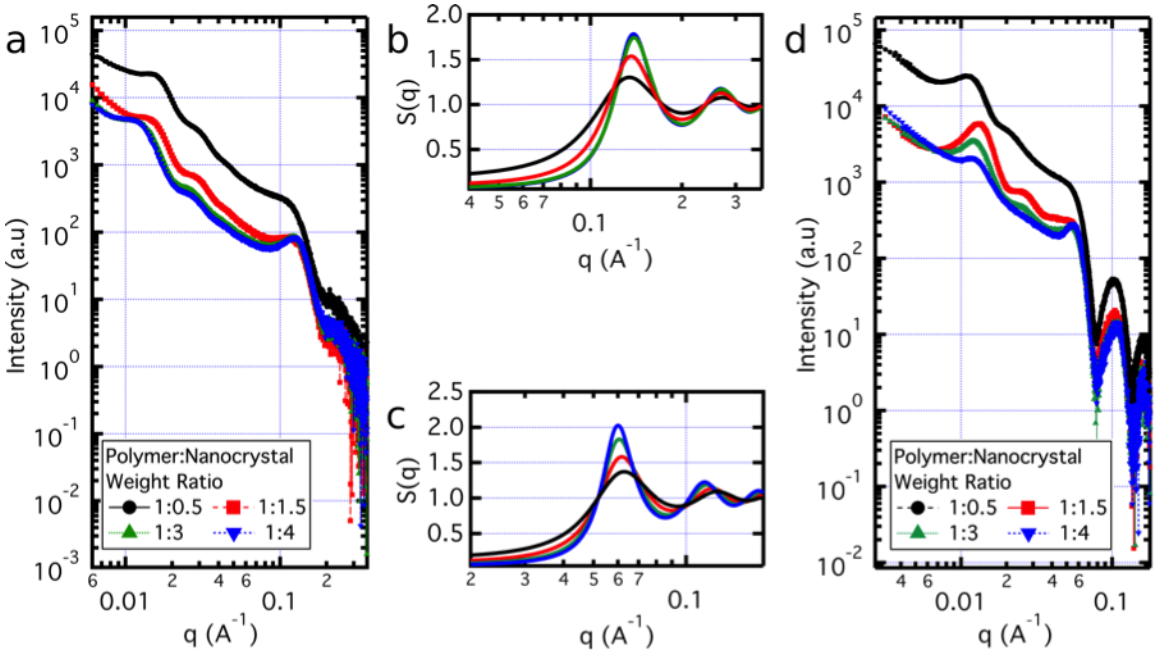

Figure 2.6: (a,b) GISAXS 1-D line-cuts for the loading series made with 4nm iron oxide nanocrystals with the corresponding structure factor for nanocrystal ordering. (d,c) GISAXS 1-D line-cuts for the loading series made with 12nm iron oxide nanocrystals with the corresponding structure factor for nanocrystal ordering. Assemblies made with 12nm iron oxide nanocrystals were spuncasted into thicker films around 200nm.

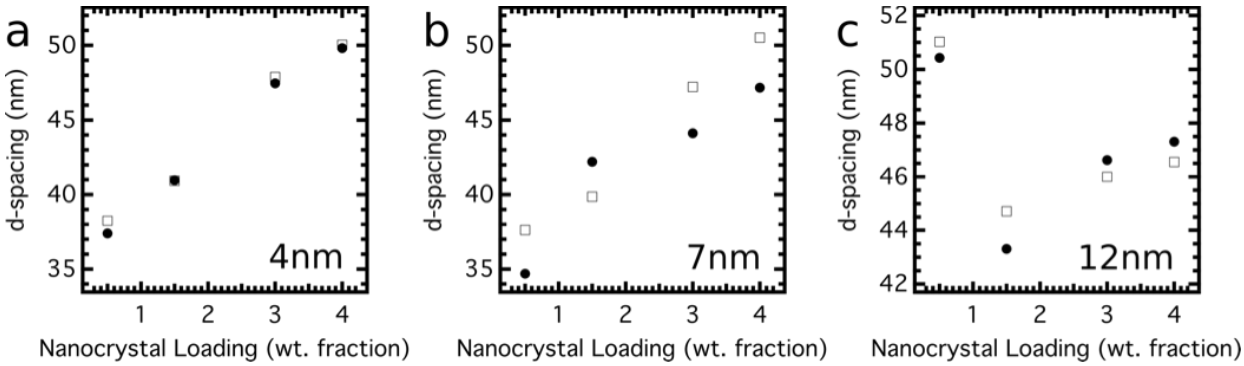

Figure 2.7: (a,b,c) Compilation of the change in d-spacing between micelles derived from the q value of the primary scattering peak, converted using $d = \frac{2\pi}{q}$ and plotted against the nanocrystal loading, demonstrating a general increase in intermicelle spacing with nanocrystal loading. The increase is prominent for nanocrystal sizes smaller than the estimated coronal width and appears to asymptote for large nanocrystals suggesting saturation and phase separation of additional nanocrystals out of the intermicellar domain. The filled and unfilled data points are from two independent sets of samples.

Examining the trends in ordering at the micellar length scale, there emerges a nanocrystal

loading at which micellar ordering is optimal, independent of nanocrystal size. Peak height ratios of the first and second order peaks at low q were once again used as a metric of ordering (Figure 2.5b). The ordering is greatest at a 1:1.5 weight ratio of polymer micelles to nanocrystals, corresponding to 25 vol % nanocrystals. At higher loading (up to 1:4 or 46 vol %), ordering diminishes for all nanocrystal sizes, though most severely for large nanocrystals, consistent with the phase segregation observed under these conditions (Figure 2.7).

2.4 Conclusions

Collectively, these trends in micellar and nanocrystal ordering can be understood by considering the nanocrystal-binding PDMA corona of the polymer micelles to have a constant width (l_0) that can be compared to nanocrystal size to differentiate assembly regimes (Figure 2.8a). For all nanocrystal sizes less than or equal to this coronal width, the most ordered composite architectures are realized at a size-independent optimal nanocrystal loading achieved when the micelle corona is completely populated by nanocrystals. Beyond this loading limit, additional nanocrystals can be incorporated but the regularity on the micellar length scale declines. When nanocrystals larger than the coronal width are assembled, they are positioned further from the PS−PDMA interface (Figure 2.8). One or two layers of large nanocrystals can thus be stabilized between adjacent micelles, though micellar ordering is limited when assembling these large nanocrystals and ordering at the nanocrystal length scale is absent.

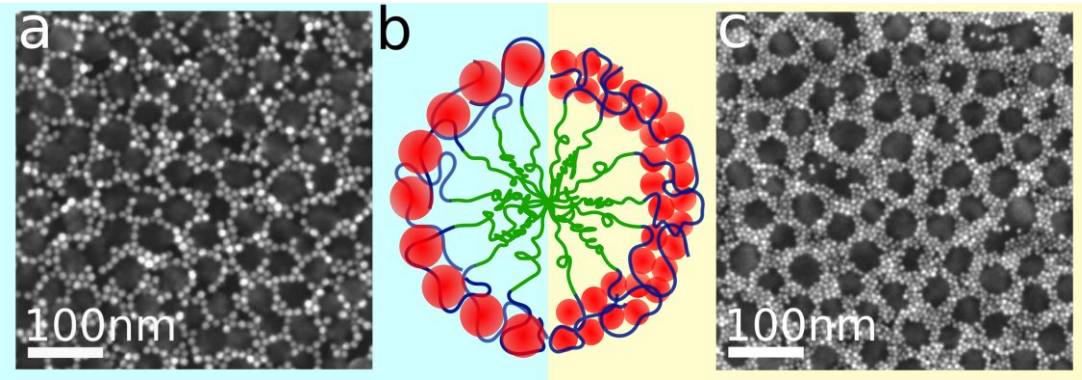

Figure 2.8: (a) SEM of a single nanocrystal network structure made with large 12 nm nanocrystals and (c) of an assembly with two length scales of order made with small 7 nm nanocrystals. (b) Schematic of the two extreme limits of assembly: green PS chain core, blue PDMA coronal chains, and red nanocrystals. Larger area images are available in Figure A.6.

In fact, the structure on the nanocrystal length scale, and its dependence on nanocrystal size are consistent with thermodynamic predictions. Especially when a favorable enthalpy of interaction exists between nanoparticles and one polymer component, smaller particles are expected to be accommodated within that polymer block; meanwhile, larger nanoparticles are excluded from the polymer to reduce entropic penalties but can remain in the space between self-assembled polymer domains. Meanwhile, ordering on the micelle length scale is kinetically determined. The

micelles pack most regularly when (smaller) nanocrystals are sequestered within the corona, whereas the presence of large nanocrystals between the micelles can disrupt ordering.

Within this framework of assembly, we can identify two structural extremes of interest: dual length scale structures made with high loading of small nanocrystals, and single nanocrystal network structures made with intermediate loading of large nanocrystals, using the micelle coronal width as a reference point for nanocrystal size (Figure 2.8). As mentioned previously, structures with high volume fractions of nanocrystals can often exhibit deep kinetically trapped states that prevent directed assembly of nanocrystals via equilibrium BCP microphase separation. It is likely that micelle templating of nanocrystals also results in structures that are kinetically trapped. However, this is leveraged advantageously in the micellar method, which enables access to the fringe limits of assembly to construct unusual structures such as single nanocrystal networks; in the case of equilibrium BCP microphase separation-driven assembles utilizing linear BCPs, large nanocrystals are commonly driven out of the system toward exposed surfaces, and the use of brush-type BCPs is required for assembly. This kinetic pathway, therefore, enables realization of a wide range of composite architectures with well-defined local ordering.

2.4.1 Acknowledgements

The authors thank Prof. Fiona Doyle, Amita Joshi, Evan Runnerstrom, Raffaella Buonsanti, Natacha Krins, and Chenhui Zhu for helpful discussions and beam-time support. Some of this research was carried out at the Molecular Foundry and at the Advanced Light Source at the Lawrence Berkeley National Laboratory, both user facilities that are supported by the Office of Science, Office of Basic Energy Sciences, of the U.S Department of Energy (DOE) under contract no. DE-AC02- 05CH11231. G.K.O. was supported by a National Science Foundation Graduate Research Fellowship under grant number DGE 1106400. A.S. was supported by the Bay Area Photovoltaics Consortium, sponsored by DOE EERE. D.J.M. acknowledges support of the Welch Foundation (F-1848).

Chapter 3

Assembly of Ligand Stripped Nanocrystals into Equilibrium Block Copolymer Morphologies

Adapted from: Gary K. Ong*, Dainah Pham*, Ankit Agrawal, Shin Hum Cho, Brett A. Helms, and Delia J. Milliron, "Assembly of Ligand Stripped Nanocrystals into Equilibrium Block Copolymer Morphologies," *In preparation*.

3.1 Introduction

Colloidal nanocrystals encompass a class of materials that are unique in both their properties as well as their suitability for bottom-up integration into more complex hierarchical structures. From metals to semiconductors, colloidal nanocrystals can exhibit properties that are not observed in their bulk counterparts with key examples such as quantum confinement[15] and localized surface plasmon resonance.[16,66] These aforementioned properties are characteristic single nanocrystal properties, and the field of assembly serves as an enabling bridge towards utilizing these nanocrystal properties in an ensemble configuration. Nanocrystal assembly, that of single components as well of multicomponents, into close packed structures has been well explored in the literature and primarily obeys sizing rules that result in arrangements that mirror traditional atomic crystal structures.[2] However, to obtain open non close packed arrangements, the use of a structure directing is often necessary.[21,24] One of the most promising methods to direct structure is the use of block copolymers to direct the assembly of nanocrystals via preferential sequestering of nanocrystals into one of the domains.[33,34]

However, incorporation of nanocrystals into a polymer matrix necessarily results in a loss of configurational entropy in the system, and this energetic penalty has to be offset by a favorable interaction between the polymer block and the nanocrystal.[34] As nanocrystals are commonly synthesized with an alkane shell, interactions between the nanocrystal and the polymer block are traditionally limited to van der Waals interactions. Even so, a variety of nanocrystals can be sequestered into a block copolymer domain at low (<10 vol%) volume fractions. However, with advances in ligand exchange and polymer grafting chemistries, new artisan ligands can now be placed on the surface of nanocrystals to enable a stronger interaction between the polymer and nanocrystal, such as that of hydrogen bonding or ionic interactions.[17,18,38,65,67] However much of these chemistries are developed mostly for metal nanoparticle systems, namely gold and platinum bases systems, and assembly of a compositionally diverse set of nanocrystals remains a challenge unless one reverts to the use of van der Waals interactions with the nanocrystal native ligand shell. With these stronger interactions, more nanocrystals can be segregated into the domain (up to ca. 45 vol%), and without these stronger interactions, macrophase separation of nanocrystals out of the polymer domain can occur. The latter is particularly common for thin film assemblies where nanocrystals can be easily segregated to the free surfaces (film-air or film-substrate).

Recently, a new class of nanocrystals distinguished by their absence of a native ligand shell has been enabled by developments in ligand stripping chemistries.[58,68,69] While this absence of the ligand shell opens up new functional opportunities, such as the possibility of charge transfer between nanocrystals and access to the bare nanocrystal surface for applications such as catalysis, this development also offers a new opportunity for directed assembly of these nanocrystals. Specifically, prior work has shown that a particular block copolymer, polystyrene-b-polydimethylacrylamide (PS-PDMA), exhibits strong interaction between the polymer and the nanocrystal surface such that mixtures of preformed micelles of the aforementioned block copolymer with ligand stripped nanocrystals yield nanocrystal decorated micelles in solution.[20,31] Subsequent deposition of these assemblies and template removal can be used to generate short-range ordered mesoporous structures useful for creating architected functional materials.[70]

While block copolymer micelle enabled assemblies provide an expeditious route to create porous nanocrystal networks, the true promise of utilizing block copolymers for directed assembly of nanocrystals lies in the precise structural control afforded by block copolymer microphase separation to direct nanocrystals into equilibrium block copolymer phase separated morphologies. Even for just linear block copolymers, the morphological space is already significant with access to cubic close packed spheres, hexagonal close packed cylinders and lamellar sheets.[3,4] However, equilibrium morphologies for PS-PDMA – the only currently known system that demonstrates strong interaction with ligand stripped nanocrystals – have not been demonstrated with or without nanocrystals, and protocols for solvent annealing of this block copolymer system have also not been established.

Here, we demonstrate the assembly of ligand stripped nanocrystals into equilibrium phase separated morphologies using polystyrene-b-polydimethylacrylamide. We begin by establishing the phase separation behavior of PS-PDMA, followed by the phase separation behavior of PS-PDMA in the presence of small 3 nm iron oxide nanocrystals as a model system. Then, we complete the investigation with a study of the influence of nanocrystal volume fraction, size and composition, show tuning of block copolymer morphology either by co-swelling with a selective solvent or change in block fractions, and finally end with a mechanistic understanding of the nature of the PDMA-nancorystal interaction.

3.2 Methods

3.2.1 Nanocrystal synthesis

Iron oxide synthesis was done using the decomposition of iron oleate, following a literature procedure.[56,57] The initial iron oleate complex was synthesized using 5.4 g iron chloride ($FeCl_3 6H_2O$, 20 mmol, Aldrich 98%) and 18.25 g of sodium oleate (60 mmol, TCI 95%) dissolved in a mixture of 40 mL ethanol, 30 mL deionized water, and 70 mL hexane. The solution was then heated to reflux at approximately 66 °C under a nitrogen atmosphere for 4 hours. After cooling to room temperature, the organic layer containing iron oleate was poured into a separatory funnel and washed 5 times using 70 mL of water per wash. After that, hexane was evaporated off using a rotovap leaving a viscous iron oleate complex.

In a typical synthesis of 3 nm iron oxide nanocrystals,[56] 1.8 g (2 mmol) of the iron oleate complex, 1.61 g oleyl alcohol (6 mmol, Aldrich 85%) and 0.57 g oleic acid (2 mmol, Aldrich 90%) is dissolved in 10 g of diphenyl ether (Aldrich >99%) at ca. 50 °C. Then, the mixture is degassed at 90 °C for 30 minutes, heated at a constant ramp rate of 10 °C/min to reflux under nitrogen (ca. 260 °C), and left to react for 30 minutes. After the reaction is completed, the solution is cooled rapidly with air until ca. 80 °C when 5 mL of toluene is added into the solution followed by 20 ml of reagent alcohol to precipitate the nanocrystals. The nanocrystals are purified three times post synthesis with a hexane/reagent alcohol combination for suspension and precipitation, filtered using a 0.5 μm PTFE filter, and stored.

In a typical synthesis of 4 nm cerium oxide nanocrystals, 0.868 g of cerium nitrate hexahydrate (2 mmol, Sigma 99.999%) and 5.36 g oleylamine (20 mmol, 90% Acros Organics) is dissolved in 10 ml 1-octadecene (Aldrich 90%). After initial mixing, the solution is stirred under nitrogen at 80 °C for one hour followed by a degassing at 120 °C for one hour under <100 mTorr vacuum. Then, the solution is heated at 10 °C/min to 230 °C. Once the solution temperature reached 230 °C, the solution is further heated to 250 °C and left to react for two hours. After the reaction is completed, the solution is left to cool in air under ca. 80 °C when 5 mL of toluene is added into the solution. The solution is then centrifuged at 1500 rpm for 10 minutes to remove bulk precipitates. The supernatant is mixed with 60 mL of isopropanol and centrifuged at 7000 rpm for 10 minutes. The nanocrystals are purified three times post synthesis with a hexane/isopropanol combination for dispersion and precipitation, filtered using a 0.2 μm PTFE filter, and stored.

In a typical synthesis of 2 nm Au nanoparticles,[71] 0.3 g of gold tetrachloride trihydrate (0.76 mmol, Sigma, > 99.99%), 0.23 g 4-mercaptophenol (1.8 mmol, Sigma 97%) is dissolved in 150 ml methanol along with 3ml of glacial acetic acid (Sigma, > 99%). 30 ml of freshly prepared 0.4 mmol/cm^3 solution of aqueous sodium borohydride (prepared by mixing 0.454 g sodium borohydride with 30 ml water) is added dropwise at a rate of 1 drop a second with a stir rate of 1000 rpm. The total time for addition is 8 minutes. The solution is left to stir for 30 minutes after which the methanol is evaporated with a rotovap. The brown residue is washed four times by sonication in 20 ml of diethyl ether for 10 minutes each time. Then, it is further washed with water four times by sonication in 20 ml of water for 10 minutes each time. Finally, the solution is suspended in ethanol and subjected to four cycles of flocculation and resuspension for purification with a ethanol/toluene combination for dispersion and precipitation, filtered using a 0.2 μm PTFE filter, and stored.

In a typical synthesis of CdSe/ZnS quantum dots[72] (QDs), an injection solution is prepared with 31.6 mg of Se powder (0.4 mmol, Sigma, >99.9%) and 128.3 mg of S powder (4 mmol, Sigma >99.9%) both dissolved in 3 mL of trioctylphosphine (TOP, Sigma 90%), and is stirred at 70 °C for 1 hour until clear in a N_2 glovebox. In a 50 mL round flask, 51.4 mg of CdO (0.4 mmol, Sigma > 99.99%), 733.9 mg of zinc acetate (4 mmol, Sigma 99.9%), 5.55 ml of oleic acid (17.6 mmol, Sigma 90%), and 20 mL of 1-octadecene (Sigma, 90%) are mixed. The flask mixture is heated to 150 °C, degassed under vacuum for 1 hour, backfilled with N_2 gas, and

further heated to 300 °C to form a clear solution. At this temperature, the Se-S TOP solution prepared previously is quickly injected into the reaction flask. After growth of QDs for 1 min, the flask was then immersed in a water bath to quench growth. QDs are purified by adding 10 mL of hexane and an excess amount of ethanol; centrifuged at 7500 rpm for 5 min and then redispersed in 10 ml hexane. The purification process is repeated 3 times.

3.2.2 Ligand exchange

For a typical ligand stripping procedure,[58] nanocrystals suspended in hexane (Aldrich >95% n-hexanes) are purified with four cycles of suspension and precipitation with hexane and reagent alcohol or acetone. The nanocrystal concentration is then diluted to 5 mg/mL, and an equivalent volume of N,N-dimethylformamide (DMF) (Aldrich ≥ 99%) is added to form a two phase mixture. Then, the two-phase mixture is agitated to ensure proper washing of the nanocrystals prior to ligand stripping. If the two phase mixture turned cloudy upon agitation, the nanocrystals are precipitated and washed two more times and the test repeated. If the mixture remains clear and phase separates back into a two-phase mixture, nitrosyl tetrafluoroborate (Aldrich 95%) equivalent to half or up to the approximate weight of nanocrystals in solution is added into the mixture, and the mixture is sonicated for thirty minutes to promote ligand stripping. After the phase transfer from hexane to DMF, the hexane phase is removed and replaced with fresh hexane and shaken. After phase separation, the hexane phase is removed, and this hexane washing is repeated twice more. Then, the nanocrystals in DMF are purified with a DMF/toluene combination for suspension and precipitation, are purified up to six times tracking the DMF/toluene ratio that changes from 1:2, 1:3, 1:4 and finally to a 1 to 6 ratio of DMF to toluene. For the final wash, the nanocrystals are resuspended in 500 μL of DMF followed by an addition of 500 μL of ethanol. The nanocrystal solution is then crashed with toluene and resuspended in anhydrous DMF to be stored.

3.2.3 Block copolymer – nanocrystal solution preparation

To prepare the BCP solution, 100 μL of anhydrous DMF is added to every 4 mg of PS-PDMA block copolymer to make a 40 mg/mL solution and stirred overnight. In a separate vial, 100 μL of the BCP solution is added along with 20 μL of DMF with the desired amount of nanocrystals. For example, the 100 μL solution contains 4 mg of polymer, so for a 1:0.5 polymer to nanocrystal weight ratio, 2 mg of nanocrystals is required for the BCP-nanocrystal solution. The desired amount of nanocrystals withdrawn from a concentrated ligand stripped nanocrystal solution is diluted to 20 μL of DMF, and added to the BCP solution. Then, the BCP-nanocrystal solution is sonicated for 30 minutes.

3.2.4 Thin-film deposition

Silicon wafers were cleaved to 1 cm by 1 cm substrates and cleaned using stepwise sonication for 10 minutes in chloroform, acetone, and isopropanol, and cleaned by UV ozone for 10 minute.

For a typical ~100 nm film (blue film), the BCP-nanocrystal films are spin-casted at 2000 rpm with a 5 second ramp using 15 μL of freshly prepared solution. As the weight ratio of polymer to nanocrystal weight ratio increased, the films are spin casted at 3000, 3500, or 4000 rpm to achieve a ~100 nm film.

3.2.5 Solvent annealing

Small glass petri dishes inside a fume hood operating at a 60 cc/minute flow rate were used as the solvent annealing chamber. Freshly spin-coated films were placed in the petri dish on a platform made from stacked glass slides. To swell the film to ~150 nm to 200 nm in film thickness (yellow/red film, a thickness to color calibration curve was first established by spin coating films of different thicknesses and subsequent measurement by profilometry), 1.5-4 mL of DMF is added to the solvent annealing chamber before closing the petri dish with the lid. The film swells within five minutes of closure and is allowed to remain swelled for 17 hours, 2, 4, or 6 days. To de-swell the film, the lid is cracked open with a 0.75 cm block (diameter of a 1 mL pipette tip) for 30 minutes before fully removing the lid.

3.2.6 Transmission electron microscopy

Transmission electron microscopy (TEM) was performed on a JOEL 2010F TEM at 200 kV accelerating voltage. Samples for nanocrystal TEM images were prepared by dropcasting a dilute nanocrystal solution in toluene on carbon Type- A (Ted Pella, 01821, 300 mesh) or ultrathin carbon film on holey carbon (Ted Pella, 01824, 400 mesh) TEM grids.

3.2.7 Scanning electron microscopy

Scanning electron microscopy was performed on a Hitachi S5500 SEM/STEM at a 2.00 kV to 3.00 kV accelerating voltage. Scanning transmission electron microscopy was performed on the same instrument at 30.00 kV accelerating voltage.

3.2.8 Small angle x-ray scattering

Small angle x-ray scattering (SAXS) was carried out at the Lawrence Berkeley National Laboratory Advance Light Source beam line 7.3.3 at a 3.6m sample-detector distance. SAXS was also collected at the university of Texas at Austin on a SAXSLAB Ganesha small angle x-ray scattering instrument. Calibration was performed using a silver behenate standard.

Grazing incidence SAXS was performed on thin films on silicon at an incident angle of 0.16 degrees for x-ray energy of 10 keV and 0.2 for 8.04 keV. A clean silicon substrate was used for background subtraction. Data extraction and fitting was performed using the Nika and Irena tool suite for modeling and analysis of small angle x-ray scattering data.[59,60]

3.2.9 Fourier transform infrared spectroscopy

Fourier transform infrared spectroscopy was done on spin-casted and solvent annealed thin films on calcium fluoride substrates (Pike Technologies 13 mm x 2 mm CaF_2 windows) in transmission geometry with a 2 cm^{-1} wavenumber resolution and an average of 64 scans on a Bruker Vertex 70 spectrometer.

3.3 Results and discussion

3.3.1 Solvent annealing of PS-PDMA without nanocrystals

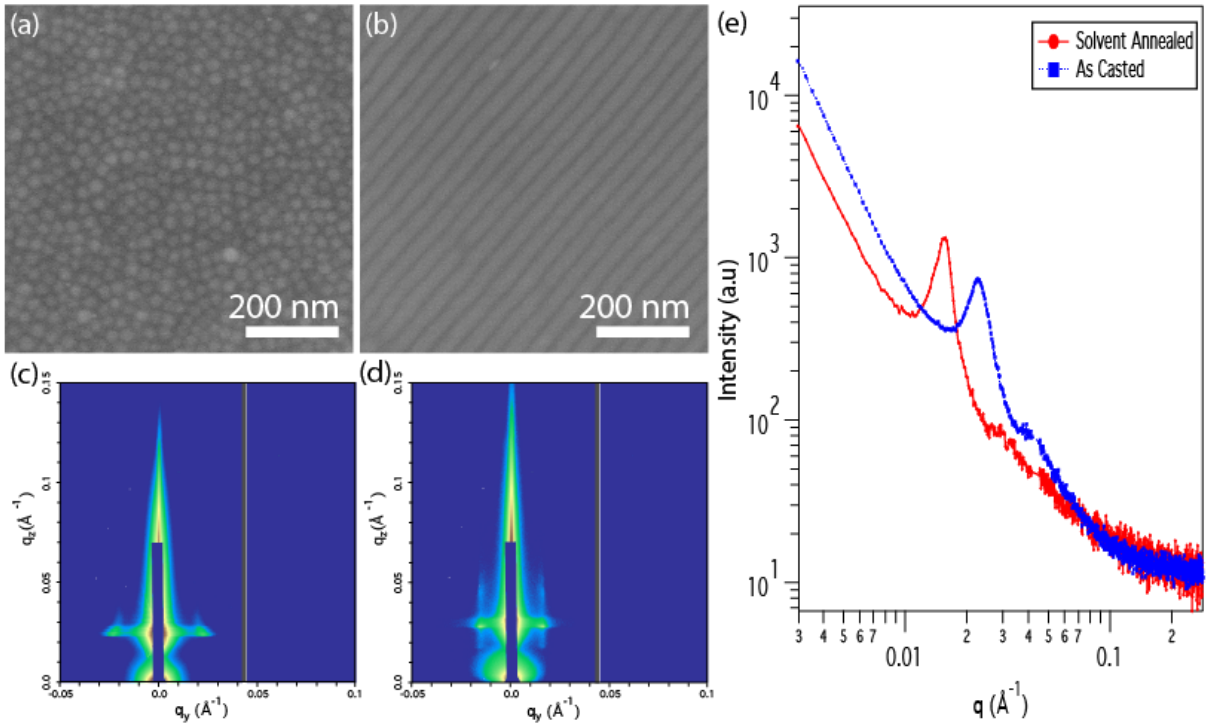

Figure 3.1: (a,c) SEM image and GISAXS of randomly packed micelles of 30k – 18k Da PS-PDMA deposited from DMF. (b,d) SEM image and GISAXS of solvent annealed 30k-18k Da PS-PDMA. (e) Line cut across the horizon for both GISAXS images showing a change in characteristic length scale after solvent annealing.

To begin, we establish the phase separation behavior of 30k-18k Da PS-PDMA and 18k-18k Da Ps-PDMA block copolymer under solvent annealing conditions with N,N-dimethylformamide (DMF). In this work, DMF was chosen as the solvent of choice for both casting and solvent annealing due to its compatibility with both blocks of the polymer as well as with ligand stripped nanocrystals. Due to the partial selectivity of DMF for the PDMA block, we observe two prominent features in the as-cast and solvent annealed films. First, films of PS-PDMA that are spun from DMF exhibit a polydispersed disordered miceller morphology. After solvent annealing, PS-PDMA successfully phase separates as shown in the scanning electron microscopy

(SEM) images in Figure 3.1. Additional SEM images at various magnifications are available in the appendix in Figure B.1.

To assign the bright and dark regions in the SEM images to PS and PDMA respectively, we compared changes in feature dimensions when we decreased the PS block length. Comparing 30k - 18k Da PS-PDMA to 18k -18k Da PS-PDMA, we observe a decrease in the average diameter from 24 nm to 18 nm for the brighter spherical regions in the as-cast condition and a decrease of the average lateral dimension from 27 nm to 20 nm for the brighter regions in the solvent annealed samples. The dark region dimension remains unchanged at 9 nm. Therefore, we can assign the bright regions to PS and the dark regions to PDMA. From this assignment, we confirm that PS-PDMA is deposited as micelles consisting of a PS core and PDMA corona, and that DMF is selective of PDMA. After solvent annealing, considering the parallel line pattern demonstrated in Figure 1 and the extended finger-print pattern shown in Figure B.1, we can preliminarily assign the solvent-annealed phase to one of three phases: hexagonal cylinder, lamellar, or inverse hexagonal cylinder. The difference in width between bright and dark domains however, suggests a higher probability of the phase being one of the two hexagonal phases.

To better deduce the actual phase separated morphology, we conducted grazing incidence small angle x-ray scattering (GISAXS) on the block copolymers before and after solvent annealing, and we estimated both the Flory-Huggins interaction parameter and the respective block lengths to deduce our location in the block copolymer phase diagram using the ideal phase diagram as a guide. From GISAXS, in addition to a shift to a larger characteristic length scale consistent with the SEM images, we observe two distinct points out of plane in the pattern characteristic of the hexagonal cylinder phase and absence of any pattern characteristic of lamellar structures. By estimating our location in the block copolymer phase diagram as in Figure B.2, we arrive at two conclusions. First, at room temperature, χ for PS-PDMA is approximately 0.104 and χN for 18k – 18k Da PS-PDMA and 30k – 18k Da PS-PDMA are approximately 37 and 49 suggesting both block copolymers can phase separate. Second, in the absence of selective solvents, 18k-18k Da PS-PDMA and 30k-18k Da PS-PDMA lie in the lamellar region. However, the selectivity of DMF for PDMA can significantly shift our location in the phase diagram in favor of a structure with a higher effective volume of PDMA. Absent significant phase change in solvent annealed structure between 30k - 18k Da PS-PDMA and 18k – 18k Da PS-PDMA, we tentatively assign the observe phase to the hexagonal cylinder phase with PS cylinders embedded in a PDMA matrix.

3.3.2 Solvent annealing of PS-PDMA with nanocrystals

Having established the phase separation behavior of PS-PDMA, we turn our attention to the phase separation of PS-PDMA in the presence of nanocrystals. Films containing 1:0.25 polymer: nanocrystal w/w (corresponding to ca. 5 vol% nanocrystal) were spin coated and solvent annealed. Scanning transmission microscopy images of the nanocrystals are presented in Figure B.3. Comparing the as-cast and solvent-annealed samples in Figure 3.2, we see that the as-cast film consists of a mixture of block copolymer micelles and nanocrystals. After solvent annealing, we see incorporation of nanocrystals into the PDMA block due to preferential interaction

between the nanocrystal surface and PDMA. In the images, contrast is reversed between the PS and PDMA domains due to the significant difference in electron density between polymer and nanocrystal: the nanocrystal rich PDMA domain appears bright while the PS domain appears dark with a sparse layer of nanocrystals on the top surface of the PS domain.

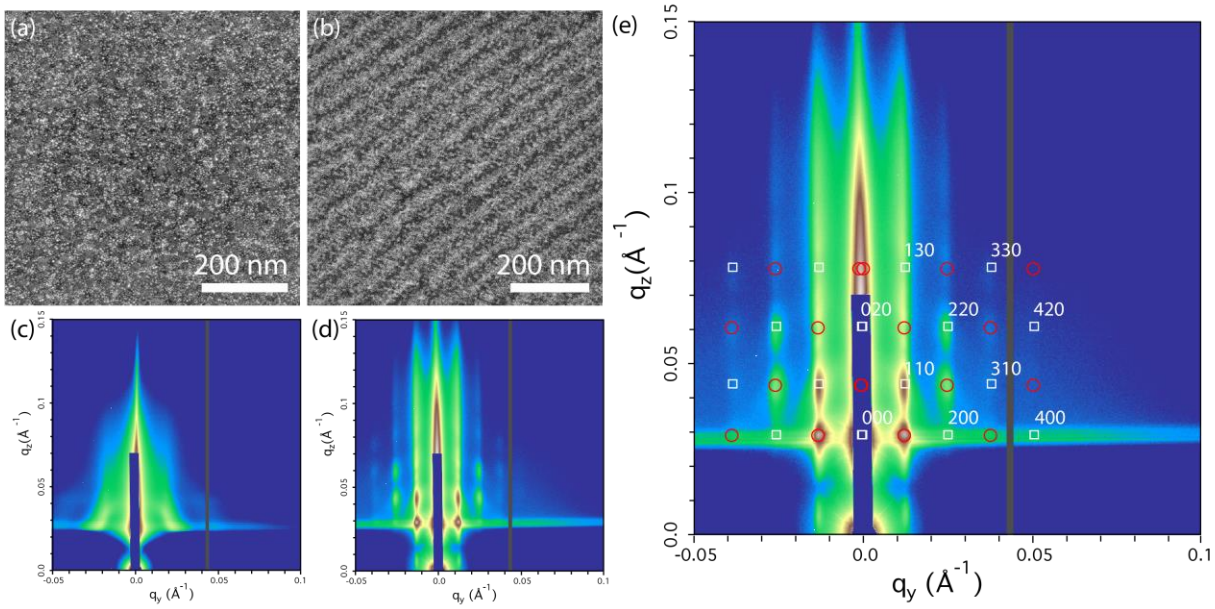

Figure 3.2: (a,c) SEM image and GISAXS of randomly packed micelles of 30k – 18k Da PS-PDMA with 1:0.25 w/w polymer: nanocrystal deposited from DMF. (b,d) SEM image and GISAXS of solvent annealed 30k-18k Da PS-PDMA with 1:0.25 w/w polymer: nanocrystal. (e) Indexed GISAXS pattern for the solvent annealed structure with white squares corresponding to the reflected beam, and red circles corresponding to the transmitted beam (scattering without prior reflection from the substrate).

This change in structure after solvent annealing is prominently reflected in the associated GISAXS patterns. Before solvent annealing, the pattern exhibits isotropic short-range order characteristic of random packing of block copolymer micelles and nanocrystals. After solvent annealing, we see distinct spots in the pattern characteristic of a long range ordered structure. The presence of these clear diffraction patterns immediately informs us that the assembly is not occurring just at the film-air interface and in fact makes a two dimensional lattice perpendicular to the substrate. To determine the actual arrangement, we simulated expected diffraction spots in GISAXS accounting for refraction and reflection effects given an expected lattice and space group using the software package GIXGUI. The details of the simulation treatment are discussed completely in the original paper by Zhang Jiang[30] and it is sufficient to mention here that the method incorporates the Distorted Wave Born Approximation to account for refraction effects from the film and the reflection effects from the substrate, and that diffraction spots are determined by the standard Laue conditions and Ewald sphere construction. The results are mapped onto the experimental data in Figure 3.2 (e) and suggest that the structure consist of a rectangular lattice that obeys space group 35 *Cmm2* with lattice vector magnitudes of approximately 50 nm and 35 nm for the in plane and out of plane directions. This result can be explained by noting that compression of the hexagonal lattice in one direction naturally generates

a rectangular lattice that breaks the symmetry of a hexagonal space group. In this case, the distortion likely occurred due to the thin film nature of the sample (constrained in-plane with the direction of solvent removal perpendicular to the substrate), and similar effects have been observed in other solvent annealed thin film in-plane hexagonal phase block copolymer structures.[73]

In the path of obtaining a successful solvent annealed structure in the presence of nanocrystals, we note two peculiar observations that significantly affected the probability of rearrangement that was, in hindsight, consistent with our understanding of the PDMA-nanocrystal system. First, stirring time to mix the polymer and nanocrystal had to be minimized with the longest stirring time resulting in films that would not rearrange after casting. Second, complete drying of the film after casting such as with mild heat renders rearrangement impossible. These results are shown in Figure B.4. The former is expected for possibly irreversible adsorption (after some critical association time) of PDMA on the nanocrystal surface. This is consistent with prior literature that suggests adsorption of polymers onto a solid surface is usually irreversible. The latter is indicative of the role that DMF plays in competing with PDMA to mediate adsorption on the nanocrystal surface. This is expected given the structural semblance between PDMA and DMF. Both are ultimately the byproduct of a strong interaction between PDMA and the nanocrystal surface.

3.3.3 Varying nanocrystal volume fraction

While the strong interaction between polymer and nanocrystal complicated the processing, prior work has highlighted the key role of a strong interaction in allowing loading of nanocrystals into a polymer domain without causing macrophase separation of nanocrystals to the free surface. This strong interaction is used to negate entropic effects of limiting polymer chain conformation and thus manifest in volume fraction limits and size limits on nancrystal incorporation into a polymer domain. In that vein, we investigated the nanocrystal volume fraction limits for the system hypothesizing that the strong interaction may allow incorporation of nanocrystals into the system at volume fractions higher than 10 vol% (the limit demonstrated in thin films for linear block copolymers exhibiting van der Waals interactions with the nanocrystal additive).
In this study, unlike the assembly shown in Figure 3.2, we chose to change the cylinder orientation to ensure that there is a continuous PDMA domain with minimal hindrance for nanocrystal and polymer diffusion out of plane during solvent removal. This was achieved by minor changes in film thickness to one that is not commensurate to the periodicity of the phase-separated structure obtained previously. As we increase the volume fraction of nanocrystals in the system, we observed successful directed assembly of nanocrystals up to a polymer: nanocrystal w/w of 1:2 (ca. 28 vol% nanocrystal), and minor rearrangement for a polymer: nanocrystal w/w of 1:3 (ca. 36 vol% nanocrystal). SEM images for the progression with increasing nanocrystal content are shown in Figure 3.3 along with accompanying GISAXS and 1-D SAXS linecuts.

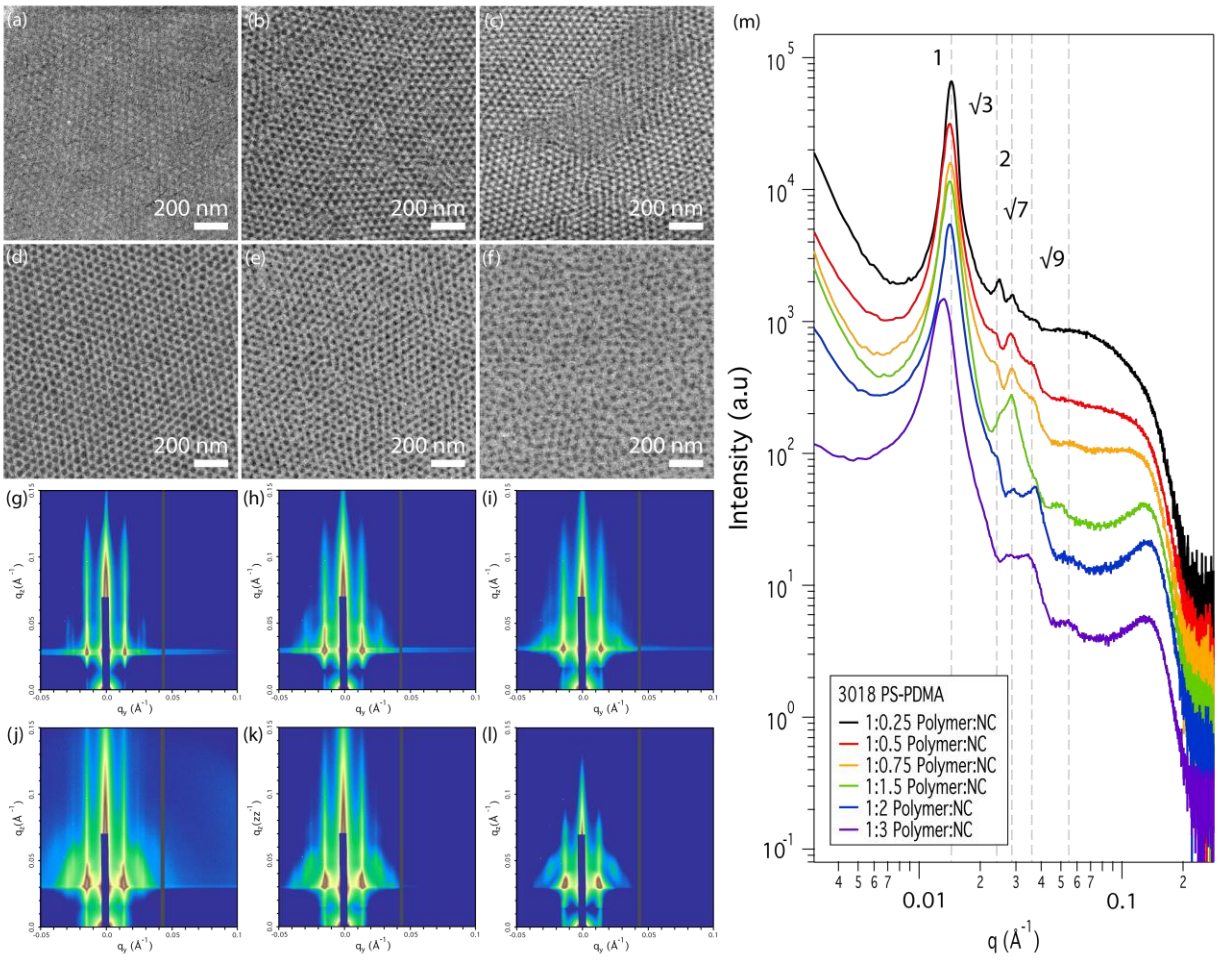

Figure 3.3: SEM and GISAXS of 30k-18k Da PS-PDMA with nanocrystals in polymer:nanocrystal w/w ratios x:y. (a, g) 1:0.25, (b, h) 1:0.5 (c, i) 1:0.75, (d, j) 1: 1.5, (e, k) 1:2, (f, l) 1:3. (e) Line cut across the horizon for the GISAXS patterns arbitrarily offset on the y-axis for clarity. The 1:3 sample is solvent annealed for 4 days as opposed to 2 days for all other samples.

From the GISAXS patterns in Figure 3.3, we observe elongated Bragg rod features in the out of plane direction characteristic of scattering from structures that exhibit orientation perpendicular to a substrate surface. This serves as the second suggestion that the solvent annealed structure consists of the hexagonal cylinder phase but this time with cylinders oriented perpendicular to the substrate surface. Since the scattering patterns show no new information in the out of plane direction apart from the aforementioned features, we can analyze the patterns with representative 1-D linecuts across the horizon. From this, we obtain our second confirmation of the structure noting the characteristic $1:\sqrt{3}:\sqrt{4}:\sqrt{7}:\sqrt{9}$ ratios of the scattering peak locations indicative of a 2D hexagonal arrangement but with no out of plane compression this time due to the perpendicular orientation of cylinders relative to the substrate. While we do not observe any gross changes in structure from this increase in nanocrystal volume fraction, we do note two prominent changes in the scattering features. First, we observe minimal shifting of the primary scattering peak suggesting minimal changes in the domain spacing in the system as nanocrystals are incorporated into the PDMA domain. Second, we observe emergence of a nanocrystal structure factor peak multiplied into the form factor shoulder indicating that we are in a volume

fraction limit where nanocrystals are interacting leading to structures with two length scales of order. As we increase the nanocrystal volume fraction in the system, we do not observe any extensive shifting of the primary scattering peak. This could be due to the small nanocrystal size used in this study (2 – 3 nm iron oxide) such that incorporation only resulted in a minimal distortion of the polymer chains. At the highest volume fraction tested (1:3 polymer:nanocrystal w/w, ca. 36 vol %), however, we see that the primary peak shifts lower indicating a larger domain spacing. It is also at this limit that rearrangement starts to get less ordered and begins to get retarded as seen in both the SEM images and in the 2D GISAXS pattern. The data presented is actually from a sample that was solvent annealed for twice as long as the other samples to allow more time for rearrangement. For this highest volume fraction tested, these observations are consistent with prior experiments that attribute failed rearrangement to both the higher tendency for chain entanglement for linear block copolymers and nanoparticle effects creating a kinetic constraint preventing rearrangement at the highest volume fractions tested. More specifically, at high volume fractions where nanocrystals occupy the majority of the PDMA domain, we now have a hard framework set up by jammed packing of nanocrystals that hinders long-range diffusion of both the block copolymer and the nanocrystals thus preventing rearrangement. In addition, given our previous observation that PDMA likely irreversibly adsorbs to the nanocrystal surface even in the presence of DMF after a week removing the possibility of rearrangement even with solvent annealing, it is possible that the kinetics of rearrangement slows over the solvent annealing period such that even longer solvent annealing times would not result in better structural reconfiguration.

3.3.4 Varying nanocrystal size

In the same vein of strong nanocrystal interactions enabling assembly of higher volume fraction of nanocrystals, this same interaction would also be responsible for enabling assembly of larger nanocrystal sizes. Hence, we investigated the influence of nanocrystal size on nanocrystal incorporation by considering the ratio between the nanocrystal diameter, d, and the polymer domain size, L. From the work presented previously in Figure 3.1, the estimated PDMA domain size L is approximately 9 nm. Therefore, we investigated three nanocrystal sizes corresponding to $d < 0.3\ L$, $d > 0.3\ L$, and $d > L$ as shown in Figure 3.4. Consistent with prior work, smaller nanocrystals with diameter $d < 0.3\ L$ and $0.3\ L < d < L$ were successfully directed into assemblies. However, deviating from prior observations, samples assembled with nanocrystals with $d > L$ were not phase separated out to the free surface of the film. Rather, the presence of large nanocrystals impedes overall rearrangement of the film even at low volume fractions. Once again, we did not observe any changes in phase morphology as a function of nanocrystal size.

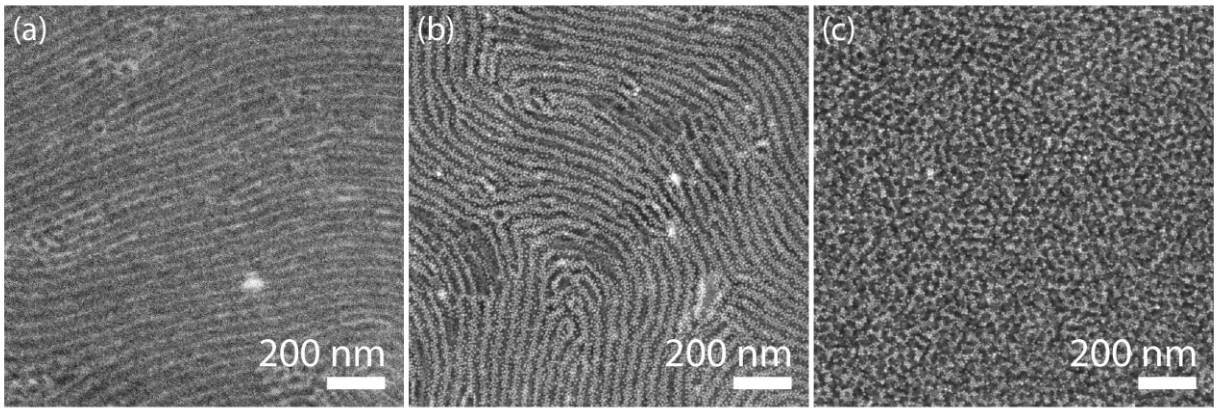

Figure 3.4: Iron oxide size series using 18k-18k Da PS-PDMA at 1:0.5 polymer:nanocrystal w/w. (a) 3 nm, (b) 7 nm, and (c) 10 nm.

3.3.5 Varying nanocrystal composition

Building on our observation of the strong interaction between PDMA and the nanocrystal surface, prior work on micelle assembly of ligand stripped nanocrystals has shown that the system enables assembly of a variety of nanocrystals without surface functionalization especially for metal oxides. In this case of solvent annealed assembly of ligand stripped nanocrystals into equilibrium morphologies, this compositional diversity is inherited as shown in Figure 3.5 (a,b). This assembly platform can be used to assemble a variety of metal oxides, and we demonstrate this utility with iron oxide, cerium oxide, indium tin oxide, and titanium dioxide nanorods. Furthermore, we wanted to extend the compositional diversity that can be accessed by this system and hypothesized that PDMA likely interacts with native hydroxyl groups on the metal oxide surface. Thus, we extended the compositional diversity for this system by working with gold and metal chalcogenide nanocrystals that are functionalized with a ligand containing a hydroxyl moiety. More specifically, we chose mercaptophenol for the test. Seen in Figure 3.5 (c,d), these nanocrystals functionalized with a hydroxyl bearing ligand can now also be assembled using PS-PDMA. This success presages our understanding of the nature of the interaction between the nanocrystal surface and PS-PDMA which will be discussed below.

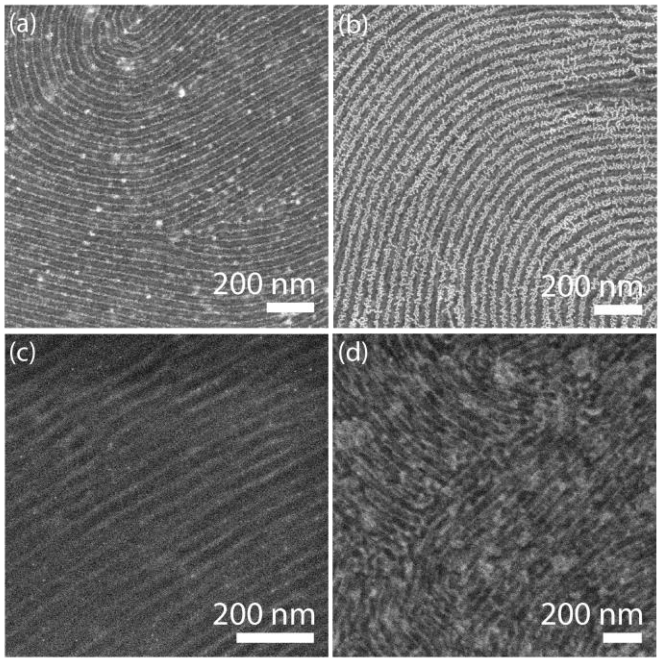

Figure 3.5: Assemblies of various nanocrystals using 18k-18k PS-PDMA at 1:0.5 polymer:nanocrystal w/w. (a) 4 nm CeO_2, (b) 6 nm $Sn:In_2O_3$, (c) 2 nm Au, (d) 6 nm CdSe-ZnS core shell particles. Au and CdSe-ZnS particles are ligand capped with mercaptophenol.

3.3.6 Tuning phase separated morphology

One of the primary merits of using block copolymer directed assembly of nanocrystals is the opportunity to access different block copolymer microphase separated morphologies. Due to the selectivity of DMF for PDMA, we have found that small changes in the block copolymer block ratios such as that between 30k-18k Da PS-PDMA and 18k-18k Da PS-PDMA were insufficient to access a different phase separated morphology.

However, we hypothesized that by using a symmetric system coupled with coswelling with a mixture of toluene and DMF - toluene is a solvent selective of polystyrene - we may regain the opportunity to access different morphologies offered in the block copolymer phase diagram. As we increase the toluene vapor fraction during solvent annealing, we observe a gradual change in morphology from standing up cylinders to a mixed phase, to a phase we believe to be that of perforated lamellae perpendicular to the substrate at a DMF:toluene mole fraction of 50:50, and finally to yet another phase we believe to be one kinetically trapped between perforated lamellae on the way towards a pure perpendicular lamellae at a DMF:toluene mole fraction of 25:75. The results of this co-swelling experiment are shown in Figure 3.6 with the DMF:toluene ratios of 100:0, 75:25, 50:50, and 25:75. This change from a hexagonal cylinder structure to that of lamellae is tentatively supported by the 1-D SAXS linecuts obtained from the 2D patterns presented with a transition of the higher order scattering peak ratios from a n=1: $\sqrt{3}$: $\sqrt{4}$: $\sqrt{7}$: $\sqrt{9}$ to a n=1, 2, 3 condition. However, lamellae structures do not have out-of-plane scattering spots. Therefore, for the 50:50 DMF:toluene condition, our preliminary assignment of the phase is to

that of perforated lamellae. Further studies to confirm this phase behavior by TEM microtoming studies are on the way.

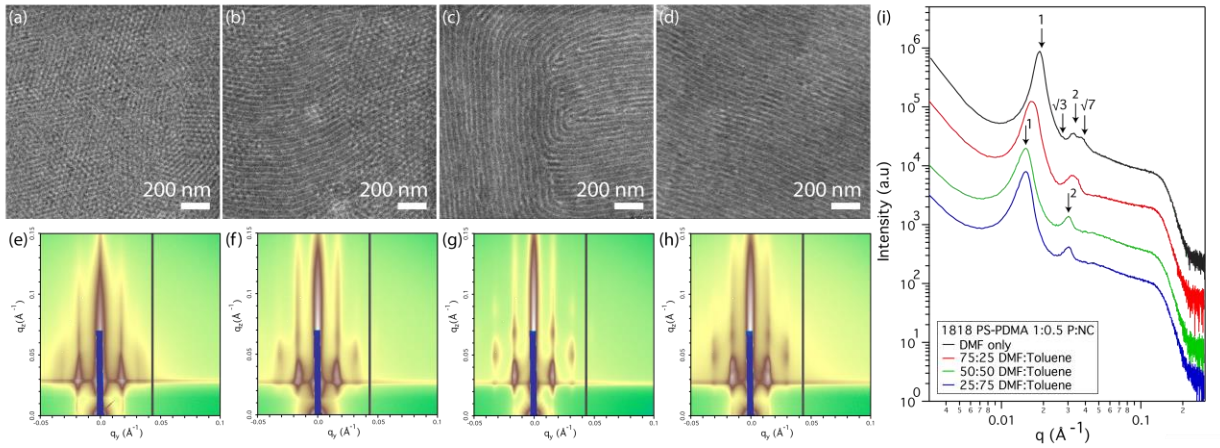

Figure 3.6: SEM and 2-D GISAXS for 18k-18k PS-PDMA with 9 vol% iron oxide nanocrystals solvent annealed with a mixed solvent of DMF:Toluene at a solvent ratio of (a,e) 100:0, (b,f) 75:25, (c,g) 50:50, and (d,h) 25:75. (i) 1-D linecuts across the horizon for the four GISAXS patterns demonstrating the transition from a scattering pattern characteristic of a hexagonal system to one of a lamellar system in plane.

Finally, one other more direct method to tune phase morphology is to tune the ratio of the block copolymer block lengths to shift our location in the block copolymer phase diagram directly. Since DMF preferentially swells PDMA, we hypothesized that a block copolymer with a significantly longer PS component would help offset the difference caused by preferential swelling and allow us to obtain a lamellar configuration accessible by symmetric block copolymers. In this vein, we solvent annealed 40k-18k PS-PDMA. In the absence of preferential swelling by DMF, 40k-18K PS-PDMA lies in the inverse-hexagonal region of the phase diagram. But as mentioned previously, preferential swelling of PDMA by DMF would reduce the effective volume fraction of PS in the system thereby shifting our location in the block copolymer phase diagram leftward. In the case of 40k-18k PS-PDMA, this would shift us into the lamellar region. The results of this solvent annealing of 40k-18k PS-PDMA in the presence of nanocrystals are shown in Figure 3.7.

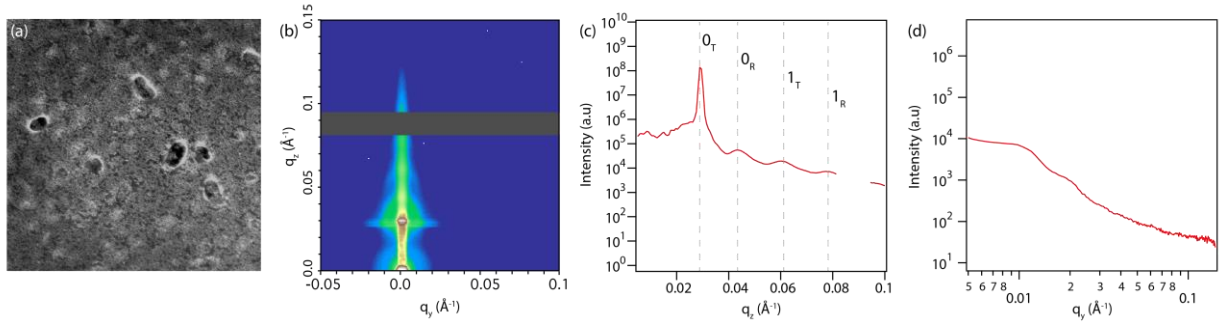

Figure 3.7: (a,b) Top-down SEM image and 2-D GISAXS data for 40k-18k PS-PDMA solvent annealed with DMF. (c,d) Linecuts along the direction perpendicular (q_z) and parallel (q_y) to the substrate surface.

(c) Indexing of lamellar peaks done in grey with the subscript T indicating scattering from the transmitted beam and R indicating scattering from the reflected beam.

Beginning our discussion with the SEM image, unlike all other images of the assemblies made using 30k-18k and 18k-18k PS-PDMA, we do not observe any fingerprint patterns or any significant features that would be immediately attributed to an assembled structure. Rather, we observe a top layer saturated with nanocrystals with regions of brighter contrast due to variations in nanocrystal concentration on the top surface. However, upon further investigation by x-ray scattering, we observe out-of-plane scattering features in the 2-D data that would be indicative of a lamellar structure orientated parallel to the substrate surface. This is made clear in the 1-D line-cut along the q_z direction perpendicular to the substrate surface where we observe periodic scattering peaks that differ only by an integer multiplier of the primary peak for a lamellar structure. In contrast, the 1-D line cut along the q_y direction parallel to the substrate surface only shows weak undulations that are apparent in a log-log plot and can be indicative of lamellae that are oriented perpendicular to the substrate surface. In short, we believe 40k-18k PS-PDMA rearranges into the lamellar configuration upon solvent annealing.

To determine the actual periodicity of the structure out of plane, we have to fit the data with a model of scattering by lamellar structures while accounting for distortions due to the refraction effects from the film and reflection effects from the substrate in GISAXS configuration. For lamellae with interfaces oriented parallel to the substrate surface, assuming complete reflection from the substrate, we can express the scattering from these diffuse Bragg sheets as

$$q_z = k_{iz} + \sqrt{k_{cp}^2 + \left[\frac{2\pi(2m+1)}{D_{lam}^{par}} \pm \sqrt{k_{iz}^2 - k_{cp}^2}\right]^2} \qquad \text{Equation 3.1}$$

$$k_{iz} = k_0 \sin\alpha_i \qquad \text{Equation 3.2}$$

$$k_{cp} = k_0 \sin\alpha_{cp} \qquad \text{Equation 3.3}$$

$$k_0 = \frac{2\pi}{\lambda} \qquad \text{Equation 3.4}$$

where q_z is the value of q where scattering is observed out of plane, α_i is the incident angle of the x-ray beam, and the α_{cp} is the critical angle of total external reflection for the film.[74,75] Each value of m provides a "minus branch" and "plus branch" corresponding to scattering from the direct beam and the reflected beam respectively. We fitted the peak locations observed in the 1-D line-cut with two floating parameters of the lamellar thickness D, and the critical angle of the film, $\alpha_{cp,}$ constraining the latter between 0.15 and 0.16 degrees (the critical angles of PS and PDMA respectively), and this result is shown in grey in Figure 3.7 (c). The result of the fitting is a lamellar thickness D of 34.7 nm and a critical angle of 0.158 degrees.

3.3.7 Deducing the nature of the PDMA–nanocrystal interaction

Since the volume fraction, size fraction and compositional diversity discussed hinges upon the interaction between PDMA and the nanocrystal, we sought to complete the investigation with an examination of this interaction. Prior work on polyacrylamide used in the flocculation of metal oxides in minerals processing has suggested that the interaction of acrylamide polymers with metal oxide surfaces in particular are actually based upon hydrogen bonding by the carbonyl of the polymer and hydroxyls on the metal oxide surface. More specifically, this interaction can be probed with Fourier transform infrared spectroscopy (FTIR) and can result in a characteristic splitting and shift of the carbonyl peak to lower wavenumbers. We conducted this study using 30k-18k Da PS-PDMA with both iron oxide nanocrystals and hydroxyl capped gold nanocrystals. In the absence of nanocrystals, the spectrum is dominated by a primary carbonyl peak at 1650 cm^{-1} with possibly a minor peak at 1600 cm^{-1} attributed to hydrogen bonding between PDMA chains.

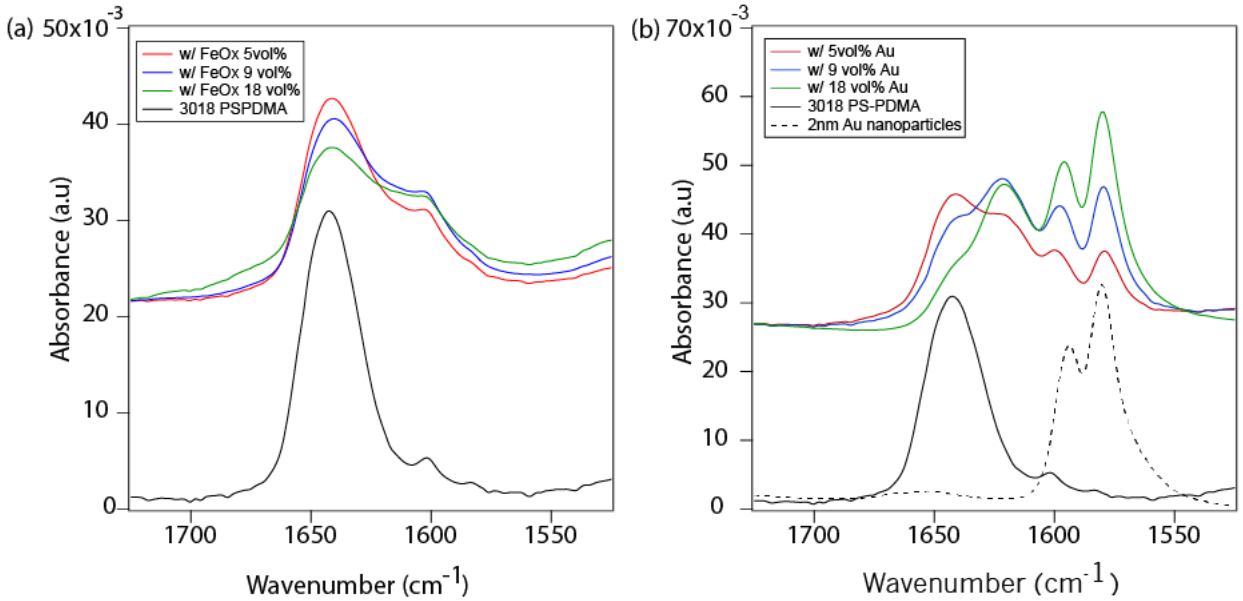

Figure 3.8: (a) Volume fraction series of iron oxide in 30k-18k PS-PDMA, and (b) volume fraction series of Au in 30k-18k PS-PDMA

Shown in Figure 3.8, with increasing nanocrystal volume fraction of iron oxide, the primary peak shifts to lower wavenumbers and relative peak intensities between the two peaks gradually equalize suggesting increasing interaction between the polymer and the nanocrystal surface. This trend is mirrored by the study done with hydroxyl capped gold nanocrystal. However, in this case, the secondary peak occurs around 1620 cm^{-1} and the relative peak intensities changes sufficiently to have the lower energy peak be the dominant peak at the highest volume fraction tested. The peaks at 1590 cm^{-1} and 1575 cm^{-1} arise from the native mercaptophenol ligands on the gold surface and their rise with increasing gold volume fraction is expected. This evidence directly suggests that the nature of the interaction between ligand stripped metal oxide nanocrystals and PDMA that facilitates assembly is strong hydrogen bonding. Furthermore, it motivates future studies that correlate differences in hydroxyl density on the particle surface with the observed shifts and changes in intensities observed in FTIR. For instance, mercaptophenol

capped Au must have a different hydroxyl density compared than iron oxide, and this may explain the difference in the observed location of the secondary peak as well as the relative intensity distribution between the two peaks.

3.4 Conclusion

In summary, we carried out a comprehensive study on the assembly of ligand stripped nanocrystals using PS-PDMA into equilibrium block copolymer phase separated morphologies examining both the method to achieve arrangement along with the phase separation behavior, volume fraction and size limits, compositional tunability, block copolymer phase tuning, and the nature of the PDMA – nanocrystal surface interaction. We show that PS-PDMA readily phase separates both in the absence and presence of nanocrystals upon solvent annealing with DMF, but the resulting morphologies are shifted relative to the expected morphologies on an ideal block copolymer phase diagram due to preferential swelling of PDMA by DMF. Size and volume fraction limits for this assembly system are consistent with prior studies in literature in that nanocrystals with diameter larger than the domain size were not directly assembled by the polymer, and this system has an intermediate volume fraction limit for successful assembly of 36 vol% nanocrystals. Then, we can tune the phase morphology of these assemblies either by adopting a coswelling approach with toluene as a cosolvent that favorably swells PS in order to shift our location in the phase diagram. Alternately, we can also move our location in the phase diagram by using a different block copolymer A-B block ratio. Finally, we show that this system can be used to assemble a variety of nanocrystals ranging from metal oxides like cerium oxide and indium tin oxide, to gold and cadmium selenide capped with mercaptophenol because the nature of the interaction between PDMA and the nanocrystal surface is hydrogen bonding.

3.4.1 Acknowledgements

The authors thank Prof. Fiona Doyle, Eric Schaible, and Chenhui Zhu for helpful discussions and beam-time support. Some of this research was carried out at the Molecular Foundry and at the Advanced Light Source at the Lawrence Berkeley National Laboratory, both user facilities that are supported by the Office of Science, Office of Basic Energy Sciences, of the U.S Department of Energy (DOE) under contract no. DE-AC02- 05CH11231. G.K.O. was supported by a National Science Foundation Graduate Research Fellowship under grant number DGE 1106400. D.J.M. acknowledges support of the Welch Foundation (F-1848).

Chapter 4

Future Work for the Assembly of Ligand Stripped Nanocrystals

4.1 Introduction

In Chapter 2, we explored the assembly of nanocrystals using PS-PDMA in micellar form and investigated the influence of nanocrystal size and volume fraction on the ordering of the assembly. This work was a follow up to prior work that demonstrated the compositional diversity inherent to the PS-PDMA system for assembling a variety of nanocrystals.[20] Then, in Chapter 3, we extended this study of size and volume fraction on equilibrium PS-PDMA nanocrystal assemblies after realizing structural control via directed assembly of nanocrystals using PS-PDMA block copolymer microphase separation behavior. As we expected, even in microphase-separated form, these assemblies inherit the compositional versatility first demonstrated for the miceller assemblies. As part of the study, we also uncovered new insight into the fundamental forces governing the interaction between PDMA and ligand stripped nanocrystals. Specifically, we understand that this interaction is based upon hydrogen bonding. Here, we will discuss promising future directions that build upon the aforementioned three aspects.

4.2 Preliminary Data and Further Studies

4.2.1 Nanocrystal coassembly with PS-PDMA block copolymer micelles

Having studied the size, volume fraction and compositional diversity for PS-PDMA micelle assemblies, a natural extension would be to investigate the coassembly of a mix of nanocrystals in the presence of PS-PDMA. The motivations for these studies are two fold. First, in the context of assembly, we can potentially understand how nanocrystal arrangement within the PDMA domain may be engineered. If we extrapolate from current knowledge in literature that base nanocrystal segregation and location in a block copolymer domain purely on nanocrystal size, then we would expect the segregation of large nanocrystals to the center of the PDMA domain and small nanocrystals closer to the PS-PDMA interface. Preliminary data utilizing the coassembly of small gold nanoparticles (2 nm) and large indium tin oxide (ITO) nanocrystals (10 nm) shown in Figure 4.1 shows that this expectation is proven in the case of a dilute amount of the large nanocrystal (panel c), but does not seem to be obeyed in the case of assemblies with an equal volume fraction of gold and ITO. Specifically, in the case of the latter, we clearly observe the formation of an internal nanocrystal-nanocrystal structure comprising of a single layer of

gold nanoparticles assembled in between large ITO nanocrystals all of which reside within the polymer domain (panel f). This is in direct contrast to equilibrium predictions extrapolated from the dilute limit of nanoparticle assembly in a block polymer domain where we should have observed only small gold nanoparticles exclusively at the PS-PDMA interface and large ITO nanocrystals away from the interface not unlike a core-shell structure.

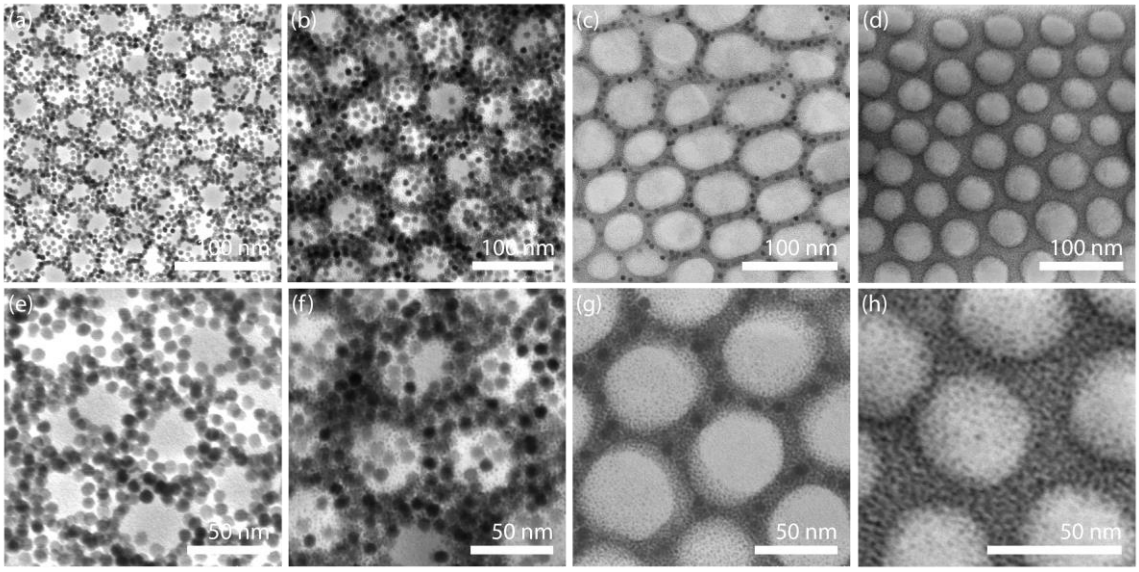

Figure 4.1: (a,e) 60k-18k PS-PDMA micelle assembly of 10 nm indium tin oxide (ITO) nanocrystals. (b,f) 60k-18k PS-PDMA micelle assembly of 10 nm indium tin oxide (ITO) nanocrystals and 2 nm Au nanoparticles at equal volume fraction. (c,g) 60k-18k PS-PDMA micelle assembly of dilute 10 nm indium tin oxide (ITO) nanocrystals with a majority of 2 nm Au nanoparticles. (d,h) 60k - 18k PS-PDMA micelle assembly of 2 nm Au nanoparticles.

Second, from the standpoint of applications, the ability to coassemble two different classes of nanocrystals such as a metal and a metal oxide could potentially open up a new avenue for nanostructuring important engineering materials. For instance, in the field of catalysis, metal oxide supported metals have shown improved performance as catalyst due to a synergistic effect between the metal oxide and the metal catalyst on the surface. Alternately, in the field of nanocrystal optics, the coassembly of a plasmonic metal oxide like ITO and a metal chalcogenide like PbSe or PbS could be used to study the coupling of optical phenomena such as plasmon enhancement of quantum dot photoluminescence.

4.2.2 Phase control of PS-PDMA in solution using a cosolvent

As we have alluded to in Chapter 1, the use of specific solvents can be used to tune the block copolymer phase in solution similar to how one might achieve morphological control in a surfactant system. While all studies in this dissertation utilized a specific solvent combination of dimethylformamide and ethanol – both of which are mostly selective for PDMA -, other solvents that balance the selectivity of PDMA and PS with the block lengths of PDMA and PS can be used to access other morphologies in solution. The SEM micrographs in Figure 4.2 are data for

an early attempt to achieve this morphological control in solution. Specifically, the change in morphology was achieved by using 50:50 v/v of tetrahydrofuran and water. Considering the solubility parameters of dimethylformamide (DMF, 24.7 $\delta/MPa^{\frac{1}{2}}$), ethanol (EtOH, 26.2 $\delta/MPa^{\frac{1}{2}}$), tetrahydrofuran (THF, 18.5 $\delta/MPa^{\frac{1}{2}}$), and water (H_2O, 48 $\delta/MPa^{\frac{1}{2}}$) and approximating the final solution Hildebrand solubility parameter by simple weightage of volume fraction, we see that the final solution parameter is shifted from 25.45 $\delta/MPa^{\frac{1}{2}}$ to 33.25 $\delta/MPa^{\frac{1}{2}}$ comparing a simple 50:50 v/v solution of DMF:EtOH to THF:H_2O.

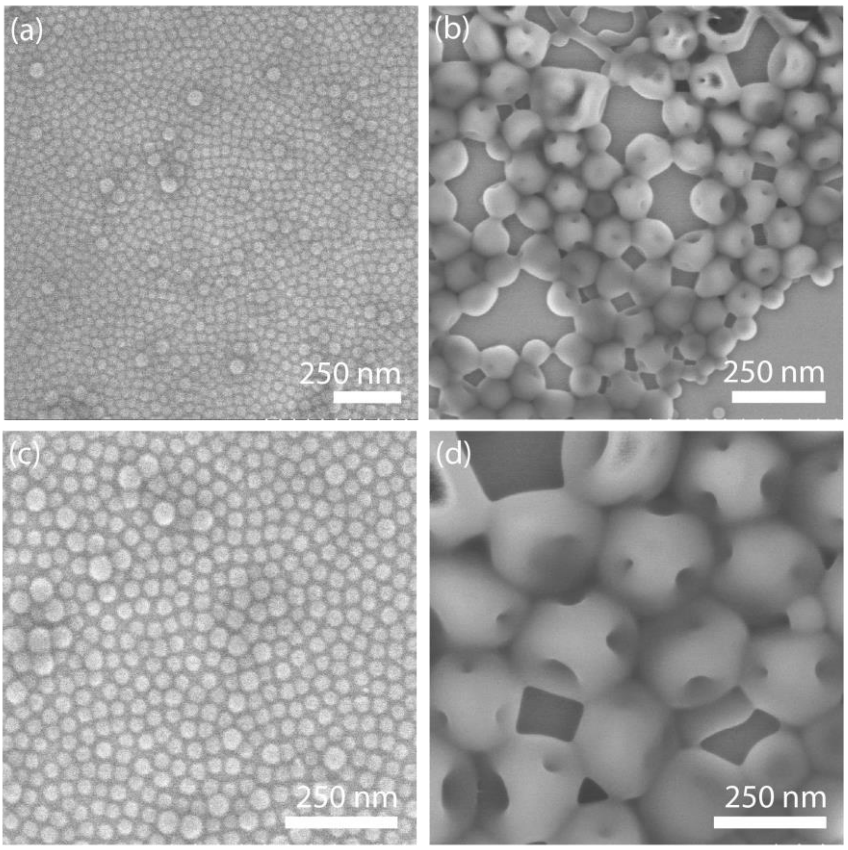

Figure 4.2: Scanning electron microscopy image of 18k – 18k PS-PDMA from a solution of 50:50 v/v THF:water (a,c), and 60k – 18k PS-PDMA from a solution of 50:50 v/v THF:water (b,d).

Shown in Figure 4.2, this phase tuning in solution is attempted with either 18k-18k PS-PDMA (panel a and c) or 60k-18k PS-PDMA (panel b and d). As observed, for symmetric PS-PDMA, changing the solvent combination to THF:water does not change the phase morphology and we continue to observe the formation of spherical micelles. In contrast, changing the solvent combination for 60k-18k PS-PDMA to THF:water changes the phase morphologies from spherical micelles to one that resemble perforated micelles.

4.2.3 Assembly of ligand stripped nanocrystals using PS-P4VP

One last insight from the work in Chapter 3 is the discovery that the PDMA-metal oxide nanocrystal interaction is based upon hydrogen bonding onto native hydroxyl moieties on the metal oxide surface. Therefore, assembly of ligand stripped nanocrystals can actually be achieved using another polymer that readily hydrogen bonds. One example is the workhorse polymer used in block copolymer assembly, PS-P4VP.

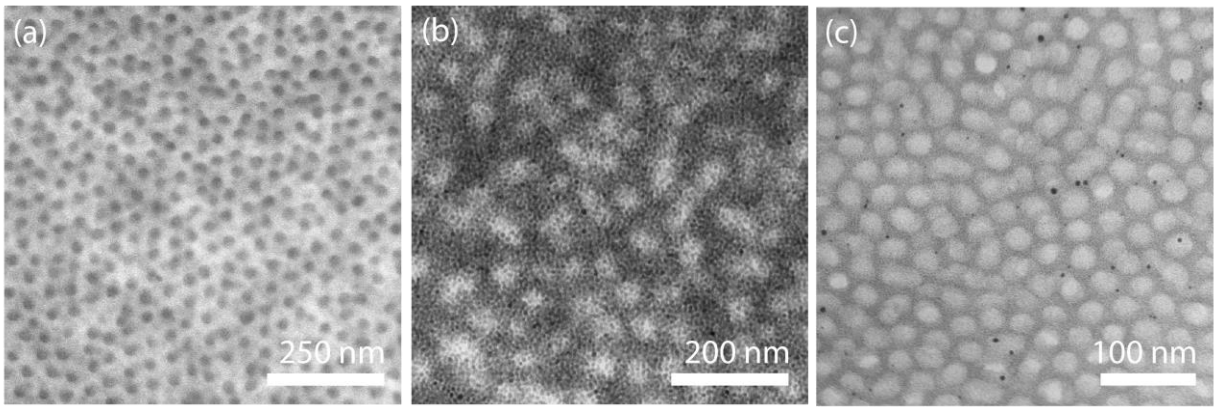

Figure 4.3: Transmission electron microscopy image of (a) PS-P4VP micelles, (b) PS-P4VP micelles decorated with 3 nm iron oxide, and (c) PS-P4VP micelles decorated with 2 nm Au nanoparticles.

Shown in Figure 4.3 is the assembly of 3 nm iron oxide and 2 nm mercaptophenol capped gold nanoparticles using PS-P4VP micelles in DMF:EtOH 20:80 v/v. As expected, we can achieve structures very similar to that made with PS-PDMA. This ability to assemble ligand stripped nanocrystals using a more conventional block copolymer opens up the accessibility of these materials for assembly to the field and is particularly enticing because it will also allow us to more precisely tune phase morphology since the phase diagram for PS-P4VP is well studied and known.

Chapter 5

Colloidal Nanocrystal Films Reveal the Mechanism for Intermediate Temperature Proton Conductivity in Porous Ceramics

Reproduced with permission from: Evan L. Runnerstrom*, Gary K. Ong*, Giuliano Gregori, Joachin Maier, and Delia Milliron, "Colloidal Nanocrystal Films Reveal the Mechanism for Intermediate Temperature Proton Conductivity in Porous Ceramics," *J. Phys. Chem. C,* **2018**, 13624-13635.

5.1 Introduction

Solid-state proton conduction is an important phenomenon with numerous consequences for electrochemical energy storage and conversion.[76–80] Nonetheless, further improving proton transport in solids remains a pressing and interesting scientific and technological challenge. Proton-conducting membranes and solid electrolytes are critical components in many electrochemical devices and clean energy technologies, particularly fuel cells, and the performance of such devices is often limited by proton transport.[76,81–84] Well-studied solid materials that support proton conduction include polymers such as Nafion,[76–80,82,84] solid acids such as $CsHSO_4$,[85,86] and high-temperature proton-conducting ternary oxides such as acceptor doped $BaZrO_3$ and $BaCeO_3$.[81,83,87] Despite the wealth of knowledge in this field, these materials have significant shortcomings. While proton exchange membranes can exhibit conductivities comparable to aqueous acid solutions at temperatures around 80°C ($\sigma>10^{-1}$ S/cm),[79] Nafion is expensive and has very poor conductivity at temperatures above 85-90°C due to dehydration.[76,78,79,82] Meanwhile, the ceramic oxide-based proton conductors require high operating temperatures (350°C-800°C, with conductivity reaching 10^{-2} S/cm only above 400°C) and are prone to decompose to their binary oxide constituents under typical fuel cell operating conditions.[79,81,83,87] Additionally, the performance of ceramic proton conductors has lagged behind those of ceramic oxygen-ion conductors (*i.e.*, yttria-stabilized zirconia and acceptor-doped ceria, with $\sigma>1$ S/cm at 1000-1250°C),[79,81,83,86] which are also more stable, favoring the development of high-temperature solid oxide fuel cells (SOFCs) based on said ceramics. Using ceramic proton or oxygen ion conductors in high-temperature fuel cell operation requires exotic and expensive electroceramic materials to connect multiple cells in series, induces thermal stresses and degradation, and requires large energy input to heat the cell up to operating temperature.[83] These requirements all complicate operation, decrease efficiency, and increase costs.[88] Hence, there is great interest in alternative proton conducting materials with the potential to enable fuel cell operation in the "gap" that currently exists at intermediate temperatures

between 200°C and 500°C, which is a desirable range for energy conversion and electrochemical processes, and which would also enable advances in fuel cell power output and mobility.[79,83,86]

Unsurprisingly, research in this field has steadily grown over the past 10 years; motivated in part by the shortcomings of polymeric and solid oxide proton-conducting materials, significant advances have recently been made to understand proton transport through inorganic and hybrid organic-inorganic materials with high porosities and/or surface area-to-volume ratios. Such porosity and high specific surface area, which may be introduced through nanostructuring or may be intrinsic to the structure of these materials, has been found to bestow significant proton conductivity to these materials under humidified atmospheres. Some noteworthy examples include porous sol-gel silica glasses,[89] sol-gel anatase titanium dioxide (TiO_2) thin films,[90,91] porous metal-organic frameworks,[92] graphene oxide nanosheets,[93] and mesoporous networks of silica-phosphotungstic acid hybrids.[94] Interestingly, porous nanocrystalline ceramics, some of which are closely related to high-temperature oxygen ion conductors, have garnered significant attention for their proton conductivity and stability at moderate temperatures. These include yttrium-stabilized zirconia (YSZ),[95–102] samarium- and gadolinium-doped cerium oxide (SDC/GDC),[96,103–105] and pure cerium oxide (CeO_2),[105–107] which are all fluorite-type oxides that are most often studied as high- temperature oxygen ion conductors. All of these materials are poor proton conductors in their bulk form, yet nanocrystalline samples of these, as well as TiO_2,[108,109] display significant proton conductivity at temperatures below 200°C in humidified atmospheres. A commonality we note is that these ceramics either contain a high number of extrinsic oxygen vacancies or can support significant intrinsic oxygen vacancy concentrations at low oxygen activity.

In early work, Kim and coworkers observed intermediate-temperature proton conductivity in fine-grained YSZ under humid environments, demonstrating conductivities of $\sigma \sim 10^{-7}$ to 10^{-10} S/cm between room temperature and 120°C.[102,110,111] The authors suggested that grain boundaries were the proton transport paths and attributed the conductivity to the high density of these defects in the sintered material. In contrast, subsequent work suggested that proton conduction in nanocrystalline YSZ arises from residual open porosity that is typically present in nanocrystalline ceramics, owing to low sintering temperatures.[101,102,105] Indeed, Pietrowski and coworkers, in 2012, observed water adsorption onto internal surfaces of nanocrystalline YSZ *via* infrared spectroscopy,[112] and an interconnected porous network with surface-adsorbed water likely facilitates proton transport at intermediate temperatures.[101,102,105] Conversely, fully dense films of nanocrystalline YSZ conduct only oxygen ions and do not support proton conduction, except along the sample surface at temperatures below 50°C. [100,102]

In 2011, Shirpour and coworkers observed proton conduction at and below 250°C in nanocrystalline CeO_2 and GDC ($\sigma \sim 10^{-4}$ to 10^{-6} S/cm between 100°C and 250°C), and demonstrated that the mechanism likely involved adsorption of a water network into wedge-shaped, interconnected pores.[105] Following up in 2013, Gregori and coworkers confirmed that only mesoporous CeO_2 thin films exhibited proton conductivity under wet conditions, up to temperatures as high as 300°C, while dense films, whether nanocrystalline or not, did not conduct protons.[106] These observations firmly established porosity, rather than grain boundaries,

as the central factor for proton transport through metal oxides at intermediate and low temperatures. Contemporary work by Oh and coworkers, studying proton conduction in CeO_2 thin films with nanoscale columnar grains, supported these conclusions by confirming that proton conduction occurs as a result of the adsorption of water inside of pores.[107] That report also suggested a possible mechanism, namely dissociative adsorption of water at CeO_2 surface oxygen vacancy sites. More recently, Tredici *et al.* examined low- and intermediate-temperature proton conductivity in nanocrystalline TiO_2 of various grain sizes and porosity using solid-state NMR.[109] They found that both physisorbed water and chemisorbed hydroxyl moieties contributed to proton conduction at low and intermediate temperatures, respectively. Other recent work includes that by Ding *et al.*, who used time –resolved Kelvin probe force microscopy to interrogate water splitting and charge transport in a nanostructured CeO_2-based electrochemical device, and Jiang and Hertz's study on intermediate proton conduction on the surface of YSZ ultrathin films. Both of these studies strongly suggest that oxygen defects in nanocrystalline ceramics play an important role in proton transport.[113,114] Nevertheless, the mechanism for proton generation and conduction in porous oxides is still not fully understood since the studies reported to date have examined only singular material compositions without systematic control over structural parameters such as pore dimensions, oxygen activity and defect equilibria, or surface chemistry.

Taken together, the results of the past few years imply that proton transport in nanocrystalline oxides is enabled by: 1) porosity, pore size, and specific surface area, which influence water adsorption, and 2) the interactions between adsorbed water and metal oxide surfaces. It is likely that the latter not only mediate proton diffusion at surfaces or through adsorbed water layers, but may also be responsible for generating protonic charge carriers in the first place. Because physical fabrication processes, such as sintering, were typically used to fabricate these nanocrystalline films in the past, fine control over crystallite size, exposed surface area, and pore size has not been possible and the effects of these variables on proton conduction at intermediate temperatures have not been systematically revealed. Here, we address this problem by using colloidal ceramic nanocrystals of CeO_2 and TiO_2 that are synthesized with controlled size. By processing the nanocrystals into continuous films and removing their native surface-bound ligands, we generate microporous nanocrystalline thin films with well-defined crystallite size, pore size, and exposed surface area. Conductivity measurements using AC impedance spectroscopy in a controlled temperature and gas environment with controlled humidity revealed proton conduction in both CeO_2 and TiO_2 films at intermediate temperatures. Furthermore, we found that the proton conductivity was strongly modulated by the partial pressure of oxygen, as samples under humid oxygen displayed orders of magnitude reduction in conductivity compared to samples under Ar, a phenomenon that appears to be general but has not been previously reported for nanocrystalline ceramics. Based on these new observations and consistencies across the literature, we conclude that proton conduction in nanocrystalline metal oxides arises from dissociative water adsorption and interface-mediated transport at active surface defect sites.

5.2 Experimental methods

5.2.1 Nanocrystal Synthesis

We synthesized CeO_2 and TiO_2 colloidal nanocrystals using adaptations of published literature methods.[115,116] Cerium (III) nitrate hexahydrate ($Ce(NO_3)_3{\cdot}6H_2O$, 99.99%), titanium (IV) butoxide ($Ti(OBu)_4$, 97%), oleic acid (OLAC, 90%), octadecylamine (ODAM, 90%), 1-octadecene (ODE, 90%), 200 proof ethanol, octane (98%)formic acid (reagent grade), and acetonitrile (MeCN, ACS grade) were purchased from Sigma Aldrich. Oleylamine (OLAM, 80-90%) was purchased from Acros Organics. Hexanes (ACS grade), chloroform ($CHCl_3$, ACS grade) and denatured ethanol (EtOH, ACS grade) were purchased from BDH. Ultra-pure water was obtained using an EMD Millipore Milli-Q water purification system.

To synthesize 3.9 nm CeO_2 nanocrystals, 2 mmol $Ce(NO_3)_3{\cdot}6H_2O$ was combined with 24 mmol OLAM and 5 mL ODE in a 50 mL round bottom flask under inert nitrogen atmosphere. Under constant magnetic stirring, the temperature of the reaction mixture was raised to 80°C for 30 minutes, and then the temperature was raised to 250°C for 2 hours to nucleate and grow the nanocrystals. After the reaction, the nanocrystals were purified by four cycles of flocculation with EtOH, centrifugation, and redispersion in hexanes. Finally, the nanocrystals were dispersed in a 1:1 volumetric mixture of hexane:octane at a concentration of 33 mg/mL and filtered with a 0.2 micron poly(tetrafluoroethylene) syringe filter.

To synthesize 9.9 nm CeO_2 nanocrystals, 15 mmol ODAM, 15 mmol OLAM, and 5mL ODE were combined in a 50 mL round bottom flask under inert nitrogen atmosphere. Under constant magnetic stirring, this mixture was heated to 70°C to melt the ODAM, upon which 10 mmol $Ce(NO_3)_3{\cdot}6H_2O$ and 0.725 mL ultra-pure water were added to the flask. The mixture was then slowly heated to 175°C over 30 minutes to homogenize the solution before raising the temperature further to 230°C to nucleate and grow the nanocrystals. After about 2 minutes at 230°C, the reaction was complete when a large amount of smoke was released (presumably NO_2 gas) and the solution instantaneously became optically clear and a deep brown color. The nanocrystals were purified by the same methods as the 3.9 nm CeO_2 nanocrystals, except that this sample was additionally subjected to three rounds of size-selective precipitation to improve uniformity. Finally, the nanocrystals were dispersed in 1:1 hexane:octane at a concentration of 37 mg/mL and filtered. **CAUTION**: without adequate ventilation or pressure relief, this reaction is prone to over-pressurization as the nitrate precursor violently decomposes to liberate large volumes of NO_2 gas.

To synthesize 6.7 nm TiO_2 nanocrystals, 5 mmol $Ti(OBu)_4$, 30 mmol OLAC, 20 mmol OLAM, and 100 mmol 200 proof ethanol were combined and stirred for 30 minutes before being transferred into a 40 mL Teflon cup. The cup was placed inside a 100 mL Teflon-lined stainless steel autoclave, which contained 19.8 mL of 200 proof ethanol and 0.8 mL of ultra-pure water. The autoclave was then sealed and placed into a 180°C oven for 18 hours. After the reaction, the nanocrystals were purified by four cycles of precipitation with EtOH, centrifugation, and

redispersion in hexanes, before finally being dispersed in 1:1 hexane:octane by volume and filtered.

5.2.2 Transmission electron microscopy

Transmission electron microscopy (TEM) was performed using a Zeiss Libra 120 operating at 120 kV accelerating voltage. TEM samples of colloidal nanocrystals were prepared by drop casting dilute solutions of nanocrystals in toluene onto TEM grids. Particle size analysis was performed on TEM micrographs using ImageJ to measure the diameters of at least 320 nanocrystals from each sample.

5.2.3 X-ray diffraction

Powder and thin film X-ray diffraction (XRD) was performed on a Bruker AXS D8 Discover X-ray diffractometer equipped with a GADDS area detector in Bragg-Bretano geometry, using Cu Kα radiation with a wavelength of 1.54 Å.

5.2.4 Thin-film deposition

We fabricated nanocrystal-based thin films by spincoating the 1:1 hexane:octane dispersions onto 1x1 cm ultrasonically-cleaned (Hellmanex detergent, acetone, isopropanol) quartz substrates. Following spincoating, we employed a ligand exchange and removal procedure previously developed in our laboratory to generate open microporosity within the films by removing the organic ligands surrounding each nanocrystal.[117] This method replaces the native OLAM or OLAC ligands on the nanocrystal surfaces with formic acid, which is volatile and easily baked off leaving no detectable residue. The films were soaked in a 0.1 M solution of formic acid in acetonitrile for 10 minutes, rinsed four times with an equal mixture of $MeCN/CHCl_3$, and baked in air for 10 minutes on a hot plate held at 300°C. The entire procedure was repeated two more times to generate films with desired thicknesses close to 300 nm for transport measurements. For TEM imaging of spincoated nanocrystals, the nanocrystal dispersion was diluted by a factor of six and 20 μL of the diluted dispersion was spincoated onto a holey carbon grid at 2000 rpm. The grid was placed on a silicon substrate with a copper slot grid spacer between the TEM grid and the substrate. Following spincoating, the same ligand exchange procedure is performed, excluding the $MeCN/CHCl_3$ rinse.

5.2.5 Impedance spectroscopy

For conductivity measurements, we prepared samples on quartz substrates (10 mm by 10 mm by 0.5 mm) and deposited two 400 nm thick, 4.5 mm by 10 mm parallel platinum electrodes onto the top surface of the nanocrystal film using an Edwards Auto 306 sputtering system (60W, 30 minutes), leaving a 1 mm by 10 mm uncoated region between them. *In situ* conductivity measurements were performed with the sample in a controlled environment measurement cell.

This cell allowed us to vary temperature, carrier gas (grade 5.0 Ar or O_2), and humidity; wet atmospheres were achieved by bubbling the carrier gas through a water bubbler held at 17°C (pH_2O = 20 mbar). To measure conductivity, we used AC impedance spectroscopy (Novocontrol Alpha-A impedance analyzer) over a frequency range of 1 MHz to 1-10 Hz, with a voltage amplitude of 0.12 V, and allowed the samples to equilibrate with the surrounding environment for at least 2 hours at each temperature before recording the reported conductivity values.

5.2.6 X-ray absorption spectroscopy

X-ray absorption spectroscopy (XAS) was performed with both normalized total electron yield (TEY) and total fluorescence yield (TFY) for surface and bulk sensitivity respectively. Experiment were conducted at beam line 8.0.1 at the Advanced Light Source, Berkeley California.

5.2.7 Ellipsometric porosimetry

EP data were acquired using a Semilab PS-1100R ellipsometric porosimeter, with toluene as the adsorbent, and analyzed the results using the Semilab SEA software.

5.3 Results and discussion

5.3.1 TEM micrographs and x-ray diffraction of model materials

TEM micrographs of nanocrystal dispersions drop cast onto TEM grids (Figure 5.1) show that the nanocrystals used in this study are relatively uniform with distinct and tunable size, which allows us to controllably study the influence of grain size and porosity on proton conduction. Particle size analysis (Figure C.1) confirms that the samples have well-defined grain sizes with respect to each other. The standard deviations in diameter for the 3.9 nm CeO_2, 9.9 nm CeO_2, and 6.7 nm TiO_2 nanocrystals were 0.6, 1.2, and 0.8 nm, respectively. The powder XRD (Figure 5.1e) patterns for both CeO_2 samples matched that of the fluorite CeO_2 crystal structure, while the XRD pattern for the TiO_2 sample was indexed to the anatase phase.

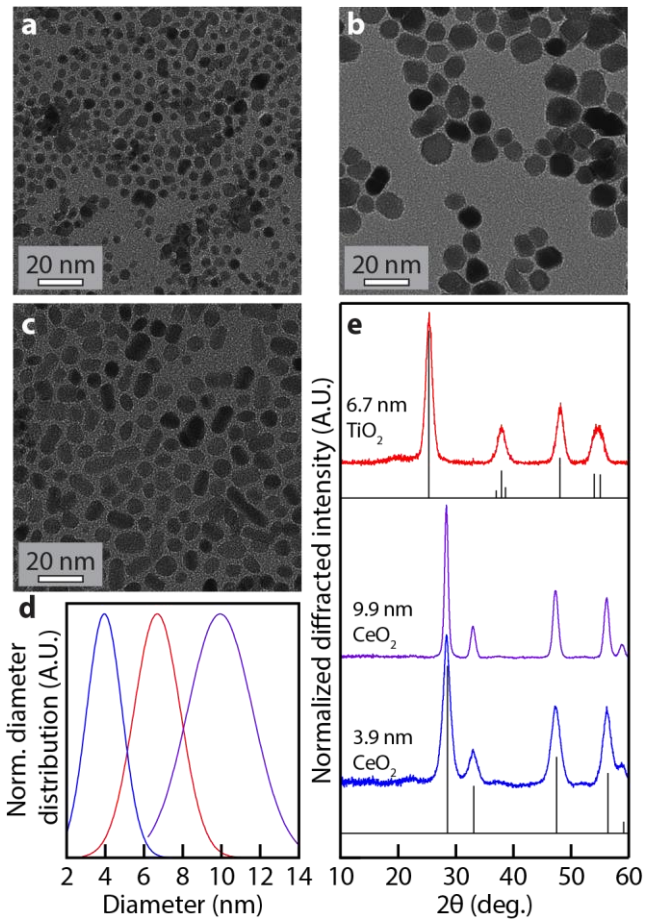

Figure 5.1: TEM and XRD characterization of colloidal CeO_2 and TiO_2 nanocrystals. **a**: TEM micrograph of CeO_2 with average diameter of 3.9 nm. **b**: TEM micrograph of CeO_2 with average diameter of 9.9 nm. **c**: TEM micrograph of TiO_2 with average diameter of 6.7 nm. **d**: Gaussian size distribution curves resulting from fits to particle diameter measurements using ImageJ. Left curve: 3.9 nm CeO_2, 1.2 nm Gaussian width. Middle curve: 6.7 nm TiO_2, 1.6 nm Gaussian width. Right curve: 9.9 nm CeO_2, 2.4 nm Gaussian width. **e**: Powder XRD patterns of CeO_2 and TiO_2 nanocrystal samples. The CeO_2 samples are indexed to the cubic fluorite structure (reference pattern from PDF card no. 01-081-0792) and the TiO_2 sample is indexed to the tetragonal anatase structure (reference pattern from PDF card no. 01-075-2547).

5.3.2 Tracking ligand exchange and introducing porosity

During nanocrystal film fabrication, we tracked the ligand exchange process using Fourier transform infrared spectroscopy (FTIR, Figure 5.2 and Figure C.2) at room temperature and under ambient conditions. FTIR allows us to monitor the alkyl C-H stretching modes between 2800-2900 cm^{-1} for films deposited on double-polished, undoped silicon. The films as deposited display strong C-H peaks, indicating the presence of organic ligands at the nanocrystal surfaces. After the formic acid soak and rinse, the C-H stretch is strongly diminished in intensity, indicating that the long alkyl chain ligands have been displaced and washed out of the film. Finally, after the film is baked and returned to room temperature under ambient conditions, the C-H stretch is eliminated, indicating the complete removal of organics from the film and the

generation of open porosity. FTIR also confirms that this process works over multiple deposition cycles to build up thick, porous films. The appearance of a broad O-H peak at around 3400 cm^{-1} after the baking step confirms that the films are porous and adsorb water vapor from the atmosphere. We note that the 3.9 nm CeO_2 appears to adsorb significantly more water than either the 9.9 nm CeO_2 or 6.7 nm TiO_2 samples, the last of which appears to adsorb the least amount of water. These differences in water uptake at room temperature presage differing abilities to conduct protons within the pores, which will be discussed below.

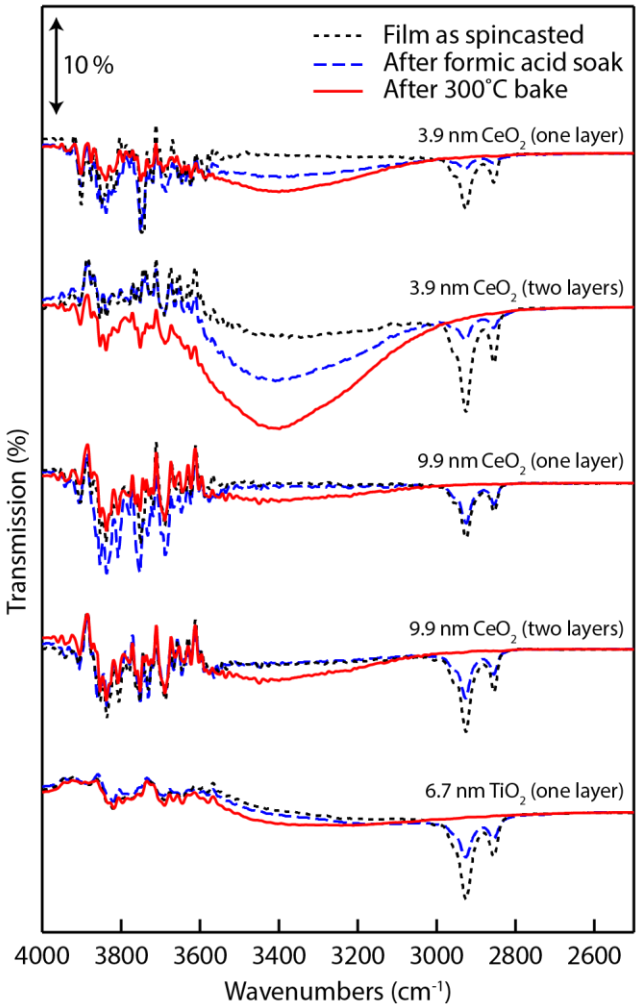

Figure 5.2: FTIR spectroscopy tracking ligand exchange process of CeO_2 and TiO_2 nanocrystal films on undoped silicon. The spectra displayed, which are offset for clarity, are of the films after spincoating (small black dashed lines), after the formic acid soak and rinse (larger blue dashes), and after the 300°C bake (solid red), confirming the removal of organics from the film by the disappearance of the C-H stretching bands at ~2800-2900 cm^{-1}. The sharp peaks between 3900 and 3600 cm^{-1} are instrumental noise. Full spectral range spectra are included in Figure C.2.

To confirm the open porosity and nanocrystalline character of our films, we imaged them using TEM and scanning electron microscopy (SEM). TEM imaging of ligand exchanged CeO_2 nanocrystal films one to two layers thick on holey carbon TEM grids revealed the presence of

spherical and cylindrical pores with diameters ranging from roughly 0.4 nm to 1 nm (Figure 5.3a). To ensure that the conditions for measuring proton transport would not coarsen the films or collapse their porosity, we further annealed samples deposited on silicon at 500°C for two hours under Ar. Representative cross-sectional and top-down SEM images (Figure 5.3b,c and Figure C.3) of these samples reveal that the films maintain their porosity and nanocrystalline character, and Scherrer analysis of XRD patterns before and after annealing confirms that the grain size did not increase appreciably (Figure C.4). Likewise, TEM imaging of cross-sections prepared from an annealed film of 9.9 nm CeO_2 nanocrystals confirmed the presence of remaining micropores (Figure C.5). Correspondingly, experimental temperatures were limited to 450°C and below to avoid changes in sample morphology during *in situ* conductivity measurements.

We also performed ellipsometric porosimetry (EP, further described in Appendix C and Figure C.6) to measure the pore size and distribution of our films deposited on undoped silicon.[118–120] The EP data were acquired using a Semilab PS-1100R ellipsometric porosimeter, with toluene as the adsorbent, and the results were analyzed using the Semilab SEA software (Figure C.6). EP allows for a direct measurement of porosity, surface area (derived using Brunauer-Emmett-Teller theory, or BET), and pore size distribution in our films by measuring how the refractive index changes with solvent partial pressure as the film takes up solvent. Representative results for a 9.9 nm CeO_2 nanocrystal film, including the porosity isotherm, mesopore size distribution, and micropore size distribution (for pore radii <1 nm, calculated using the Dubinin-Raduchkevish model)[120,121] are shown in Figure 5.3d-f. The hysteresis in the adsorption and desorption curves (Figure 5.3d) is characteristic of open and accessible mesopores throughout the film. The hysteresis occurs because the radius of curvature of the liquid meniscus within the pores is different during adsorption than during desorption, leading to different critical pore radii for capillary condensation and evaporation during the adsorption and desorption steps, respectively. Additionally, the significant solvent uptake and lack of hysteresis at low pressures indicates the presence of significant microporosity within the film. Finally, the shape of the hysteresis loop (broader on adsorption, steeper during desorption) is indicative of approximately spherical or cylindrical pores connected by smaller cylindrical pore necks in an "ink bottle" geometry. This effect arises from solvent in the larger pores being unable to evaporate at the partial pressure associated with the critical pore radius, because the partial pressure is still too high for the adsorbed solvent in the smaller pore necks or interconnections to undergo capillary evaporation. Ultimately, once the pressure is low enough to evacuate the smaller pore necks, the solvent evaporates from the large and small pores simultaneously, leading to the sharper drop in the desorption curve.[122] Scanning tunneling electron microscopy (STEM, Figure C.5) imaging of the 9.9 nm CeO_2 nanocrystal film allowed us to more clearly resolve the residual open porosity, providing an additional qualitative measure of pore shape and confirming the ink bottle geometry.

The rest of the EP results are displayed in Figure C.7 and summarized in Table 5.1. While the 9.9 nm CeO_2 nanocrystal film presents a higher overall porosity, surface area, and larger mesopore size, visual examination of the SEM micrographs (see Figure C.3) indicates that these differences arise mostly from some small cracks and voids in the film. The 3.9 nm CeO_2

and 6.7 nm TiO_2 nanocrystal films present nearly identical morphologies with respect to porosity, surface area, and pore size; this similarity means that differences in proton transport will result from material, rather than morphological, differences. This will prove valuable when we compare the proton transport characteristics of both films, below. Notably, the micropore radii for all three samples are very similar.

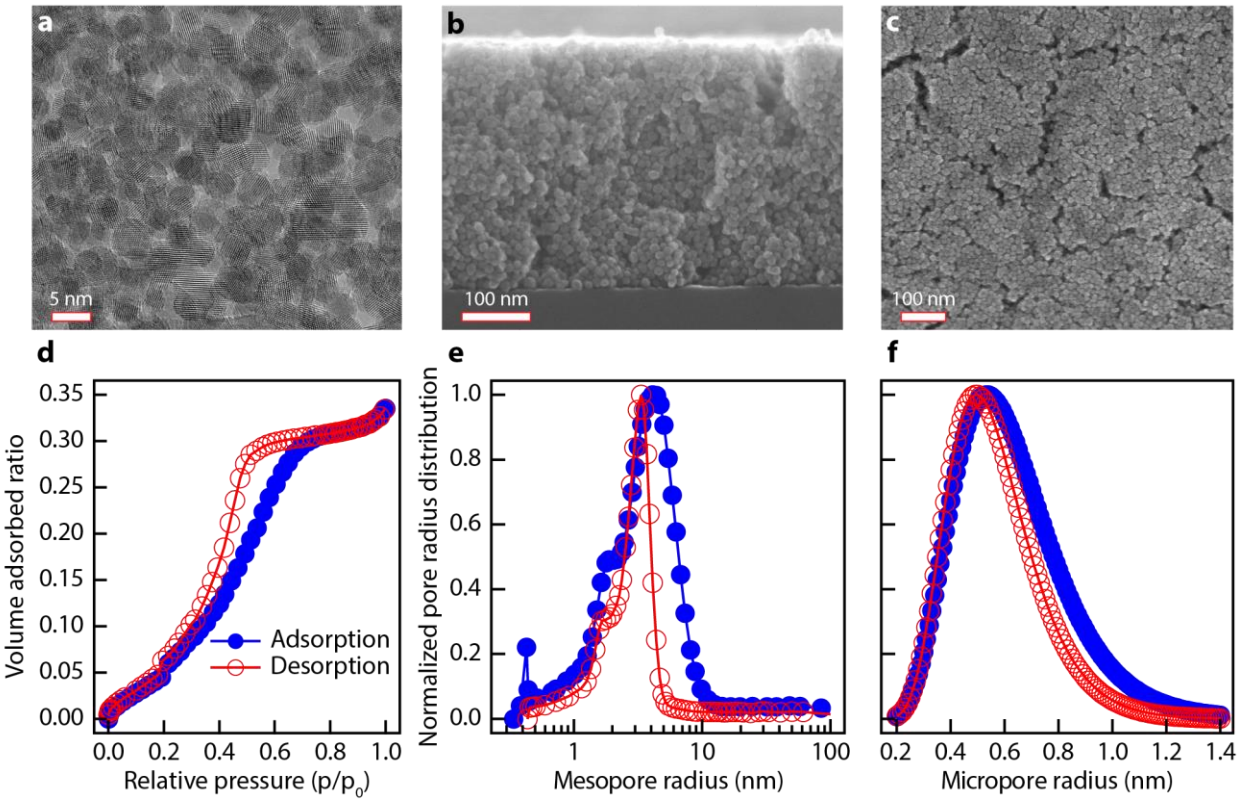

Figure 5.3: TEM, SEM and EP characterization of porous nanocrystal films. a) TEM micrograph of a one- to two-monolayer film of 3.9 nm CeO_2 nanocrystals spincoated onto a carbon grid and ligand exchanged, displaying residual porosity. b) Cross-section SEM micrograph of a film made from 9.9 nm CeO_2 nanocrystals after annealing at 500°C for two hours. c) Top-down SEM micrograph of same film. d) Volume adsorption and desorption isotherm (for toluene) of a film made from 9.9 nm CeO_2 nanocrystals, measured with EP. e) Normalized mesopore radius distribution for the same film derived from EP. f) Derived micropore radius distribution for the same film.

Table 5.1: Summary of porosity results for the samples used in this study as measured by EP.

Nanocrystal size	Porosity	Surface area (BET)	Avg. mesopore radius (adsorption/desorption)	Avg. micropore radius (ads./des.)
3.9 nm CeO_2	22.6%	567 m^2/cm^{-3}	1.7 nm/1.6 nm	0.46 nm/0.42 nm
9.9 nm CeO_2	33.7 %	833 m^2/cm^{-3}	4.1 nm/3.3 nm	0.53 nm/0.50 nm
6.7 nm TiO_2	19.8 %	537 m^2/cm^{-3}	1.6 nm/1.6 nm	0.45 nm/0.36 nm

5.3.3 Proton transport under dry and humidified environments

We used impedance spectroscopy to compare the conductivity of nanocrystal films at different temperatures and under different gas and humidity environments. To determine conductivity values, we fitted the Nyquist impedance plots using ZView software and extrapolated a semicircle to the real axis to obtain a low-frequency intercept. In some cases, a model with two time constants/semicircles provided a better fit, though the low-frequency intercept (*i.e.*, the total resistance) was always used to calculate the measured conductivity of the film. Reliable capacitance values for the film could not be determined, due to the stray capacitance between the two electrodes on the top surface of the film. Representative Nyquist plots and fits for the conductivity of a 290 nm thick film of 3.9 nm CeO_2 nanocrystals under humidified Ar are shown in Figure 5.4.

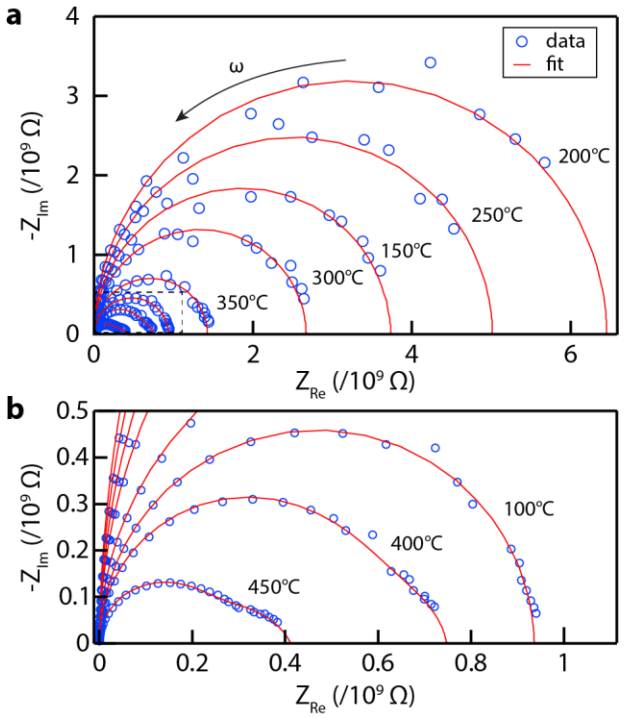

Figure 5.4: a) Nyquist plots showing the AC impedance response of a 290 nm thick film of 3.9 nm CeO_2 nanocrystals exposed to humidified Ar at different temperatures, and fits to the data. b) Zoomed in view of lower left region of part a.

Under a dry Ar atmosphere, 3.9 nm CeO_2 nanocrystals exhibit conductivity that increases with temperature (Figure 5a), with an activation energy of 0.76 eV. This is expected to be predominantly electronic conductivity since, at low partial pressures of oxygen (here, about 10^{-5} atm), electrons are generated by the reduction reaction (expressed here using Kröger-Vink notation):

$$2Ce_{Ce}^{x} + O_{O}^{x} \rightarrow 2Ce_{Ce}^{'} + V_{O}^{\cdot\cdot} + \frac{1}{2}O_2 \qquad \text{Equation 5.1}$$

The electrons liberated here localize onto cerium ions (Ce'_{Ce}) and form small polarons, which can hop from between cerium cation sites *via* thermally activated hopping transport.[123] Note that nanocrystalline ceria exhibits enhanced n-type conductivity due to space charge effects.[124–128] The activation energy for electronic conduction observed here (0.76 eV) is rather low compared to bulk and porous nanocrystalline CeO_2,[105,124,125,127,129,130] , but comparable to the value of 0.73 eV obtained for nanocrystalline undoped CeO_2 films measured under comparable conditions.[128] Note also that the oxygen vacancy formation energy is significantly lower at surfaces or grain boundaries in ceria,[131] in part because the lattice strain associated with forming Ce^{3+} is more easily accommodated at surfaces.[132] Decreasing particle size therefore leads to significantly enhanced thermodynamic concentrations of oxygen vacancies and polarons at interfaces and surfaces in nanocrystalline ceria.[133,134] Indeed, X-ray absorption spectroscopy (XAS) measurements at the Ce $M_{4,5}$-edge (Figure C.8)[135] reveal that, even as synthesized, the 3.9 nm CeO_2 nanocrystals are significantly enriched in Ce^{3+} compared to the 9.9 nm nanocrystals: the fraction of Ce^{3+} (calculated using XAS in surface-sensitive total electron yield mode) at the surface of the 3.9 nm nanocrystals is about 30%, while it is about 20% for the 9.9 nm nanocrystals. By contrast, total fluorescence yield XAS shows that the Ce^{3+} content is lowered in the nanocrystal cores, and the difference between the two samples is also reduced (22% for 3.9 nm vs. 17% for 9.9 nm). This indicates that the smaller nanocrystals support higher intrinsic concentrations of oxygen vacancies and n-type polarons, and underlines the importance of surfaces in dictating the defect behavior of nanocrystalline CeO_2.

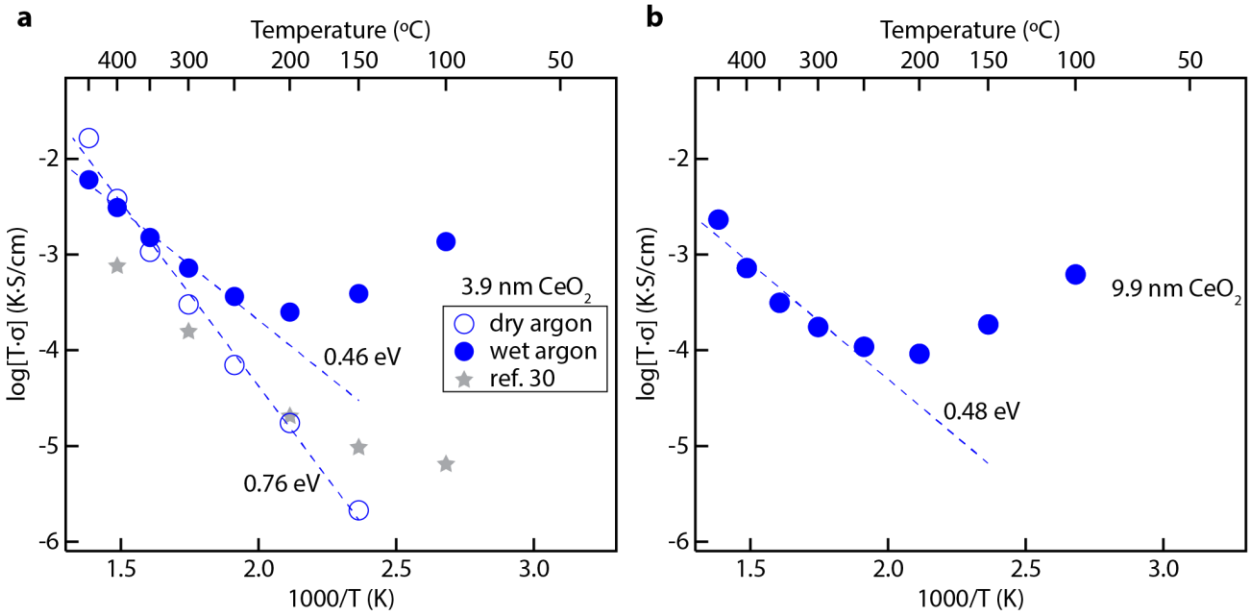

Figure 5.5: Arrhenius plots of the conductivity of CeO_2 nanocrystals under wet and dry Ar. a) Conductivity of a 290 nm thick film of 3.9 nm CeO_2 nanocrystals under dry and wet Ar. b) Conductivity of a 360 nm thick film of 9.9 nm CeO_2 nanocrystals under wet Ar.

When the impedance measurements are repeated under humidified Ar (pH_2O=20 mbar) at the same temperatures (Figure 5.5a), the high temperature conductivity is similar or slightly smaller than under dry Ar, indicating that electronic conductivity is dominating at higher temperatures.

However, beginning at 350°C, and especially at lower temperatures, the sample exhibits a strong conductivity enhancement under humidified conditions, and a much lower activation energy. Furthermore, the conductivity begins to increase again at 150°C. To confirm that these conductivity trends were not due to any physical changes in the samples during measurement, we performed grazing incidence small angle X-ray scattering (GISAXS) on our films as-fabricated and after conductivity measurements in both dry and wet Ar. The GISAXS scattering patterns (Figure C.9) are essentially equivalent in all three cases, with the scattering form factor edge and structure factor peaks indicating no change in nanocrystal size or film microstructure.

These observations are consistent with previous reports, and the difference between conductivity in wet and dry atmosphere can be attributed to proton conduction.[105,129] The proton conductivities here, however, are also significantly higher than in the previous study on mesoporous nanocrystalline CeO_2, which we attribute to the much smaller grain sizes used here (3.9 nm vs. 20 nm).[129] In agreement with this hypothesis, the proton conductivities in a film of 9.9 nm CeO_2 nanocrystals are 2-4 times smaller than in the 3.9 nm nanocrystal film (Figure 5.5b).

5.3.4 Ruling out the influence of capillary condensation

The difference in conductivity between the two CeO_2 samples is particularly intriguing, especially considering that the micropore radius of the 9.9 nm CeO_2 sample is only 0.7 Å larger (Table 1). On the other hand, the conductivity difference could arise from the higher porosity or the larger mesopore radius in the 9.9 nm CeO_2 sample compared to the 3.9 nm sample (4.1 nm vs. 1.7 nm). Prior reports suggested that proton transport is enabled by sufficiently small mesopores containing adsorbed liquid water *via* capillary condensation.[129] The critical pore radius-dependence of capillary condensation may account for the substantial conductivity difference between our samples. To evaluate this hypothesis, we solved the Kelvin equation for our experimental conditions:

$$\frac{1}{r} = \frac{RT}{\gamma V_m} \ln\left(\frac{p}{p_0}\right) \qquad \text{Equation 5.2}$$

where r is the critical pore radius for capillary condensation, R is the gas constant, T is the temperature, γ is the surface tension of water, V_m is the molar volume of water, p is the vapor pressure of water (constant here at 20 mbar), and p_0 is the saturated vapor pressure of water. Note that γ, V_m, and p_0 are all temperature-dependent quantities. The result of this analysis (Figure 5.6) shows that capillary condensation is not possible in our films and it therefore cannot explain the proton conductivity we observe. The maximum temperature for which we can expect capillary condensation into the pores in our CeO_2 nanocrystal films is about 50-60°C, based on a micropore radius of 0.46 nm. Furthermore, if capillary condensation into mesopores were responsible for proton conductivity, then conductivity differences between the 3.9 nm and 9.9 nm nanocrystals would only manifest near room temperature. Capillary condensation cannot explain the significant proton conductivity in either sample at and above 250°C, where condensation would require pore radii less than 0.3 Å (more than four times smaller than the

radius of a water molecule), nor can it explain the significant decrease in proton conductivity when the nanocrystal size is increased from 3.9 nm to 9.9 nm. For completeness, we also considered the Dubinin-Radushkevich equation (Figure C.10), which describes pore filling more accurately than the Kelvin equation for pore radii <2nm.[121] Even for a very wide range of adsorption energies up to those of water in microporous carbon (see SI for more detail), the micropore filling fraction was <0.1 at 150°C, further underscoring that capillary condensation cannot explain the intermediate temperature proton conductivity in this system.

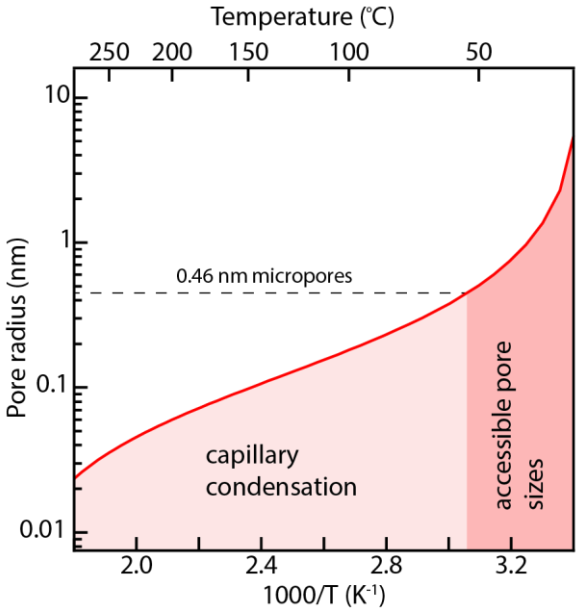

Figure 5.6: Solution to the Kelvin equation for our experimental conditions. The shaded area depicts the temperatures and pore radii where capillary condensation is expected. The deeply shaded region shows the temperatures for which capillary condensation is possible in our samples.

5.3.5 The influence of defect chemistry on proton conductivity

We instead propose that the proton conductivity depends on nanocrystal size through the associated changes in specific surface area and the size-dependent surface chemistry and defect equilibria. The surface area-to-volume ratio of a 3.9 nm nanocrystal is about two times that of a 9.9 nm nanocrystal. Coincidentally, our XAS results show that the surface fraction of Ce^{3+} (and oxygen vacancy concentration) in 3.9 nm CeO_2 is about 1.5 times greater than in 9.9 nm CeO_2 at room temperature. The difference in Ce^{3+} concentration is of the same order as the difference in conductivity between the two samples and suggests that surface defects are playing a significant role in proton transport here, and that the size-dependent formation energy and population of these defects dictates the magnitude of the proton conductivity.

To further investigate the relationship between proton conductivity and defect chemistry at the surface, we again measured the conductivity of 3.9 nm CeO_2 nanocrystals under humid conditions while using pure oxygen, rather than Ar, as the carrier gas (Figure 5.7). It is immediately apparent that the conductivity under wet O_2 is drastically lower than under wet Ar,

and that the activation energy is higher. Furthermore, there is a much less pronounced uptick in conductivity between 200°C at 100°C. Based on the defect equilibrium described by Equation 5.1, the equilibrium concentration of oxygen vacancies and polarons is described by the equilibrium constant:

$$K = (pO_2)^{1/2}[V_O^{\cdot\cdot}][Ce'_{Ce}]^2 \qquad \text{Equation 5.3}$$

The electroneutrality condition ($2[V_O^{\cdot\cdot}] = [Ce'_{Ce}]$) can be invoked to show that, in the bulk, the concentration of oxygen vacancies and polarons is proportional to $(pO_2)^{-1/6}$. A change in atmosphere from pure Ar (pO_2~10^{-5} to 10^{-6} atm) to pure O_2 (pO_2~1 atm) will then change the equilibrium concentration of both defects by about one order of magnitude.

If the concentration of oxygen vacancies or polarons affects water adsorption or proton transport, then this concentration change should correspond to a significant change in conductivity. Indeed, we observe a very large decrease in the intermediate temperature proton conductivity when pure oxygen is used as a carrier gas. Under wet O_2, the proton conductivity decreases by a factor of 5 (at 300°C) to 64 (at 100°C).

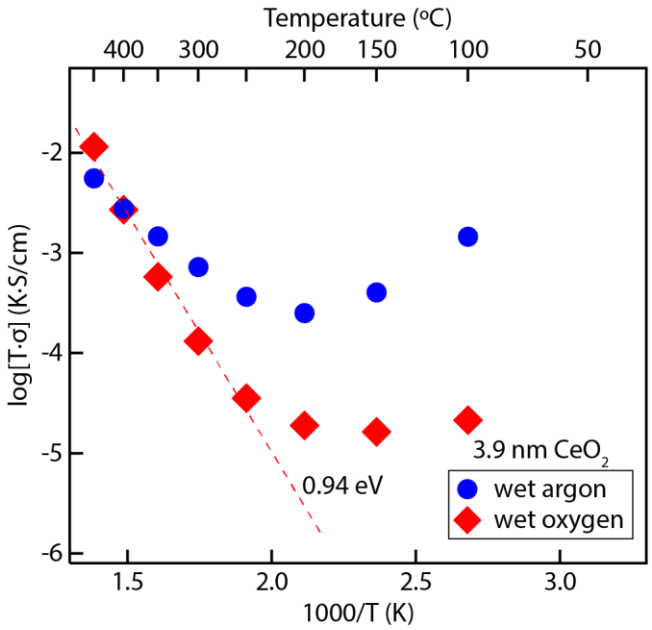

Figure 5.7: Arrhenius plot of the conductivity of a 290 nm thick film of 3.9 nm CeO_2 nanocrystals under wet oxygen. (Wet Ar results included for comparison).

This drastic decrease in proton conductivity under O_2 atmosphere further rules out capillary condensation as a major contributor to conductivity because changing the carrier gas would not change the critical pore radius in Equation 5.2. The self-dissociation of water into hydronium and hydroxide ions also cannot describe our conductivity results; the self-dissociation constant at 100°C is only 5.4×10^{-13} (5.2×10^{-12} at 200°C), and the conductivity of pure water at 100°C is only 7.6×10^{-7} S/cm (3×10^{-6} S/cm at 200°C).[136] By contrast, the proton conductivities in our films are two to four times higher despite the majority of their volume being crystalline ceramic, meaning that protons must be generated by some other mechanism.

Instead, this strong suppression of proton conductivity by O_2 indicates that surface oxygen vacancies play a critical role generating protons at the surface of nanocrystalline CeO_2. Previous atomistic simulation studies have shown that the amount of water adsorbed to ceria surfaces and the dissociative binding enthalpy increases at chemically reduced and defective ceria surfaces.[137,138] To understand how oxygen vacancies and cerium oxidation state influence water uptake in our nanocrystal films, we performed thermogravimmetric analysis (TGA) on 3.9 nm CeO_2 nanocrystals with their surface ligands removed in an alumina crucible (Figure C.11). After equilibrating under dry Ar at 450°C to generate oxygen vacancies, the temperature was reduced to 150°C to stabilize for 2 hours. Then, the nanocrystals were exposed to humidified Ar (pH_2O=20 mbar) inside the TGA furnace. The mass of the sample (corrected for buoyancy and water adsorption by running an equivalent experiment with an empty crucible) subsequently increased as the nanocrystals adsorbed water. The experiment was then repeated using 25% O_2. Under dry conditions, the sample mass was higher, indicating a decrease in the oxygen vacancy concentration. Furthermore, the mass gained upon switching to a humid oxygen atmosphere at 150°C was significantly diminished. Comparing the time-averaged sample mass over one hour before switching between a dry and wet environment to the time-averaged sample mass over one hour after exposure to moisture (averaged to improve precision) reveals that the sample under pure Ar gained 62 times more mass than the one in an oxidative environment. This further supports the notion that oxygen vacancy concentration directly influences water adsorption in CeO_2 nanocrystals, and in porous nanocrystal films the pore surfaces determine the chemistry of water adsorption and how much water adsorbs to the pore walls.

We hypothesize here that mobile protons are generated *in situ* by dissociative adsorption of water at surface oxygen vacancies. Oxygen vacancies serve as active or catalytic sites for water dissociation at CeO_2 surfaces, generating two protonic defects according to the following reaction:[99,138,139]

$$H_2O_{(g)} + V_O^{\bullet\bullet} + O_O^x \rightarrow 2OH_O^{\cdot} \qquad \text{Equation 5.4}$$

The hypothesized dissociation process, also shown schematically in Figure 5.8a-b, is well supported by atomistic simulations reported in the literature, as well as experimental scanning tunneling microscopy and X-ray photoelectron spectroscopy studies showing that $OH_O^{\cdot}$ defects saturate surface oxygen vacancies in reduced CeO_2 under humid conditions.[137,138,140–142] In fact, this is the very process by which ceramic high temperature proton conductors such as ternary oxides like $BaCeO_3$ generate mobile protons.[143,144] The important difference between those oxides and CeO_2 is that CeO_2 does not have the open perovskite structure to support protonic defect rotation and diffusion between neighboring oxygen sites *via* phonon-assisted proton migration, [81,83,87,145] so the resulting solubility and conductivity of protons in bulk fluorite structures is low, and protonic defects are expected to remain on the surface.[146] Once the protonic defects are formed, proton conduction may follow a few different pathways, such as proton hopping along neighboring adsorbed surface hydroxide defects (Figure 8c),[95] which may be facilitated by partial solvation from adsorbed water or space charge effects.[129] Alternatively, the proton may be exchanged between the surface protonic defect and physisorbed water molecules in the pores (Figure 8d),[95,139] followed by proton conduction within this adsorbed

water layer either *via* diffusion or the Grotthus mechanism.[102] We do not have sufficient experimental evidence to determine which transport process is dominant, although recent studies on proton conduction in TiO_2 and YSZ, which used solid-state NMR,[109] *in situ* FTIR,[147] and ultrathin YSZ films,[113] indicate that the surface hopping mechanism is dominant at higher temperatures (300+°C), where there is little physisorbed water. At intermediate temperatures, conduction through the "ice-like" chemisorbed water layer is likely dominant, while hydronium ion conduction within adsorbed water is dominant at lower temperatures where the physisorbed water layer is thicker and water molecules are more mobile.[109,148]

We note that extracting a proton from the surface defect will result in a charged nanocrystal, due to the presence of the polarons that originally compensated the oxygen vacancies and now the protonic defects. Thus, if the proton is conducted within the water layer, it is likely confined to the near-surface region, where, coincidentally, confinement can strongly influence diffusivity and other transport characteristics.[148,149]

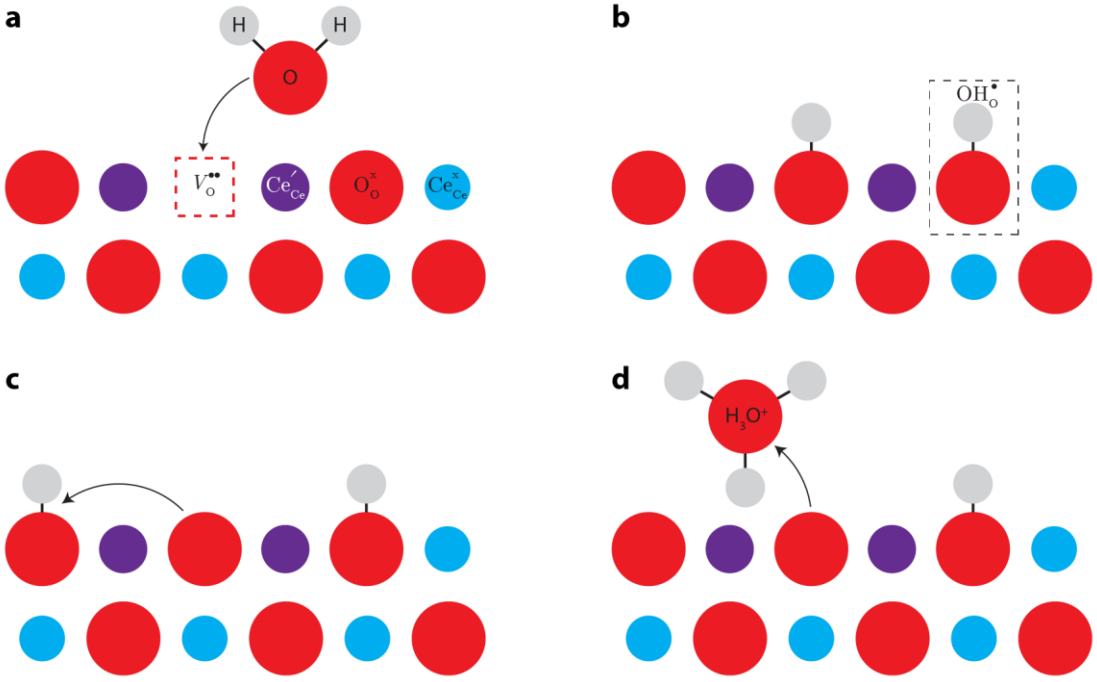

Figure 5.8: Proposed mechanism for surface-mediated proton transport in nanocrystalline CeO_2. a) An oxygen vacancy serves as the active site for dissociative water adsorption, forming b) two protonic defects. c) Proton conduction can occur by hopping along the oxide surface, or by d) Exchange with adsorbed water at the surface.

The hypothesis of oxygen vacancy-mediated dissociative adsorption of water can explain the observed differences in conductivity as a consequence of the change in the number of protonic charge carriers that are generated for a given nanocrystal size, temperature, and gaseous environment. Increasing the nanocrystal diameter from 3.9 nm to 9.9 nm results in a lower intrinsic concentration of oxygen vacancies at a given equilibrium, due to the decreased surface-to-volume ratio. Based on our XAS results, this decrease is expected to be about 1.5 to 2. The decrease in oxygen vacancy concentration corresponds to a decrease in proton conductivity of

the same order, because fewer mobile protons are generated. It is also clear from the O-H vibrations in our FTIR data (Figure 5.2) that the film of 9.9 nm CeO_2 nanocrystals adsorbs significantly less water under ambient conditions, supporting our hypothesis. Finally, using pure oxygen as a carrier gas, which corresponds to a pO_2 increase of 10^5-10^6 orders of magnitude, should reduce the oxygen vacancy concentration by approximately an order of magnitude, and our TGA results confirm that the amount of water adsorbed also decreases by over an order of magnitude. The corresponding drop in proton conductivity under these conditions is, correspondingly, about an order of magnitude or even greater (up to a factor of 64). Note that changes greater than an order of magnitude upon switching from Ar to O_2 suggest that the oxygen vacancies at nanocrystal surfaces may not all be 2+ charged, and that charged acceptor impurities might also be present near the nanocrystal surfaces.[134] Note however that in the presence of impurities (which are typically acceptor dopants in CeO_2), the partial pressure dependence of the conductivity follows a power law with the exponent -1/4.

To evaluate the generality of proton conduction in porous nanocrystal films, and the generality of our hypothesized mechanism, we measured the conductivity of a thin film consisting of 6.7 nm TiO_2 nanocrystals under dry Ar, humidified Ar, and humidified O_2 (Figure 5.9). Note that, based on our EP data Table 5.1, the pore morphology of this sample is nearly equivalent to the 3.9 nm CeO_2 nanocrystal sample: the surface areas as well as mesopore and micropore radii are identical within the precision of the analysis, and the overall porosity is comparable. Any observed changes in proton conductivity should then arise mainly from differences in the surface chemistry of TiO_2 compared to CeO_2. Indeed, both the high temperature electronic conductivity (under both dry and wet Ar) and the intermediate temperature proton conductivity (under wet Ar) are significantly lower in the TiO_2 nanocrystal film. This is easily explained by the higher energy required to form an oxygen vacancy in TiO_2 compared to CeO_2: *e.g.*, 3.2 eV at a TiO_2 (110) surface vs. 1.8 eV at a CeO_2 (111) surface.[132] As a result, for a given temperature and pO_2, TiO_2 is less reducible than CeO_2 and is expected to have significantly fewer oxygen vacancies and polarons. This is undoubtedly why TiO_2 has a decreased electronic conductivity under dry Ar. Based on our proposed mechanism, a lower oxygen vacancy concentration also explains why TiO_2 displays lower proton conductivity at intermediate temperatures. Finally, we also observed that the proton conductivity in the TiO_2 nanocrystal film is strongly diminished under humidified oxygen. These results further support our assertion that water dissociatively adsorbs at oxygen vacancies to form mobile protonic defects. Ultimately, while previous studies firmly established the fact that open porosity is a critical requirement for proton conduction in nanocrystalline ceramics, we have found here that defect equilibria and surface chemistry play an additionally critical role.

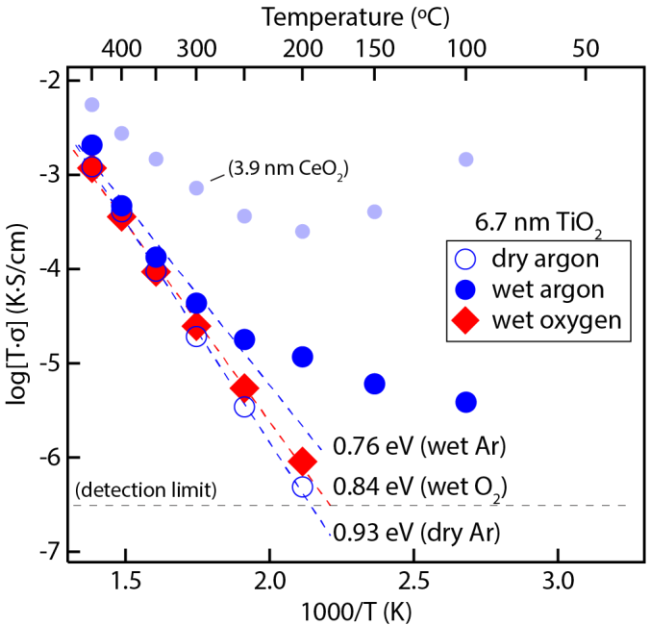

Figure 5.9: Arrhenius plot of the conductivity of a 265 nm thick film of 6.7 nm TiO_2 nanocrystals under dry Ar, wet Ar, and wet oxygen. (Conductivity of 3.9 nm CeO_2 nanocrystal film under wet Ar included for comparison).

5.3.6 Addendum on the influence of oxygen partial pressure on defect chemistry and intermediate temperature proton transport

In reproduction experiments, we found that the conductivity behavior of both cerium oxide and titanium dioxide is reproducible with the same order of magnitude of conductivity. However, the new oxgen partial pressure dependence of conductivity under humidified atmospheres that was measured is significantly weaker than previously observed. Our prior study of partial pressure dependence was done sequentially on a single sample assuming no structural degradation that might convolute the results of the measurement. This assumption was confirmed with grazing incidence small angle x-ray scattering measurements where we saw no gross-changes in structure as a result of the measurement.

In our further studies to confirm the results, we conducted a series study to investigate the changes of sample conductivity upon cyclic measurements (sequential repeat measurements). Shown in Figure 5.10 is the result of this experiment that measured the conductivity of the sample in the second cycle either under humidified oxygen or humidified Ar. Starting at the high temperature regime above 300 °C, we see that the repeat measurement under humidified Ar asymptotes to the same values in Figure 5.10 (b), while the repeated measurement under humidified oxygen is lower than that under humidified Ar in Figure 5.10 (a). This is expected given the defect chemistry of cerium oxide where polaronic conductivity is expected to have partial pressure dependence. However, at temperatures below 200 °C where intermediate temperature proton conduction dominates, the order of magnitude change in conductivity either in humidified oxygen or in humidified Ar is comparable suggesting that there may not be partial

pressure dependence or the partial pressure dependence is convoluted with an unknown degradation mechanism that is not structural. This crucial observation presages our investigation on stability in Chapter 6.

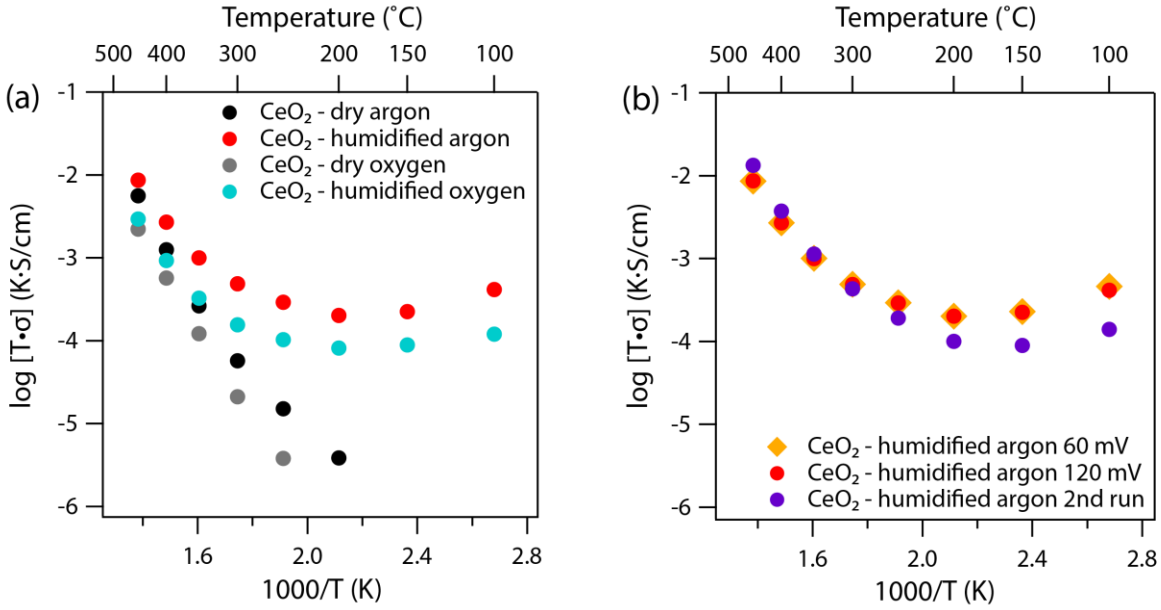

Figure 5.10: (a) Arrhenius plot of conductivity for a 300 nm CeO_2 sample under dry or humidified oxygen measured after measurements of conductivity under dry and humidified Ar. (b) Arrhenius plot of conductivity for a 300 nm CeO_2 sample under dry or humidified Ar measured after measurements of conductivity under dry and humidified Ar.

Given the observation of sample history convoluting the partial pressure dependence, we chose to examine the partial pressure dependence utilizing duplicate samples instead. Here, we measured the sample conductivity under dry and humidified Ar and under dry and humidified oxygen using separate sister samples. This result is shown in Figure 5.11. Like the previous experiment, we once again recover the partial pressure dependence of conductivity at high temperatures above 300 °C due to the dependence of polaronic conductivity in cerium oxide and titanium dioxide on oxygen partial pressure. At temperatures at or below 200 °C, however, it is now evident that there is no oxygen partial pressure dependence for intermediate temperature proton conductivity for cerium oxide. For titanium dioxide, however, we do observe minor oxygen partial pressure dependence.

Mentioned previously, our control studies on the influence of the measurement conditions on structure have elucidated that there should be no pronounced structural changes to causes the intermediate temperature proton conductivity to degrade over time. As we will discuss in Chapter 6, we now understand that this degradation is actually due to surface passivation and a change in surface chemistry of the metal oxide under a humidified environment. Returning back to the non-dependence of intermediate temperature proton conduction of cerium oxide on oxygen partial pressure however, this result is actually consistent with prior surface studies on cerium oxide. Specifically, it has been observed that i) the surface of cerium oxide is significantly more

reduced than its bulk and, ii) the concentration of Ce^{3+} and associated oxygen vacancy concentration on the surface of nano-sized ceria is largely independent of oxygen partial pressure.[150–152] An alternate hypothesis is that the presence of trace surface impurities on nanocrystal surface can pin the defect concentrations. This is a possible candidate given results of our investigations in Chapter 6.

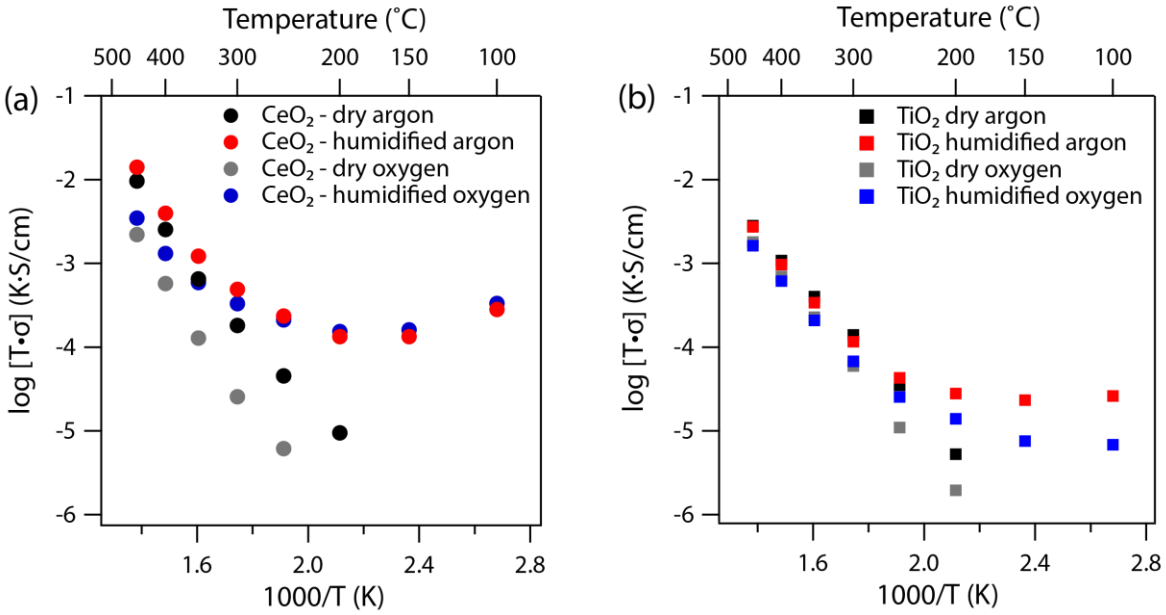

Figure 5.11: (a) Arrhenius plot of conductivity for a 300 nm CeO_2 sample under dry or humidified Ar or oxygen measured using sister samples to remove the effect of sample history. (b) Arrhenius plot of conductivity for a 290 nm TiO_2 sample under dry or humidified Ar or oxygen measured using sister samples to remove the effect of sample history.

5.4 Conclusion

In conclusion, we systematically varied grain and pore sizes as well as surface chemistry to shed light on the proton conduction mechanism in nanocrystalline ceramics. By utilizing and manipulating colloidal CeO_2 and TiO_2 nanocrystals, we achieved enhanced proton conductivity in nanocrystal films under humid atmospheres, particularly for small (3.9 nm) CeO_2 nanocrystals. From both scientific and application perspectives, colloidal nanocrystals offer an attractive route to generate nanocrystalline ceramic films with engineered and controlled porosity and grain size that is not typically achievable with sintering or other physical fabrication methods. Achieving these small grain sizes also enabled us to easily manipulate their surfaces and defect chemistries *in situ*. In turn, these manipulations revealed the strong influence of defect chemistry on proton transport in nanocrystalline oxides, allowing us to conclude that dissociative water adsorption into oxygen vacancies is the likely source of mobile protons. Our observation of surface-mediated proton transport in both CeO_2 and TiO_2 suggests that this may be a general phenomenon for nanocrystalline metal oxides, particularly for reducible oxides that easily form oxygen vacancies. Thus, nanocrystals of the oxides of transition metals like vanadium,

molybdenum, manganese, and tungsten may also support intermediate temperature proton conductivity.

This report motivates future work to further study and manipulate surface-mediated proton transport. We note that when we exposed our films to wet conditions at 150°C (20+ hours), the conductivity slowly, but significantly, decreased over time. This decline could be a result of protons and polarons reacting to form H_2 gas, thus diminishing the number of protonic charge carriers.[141] It could alternatively be the result of contaminants poisoning the nanocrystal surface.[132] We did observe that the conductivity decreased more quickly with higher pO_2, which implicates adventitious contaminants. In either case, this effect warrants further study, particularly if these materials are to be used in electrochemical devices. Additionally, we hope the results reported here will motivate deeper examinations into the mechanism for proton transport in colloidal nanocrystal films and other micro- and mesoporous ceramics. Techniques like solid-state NMR could elucidate whether surface proton hopping or proton transport in the adsorbed liquid layer dominate the conductivity, or if different processes dominate at different temperatures. Finally, our results suggest that deliberate attempts to maximize oxygen vacancy concentration could maximize proton conductivity in nanocrystalline ceramics. This could be accomplished either by choosing a material with a low oxygen vacancy formation energy, or by extrinsic generation of high oxygen vacancy concentrations by acceptor doping. For example, Gd-doping of CeO_2 nanocrystals is expected to fix the oxygen vacancy concentration, as Gd'_{Ce} defects would be compensated by oxygen vacancies. Deliberate and controlled acceptor doping may then enable systematic tuning and maximization of proton conductivity in nanocrystalline GDC. While previous studies showed no significant difference in proton conductivity between undoped nanocrystalline CeO_2 and GDC thin films with grain sizes of around 40 nm,[105] sufficiently small colloidal GDC nanocrystals may be revealed to have further enhanced proton transport properties.

5.4.1 Acknowledgements

This work was supported by a U.S. Department of Energy (DOE) ARPA-E grant (E.L.R.) and the Welch Foundation (G.K.O., D.J.M.; grant no. F-1848. E.L.R. also acknowledges support from the UC Berkeley Chancellor's Fellowship. Additional support was provided by a National Science Foundation (NSF) Graduate Student Research Fellowship (G.K.O.) under Grant No. DGE-1106400. XAS experiments were performed on beamlines 8.0.1 and 6.3.2, and GISAXS on beamline 7.3.3, at the Advanced Light Source, Lawrence Berkeley National Laboratory, funded by the Office of Science, Office of Basic Energy Sciences, of the DOE under contract DE-AC02-05CH11231.

Chapter 6

Stability of Intermediate Temperature Proton Conductivity in Porous Metal Oxide Thin Films

Adapted from: Gary K. Ong, Lauren C. Reimnitz, Fiona M. Doyle, and Delia J. Milliron, "Passivation and Surface Stability Relating to Intermediate Temperature Proton Conductivity in Porous Metal Oxide Thin Films," *In preparation.*

6.1 Introduction

One defining characteristic of nanomaterials is a high surface to volume ratio. While simple, this key characteristic shifts the properties of a material to one dominated by surfaces allowing significant deviation of overall properties from their bulk counterpart. Within the context of ion transport materials, one recent discovery in this vein of an interface driven property is the observation of intermediate temperature (200 °C to 100 °C) proton conduction in porous nanocrystalline metal oxides systems such as cerium oxide,[105–107] zirconium oxide,[95,99–102,110,111,139] and titanium oxide.[90,91] Prior work on metal oxides has established these materials as poor proton conductors in their bulk form. However, when they are made nanosized and porous, these same materials exhibit significant proton conductivity under humid conditions, and this deviation has been attributed to the change in interface density moving from bulk to nanocrystalline sizes and introduction of a solid-vapor interface to enable ion transport.[105,106]

The discovery of intermediate temperature proton conduction for these materials arrives at an opportune time in line with current interest to run proton exchange membrane fuel cells (PEMFCs) at elevated temperatures. This push for higher temperatures is rationalized by three primary reasons. First, gains in electrochemical efficiency and catalytic rates, which are particularly important for the slow oxygen reduction reaction. Second, fuel cells operated at higher temperatures may be less tolerant of impurities in the gas stream such as CO and H_2S; these cause poisoning of the catalysts in the fuel cell. Third, fuel cell design can be greatly simplified by removing the need for external heat management and complicated water management.[153,154] However, the operation temperature of current PEMFCs is limited by the operation temperature of the proton exchange membrane (mostly Nafion) that dehydrates at temperatures above 80 °C, leading to a significant loss in proton conductivity.[76,78,79,82,155] Efforts to open the temperature window for operation have yielded new proton conducting materials, such as solid acids like $CsHSO_4$,[85,156] $BaZrO_3$ and $BaCeO_3$ ceramics,[83,87,155] sol-gel silica glasses,[89] metal organic frameworks,[157] and silica phosphotungstic acid hybrids.[94]

When considering a material for proton transport in a fuel cell, in addition to the material's ionic conductivity, another important parameter is its stability. Prior studies have preliminarily

demonstrated the order of magnitude ionic conductivity exhibited by these materials; investigations have focused on the influence of doping to tune defect chemistry and influences of fabrication method to introduce porosity, both ultimately influencing ionic conductivity. Here, we contribute to the latter by investigating the stability of ionic conductivity, and by extension, the material stability of oxides that demonstrate this property. It is crucial to address stability on top of just ionic conductivity, given that material degradation under a humid and oxidizing atmosphere of fuel cell operation is often the norm rather than the exception. Prior work on other solid state proton transport candidates such as $BaCeO_2$, for instance, has shown that while these materials exhibit good proton conductivities, their degradation under humid environments limit their use in actual devices. While the aforementioned solid-state acids demonstrate promising proton conductivity, they also degrade under humid environments.

Building on previous work where we demonstrated the feasibility of using colloidal metal oxide nanocrystals as a platform to study intermediate temperature proton conduction in porous metal oxide thin films, here we continue that work with an exploration of the stability of proton conductivity for two model oxide material systems, namely cerium oxide and titanium dioxide. Our investigations show that the proton conductivity exhibited by cerium oxide decreases with time. In contrast, the proton conductivity exhibited by porous titanium dioxide is stable over time. Spectroscopic studies reveal that the degradation is likely due to carbonate and hydroxycarbonate formation on the metal oxide surface. Attempts to ameliorate this passivation behavior by altering the surface affinity towards carbonate formation through gallium doping proved unsuccessful. Simple free energy analysis further showed that the formation of hydroxycarbonate from cerium oxide under humidified conditions in the presence of trace carbon dioxide is indeed favorable at the measurement conditions. Ultimately, this study demonstrates the need to consider surface stability in addition to defect chemistry in future work on materials that exhibit intermediate temperature proton conduction.

6.2 Experimental methods

6.2.1 Nanocrystal synthesis

In a typical synthesis of 4 nm cerium oxide nanocrystals, 0.868 g of cerium nitrate hexahydrate (2 mmol, Sigma 99.999%) and 5.36 g oleylamine (20 mmol, 90% Acros Organics) was dissolved in 10 ml 1-octadecene (Aldrich 90%). After initial mixing, the solution was stirred under nitrogen at 80 °C for one hour, followed by degassing at 120 °C for one hour under <100 mTorr vacuum. The solution was then heated to 230 °C. Once the solution temperature reached 230 °C, the solution was further heated to 250 °C and left to react for two hours. After two hours, the solution was left to cool in air to below 80 °C, when 5 mL of toluene was added into the solution. The mixture was then centrifuged at 1500 rpm for 10 minutes to remove bulk precipitates. The supernatant was mixed with 60 mL of isopropanol and centrifuged at 7000 rpm for 10 minutes. The nanocrystals were washed three times post synthesis with a hexane/isopropanol combination for dispersion and precipitation, filtered using a 0.2 □m PTFE

filter, and stored.

In a typical synthesis of titanium oxide nanocrystals, 5 mmol of titanium butoxide ($Ti(OBu)_4$, Sigma 97%). 30 mmol oleic acid (Sigma 90%), 20 mmol oleylamine (90% Acros Organics), and 100 mmol 200 proof ethanol (Sigma > 99.5%) were combined and stirred for 30 minutes before being transferred into a 40 mL Teflon cup. The cup was placed inside a 100 mL Teflon-lined stainless steel autoclave, which contained 19.8 mL of 200 proof ethanol and 0.8 mL of ultra-pure water. The autoclave was then sealed and placed into a 180°C oven for 18 hours. After the reaction, the nanocrystals were purified three times with a hexane/reagent alcohol combination for dispersion and precipitation, filtered using a 0.2 □m PTFE filter, and stored.

6.2.2 Thin-film processing: deposition and ligand exchange

Nanocrystals were spincasted onto silicon or quartz substrates (1 cm by 1 cm by 1 mm to 1.5 mm thickness) from a non-polar solvent (1:1 hexane:octane, heptane, or pure octane) from a solution of 60 mg/mL of nanocrystals. This yielded a film around 150 nm thick. The film was then submerged into a solution of 0.1 M formic acid in acetonitrile for fifteen minutes, to allow the short formate ligands to displace the original bulky inorganic ligands. The film was then rinsed five times with a 1:1 mixture of chloroform:acetonitrile to rinse off products of the ligand exchange process. Finally, the substrate was heated on a hotplate at 300 °C for 15 minutes to decompose formate. This process was repeated 3 to 5 times to build up a film between 300 nm to 500 nm.

6.2.3 Platinum contact deposition

A 400 nm film of Pt was sputtered onto the top surface of the nanocrystal film with a shadow mask that defines a 1 mm gap in the middle using a Cooke RF sputtering system operating at 60 Watts and 1.5 millitorr Ar pressure at a deposition rate of 10 nm/min. The chamber pressure was pumped down to <1e-6 Torr prior to the introduction of Ar to minimize extraneous contamination from oxygen.

6.2.4 Impedance spectroscopy

Impedance spectroscopy was performed in two-point configuration using a Novocontrol Alpha-A impedance analyzer over a frequency range of 1 MHz to 1-10 Hz, with a voltage amplitude of 0.12 V, using a custom stage that allowed independent temperature and environmental control. Inert gases were passed through an oxygen trap (Agilent OT1-4), and all gases were passed through CO_2 and H_2O traps prior to flowing into the stage. Humidity was introduced into the cell by bubbling the solution through water set at 17 ^oC, corresponding to $pH_2O \sim 20$ mbar. The samples were equilibrated for six hours at 450 °C, and two hours at all other temperatures in between 450 °C and 100 °C, with one measurement from 1 MHz to 1 Hz or 0.1 Hz every 30 minutes after an initial equilibration of 30 minutes at each temperature. Conductivity values are

normalized to film thicknesses of the samples. Oxygen partial pressure was measured with a Cambridge Sensotech Rapidox 2100 Oxygen Analyzer.

6.2.5 Fourier transform infrared spectroscopy

Fourier transform infrared spectroscopy was done on spincasted and ligand exchanged thin films on calcium fluoride substrates (Pike Technologies 13 mm x 2 mm CaF_2 windows) or undoped silicon substrates in transmission geometry with a 2 cm^{-1} wavenumber resolution and an average of 128 scans on a Bruker Vertex 70 spectrometer.

6.3 Results and discussion

6.3.1 Forming porous nanocrystal thin films

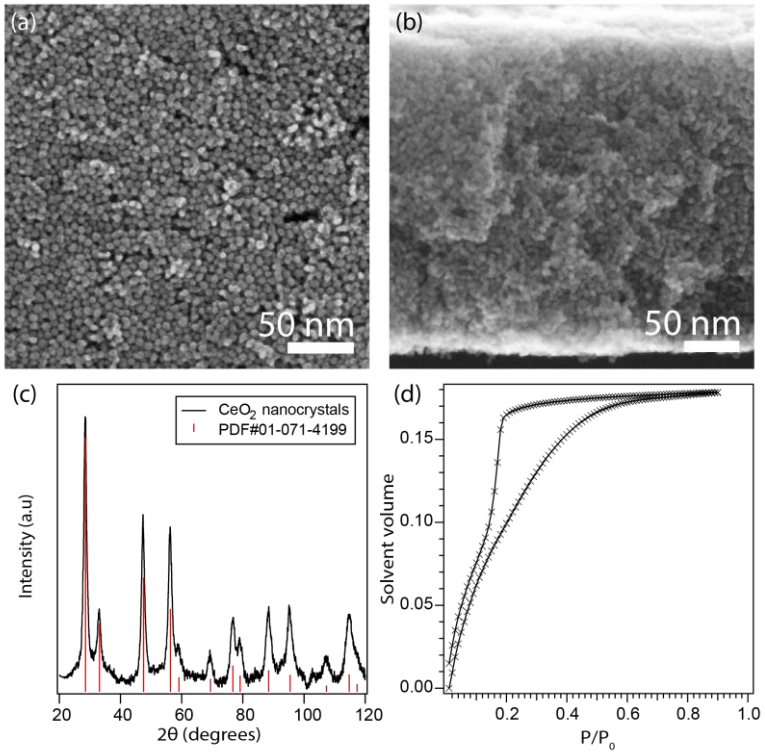

Figure 6.1: (a,b) Top-down and cross-section SEM of a prototypical 300 nm cerium oxide nanocrystal film used for transport measurements. (c,d) X-ray diffraction data mapped to PDF#01-071-4199 for cerium oxide, and adsorption isotherm derived from ellipsometric porosimetry fitting for the same film.

A prototypical porous metal oxide thin film generated using colloidal cerium oxide nanocrystals and ligand exchange techniques outlined above is shown in Figure 6.1. Nanocrystals are pseudo-spherical with diameter around 4 nm, and x-ray diffraction confirms phase purity with the pattern indexed to the cerium oxide fluorite structure. Thin films consist of randomly close-packed

nanocrystals with residual porosity between nanocrystals. Ellipsometric porosimetry data further confirm that the film has open porosity of about 18 percent. Scanning transmission electron microscopy of nanocrystals used in this study are presented in Appendix D in Figure D.1. A similar compilation for titanium dioxide is provided in Figure D.2.

6.3.2 Time dependent conductivity under dry and humid Ar atmospheres for CeO_2

Having noted the key structural characteristics of the model nanocrystal thin films, we turn our attention to the conductivity of the porous films under dry and humidified atmospheres. Unlike prior studies, here we report the time dependence of the conductivity at each temperature with emphasis on the lowest temperature tested (100 °C). The conductivity values are derived from equivalent circuit fitting of impedance data with the conductivity derived from the resistance extrapolated from the intercept to the real axis on a Nyquist plot. For an example of this fitting, the reader is referred to Figure 5.4 in Chapter 5.

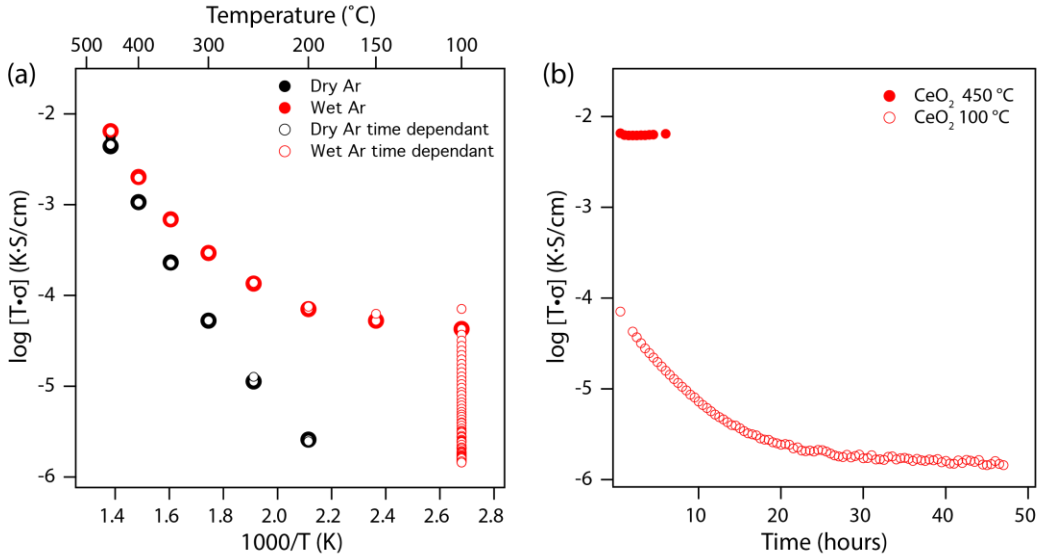

Figure 6.2: (a) Time and temperature dependent conductivity data under dry and humidified Ar for CeO_2. Open white circles denote time dependent data while the solid circles denote the measurement after 6 hours (at 450 °C), and after 2 hours at all other temperatures. (b) Time dependent conductivity at 450 °C and 100 °C under humidified Ar depicted as a function of time.

In Figure 6.2 (a), both temperature dependent and time dependent data are presented simultaneously. Conductivity values taken every 30 minutes is shown in open circles, and the final conductivity value measured after 6 hours of equilibration at 450 °C or 2 hours of equilibration at all other temperatures is enlarged and shown as a colored closed circle. Beginning the discussion with the conductivity of CeO_2 under dry Ar conditions, the system exhibits conductivity that increases linearly with temperatures when plotted in the axes above because the nature of the conductivity is polaronic. This is consistent with all prior investigations of cerium oxide.[106,158]. At temperatures below 200 °C under dry Ar conditions, the sample is too

resistive to measure the conductivity. From the overlap of the time dependent points, we see that the conductivity values are stable at least over the 6 hour period at 450 °C and 2 hour period at all other temperatures. Moving the discussion to the conductivity of CeO_2 under humidified Ar conditions, we observe a gradually convergence in conductivity between 350 °C and 450 °C and a significant deviation in conductivity between dry and humidified conditions at 300 °C and 100 °C. This difference in conductivity between the dry and humidified condition is the conductivity attributed to protonic conductivity. Once again, examining the time dependent conductivity under humidified conditions, we see that the conductivity is stable over the 6 hour period at 450 °C and 2 hour periods between 400 °C and 200 °C with time dependent deviation at 150 °C and 100 °C. Examining this time dependence at 100 °C more closely over a 48 hour period as shown in Figure 6.2 (b), we see that the conductivity decreases two orders of magnitude over the 48 hour period. This degradation is the subject of our current investigation.

6.3.3 Surface characterization before and after conductivity measurement for CeO_2

Our previous studies of the intermediate temperature proton transport of porous cerium oxide showed that both nanocrystal arrangement and porosity remain stable during the measurement, and that proton transport is strongly surface driven. Coupled with the low temperature at which the time-dependent degradation occurs, it is possible that this decrease in conductivity is due to passivation of the surface (colloquially known as poisoning of the surface). To investigate this hypothesis, we characterized the system with FTIR, tracking the material at every step of processing starting from the as-synthesized material, through the formic acid exchange, heating to desorb formate, after the conductivity measurement under dry Ar, and after the conductivity measurement under humidified Ar. This sequential study with FTIR is shown in Figure 6.3. The data presented is piecewise background subtracted using either a constant background in the finger print region between 1000 cm^{-1} and 1800 cm^{-1} or a fifth order polynomial for the hydroxyl region between 2400 cm^{-1} and 3800 cm^{-1}. A sample of this background subtraction is provided in Figure D.3.

From the FTIR spectra, starting with the as-synthesized nanocrystals, we observe alkyl C-H stretches between 2800 cm^{-1} and 3000 cm^{-1} characteristic of the native oleylamine ligands on the nanocrystal surface. This is corroborated further with peaks between 1200 cm^{-1} and 1600 cm^{-1} attributed to the amine bending and alkene stretching modes. After formic acid ligand exchange, we observe a marked decrease in the C-H stretch, consistent with the shorter alkyl chain of formate, and sharp peaks at 1566 cm^{-1} and 1373 cm^{-1} which we attribute to the carboxylate stretches for formate adsorbed on the surface of cerium oxide. Specifically, this location of the C=O vibration for formate is characteristic of formate bound to Ce^{3+} and Ce^{4+} sites. After heating to 350 °C, we observe the disappearance of the C-H stretches accompanied by a broad hydroxyl stretch, suggesting desorption of formate from the surface of the nanocrystals accompanied by the capillary condensation of water on the oxide surface as the measurement was conducted under ambient conditions. However, when we examine the fingerprint region, we see broad peaks between 1200 cm^{-1} and 1600 cm^{-1} accompanied by a shoulder at 1643 cm^{-1}, which we

assign to the water-bending mode. These peaks will be deconvoluted and discussed in further detail in Figure 6.4, but they provide qualitative indication of the decomposition of formates to surface carbonates. After the conductivity measurement under dry Ar, the same assignments hold for the spectra, given that we do not observe pronounced changes, suggesting that these carbonate species are stable even at 450 °C under dry Ar. Finally, after the conductivity measurement under humidified Ar, we observe a large array of peaks that we attribute to the passivation species. These peaks are also deconvoluted in Figure 6.4 and discussed below.

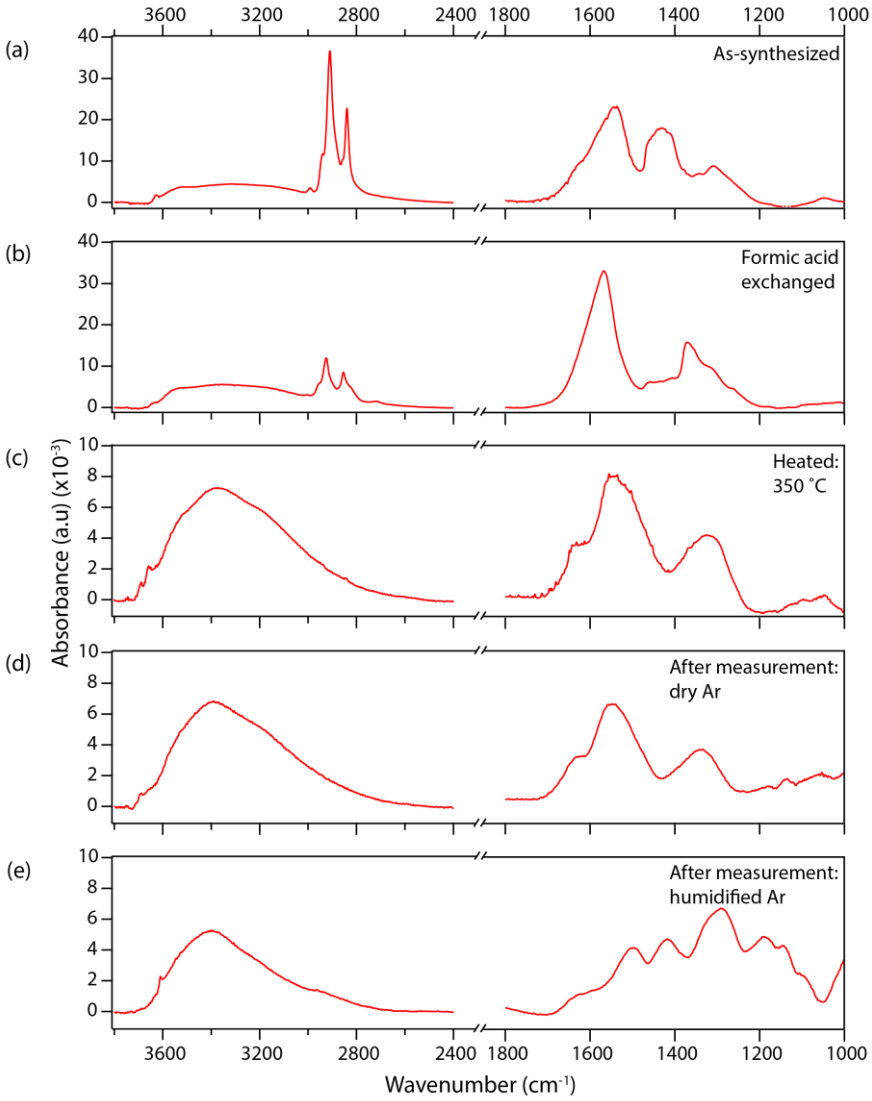

Figure 6.3: FTIR spectra of nanocrystal films prepared and processed on calcium fluoride substrates tracking changes in surface organic species throughout sample processing: (a) as synthesized nanocrystals, (b) after formic acid ligand exchange, (c) after heating to 350 °C to desorb formate, (d) after conductivity measurements under dry Ar, and (e) after conductivity measurements under humidified Ar.

To deconvolute the FTIR spectra, we fitted both the finger print region between 1000 cm^{-1} and 1800 cm^{-1} and the hydroxyl region between 2400 cm^{-1} and 3800 cm^{-1} with primarily Gaussian peaks, with one or two Lorentzian peaks for clear sharp signatures. An example of this data

treatment is shown in Figure D.4, and the results of the deconvolution and assignment for the respective peaks are tabulated in Table D.1 along with the references used. To simplify the discussion, we will hereby refer to the sample that has undergone conductivity measurements under dry Ar conditions as the 'dry sample' and similarly the sample that has been subjected to conductivity measurements under humidified Ar conditions as the 'humidified sample.'

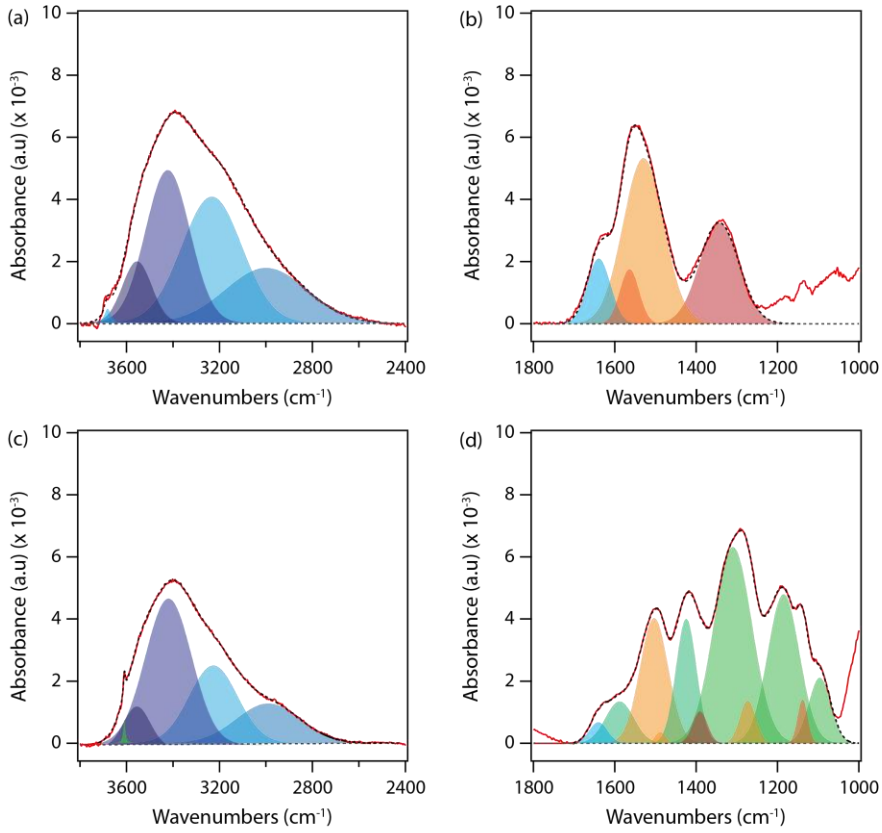

Figure 6.4: (a,b) Deconvoluted FTIR spectra for CeO_2 after conductivity measurements under dry Ar. The peaks between 1200 cm^{-1} and 1800 cm^{-1} are characteristic of monocarbonates on the surface of CeO_2. (c,d) Deconvoluted FTIR spectra for CeO_2 after conductivity measurements under humidified Ar. The peaks between 1000 cm^{-1} and 1800 cm^{-1} are composed of peaks characteristic of monodentate carbonates (shown in warm colors), and hydroxycarbonates (shown in greens). The deconvoluted spectra for both conditions from 2400 cm^{-1} and 3800 cm^{-1} show both liquid water peaks shown in darker blue, and structured water peaks shown in lighter blue. For panel (c), a sharp Lorentzian peak at 3600 cm^{-1} is characteristic of the hydroxyl for molecular hydroxycarbonate moieties.

Starting the discussion in the hydroxyl region, for both the dry sample and the humidified sample, we see a broad hydroxyl band that can be deconvoluted into four peaks: 2 at higher wavenumbers that are tentatively assigned to liquid water and two at lower wavenumbers that are tentatively assigned to structured water on the oxide interface. For the dry sample, we also see a small peak at 3700 cm^{-1} that is assigned to hydroxyls on the surface of cerium oxide. Note that the presence of the hydroxyl is a result of immediate capillary condensation during sample transfer from the measurement furnace to the FTIR, since these spectra were ultimately taken under ambient conditions. To further confirm this, we have also conducted an *in situ* FTIR study

for the decomposition of formate on the surface of cerium oxide under inert atmosphere, shown in Figure D.5, and saw no broad hydroxyl peak. For the humidified sample, we see a sharp peak at 3600 cm^{-1} that cannot be assigned to hydroxyls on cerium oxide. Rather, it belongs to the hydroxyl group associated with cerium hydroxycarbonate. This signature supports insights we will uncover from the peaks in the fingerprint region. From the deconvoluted peaks in the fingerprint region, apart from the water-bending mode at 1640 cm^{-1}, the dry sample shows three characteristic peaks at 1343, 1530, and 1564 cm^{-1} that can be assigned to monodentate carbonates on the surface of cerium oxide. Upon exposure to the humidified environment, the data strongly suggest that the primary surface species on cerium oxide is cerium hydroxycarbonate. Specifically, the eleven peaks can be deconvoluted and assigned to two families of surface species, namely carbonates (reds) and hydroxycarbonates (greens).

6.3.4 Decomposition of the surface passivation species

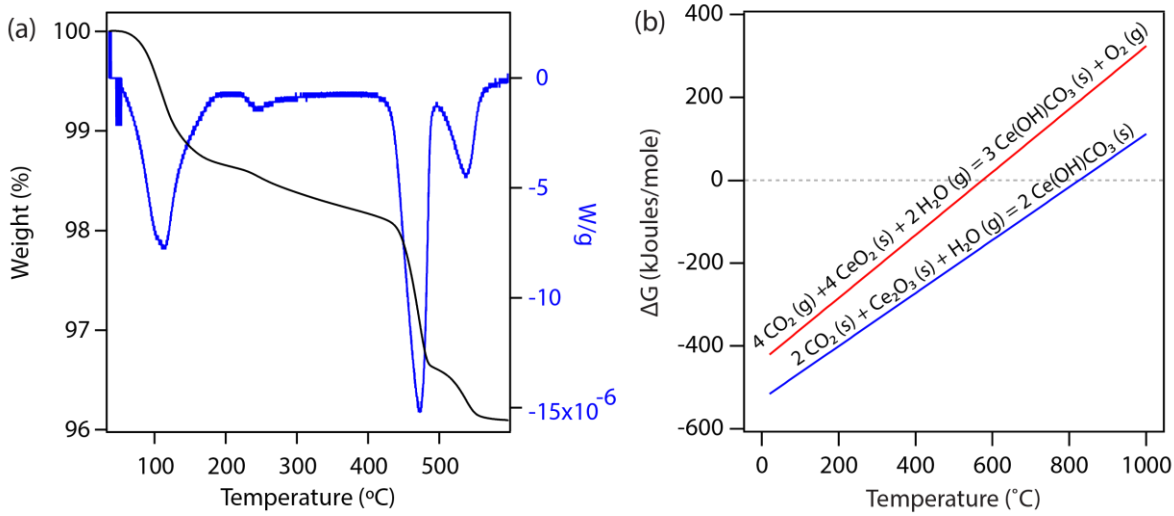

Figure 6.5: (a) Thermogravimetric analysis of hydrated cerium carbonate exhibiting a primary exothermic peak at 460 °C due to the conversion from cerium carbonate to cerium oxide. A change in mass is shown in black and corresponds to the left axis, and a change in heat flow is shown in blue and corresponds to the right axis with negative indicating exothermicity. (b) Thermodynamic analysis of two proposed reactions that convert cerium oxide into cerium hydroxycarbonate in the presence of CO_2 and water.

From the spectroscopic studies, assuming that hydroxycarbonate formation is the primary cause for degradation, we hypothesized that intermediate temperature proton conduction could be recovered if a sample is heated sufficiently to decompose cerium hydroxycarbonate. Prior work on carbonate stability on oxide surfaces has suggested that carbonate species tend to persist on the surface of cerium oxide up to temperatures around 350 °C. However, to get a lower bound of decomposition temperature, we approximated the decomposition temperature two ways. First, we measured simultaneous differential scanning calorimetry and thermogravimetric analysis of bulk hydrated cerium carbonate hypothesizing that the necessary conditions to decompose hydrated cerium carbonate should be a good estimate of the lower bound temperature needed to fully remove carbonates and reactivate the surface. Second, we estimated the bulk Gibbs free

energy of reaction for a proposed reaction that converts cerium oxide into cerium hydroxycarbonate. Details for the thermodynamic analysis are provided in Figure D.6, Table D.2 and Table D.3 of which the results are presented in Figure 6.5 (b).

Here in Figure 6.5, we see that a sample of bulk hydrated cerium carbonate initially decomposes into cerium oxide at 440 °C, exhibiting an exothermic peak centered at 460 °C. From the thermodynamic analysis on the other hand, we see that the Gibbs free energy of reaction is negative up to 575 °C for the reaction involving CeO_2 and up to 829 °C for the reaction involving Ce_2O_3. The latter reaction involving Ce_2O_3 was investigated as a proxy for the reaction on the surface of CeO_2 since it is known that the surface of CeO_2 nanocrystals is inherently enriched with Ce^{3+} defects. Though this analysis relies on bulk thermodynamics, the analysis does suggest that formation of cerium hydroxycarbonate would be thermodynamically favorable in the presence of carbon dioxide and water such as the conditions of our humidified measurements assuming the presence of trace carbon dioxide impurity in the gas. Applying this insight to our system, we reheated a passivated sample to the highest measurement temperature of 450 °C under dry Ar to decompose the passivation species prior to conductivity measurements under humidified Ar. The conductivity and spectroscopy results of this experiment are presented in Figure 6.6.

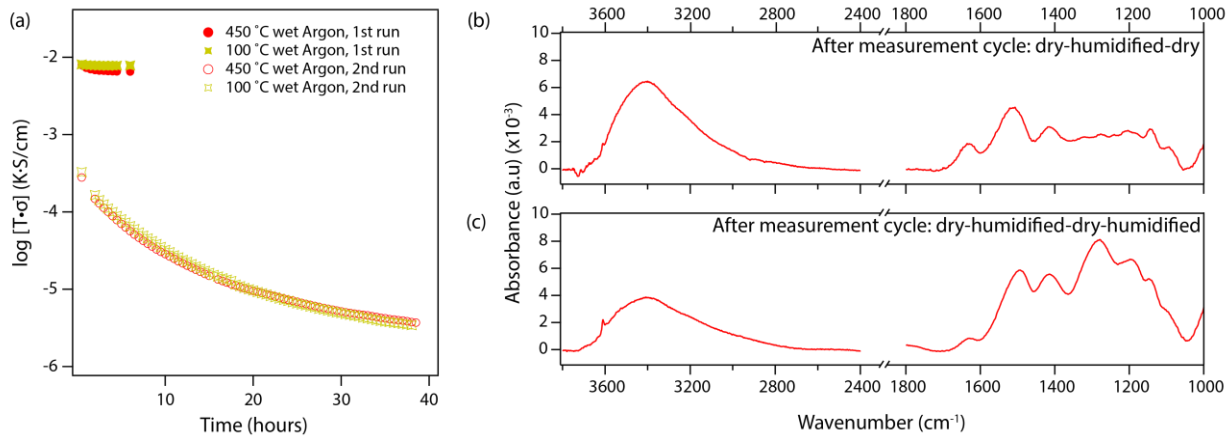

Figure 6.6: (a) Conductivity at 450 °C and 100 °C demonstrating recovery of the conductivity after re-equilibration at 450 °C under dry Ar prior to measurement under humidified Ar. FTIR spectra for sample after the re-equilibration under (b) dry Ar and (c) after measurement under humidified Ar.

Examining the accompanying FTIR spectra for the sample after equilibration under dry Ar and after re-measurement under humidified Ar, we see the partial disappearance and reappearance of the lower wavenumber peaks between 1400 cm^{-1} and 1000 cm^{-1} further confirming our prior observation that these peaks are organic signatures characteristic of the passivation species. Coupled with our assignment of these peaks to hydroxycarbonate moieties on the surface, we can deduce that the re-equilibration under dry Ar works to restore conductivity by partially decomposing surface hydroxycarbonates.

6.3.5 Surface passivation behavior of cerium oxide under humidified conditions as a function of oxygen partial pressure

Having observed the importance of hydroxycarbonate species on the surface and given the proposed reactions in Figure 6.5, a clear testable hypothesis resulting from the proposed reaction mechanism is the dependence of the degradation on oxygen partial pressure. Specifically, we would expect a lower driving force for the formation of cerium hydroxycarbonate under high oxygen partial pressure environments. We tested this hypothesis, and the results are presented in Figure 6.7.

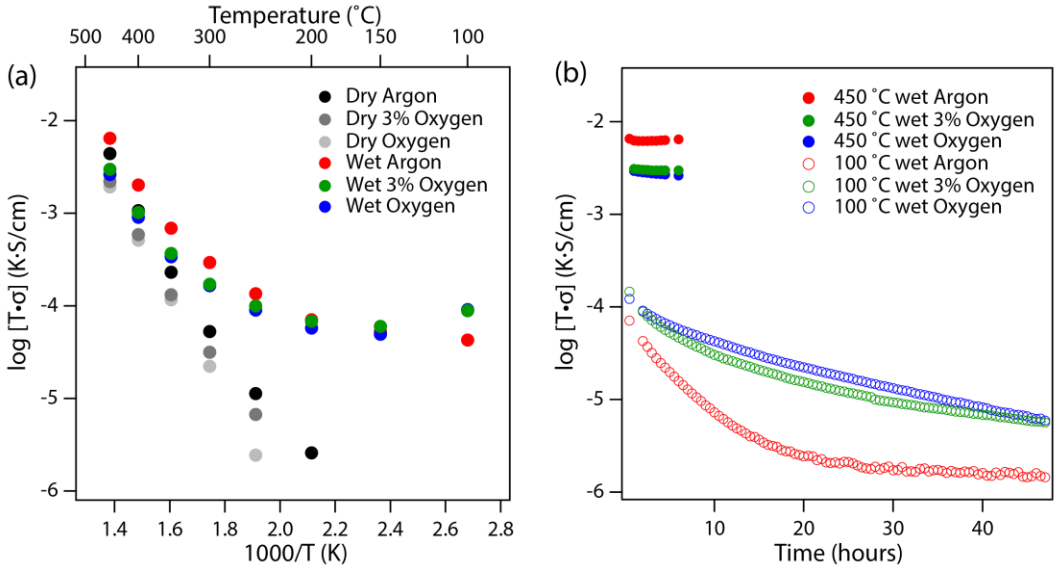

Figure 6.7: Partial pressure dependence of conductivity under dry and humidified Ar and their time dependence at 450 °C and 100 °C. With increasing oxygen partial pressure, the rate of passivation clearly decreases.

From the partial pressure dependence of the passivation behavior, we see that passivation of the species is significantly slower under pure oxygen conditions thus supporting our proposed reaction. With this evidence, we can now assert that hydroxycarbonates are most likely the responsible surface passivating species that lead to the degradation of intermediate temperature proton conductivity for cerium oxide. Specifically, the passivation occurs due to the thermodynamically favored formation of cerium hydroxycarbonate in the presence of carbon dioxide and water.

Within a broader context beyond our discussion of surface passivation and its influence on conductivity, this surface passivation behavior on ceria under humidified conditions is actually consistent with other prior works and observations in the literature. Specifically, CeO_2 - supported platinum systems used in water-gas shift reactions exhibit gradual deactivation that is attributed to carbonate formation on the surface of the ceria support.[159,160] Decomposition of cerium carbonate is also a known method to controllably generate cerium oxide nanostructures.[161,162] Last, rare earth elements, including cerium appear in nature as carbonate

minerals because of the thermodynamic stability of these compounds, while prior studies have shown that the surface of rare earths aged in air gradually revert to carbonate or hydroxycarbonate.[163–165]

6.3.6 Time dependent conductivity under dry and humidified atmospheres for gallium doped CeO_2

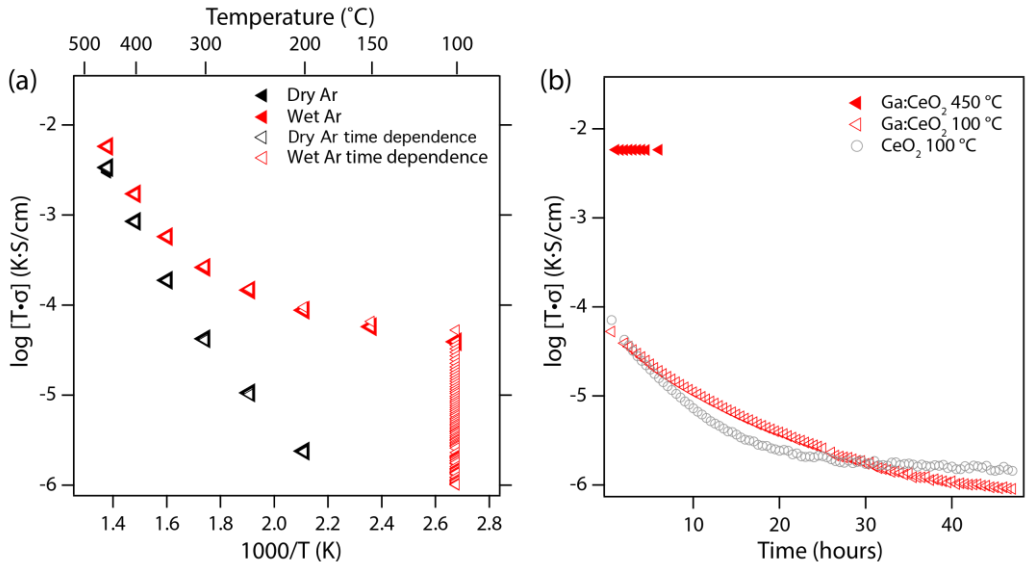

Figure 6.8: (a) Time and temperature dependent conductivity data under dry and humidified Ar for $Ga:CeO_2$. (b) Time dependent conductivity at 450 °C and 100 °C depicted as a function of time.

Having observed that surface deactivation due to carbonate formation is the likely cause for the time dependent proton conductivity observed, we considered how one might ameliorate this issue either by tuning the surface properties of cerium oxide by doping or by judicious material selection. Doping may be a viable solution to the problem because it is well established that the properties of cerium oxide can tuned by aliovalent doping. For instance, dopants such as Sm and Gd are commonly introduced into cerium oxide in order to utilize defect chemistry to tune oxygen vacancy concentrations. More recently, other dopants such as gallium and indium have been shown to play a dual role of both creating oxygen vacancies in the system as well as decreasing the affinity for carbonate formation on the doped oxide surface.[166–169] Building upon this investigation, we investigated the proton conduction of $Ga:CeO_2$ as a prototypical study.

Shown in Figure 6.8 is the temperature and time dependence of conductivity for a sample of $Ga:CeO_2$ with doping percentage of 20 % Ga (confirmed by x-ray photoelectron spectroscopy). Both the overall mixed conductivity of the sample as well as the time dependence of the conductivity at 100 °C is comparable to that of cerium oxide. We observe a small decrease in overall conductivity relative to CeO_2, and possibly a small decrease in degradation rate in the first 20 hours of the measurement.

6.3.7 Surface characterization before and after conductivity measurement for gallium doped CeO_2

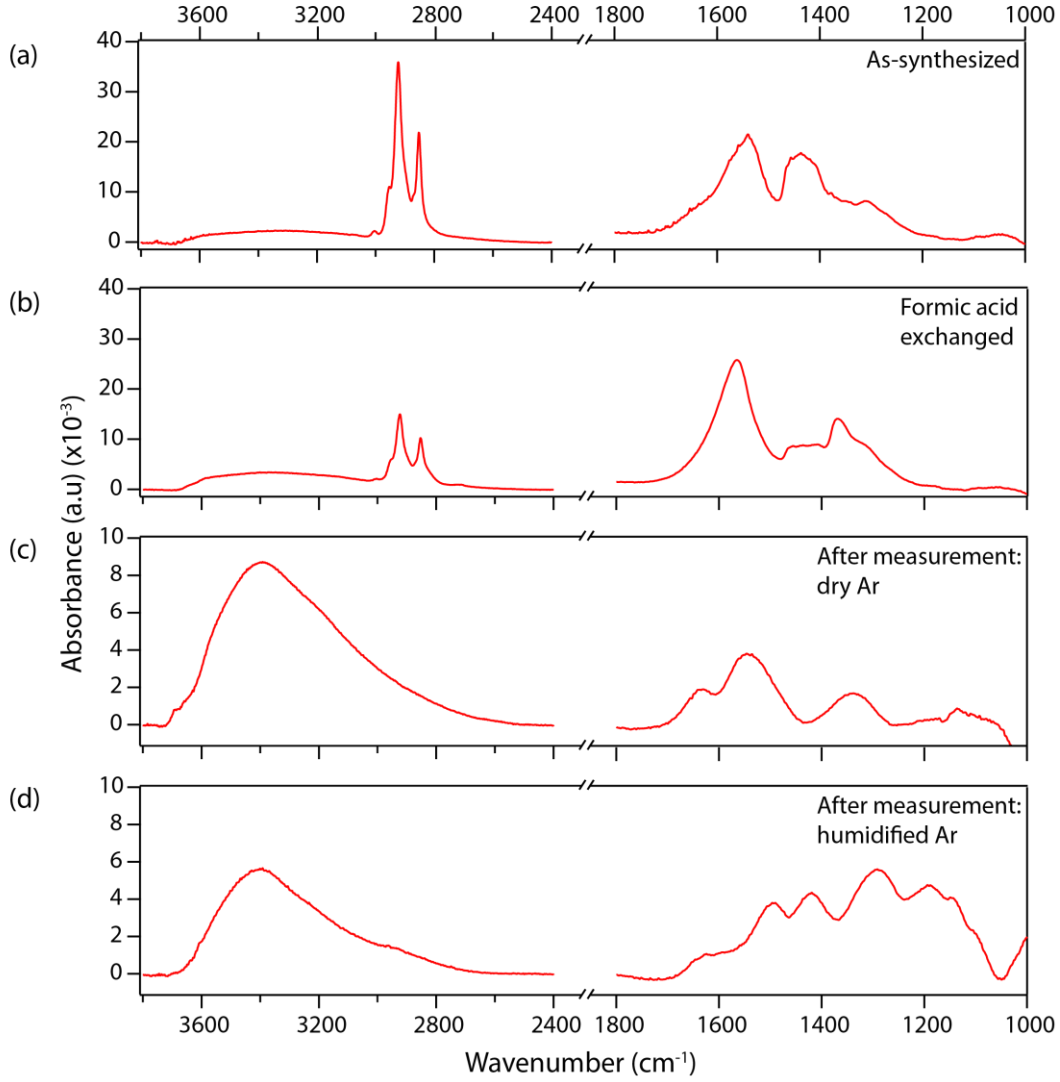

Figure 6.9: FTIR spectra of Ga:CeO_2 nanocrystal films prepared and processed on calcium fluoride substrates tracking changes in surface organic species throughout sample processing: (a) as synthesized nanocrystals, (b) after formic acid ligand exchange, (c) after conductivity measurements under dry Ar, and (d) after conductivity measurements under humidified Ar.

Upon tracking the surface characteristics of Ga:CeO-2, we found very similar FTIR spectra to those of CeO_2 which explains the similar conductivity behavior mentioned previously. While prior studies have suggested that Ga doping on CeO_2 can help mitigate the formation of hydroxycarbonates on the surface due to the increased acidity of Ga relative to Ce, logically, the surface of the nanocrystal is still composed of a majority of cerium oxide even at high Ga doping levels. Therefore, it is unsurprising that this approach failed. Future studies attempting this strategy should consider either higher Ga doping in the material which may be difficult to

achieve without secondary nucleation leading to the formation of gallium oxide or a new investigation of the intermediate temperature proton conduction of gallium oxide altogether. This strategy of examining an alternate material that demonstrates the necessary surface stability coupled with intermediate temperature proton conduction is explored further as follows with titanium dioxide.

6.3.8 Time dependent conductivity under dry and humid atmospheres for TiO_2

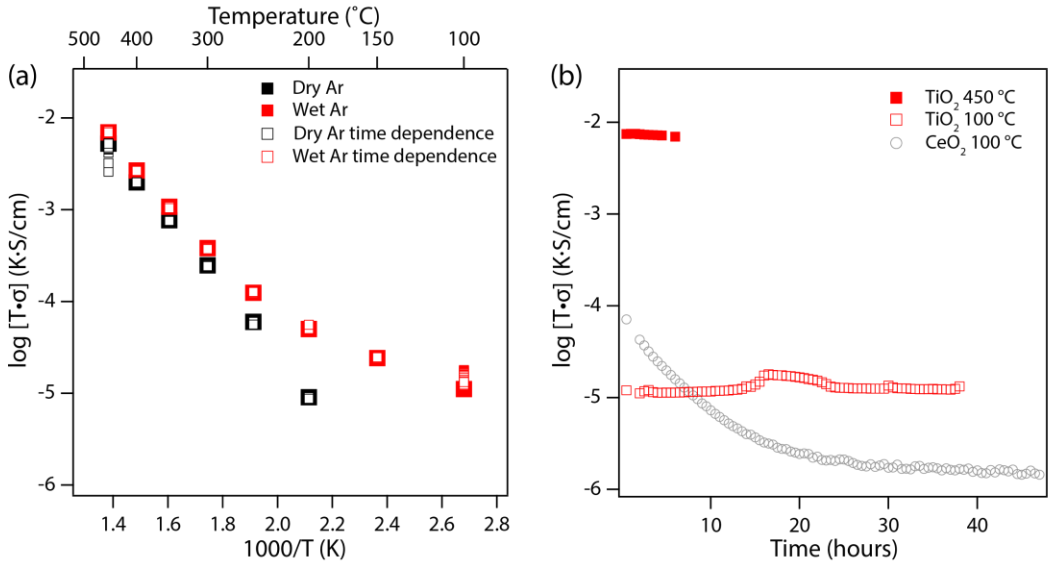

Figure 6.10: (a) Time and temperature dependent conductivity data under dry and humidified Ar for TiO_2. (b) Time dependent conductivity at 450 °C and 100 °C depicted as a function of time for TiO_2 and CeO_2 for reference.

Because doping of cerium oxide failed as a strategy to ameliorate this issue of surface passivation by hydroxycarbonate, we adopted a different approach based upon judicious material selection. Mentioned previously, one obvious hint to the instability of rare earth oxides and their gradual conversion to carbonates is their propensity to exist as carbonate minerals in nature. For instance, cerium exists in its mineral form as bastnasite, a cerium fluorocarbonate. Building upon this observation, we hypothesized that a metal oxide that exists as a metal oxide mineral in nature should exhibit the surface stability we desire. One such example is titanium oxide, which exists, in its mineral form as anatase and rutile. Shown in Figure 6.10 is the intermediate temperature proton conduction behavior as a function of temperature and time for porous titanium dioxide.

Once again, consistent with prior literature, we observe a significant enhancement in conductivity below 300 °C under humidified conditions that is commonly attributed to proton transport. When we examine the time dependent conductivity at 100 C, we see that the conductivity did not degrade. There are minor fluctuations in conductivity around the 20-hour mark, and we believe this was because of minor fluctuations in gas flow over the long measurement. Regardless, the conductivity at the start and end of the measurement are

comparable thus demonstrating the stability of this material at 100 °C under the humidified Ar measurement conditions.

6.3.9 Surface characterization before and after conductivity measurement for TiO_2.

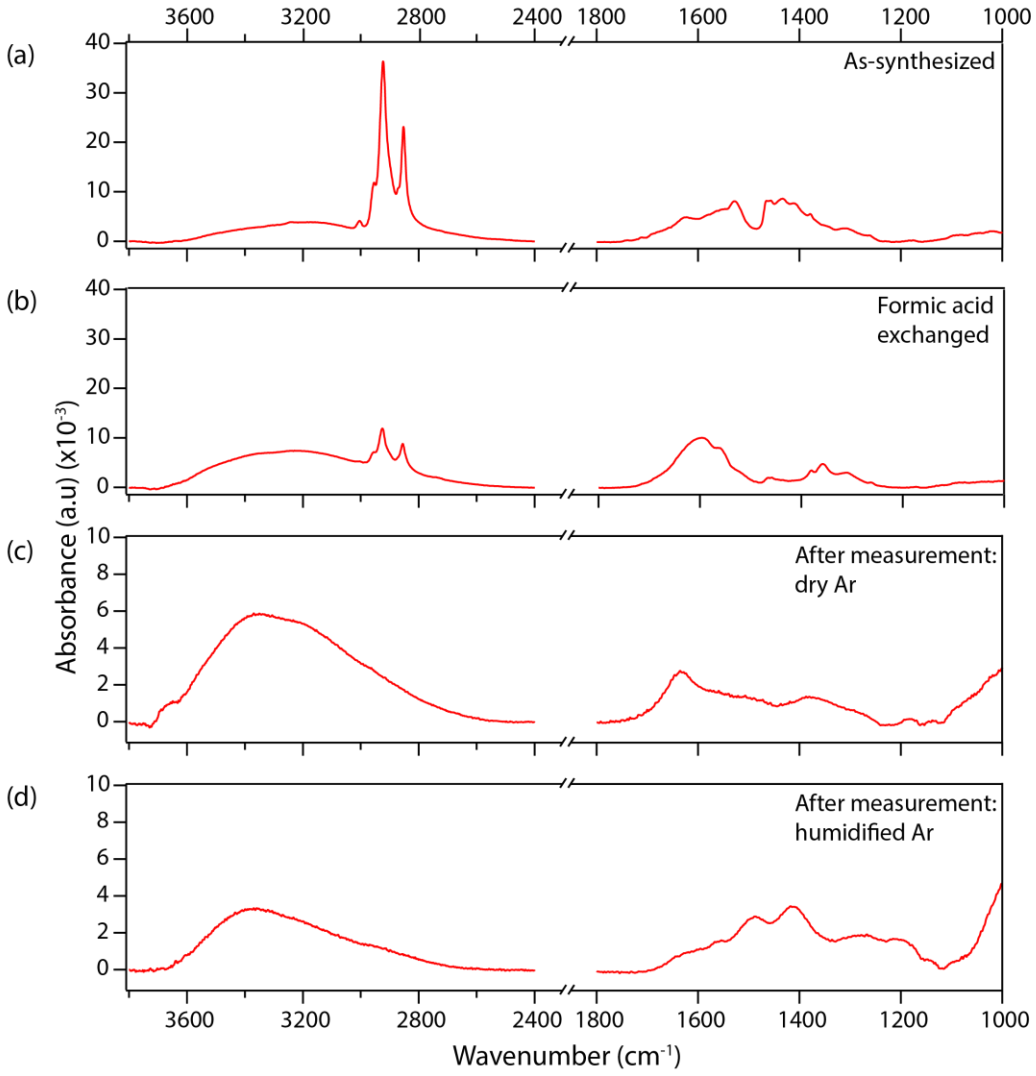

Figure 6.11: FTIR spectra of TiO_2 nanocrystal films prepared and processed on calcium fluoride substrates tracking changes in surface organic species throughout sample processing: (a) as synthesized nanocrystals, (b) after formic acid ligand exchange, (c) after conductivity measurements under dry Ar, and (d) after conductivity measurements under humidified Ar.

Similar to our investigation of cerium oxide, though we did not observe any degradation of conductivity over the measurement time, we conducted the same surface study tracking the changes in surface organics on the titanium dioxide surface as a function of processing starting

from the as synthesized material, to the formic acid exchange, after the measurement under dry Ar and finally after the measurement under humidified Ar.

Starting with the as-synthesized nanocrystals, we observe alkyl C-H stretches between 2800 cm^{-1} and 3000 cm^{-1} that are characteristic of the native alkyl ligands on the nanocrystal surface. While the nanocrystal synthesis was conducted in the presence of both oleic acid and oleylamine ligands, the absence of any clear carboxylate stretches in the region between 1200 cm^{-1} and 1600 cm^{-1} suggest that the surface of the nanocrystal is mainly populated by oleylamine ligands and the weak peaks can be attributed to the amine bending and alkene stretching modes. After the sample is subjected to formic acid ligand exchange, we observe a marked decrease in the C-H stretch given the shorter alkyl chain of formate. Between 1200 cm^{-1} and 1600 cm^{-1}, we observe a broad peak centered around 1600 cm^{-1} next to a sharp peak at 1558 cm^{-1} along with multiple small peaks at 1356 cm^{-1}. We are unable to assign the peak at 1600 cm^{-1} but the remaining peaks correspond to those of formate on the surface of titanium dioxide. Following measurement under dry Ar, we see one definitive peak at 1640 cm^{-1} corresponding to the water bending mode and multiple broad peaks that must be deconvoluted prior to assignment. The latter is carried out in Figure 6.12. Finally, after measurement under humidified Ar, we see multiple peaks emerge; these are also deconvoluted and assigned in Figure 6.12. However, it should be emphasized that the proton conductivity at 100 °C for titanium dioxide does not degrade as a function of time. Therefore, these surface species, while they exist, do not passivate the nanocrystal surface and adversely affect intermediate temperature proton transport.

To deconvolute the FTIR spectra, identical to our approach with the FTIR spectra of cerium oxide, we fitted both the finger print region between 1000 cm^{-1} and 1800 cm^{-1} and the hydroxyl region between 2400 cm^{-1} and 3800 cm^{-1} with primarily Gaussian peaks with one or two Lorentzian peaks for clear sharp signatures. The results of the deconvolution and assignment for the respective peaks are tabulated in Table D.1. Once again, to simplify the discussion, we will hereby refer to the sample that has undergone conductivity measurements under dry Ar conditions as the ‘dry sample’ and similarly the sample that has been subjected to conductivity measurements under humidified Ar conditions as the ‘humidified sample.’

Starting the discussion in the hydroxyl region, for both the dry sample and the humidified sample, we see a broad hydroxyl band that can be deconvoluted into four peaks: 2 at higher wavenumbers that are tentatively assigned to liquid water and two at lower wavenumbers that are assigned to structured water on the oxide interface. For the dry sample, we also see a small peak at 3667 cm^{-1} that is assigned to hydroxyls on the surface of titanium oxide. Note that the presence of the hydroxyl is a result of immediate capillary condensation during sample transfer from the measurement furnace to the FTIR since these spectra were ultimately taken under ambient conditions. For the humidified sample, we see the same four peaks assigned to liquid water and structured water but absent the free hydroxyl signature at 3667 cm^{-1}.

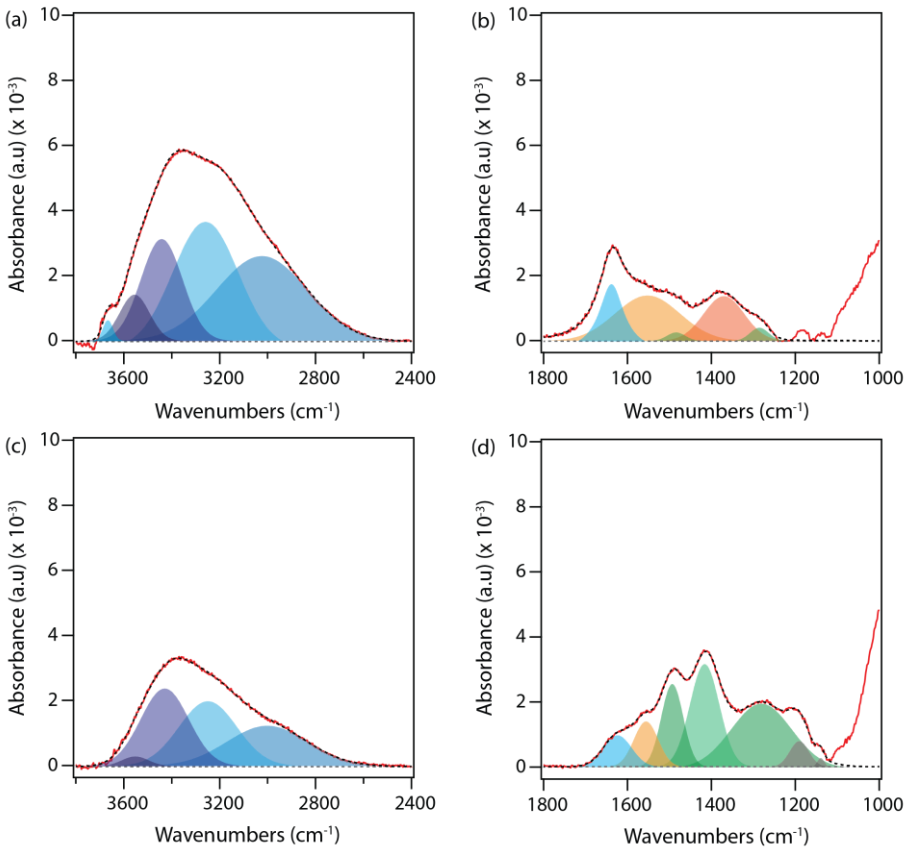

Figure 6.12: (a,b) Deconvoluted FTIR spectra for TiO_2 after conductivity measurements under dry Ar. The peaks between 1200 cm^{-1} and 1800 cm^{-1} are characteristic of monocarbonates on the surface of TiO_2. (c,d) Deconvoluted FTIR spectra for CeO_2 after conductivity measurements under humidified Ar. The peaks between 1000 cm^{-1} and 1800 cm^{-1} are composed of peaks characteristic of monodentate carbonates (shown in warm colors), and bicarbonates (shown in greens). The deconvoluted spectra for both conditions from 2400 cm^{-1} and 3800 cm^{-1} show both liquid water peaks shown in darker blue, and structured water peaks shown in lighter blue. For panel (b), a Lorentzian was used to fit the peak at 1640 cm^{-1} whereas all other peaks are fitted with Gaussian peaks.

From the deconvoluted peaks in the fingerprint region, apart from the water-bending mode at 1638 cm^{-1}, the dry sample shows two dominant peaks at 1370 and 1552 cm^{-1} and two minor peaks at 1286 and 1484 cm^{-1}. The former can be assigned to monodentate and bidentate carbonates on the surface of titanium dioxide, while the latter is assigned to bicarbonates (hydrogen carbonate) on the surface of titanium dioxide. Upon exposure to the humidified conditions for the extended period of time in measurement, we see the emergence of more features in the fingerprint region but most of the peaks can be assigned to that of bicarbonates on a titanium dioxide surface. This is logically consistent given the availability of water to react with existing carbonates and the ability of titanium dioxide to assist the reaction by dissociatively adsorbing water to generate reactive protons. The peaks at lower wavenumbers in the fingerprint region at 1281, 1416, 1493, and 1556 cm^{-1} can be assigned to bicarbonate signatures while the peak at 1556 cm^{-1} is assigned to a bidentate carbonate. We were unable to assign the remaining two minor peaks shown in grey at 1139 and 1190 cm^{-1}.

6.3.10 Proton conductivity of TiO_2 as a function of oxygen partial pressure

For completeness, we investigated the intermediate temperature proton conductivity as well as stability of titanium dioxide under pure oxygen as shown in Figure 6.13. Unsurprisingly, we do not observe any pronounced change in the stability behavior, and titanium dioxide exhibits stable albeit lower conductivity under pure oxygen. The decrease in conductivity is expected given the dependence of oxygen vacancy concentration on oxygen partial pressure with a lower oxygen vacancy associated with a higher oxygen partial pressure.

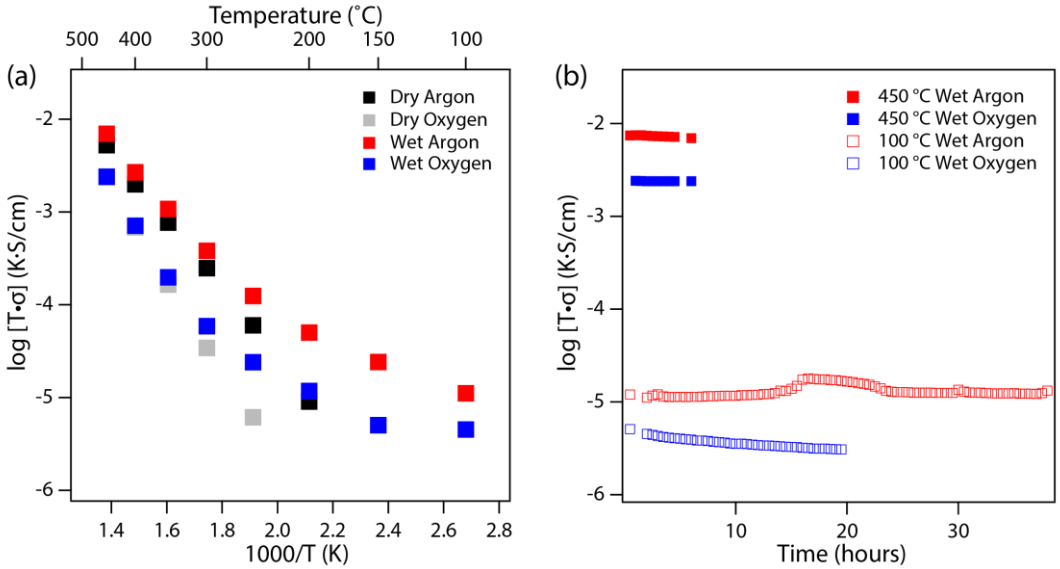

Figure 6.13: Oxygen partial pressure dependence of conductivity for TiO_2 under dry and humidified Ar and under dry or humidified oxygen with their time dependence at 450 °C and 100 °C. Under a pure oxygen environment, the conductivity for TiO_2 decreases but the stability remains.

6.4 Conclusion

In summary, we investigated the surface stability of cerium oxide and titanium dioxide within the context of intermediate temperature proton conduction under humidified atmospheres. Our investigations demonstrate that cerium oxide exhibits passivation that leads to a significant decrease in protonic conductivity at 100 °C due to the formation of cerium hydroxycarbonate. This process is thermodynamically favorable in the presence of a humidified atmosphere in the presence of trace CO_2. Gallium doping was attempted as a strategy to reduce the affinity for carbonate formation on the surface of cerium oxide but proved unsuccessful. In contrast, titanium oxide shows stable intermediate temperature proton conduction albeit at a lower absolute conductivity compared to that of cerium oxide.

6.4.1 Acknowledgements

The authors thank Ankit Agrawal, and Evan Runnerstrom for helpful discussions. G.K.O. was supported by a National Science Foundation Graduate Research Fellowship under grant number DGE 1106400. D.J.M. acknowledges support of the Welch Foundation (F-1848).

Chapter 7 : Future Work for Studies Involving Intermediate Temperature Proton Conductivity in Porous Metal Oxides

7.1 Introduction

In Chapter 5, we introduced the idea of intermediate temperature proton conductivity exhibited by porous metal oxide structures, showed that the phenomenon is not a result of water capillary condensation, and provided preliminary postulations on the influence of defect chemistry. Then, we examined the stability of this phenomenon in Chapter 6 and through careful FTIR analysis concluded that the intermediate temperature proton conductivity exhibited by cerium oxide eventually disappears due to the formation of cerium hydroxycarbonate under humidified conditions. Here, we will finish our discussion with final results that support our preliminary hypothesis of dissociative water adsorption on the metal oxide surface leading to proton generation, and propose future work that would extend our earlier discussion of defect chemistry on this phenomenon, with an emphasis on doping and nanocrystal shape control as an avenue to tune defect chemistry.

7.2 Preliminary Data and Discussion

7.2.1 *In situ* FTIR for observing dissociative water adsorption for proton formation on a metal oxide surface

In Chapter 5, we hypothesized that protons are generated on the surface of porous metal oxides via dissociate adsorption of water into surface oxygen vacancies. However, we have not yet proven this phenomenon directly. Prior studies have attempted to measure the concentration of oxygen vacancies and hydroxyls on the surface of cerium oxide to argue in favor of the same hypothesis, but no studies have directly shown the formation of the dissociated proton on the surface of a metal oxide under humidified conditions. Here, we propose this direct measurement using *in situ* FTIR of porous cerium oxide under humidified conditions.

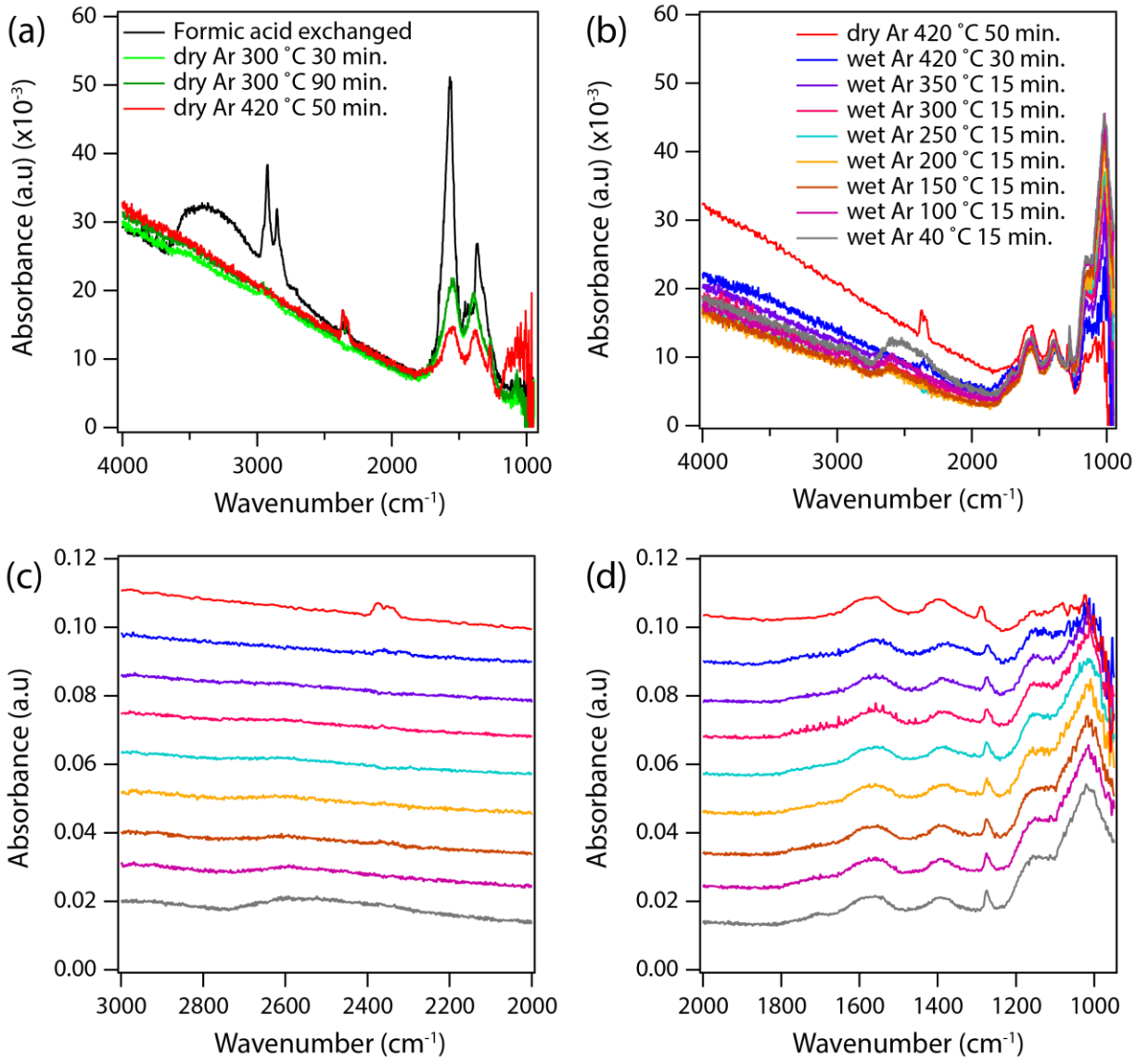

Figure 7.1: (a) *In situ* FTIR of CeO_2 under dry nitrogen with increasing temperature at 300 °C and 420 °C. (b) *In situ* FTIR of CeO_2 under humidified nitrogen using deuterium oxide with decreasing temperature and humidity introduced initially at 420 °C. (c,d) Zoomed in regions of spectra in (b) with offsets for clarity.

Shown in Figure 7.1 is the *in situ* FTIR of cerium oxide heated under dry and or humidified nitrogen using deuterium oxide (D_2O). Starting with heating under dry nitrogen (panel a), we observe the same change previously observed in *ex situ* experiments whereby the carboxylate peak for formate at 1570 cm^{-1} transforms to weaker broader monodentate carbonate peaks after heating to 300 °C. These peaks persist but decrease at 420 °C under dry nitrogen. Upon the introduction of D_2O, we observe two interesting trends with decreasing temperature: i) the emergence of the broad hydroxyl peak around 2600 cm^{-1} characteristic of structured or liquid D_2O that gradually form in the pores of the porous oxide thin film, and ii) the emergence of a strong peak and shoulder centered at 1000 cm^{-1} that may be characteristic of the acidic deuterium

peak. This would be consistent with prior work demonstrating the presence of an acidic proton peak at lower wavenumbers, and we would expect the acidic deuterium peak to be shifted to even lower numbers.[170] For analysis, the hydroxyl peak can be deconvoluted to determine the amount of structured and liquid water on the surface of cerium oxide that is responsible for providing the matrix for proton transport. The dissociated deuterium peak at 1000 cm^{-1}, on the other hand, can be fitted to determine the actual proton concentration on the surface due to the phenomena of dissociative water adsorption on the cerium oxide surface as a function of temperature. These analyses are underway, but preliminary examination of the data in Figure 7.1 is sufficient to support the hypothesis previously proposed in Chapter 5.

7.2.2 The influence of surface defect chemistry on intermediate temperature proton transport

While the data in Chapter 5 and Chapter 6 preliminarily explored the influence of doping (trivalent Ga doping) and defect chemistry (via oxygen partial pressure) on intermediate temperature proton transport, significant opportunity remains in the tuning and maximization of intermediate temperature proton conductivity via changes in defect chemistry. Two future directions in this vein are suggested here. First, recent works studying the surface defect chemistry of cerium oxide have shown that the surface defect concentration should be responsive to doping. These studies are supported by experimental verification by x-ray photoelectron spectroscopy as well as simulations built upon a combination of space-charge theory, Poison-Boltzman and Cahn-Hillard thermodynamics.[152,171] Therefore, it remains to see how these properties translate to intermediate temperature proton conduction under humidified atmospheres. Seminal results from literature that will be useful as guidance are reproduced in Figure 7.2. First, shown in panels (a) and (b), we see that upon doping with a trivalent acceptor, we see a predicted enrichment of the surface with oxygen vacancies that is compensated by a similar enrichment of dopants on the surface. Second, for a particular acceptor doping, we also obtain an accompanying Ce^{3+} enrichment on the crystal surface that is weakly dependent upon oxygen partial pressure. If we extrapolate this to an oxygen vacancy concentration, we would expect a similar weak dependence of oxygen vacancy concentration on oxygen partial pressure as well.

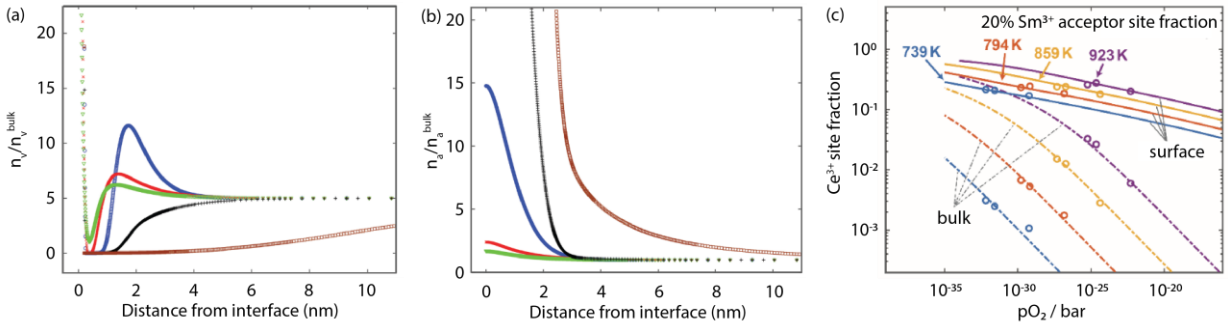

Figure 7.2: Normalized vacancy concentration (a) and dopant concentration (b) on the surface relative to the bulk showing the enrichment of oxygen vacancy on the surface of cerium oxide upon thermodynamic

equilibration as a function of acceptor doping. The color scheme for the plots are 0.01% (brown), 0.1% (black), 1% (blue), 10% (red), and 20 % (green) acceptor doping. (c) Partial pressure dependence of Ce^{3+} site fraction on the surface versus the bulk of samarium doped cerium oxide demonstrating both the enrichment of Ce^{3+} and relative insensitivity of the Ce^{3+} surface concentration to oxygen partial pressure. Figures adapted from reference [171] and reference [152].

Second, while the amount of difference in reactivity between different surfaces of cerium oxide such as the {100}, {110} and {111} surfaces remains under debate in literature, general consensus in the field is that a difference exist.[172–174] For instance, work examining the reactivity of faceted cerium oxide nanocrystals in the presence of gold catalyst with selectively exposed (200), (220), or (111) family of planes for the water-gas shift reaction ($CO + H_2O = CO_2 + H_2$) have shown that cerium oxide enclosed by {100} or {110} family of planes are more active for the reaction.[175] This approach of tuning surface reactivity and surface defect chemistry by tuning nanocrystal shape without doping would be especially suitable for future studies that utilize colloidal nanocrystal synthesis given the synthetic precision enabled by colloidal synthesis for the control of nanocrystal size and shape.

Bibliography

(1) Aizenberg, J.; Weaver, J. C.; Thanawala, M. S.; Sundar, V. C.; Morse, D. E.; Fratzl, P. "Skeleton of Euplectella Sp.: Structural Hierarchy from the Nanoscale to the Macroscale." *Science* **2005**, *309* (5732), 275–278.

(2) Shevchenko, E. V.; Talapin, D. V.; Kotov, N. A.; O'Brien, S.; Murray, C. B. "Structural Diversity in Binary Nanoparticle Superlattices." *Nature* **2006**, *439* (7072), 55–59.

(3) Matsen, M. W.; Bates, F. S. "Unifying Weak- and Strong-Segregation Block Copolymer Theories." *Macromolecules* **1996**, *29* (4), 1091–1098.

(4) Bates, F. S.; Fredrickson, G. H. "Block Copolymer Thermodynamics: Theory and Experiment." *Annu. Rev. Phys. Chem.* **1990**, *41* (1), 525–557.

(5) Fredrickson, G. H.; Bates, F. S. "Dynamics of Block Copolymers: Theory and Experiment." *Annu. Rev. Muter. Sci* **1996**, *26*.

(6) Tseng, Y.C.; Darling, S. B. "Block Copolymer Nanostructures for Technology." *Polymers (Basel).* **2010**, *2* (4), 470–489.

(7) Floudas, G.; Vazaiou, B.; Schipper, F.; Ulrich, FR.; Wiesner, U.; Iatrou, H. and; Hadjichristidis, N. "Poly(Ethylene Oxide-b-Isoprene) Diblock Copolymer Phase Diagram." Macromolecules **2001**, 34(9), 2947-2957.

(8) Garcia, B. C.; Kamperman, M.; Ulrich, R.; Jain, A.; Gruner, S. M.; Wiesner, U. "Morphology Diagram of a Diblock Copolymer−Aluminosilicate Nanoparticle System." *Chem. Mater.* **2009**, *21* (22), 5397–5405.

(9) Lee, J.; Christopher Orilall, M.; Warren, S. C.; Kamperman, M.; DiSalvo, F. J.; Wiesner, U. "Direct Access to Thermally Stable and Highly Crystalline Mesoporous Transition-Metal Oxides with Uniform Pores." *Nat. Mater.* **2008**, *7* (3), 222–228.

(10) Gutierrez, J.; Tercjak, A.; Garcia, I.; Peponi, L.; Mondragon, I. "Hybrid Titanium Dioxide/PS-b-PEO Block Copolymer Nanocomposites Based on Sol–Gel Synthesis." *Nanotechnology* **2008**, *19* (15), 155607.

(11) Göltner, C. G.; Henke, S.; Weissenberger, M. C.; Antonietti, M. "Mesoporous Silica from Lyotropic Liquid Crystal Polymer Templates." *Angew. Chemie Int. Ed.* **1998**, *37* (5), 613–616.

(12) Scherer, M. R. J.; Li, L.; Cunha, P. M. S.; Scherman, O. A.; Steiner, U. "Enhanced Electrochromism in Gyroid-Structured Vanadium Pentoxide." *Adv. Mater.* **2012**, *24* (9), 1217–1221.

(13) Kwon, S. G.; Hyeon, T. "Formation Mechanisms of Uniform Nanocrystals via Hot-Injection and Heat-Up Methods." *Small* **2011**, *7* (19), 2685–2702.

(14) Gilroy, K. D.; Ruditskiy, A.; Peng, H.-C.; Qin, D.; Xia, Y. "Bimetallic Nanocrystals: Syntheses, Properties, and Applications." *Chem. Rev.* **2016**, *116* (18), 10414–10472.

(15) Pietryga, J. M.; Park, Y.-S.; Lim, J.; Fidler, A. F.; Bae, W. K.; Brovelli, S.; Klimov, V. I. "Spectroscopic and Device Aspects of Nanocrystal Quantum Dots." *Chem. Rev.* **2016**, *116* (18), 10513–10622.

(16) Naik, G. V.; Shalaev, V. M.; Boltasseva, A. "Alternative Plasmonic Materials: Beyond Gold and Silver." *Adv. Mater.* **2013**, *25* (24), 3264–3294.

(17) Jang, S. G.; Khan, A.; Hawker, C. J.; Kramer, E. J. "Morphology Evolution of PS- *b* -P2VP Diblock Copolymers via Supramolecular Assembly of Hydroxylated Gold Nanoparticles." *Macromolecules* **2012**, *45* (3), 1553–1561.

(18) Jang, S. G.; Kramer, E. J.; Hawker, C. J. "Controlled Supramolecular Assembly of Micelle-Like Gold Nanoparticles in PS- *b* -P2VP Diblock Copolymers via Hydrogen Bonding." *J. Am. Chem. Soc.* **2011**, *133* (42), 16986–16996.

(19) Warren, S. C.; Messina, L. C.; Slaughter, L. S.; Kamperman, M.; Zhou, Q.; Gruner, S. M.; DiSalvo, F. J.; Wiesner, U. "Ordered Mesoporous Materials from Metal Nanoparticle-Block Copolymer Self-Assembly." *Science* **2008**, *320* (5884), 1748–1752.

(20) Buonsanti, R.; Pick, T. E.; Krins, N.; Richardson, T. J.; Helms, B. A.; Milliron, D. J. "Assembly of Ligand-Stripped Nanocrystals into Precisely Controlled Mesoporous Architectures." *Nano Lett.* **2012**, *12* (7), 3872–3877.

(21) Helms, B. A.; Williams, T. E.; Buonsanti, R.; Milliron, D. J. "Colloidal Nanocrystal Frameworks." *Adv. Mater.* **2015**, *27* (38), 5820–5829.

(22) Rauda, I. E.; Buonsanti, R.; Saldarriaga-Lopez, L. C.; Benjauthrit, K.; Schelhas, L. T.; Stefik, M.; Augustyn, V.; Ko, J.; Dunn, B.; Wiesner, U.; et al. "General Method for the Synthesis of Hierarchical Nanocrystal-Based Mesoporous Materials." *ACS Nano* **2012**, *6* (7), 6386–6399.

(23) Rivest, J. B.; Buonsanti, R.; Pick, T. E.; Zhu, L.; Lim, E.; Clavero, C.; Schaible, E.; Helms, B. A.; Milliron, D. J. "Evolution of Ordered Metal Chalcogenide Architectures through Chemical Transformations." *J. Am. Chem. Soc.* **2013**, *135* (20), 7446–7449.

(24) Milliron, D. J.; Buonsanti, R.; Llordes, A.; Helms, B. A. "Constructing Functional Mesostructured Materials from Colloidal Nanocrystal Building Blocks." *Acc. Chem. Res.* **2014**, *47* (1), 236–246.

(25) Gilroy, K. D.; Ruditskiy, A.; Peng, H.-C.; Qin, D.; Xia, Y. "Bimetallic Nanocrystals: Syntheses, Properties, and Applications." *Chem. Rev.* **2016**, *116* (18), 10414–10472.

(26) Lamer, V. K.; Dinegar, R. H. "Theory, Production and Mechanism of Formation of Monodispersed Hydrosols." *Edwards Bros. J. J. Frenkel* **1949**, No. 23.

(27) Kohlbrecher, J.; Bressler, I. "User Guide for the SASfit Software Package." 2010.

(28) Burle, J.; Fisher, J. M.; Ganeva, M.; Pospelov, G.; Herck, W. Van; Wuttke, J. "BornAgain - Software for Simulating and Fitting X-Ray and Neutron Small-Angle Scattering at Grazing Incidence." 2017.

(29) Meyer, Andreas, Institute of Physical Chemistry, U. of Hamburg, GISAXS.de

www.gisaxs.de (accessed Jun 8, 2018).

(30) Jiang, Z., "*GIXSGUI* : A MATLAB Toolbox for Grazing-Incidence X-Ray Scattering Data Visualization and Reduction, and Indexing of Buried Three-Dimensional Periodic Nanostructured Films." *J. Appl. Crystallogr.* **2015**, *48* (3), 917–926.

(31) Ong, G. K.; Williams, T. E.; Singh, A.; Schaible, E.; Helms, B. A.; Milliron, D. J. "Ordering in Polymer Micelle-Directed Assemblies of Colloidal Nanocrystals." *Nano Lett.* **2015**, *15* (12), 8240–8244.

(32) Shevchenko, E. V.; Talapin, D. V.; Kotov, N. A.; O'Brien, S.; Murray, C. B. "Structural Diversity in Binary Nanoparticle Superlattices." *Nature* **2006**, *439* (7072), 55–59.

(33) Bockstaller, M. R.; Mickiewicz, R. A.; Thomas, E. L. "Block Copolymer Nanocomposites: Perspectives for Tailored Functional Materials." *Adv. Mater.* **2005**, *17* (11), 1331–1349.

(34) Kao, J.; Thorkelsson, K.; Bai, P.; Rancatore, B. J.; Xu, T. "Toward Functional Nanocomposites: Taking the Best of Nanoparticles, Polymers, and Small Molecules." *Chem. Soc. Rev.* **2013**, *42* (7), 2654–2678.

(35) Hoheisel, T. N.; Hur, K.; Wiesner, U. B. "Block Copolymer-Nanoparticle Hybrid Self-Assembly." *Prog. Polym. Sci.* **2015**, *40*, 3–32.

(36) Kao, J.; Xu, T. "Nanoparticle Assemblies in Supramolecular Nanocomposite Thin Films: Concentration Dependence." *J. Am. Chem. Soc.* **2015**, *137* (19), 6356–6365.

(37) Li, Z.; Hur, K.; Sai, H.; Higuchi, T.; Takahara, A.; Jinnai, H.; Gruner, S. M.; Wiesner, U. "Linking Experiment and Theory for Three-Dimensional Networked Binary Metal Nanoparticle–Triblock Terpolymer Superstructures." *Nat. Commun.* **2014**, *5*.

(38) Song, D.-P.; Lin, Y.; Gai, Y.; Colella, N. S.; Li, C.; Liu, X.-H.; Gido, S.; Watkins, J. J. "Controlled Supramolecular Self-Assembly of Large Nanoparticles in Amphiphilic Brush Block Copolymers." *J. Am. Chem. Soc.* **2015**, *137* (11), 3771–3774.

(39) Deng, R.; Liu, S.; Li, J.; Liao, Y.; Tao, J.; Zhu, J. "Mesoporous Block Copolymer Nanoparticles with Tailored Structures by Hydrogen-Bonding-Assisted Self-Assembly." *Adv. Mater.* **2012**, *24* (14), 1889–1893.

(40) Dormidontova, E. E. "Micellization Kinetics in Block Copolymer Solutions: Scaling Model." *Macromolecules* **1999**, *32* (22), 7630–7644.

(41) Lund, R.; Willner, L.; Richter, D.; Dormidontova, E. E. "Equilibrium Chain Exchange Kinetics of Diblock Copolymer Micelles: Tuning and Logarithmic Relaxation." *Macromolecules* **2006**, *39* (13), 4566–4575.

(42) Jain, S.; Bates, F. S. "Consequences of Nonergodicity in Aqueous Binary PEO−PB Micellar Dispersions." *Macromolecules* **2004**, *37* (4), 1511–1523.

(43) Bastakoti, B. P.; Li, Y.; Imura, M.; Miyamoto, N.; Nakato, T.; Sasaki, T.; Yamauchi, Y. "Polymeric Micelle Assembly with Inorganic Nanosheets for Construction of Mesoporous Architectures with Crystallized Walls." *Angew. Chemie Int. Ed.* **2015**, *54* (14), 4222–

4225.

(44) Smarsly, B.; Antonietti, M. “Block Copolymer Assemblies as Templates for the Generation of Mesoporous Inorganic Materials and Crystalline Films.” *Eur. J. Inorg. Chem.* **2006**, *2006* (6), 1111–1119.

(45) Lu, Y.; Ganguli, R.; Drewien, C. A.; Anderson, M. T.; Brinker, C. J.; Gong, W.; Guo, Y.; Soyez, H.; Dunn, B.; Huang, M. H.; “Continuous Formation of Supported Cubic and Hexagonal Mesoporous Films by Sol-gel Dip-Coating.” *Nature* **1997**, *389* (6649), 364–368.

(46) Moller, K.; Bein, T.; Fischer, R. X. “Synthesis of Ordered Mesoporous Methacrylate Hybrid Systems: Hosts for Molecular Polymer Composites.” *Chem. Mater.* **1999**, *11* (3), 665–673.

(47) Bagshaw, S. A.; Prouzet, E.; Pinnavaia, T. J. “Templating of Mesoporous Molecular Sieves by Nonionic Polyethylene Oxide Surfactants.” *Science* **1995**, *269* (5228), 1242–1244.

(48) Chen, D.; Park, S.; Chen, J.-T.; Redston, E.; Russell, T. P. “A Simple Route for the Preparation of Mesoporous Nanostructures Using Block Copolymers.” *ACS Nano* **2009**, *3* (9), 2827–2833.

(49) Wills, A. W.; Michalak, D. J.; Ercius, P.; Rosenberg, E. R.; Perciano, T.; Ushizima, D.; Runser, R.; Helms, B. A. “Block Copolymer Packing Limits and Interfacial Reconfigurability in the Assembly of Periodic Mesoporous Organosilicas.” *Adv. Funct. Mater.* **2015**, *25* (26), 4120–4128.

(50) Krins, N.; Faustini, M.; Louis, B.; Grosso, D. “Thick and Crack-Free Nanocrystalline Mesoporous TiO_2 Films Obtained by Capillary Coating from Aqueous Solutions.” *Chem. Mater.* **2010**, *22* (23), 6218–6220.

(51) Stefik, M.; Song, J.; Sai, H.; Guldin, S.; Boldrighini, P.; Orilall, M. C.; Steiner, U.; Gruner, S. M.; Wiesner, U. “Ordered Mesoporous Titania from Highly Amphiphilic Block Copolymers: Tuned Solution Conditions Enable Highly Ordered Morphologies and Ultra-Large Mesopores.” *J. Mater. Chem. A* **2015**, *3* (21), 11478–11492.

(52) Fattakhova-Rohlfing, D.; Szeifert, J. M.; Yu, Q.; Kalousek, V.; Rathouský, J.; Bein, T. “Low-Temperature Synthesis of Mesoporous Titania−Silica Films with Pre-Formed Anatase Nanocrystals.” *Chem. Mater.* **2009**, *21* (12), 2410–2417.

(53) Szeifert, J. M.; Feckl, J. M.; Fattakhova-Rohlfing, D.; Liu, Y.; Kalousek, V.; Rathousky, J.; Bein, T. “Ultrasmall Titania Nanocrystals and Their Direct Assembly into Mesoporous Structures Showing Fast Lithium Insertion.” *J. Am. Chem. Soc.* **2010**, *132* (36), 12605–12611.

(54) Vamvasakis, I.; Subrahmanyam, K. S.; Kanatzidis, M. G.; Armatas, G. S. “Template-Directed Assembly of Metal–Chalcogenide Nanocrystals into Ordered Mesoporous Networks.” *ACS Nano* **2015**, *9* (4), 4419–4426.

(55) Thompson, R. B.; Ginzburg, V. V.; Matsen, M. W.; Balazs, A. C. “Block Copolymer-Directed Assembly of Nanoparticles: Forming Mesoscopically Ordered Hybrid

Materials." *Macromolecules* **2002**, *35* (3), 1060–1071.

(56) Kim, B. H.; Lee, N.; Kim, H.; An, K.; Park, Y. Il; Choi, Y.; Shin, K.; Lee, Y.; Kwon, S. G.; Na, H. Bin; et al. "Large-Scale Synthesis of Uniform and Extremely Small-Sized Iron Oxide Nanoparticles for High-Resolution T_1 Magnetic Resonance Imaging Contrast Agents." *J. Am. Chem. Soc.* **2011**, *133* (32), 12624–12631.

(57) Park, J.; An, K.; Hwang, Y.; Park, J.-G.; Noh, H.-J.; Kim, J.-Y.; Park, J.-H.; Hwang, N.-M.; Hyeon, T. "Ultra-Large-Scale Syntheses of Monodisperse Nanocrystals." *Nat. Mater.* **2004**, *3* (12), 891–895.

(58) Dong, A.; Ye, X.; Chen, J.; Kang, Y.; Gordon, T.; Kikkawa, J. M.; Murray, C. B. "A Generalized Ligand-Exchange Strategy Enabling Sequential Surface Functionalization of Colloidal Nanocrystals." *J. Am. Chem. Soc.* **2011**, *133* (4), 998–1006.

(59) Ilavsky, J.; Jemian, P. R. "*Irena* : Tool Suite for Modeling and Analysis of Small-Angle Scattering." *J. Appl. Crystallogr.* **2009**, *42* (2), 347–353.

(60) Ilavsky, J. "*Nika* : Software for Two-Dimensional Data Reduction." *J. Appl. Crystallogr.* **2012**, *45* (2), 324–328.

(61) Thompson, R. B. "Predicting the Mesophases of Copolymer-Nanoparticle Composites." *Science* **2001**, *292* (5526), 2469–2472.

(62) Bockstaller, M. R.; Lapetnikov, Y.; Margel, S.; Thomas, E. L. "Size-Selective Organization of Enthalpic Compatibilized Nanocrystals in Ternary Block Copolymer/Particle Mixtures." *J. Am. Chem. Soc.* **2003**, *125* (18), 5276–5277.

(63) Percus, J. K.; Yevick, G. J. "Analysis of Classical Statistical Mechanics by Means of Collective Coordinates." *Phys. Rev.* **1958**, *110* (1), 1–13.

(64) Curk, T.; Martinez-Veracoechea, F. J.; Frenkel, D.; Dobnikar, J. "Nanoparticle Organization in Sandwiched Polymer Brushes." *Nano Lett.* **2014**, *14* (5), 2617–2622.

(65) Hur, K.; Hennig, R. G.; Escobedo, F. A.; Wiesner, U. "Predicting Chiral Nanostructures, Lattices and Superlattices in Complex Multicomponent Nanoparticle Self-Assembly." *Nano Lett.* **2012**, *12* (6), 3218–3223.

(66) Agrawal, A.; Johns, R. W.; Milliron, D. J. "Control of Localized Surface Plasmon Resonances in Metal Oxide Nanocrystals." *Annu. Rev. Mater. Res.* **2017**, *47* (1), 1–31.

(67) Warren, S. C.; Messina, L. C.; Slaughter, L. S.; Kamperman, M.; Zhou, Q.; Gruner, S. M.; DiSalvo, F. J.; Wiesner, U. "Ordered Mesoporous Materials from Metal Nanoparticle-Block Copolymer Self-Assembly." *Science* **2008**, *320* (5884), 1748–1752.

(68) Doris, S. E.; Lynch, J. J.; Li, C.; Wills, A. W.; Urban, J. J.; Helms, B. A. "Mechanistic Insight into the Formation of Cationic Naked Nanocrystals Generated under Equilibrium Control." *J. Am. Chem. Soc.* **2014**, *136* (44), 15702–15710.

(69) Rosen, E. L.; Buonsanti, R.; Llordes, A.; Sawvel, A. M.; Milliron, D. J.; Helms, B. A. "Exceptionally Mild Reactive Stripping of Native Ligands from Nanocrystal Surfaces by Using Meerwein's Salt." *Angew. Chemie Int. Ed.* **2012**, *51* (3), 684–689.

(70) Kim, J.; Ong, G. K.; Wang, Y.; LeBlanc, G.; Williams, T. E.; Mattox, T. M.; Helms, B. a.; Milliron, D. J. "Nanocomposite Architecture for Rapid, Spectrally-Selective Electrochromic Modulation of Solar Transmittance." *Nano Lett.* **2015**, 5574–5579.

(71) Brust, M.; Fink, J.; Bethell, D.; Schiffrin, D. J.; Kiely, C. "Synthesis and Reactions of Functionalised Gold Nanoparticles." *J. Chem. Soc. Chem. Commun.* **1995**, *0* (16), 1655.

(72) Bae, W. K.; Char, K.; Hur, H.; Lee, S. "Single-Step Synthesis of Quantum Dots with Chemical Composition Gradients." *Chem. Mater.* **2008**, *20* (2), 531–539.

(73) Kao, J.; Bai, P.; Chuang, V. P.; Jiang, Z.; Ercius, P.; Xu, T. "Nanoparticle Assemblies in Thin Films of Supramolecular Nanocomposites." *Nano Lett.* **2012**, *12* (5), 2610–2618.

(74) Di, Z.; Posselt, D.; Smilgies, D.-M.; Papadakis, C. M. "Structural Rearrangements in a Lamellar Diblock Copolymer Thin Film during Treatment with Saturated Solvent Vapor." *Macromolecules* **2010**, *43* (1), 418–427.

(75) Busch, P.; Rauscher, M.; Smilgies, D.-M.; Posselt, D.; Papadakis, C. M.; IUCr. "Grazing-Incidence Small-Angle X-Ray Scattering from Thin Polymer Films with Lamellar Structures – the Scattering Cross Section in the Distorted-Wave Born Approximation." *J. Appl. Crystallogr.* **2006**, *39* (3), 433–442.

(76) Kreuer, K.-D. "Ion Conducting Membranes for Fuel Cells and Other Electrochemical Devices." *Chem. Mater.* **2014**, *26* (1), 361–380.

(77) Steele, B. C. H.; Heinzel, A. "Materials for Fuel-Cell Technologies." *Nature* **2001**, *414* (6861), 345–352.

(78) Kreuer, K. D. "On the Development of Proton Conducting Polymer Membranes for Hydrogen and Methanol Fuel Cells." *J. Memb. Sci.* **2001**, *185* (1), 29–39.

(79) Norby, T. "Solid-State Protonic Conductors: Principles, Properties, Progress and Prospects." *Solid State Ionics* **1999**, *125* (1–4), 1–11.

(80) Schmidt-Rohr, K.; Chen, Q. "Parallel Cylindrical Water Nanochannels in Nafion Fuel-Cell Membranes." *Nat. Mater.* **2008**, *7* (1), 75–83.

(81) Malavasi, L.; Fisher, C. A. J.; Islam, M. S. "Oxide-Ion and Proton Conducting Electrolyte Materials for Clean Energy Applications: Structural and Mechanistic Features." *Chem. Soc. Rev.* **2010**, *39* (11), 4370.

(82) Aricò, A. S.; Bruce, P.; Scrosati, B.; Tarascon, J.-M.; van Schalkwijk, W. "Nanostructured Materials for Advanced Energy Conversion and Storage Devices." *Nat. Mater.* **2005**, *4* (5), 366–377.

(83) Fabbri, E.; Pergolesi, D.; Traversa, E. "Materials Challenges toward Proton-Conducting Oxide Fuel Cells: A Critical Review." *Chem. Soc. Rev.* **2010**, *39* (11), 4355.

(84) Kreuer, K.D.; Paddison, S.J.; Spohr, E.; and Schuster, M. "Transport in Proton Conductors for Fuel-Cell Applications: Simulations, Elementary Reactions, and Phenomenology." **2004**, *104 (*10), 4637 - 4678

(85) Haile, S. M.; Boysen, D. A.; Chisholm, C. R. I.; Merle, R. B. "Solid Acids as Fuel Cell

Electrolytes." *Nature* **2001**, *410* (6831), 910–913.

(86) Kreuer, K.D. "On Solids with Liquidlike Properties and the Challenge To Develop New Proton-Conducting Separator Materials for Intermediate-Temperature Fuel Cells." *ChemPhysChem* **2002**, *3* (9), 771–775.

(87) Kreuer, K. D. "Proton-Conducting Oxides." *Annu. Rev. Mater. Res.* **2003**, *33* (1), 333–359.

(88) Fabbri, E.; Pergolesi, D.; Traversa, E. "Materials Challenges toward Proton-Conducting Oxide Fuel Cells: A Critical Review." *Chem. Soc. Rev.* **2010**, *39* (11), 4355.

(89) Nogami, M.; Nagao, R.; Wong, C. "Proton Conduction in Porous Silica Glasses with High Water Content," *J. Phys. Chem. C,* **1998**, *102* (30), 5772 - 5775.

(90) Colomer, M. T. "Nanoporous Anatase Ceramic Membranes as Fast-Proton-Conducting Materials." *J. Eur. Ceram. Soc.* **2006**, *26* (7), 1231–1236.

(91) Colomer, M. T. "Nanoporous Anatase Thin Films as Fast Proton-Conducting Materials." *Adv. Mater.* **2006**, *18* (3), 371–374.

(92) Yoon, M.; Suh, K.; Natarajan, S.; Kim, K. "Proton Conduction in Metal-Organic Frameworks and Related Modularly Built Porous Solids." *Angew. Chemie Int. Ed.* **2013**, *52* (10), 2688–2700.

(93) Karim, M. R.; Hatakeyama, K.; Matsui, T.; Takehira, H.; Taniguchi, T.; Koinuma, M.; Matsumoto, Y.; Akutagawa, T.; Nakamura, T.; Noro, S.; et al. "Graphene Oxide Nanosheet with High Proton Conductivity." *J. Am. Chem. Soc.* **2013**, *135* (22), 8097–8100.

(94) Zhou, Y.; Yang, J.; Su, H.; Zeng, J.; Jiang, S. P.; Goddard, W. A. "Insight into Proton Transfer in Phosphotungstic Acid Functionalized Mesoporous Silica-Based Proton Exchange Membrane Fuel Cells." **2014**, *136* (13), 4954 - 4964.

(95) Raz, S.; Sasaki, K.; Maier, J.; Riess, I. "Characterization of Adsorbed Water Layers on Y2O3-Doped ZrO2." *Solid State Ionics* **2001**, *143* (2), 181–204.

(96) Kim, S.; Anselmi-Tamburini, U.; Park, H. J.; Martin, M.; Munir, Z. A. "Unprecedented Room-Temperature Electrical Power Generation Using Nanoscale Fluorite-Structured Oxide Electrolytes." *Adv. Mater.* **2008**, *20* (3), 556–559.

(97) Kim, S.; Avila-Paredes, H. J.; Wang, S.; Chen, C.-T.; Souza, R. A. De; Martin, M.; Munir, Z. A. "On the Conduction Pathway for Protons in Nanocrystalline Yttria-Stabilized Zirconia." *Phys. Chem. Chem. Phys.* **2009**, *11* (17), 3035–3038.

(98) Chiodelli, G.; Maglia, F.; Anselmi-Tamburini, U.; Munir, Z. A. "Characterization of Low Temperature Protonic Conductivity in Bulk Nanocrystalline Fully Stabilized Zirconia." *Solid State Ionics* **2009**, *180* (4–5), 297–301.

(99) Avila-Paredes, H. J.; Zhao, J.; Wang, S.; Pietrowski, M.; De Souza, R. A.; Reinholdt, A.; Munir, Z. A.; Martin, M.; Kim, S. "Protonic Conductivity of Nano-Structured Yttria-

Stabilized Zirconia: Dependence on Grain Size." *J. Mater. Chem.* **2010**, *20* (5), 990–994.

(100) Tandé, C.; Pérez-Coll, D.; Mather, G.C. "Surface Proton Conductivity of Dense Nanocrystalline YSZ." *J. Mater. Chem.* **2012**, *22* (22), 11208–11213.

(101) Miyoshi, S.; Akao, Y.; Kuwata, N.; Kawamura, J.; Oyama, Y.; Yagi, T.; Yamaguchi, S. "Water Uptake and Conduction Property of Nano-Grained Yttria-Doped Zirconia Fabricated by Ultra-High Pressure Compaction at Room Temperature." *Solid State Ionics* **2012**, *207*, 21–28.

(102) Scherrer, B.; Schlupp, M. V. F.; Stender, D.; Martynczuk, J.; Grolig, J. G.; Ma, H.; Kocher, P.; Lippert, T.; Prestat, M.; Gauckler, L. J. "On Proton Conductivity in Porous and Dense Yttria Stabilized Zirconia at Low Temperature." *Adv. Funct. Mater.* **2013**, *23* (15), 1957–1964.

(103) Takamura, H.; Takahashi, N. "Electrical Conductivity of Dense Nanocrystalline Ceria under Humidified Atmosphere." *Solid State Ionics* **2010**, *181* (3–4), 100–103.

(104) Pérez-Coll, D.; Sánchez-López, E.; Mather, G. C. "Influence of Porosity on the Bulk and Grain-Boundary Electrical Properties of Gd-Doped Ceria." *Solid State Ionics* **2010**, *181* (21–22), 1033–1042.

(105) Shirpour, M.; Gregori, G.; Merkle, R.; Maier, J. "On the Proton Conductivity in Pure and Gadolinium Doped Nanocrystalline Cerium Oxide." *Phys. Chem. Chem. Phys.* **2011**, *13* (3), 937–940.

(106) Gregori, G.; Shirpour, M.; Maier, J. "Proton Conduction in Dense and Porous Nanocrystalline Ceria Thin Films." *Adv. Funct. Mater.* **2013**, *23* (47), 5861–5867.

(107) Oh, T.-S.; Boyd, D. A.; Goodwin, D. G.; Haile, S. M. "Proton Conductivity of Columnar Ceria Thin-Films Grown by Chemical Vapor Deposition." *Phys. Chem. Chem. Phys.* **2013**, *15* (7), 2466.

(108) Maglia, F.; Tredici, I. G.; Spinolo, G.; Anselmi-Tamburini, U. "Low Temperature Proton Conduction in Bulk Nanometric TiO2 Prepared by High-Pressure Field Assisted Sintering." *J. Mater. Res.* **2012**, *27* (15), 1975–1981.

(109) Tredici, I. G.; Maglia, F.; Ferrara, C.; Mustarelli, P.; Anselmi-Tamburini, U. "Mechanism of Low-Temperature Protonic Conductivity in Bulk, High-Density, Nanometric Titanium Oxide." *Adv. Funct. Mater.* **2014**, *24* (32), 5137–5146.

(110) Kim, S.; Anselmi-Tamburini, U.; Park, H. J.; Martin, M.; Munir, Z. A. "Unprecedented Room-Temperature Electrical Power Generation Using Nanoscale Fluorite-Structured Oxide Electrolytes." *Adv. Mater.* **2008**, *20* (3), 556–559.

(111) Kim, S.; Avila-Paredes, H. J.; Wang, S.; Chen, C.-T.; De Souza, R. A.; Martin, M.; Munir, Z. A. "On the Conduction Pathway for Protons in Nanocrystalline Yttria-Stabilized Zirconia." *Phys. Chem. Chem. Phys.* **2009**, *11* (17), 3035.

(112) Pietrowski, M. J.; De Souza, R. A.; Kim, S.; Munir, Z. A.; Martin, M. "Dehydration Kinetics of Nano-YSZ Ceramics Monitored by in-Situ Infrared Spectroscopy." *Solid State*

Ionics **2012**, *225*, 241–244.

(113) Jiang, J.; Hertz, J. L. "Intermediate Temperature Surface Proton Conduction on Dense YSZ Thin Films." *J. Mater. Chem. A* **2014**, *2* (45), 19550–19555.

(114) Ding, J.; Strelcov, E.; Kalinin, S. V.; Bassiri-Gharb, N. "Spatially Resolved Probing of Electrochemical Reactions via Energy Discovery Platforms." *Nano Lett.* **2015**, *15* (6), 3669–3676.

(115) Lee, S. S.; Zhu, H.; Contreras, E. Q.; Prakash, A.; Puppala, H. L.; Colvin, V. L. "High Temperature Decomposition of Cerium Precursors To Form Ceria Nanocrystal Libraries for Biological Applications." *Chem. Mater.* **2012**, *24* (3), 424–432.

(116) Dinh, C.-T.; Nguyen, T.-D.; Kleitz, F.; Do, T.-O. "Shape-Controlled Synthesis of Highly Crystalline Titania Nanocrystals." *ACS Nano* **2009**, *3* (11), 3737–3743.

(117) Garcia, G.; Buonsanti, R.; Runnerstrom, E. L.; Mendelsberg, R. J.; Llordes, A.; Anders, A.; Richardson, T. J.; Milliron, D. J. "Dynamically Modulating the Surface Plasmon Resonance of Doped Semiconductor Nanocrystals." *Nano Lett.* **2011**, *11* (10), 4415–4420.

(118) Baklanov, M. R.; Mogilnikov, K. P.; Polovinkin, V. G.; Dultsev, F. N. "Determination of Pore Size Distribution in Thin Films by Ellipsometric Porosimetry." *J. Vac. Sci. Technol. B Microelectron. Nanom. Struct.* **2000**, *18* (3), 1385.

(119) Boissiere, C.; Grosso, D.; Lepoutre, S.; Nicole, L.; Bruneau, A.B.; and; Sanchez, C., "Porosity and Mechanical Properties of Mesoporous Thin Films Assessed by Environmental Ellipsometric Porosimetry." **2005**.

(120) Dubinin, M. M. "The Potential Theory of Adsorption of Gases and Vapors for Adsorbents with Energetically Nonuniform Surfaces." *Chem. Rev.* **1960**, *60* (2), 235–241.

(121) Nguyen, C.; Do, D. "The Dubinin–Radushkevich Equation and the Underlying Microscopic Adsorption Description." *Carbon N. Y.* **2001**, *39* (9), 1327–1336.

(122) Gidley, D. W.; Peng, H.; Vallery, R.; Soles, C. L.; Lee, H.; Vogt, B. D.; Lin, E. K.; Wu, W.; Baklanov, M. R. "Porosity of Low Dielectric Constant Materials." 85–136.

(123) Tuller, H. L. "Ionic Conduction in Nanocrystalline Materials." *Solid State Ionics* **2000**, *131* (1), 143–157.

(124) Chiang, Y.-M.; Lavik, E. B.; Kosacki, I.; Tuller, H. L.; Ying, J. Y. "Defect and Transport Properties of Nanocrystalline CeO 2-X." *Cit. Appl. Phys. Lett* **1996**, *69* (185).

(125) Tschöpe, A.; Sommer, E.; Birringer, R. "Grain Size-Dependent Electrical Conductivity of Polycrystalline Cerium Oxide: I. Experiments." *Solid State Ionics* **2001**, *139* (3–4), 255–265.

(126) Suzuki, T.; Kosacki, I.; Anderson, H. U.; Colomban, P. "Electrical Conductivity and Lattice Defects in Nanocrystalline Cerium Oxide Thin Films." *J. Am. Ceram. Soc.* **2004**, *84* (9), 2007–2014.

(127) Kim, S.; Maier, J. "On the Conductivity Mechanism of Nanocrystalline Ceria." *J. Electrochem. Soc.* **2002**, *149* (10), J73–J83.

(128) Göbel, M. C.; Gregori, G.; Maier, J. "Mixed Conductivity in Nanocrystalline Highly Acceptor Doped Cerium Oxide Thin Films under Oxidizing Conditions." *Phys. Chem. Chem. Phys.* **2011**, *13* (23), 10940.

(129) Gregori, G.; Shirpour, M.; Maier, J. "Proton Conduction in Dense and Porous Nanocrystalline Ceria Thin Films." *Adv. Funct. Mater.* **2013**, *23* (47), 5861–5867.

(130) Gregori, G.; Rahmati, B.; Sigle, W.; van Aken, P. A.; Maier, J. "Electric Conduction Properties of Boron-Doped Ceria." *Solid State Ionics* **2011**, *192* (1), 65–69.

(131) Sayle, T. X. T.; Parker, S. C.; Catlow, C. R. A. "Surface Oxygen Vacancy Formation on CeO2 and Its Role in the Oxidation of Carbon Monoxide." *J. Chem. Soc. Chem. Commun.* **1992**, *0* (14), 977.

(132) Paier, J.; Penschke, C.; Sauer, J. "Oxygen Defects and Surface Chemistry of Ceria: Quantum Chemical Studies Compared to Experiment." *Chem. Rev.* **2013**, *113* (6), 3949–3985.

(133) Deshpande, S.; Patil, S.; Kuchibhatla, S. V.; Seal, S. "Size Dependency Variation in Lattice Parameter and Valency States in Nanocrystalline Cerium Oxide." *Appl. Phys. Lett.* **2005**, *87* (13), 133113.

(134) Kim, S.; Merkle, R.; Maier, J. "Oxygen Nonstoichiometry of Nanosized Ceria Powder." *Surf. Sci.* **2004**, *549* (3), 196–202.

(135) Smythe, D. J.; Brenan, J. M.; Bennett, N. R.; Regier, T.; Henderson, G. S. "Quantitative Determination of Cerium Oxidation States in Alkali-Aluminosilicate Glasses Using M4,5-Edge XANES." *J. Non. Cryst. Solids* **2013**, *378*, 258–264.

(136) Light, T. S.; Licht, S. L. "Conductivity and Resistivity of Water from the Melting to Critical Point." *Anal. Chem.* **1987**, *59* (19), 2327–2330.

(137) Watkins, M.B.; Foster, A.S.; and Shluger, A. L. "Hydrogen Cycle on CeO2 (111) Surfaces: Density Functional Theory Calculations." **2007**.

(138) Molinari, M.; Parker, S. C.; Sayle, D. C.; Islam, M. S. "Water Adsorption and Its Effect on the Stability of Low Index Stoichiometric and Reduced Surfaces of Ceria." *J. Phys. Chem. C* **2012**, *116* (12), 7073–7082.

(139) Chiodelli, G.; Maglia, F.; Anselmi-Tamburini, U.; Munir, Z. A. "Characterization of Low Temperature Protonic Conductivity in Bulk Nanocrystalline Fully Stabilized Zirconia." *Solid State Ionics* **2009**, *180* (4–5), 297–301.

(140) Matolín, V.; Matolínová, I.; Dvořák, F.; Johánek, V.; Mysliveček, J.; Prince, K. C.; Skála, T.; Stetsovych, O.; Tsud, N.; Václavů, M.; et al. "Water Interaction with CeO2(1 1 1)/Cu(1 1 1) Model Catalyst Surface." *Catal. Today* **2012**, *181* (1), 124–132.

(141) Feng, Z. A.; El Gabaly, F.; Ye, X.; Shen, Z.-X.; Chueh, W. C. "Fast Vacancy-Mediated Oxygen Ion Incorporation across the Ceria–Gas Electrochemical Interface." *Nat. Commun.* **2014**, *5*, 4374.

(142) Fronzi, M.; Piccinin, S.; Delley, B.; Traversa, E.; Stampfl, C. "Water Adsorption on the

Stoichiometric and Reduced CeO2(111) Surface: A First-Principles Investigation." *Phys. Chem. Chem. Phys.* **2009**, *11* (40), 9188–9199.

(143) Kreuer, K. D. "Proton-Conducting Oxides." *Annu. Rev. Mater. Res.* **2003**, *33* (1), 333–359.

(144) Karlsson, M. "Proton Dynamics in Oxides: Insight into the Mechanics of Proton Conduction from Quasielastic Neutron Scattering." *Phys. Chem. Chem. Phys.* **2015**, *17* (1), 26–38.

(145) Münch, W.; Kreuer, K.-D.; Seifert, G.; Maier, J. "Proton Diffusion in Perovskites: Comparison between BaCeO3, BaZrO3, SrTiO3, and CaTiO3 Using Quantum Molecular Dynamics." *Solid State Ionics* **2000**, *136–137*, 183–189.

(146) Sakai, N.; Yamaji, K.; Horita, T.; Yokokawa, H.; Hirata, Y.; Sameshima, S.; Nigara, Y.; Mizusaki, J. "Determination of Hydrogen Solubility in Oxide Ceramics by Using SIMS Analyses." *Solid State Ionics* **1999**, *125* (1–4), 325–331.

(147) Köck, E.M.; Kogler, M.; Klötzer, B.; Noisternig, M. F.; Penner, S. "Structural and Electrochemical Properties of Physisorbed and Chemisorbed Water Layers on the Ceramic Oxides Y2O3, YSZ, and ZrO2," *ACS Appl. Mater. Interfaces* **2016**, *8* (25), 16428 - 16443.

(148) Rasaiah, J. C.; Garde, S.; Hummer, G. "Water in Nonpolar Confinement: From Nanotubes to Proteins and Beyond." *Annu. Rev. Phys. Chem.* **2008**, 59, 713-740

(149) Bourg, I. C.; Steefel, C. I. "Molecular Dynamics Simulations of Water Structure and Diffusion in Silica Nanopores." *J. Phys. Chem. C* **2012**, *116* (21), 11556 - 11564.

(150) Feng, Z. A.; El Gabaly, F.; Ye, X.; Shen, Z.-X.; Chueh, W. C. "Fast Vacancy-Mediated Oxygen Ion Incorporation across the Ceria–Gas Electrochemical Interface." *Nat. Commun.* **2014**, *5*, 4374.

(151) Chueh, W. C.; McDaniel, A. H.; Grass, M. E.; Hao, Y.; Jabeen, N.; Liu, Z.; Haile, S. M.; McCarty, K. F.; Bluhm, H.; El Gabaly, F. "Highly Enhanced Concentration and Stability of Reactive Ce^{3+} on Doped CeO_2 Surface Revealed In Operando." *Chem. Mater.* **2012**, *24* (10), 1876–1882.

(152) Zurhelle, A. F.; Tong, X.; Klein, A.; Mebane, D. S.; De Souza, R. A. "A Space-Charge Treatment of the Increased Concentration of Reactive Species at the Surface of a Ceria Solid Solution." *Angew. Chemie Int. Ed.* **2017**, *56* (46), 14516 - 14520.

(153) Shao, Y.; Yin, G.; Wang, Z.; Gao, Y. "Proton Exchange Membrane Fuel Cell from Low Temperature to High Temperature: Material Challenges." *J. Power Sources* **2007**, *167* (2), 235–242.

(154) Li, Q.; He, R.; Jensen, J. O.; Bjerrum, N. J. "Approaches and Recent Development of Polymer Electrolyte Membranes for Fuel Cells Operating above 100 °C." *Chem. Mater.* **2003**, *15* (26), 4896–4915.

(155) Malavasi, L.; Fisher, C. A. J.; Islam, M. S. "Oxide-Ion and Proton Conducting Electrolyte Materials for Clean Energy Applications: Structural and Mechanistic Features." *Chem. Soc. Rev.* **2010**, *39* (11), 4370.

(156) Merle, R.B.; Chisholm, C.R.I.; Boysen, D.A.; and ; Haile, S. M. "Instability of Sulfate and Selenate Solid Acids in Fuel Cell Environments." *Energy Fuels,* **2002**, 17(1), 210-215.

(157) Yoon, M.; Suh, K.; Natarajan, S.; Kim, K. "Proton Conduction in Metal-Organic Frameworks and Related Modularly Built Porous Solids." *Angew. Chemie Int. Ed.* **2013**, *52* (10), 2688–2700.

(158) Shirpour, M.; Gregori, G.; Merkle, R.; Maier, J. "On the Proton Conductivity in Pure and Gadolinium Doped Nanocrystalline Cerium Oxide." *Phys. Chem. Chem. Phys.* **2011**, *13* (3), 937–940.

(159) Deng, W.; Flytzani-Stephanopoulos, M. "On the Issue of the Deactivation of Au–Ceria and Pt–Ceria Water–Gas Shift Catalysts in Practical Fuel-Cell Applications." *Angew. Chemie Int. Ed.* **2006**, *45*, 2285-2289.

(160) Fu, Q.; Deng, W.; Saltsburg, H.; Flytzani-Stephanopoulos, M. "Activity and Stability of Low-Content Gold–Cerium Oxide Catalysts for the Water–Gas Shift Reaction." *Appl. Catal. B Environ.* **2005**, *56* (1), 57–68.

(161) Viricelle, J.P.; Pijolat, M.; Soustelle, M.; Zing, C. "Transformation of Cerium(III) Hydroxycarbonate into Ceria. Part 1.—Nucleation and Growth Rates of Ceria." *J. Chem. Soc., Faraday Trans.* **1995**, *91* (24), 4431–4435.

(162) Wang, H.C.; Lu, C.-H. "Synthesis of Cerium Hydroxycarbonate Powders via a Hydrothermal Technique." *Mater. Res. Bull.* **2002**, *37* (4), 783–792.

(163) Alvero, R.; Odriozola, J. A.; Trillo, J. M.; Bernal, S. "Lanthanide Oxides: Preparation and Ageing." *J. Chem. Soc. Dalt. Trans.* **1984**, *0* (1), 87.

(164) Bernal, S.; Blanco, G.; Calvino, J. J.; Omil, J. A. P.; Pintado, J. M. "Some Major Aspects of the Chemical Behavior of Rare Earth Oxides: An Overview." *J. Alloys Compd.* **2006**, *408–412*, 496–502.

(165) Bernal, S.; Blanco, G.; Gatica, J. M.; Pérez-Omil, J. A.; Pintado, J. M.; Vidal, H. "Chemical Reactivity of Binary Rare Earth Oxides." In *Binary Rare Earth Oxides*; Kluwer Academic Publishers: Dordrecht; pp 9–55.

(166) Collins, S.; Finos, G.; Alcántara, R.; Del Rio, E.; Bernal, S.; Bonivardi, A. "Effect of Gallia Doping on the Acid-Base and Redox Properties of Ceria." *Appl. Catal. A Gen.* **2010**, *388* (1–2), 202–210.

(167) Finos, G.; Collins, S.; Blanco, G.; del Rio, E.; C?es, J. M.; Bernal, S.; Bonivardi, A. "Infrared Spectroscopic Study of Carbon Dioxide Adsorption on the Surface of Cerium?Gallium Mixed Oxides." *Catal. Today* **2012**, *180* (1), 9–18.

(168) Finos, G.; Collins, S.; Blanco, G.; del Rio, E.; Cíes, J. M.; Bernal, S.; Bonivardi, A. "Infrared Spectroscopic Study of Carbon Dioxide Adsorption on the Surface of Cerium–Gallium Mixed Oxides." *Catal. Today* **2012**, *180* (1), 9–18.

(169) Vecchietti, J.; Collins, S.; Xu, W.; Barrio, L.; Stacchiola, D.; Calatayud, M.; Tielens, F.; Joseelgado, J.; Bonivardi, A. "Surface Reduction Mechanism of Cerium−Gallium Mixed Oxides with Enhanced Redox Properties." *J. Phys. Chem. C* **2013**, 117 (17), 8822-8831.

(170) Daly, C. A.; Streacker, L. M.; Sun, Y.; Pattenaude, S. R.; Hassanali, A. A.; Petersen, P. B.; Corcelli, S. A.; Ben-Amotz, D. "Decomposition of the Experimental Raman and Infrared Spectra of Acidic Water into Proton, Special Pair, and Counterion Contributions." *J. Phys. Chem. Lett.* **2017**, *8* (21), 5246–5252.

(171) Mebane, D. S.; De Souza, R. A. "A Generalised Space-Charge Theory for Extended Defects in Oxygen-Ion Conducting Electrolytes: From Dilute to Concentrated Solid Solutions." *Energy Environ. Sci.* **2015**, *8* (10), 2935–2940.

(172) Wang, D.; Kang, Y.; Doan-Nguyen, V.; Chen, J.; Küngas, R.; Wieder, N. L.; Bakhmutsky, K.; Gorte, R. J.; Murray, C. B. "Synthesis and Oxygen Storage Capacity of Two-Dimensional Ceria Nanocrystals." *Angew. Chemie Int. Ed.* **2011**, *50* (19), 4378–4381.

(173) Wang, D.; Kang, Y.; Ye, X.; Murray, C. B. "Mineralizer-Assisted Shape-Control of Rare Earth Oxide Nanoplates." *Chem. Mater.* **2014**, *26* (22), 6328–6332.

(174) Mai, H.X.; Sun, L.D.; Zhang, Y.W.; Si, R.; Feng, W.; Zhang, H.P.; Liu, H.C.; Yan, C.H. "Shape-Selective Synthesis and Oxygen Storage Behavior of Ceria Nanopolyhedra, Nanorods, and Nanocubes."

(175) Si, R.; Flytzani-Stephanopoulos, M. "Shape and Crystal-Plane Effects of Nanoscale Ceria on the Activity of Au-CeO2 Catalysts for the Water–Gas Shift Reaction." *Angew. Chemie* **2008**, *120* (15), 2926–2929.

(176) Wood, G. O. "Affinity Coefficients of the Polanyi/Dubinin Adsorption Isotherm Equations." *Carbon N. Y.* **2001**, *39* (3), 343–356.

(177) Ambrożek, B.; Zwarycz-Makles, K.; Szaflik, W. "Equilibrium and Heat of Adsorption for Selected Adsorbent-Adsorbate Pairs Used in Adsoprtion Heat Pumps." *polska energyetyka sloneczna,* **2012**.

(178) Vayssilov, G. N.; Mihaylov, M.; Petkov, P. St.; Hadjiivanov, K. I.; Neyman, K. M. "Reassignment of the Vibrational Spectra of Carbonates, Formates, and Related Surface Species on Ceria: A Combined Density Functional and Infrared Spectroscopy Investigation." *J. Phys. Chem. C* **2011**, *115* (47), 23435–23454.

(179) Nanayakkara, C. E.; Dillon, J. K.; Grassian, V. H. "Surface Adsorption and Photochemistry of Gas-Phase Formic Acid on TiO_2 Nanoparticles: The Role of Adsorbed Water in Surface Coordination, Adsorption Kinetics, and Rate of Photoproduct Formation." *J. Phys. Chem. C* **2014**, *118* (44), 25487–25495.

(180) Mino, L.; Spoto, G.; Ferrari, A. M. "CO_2 Capture by TiO_2 Anatase Surfaces: A Combined DFT and FTIR Study." *J. Phys. Chem. C* **2014**, *118* (43), 25016–25026.

(181) Su, W.; Zhang, J.; Feng, Z.; Chen, T.; Ying, P.; Li, C. "Surface Phases of TiO_2 Nanoparticles Studied by UV Raman Spectroscopy and FT-IR Spectroscopy." *J. Phys. Chem. C* **2008**, *112* (20), 7710–7716.

(182) Chen, S.; Cao, T.; Gao, Y.; Li, D.; Xiong, F.; Huang, W. "Probing Surface Structures of CeO_2 , TiO_2 , and Cu_2O Nanocrystals with CO and CO_2 Chemisorption." *J. Phys. Chem. C* **2016**, *120* (38), 21472–21485.

(183) Merli, *L.* "Thermochemistry of Selected Lanthanide and Actinide Hydroxycarbonates and Carbonates." *Radiochimica Acta* **1996**, *74, 37-43.*

Appendix A

Supporting information to Chapter 2

A.1 Experimental supporting information

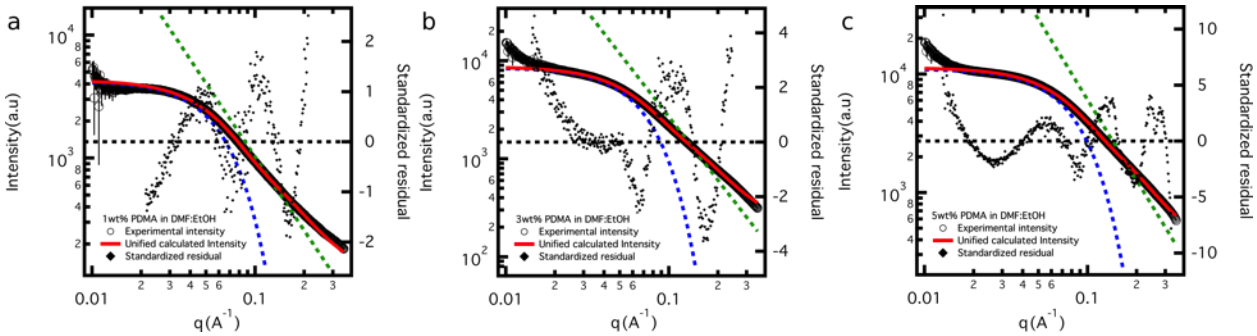

Figure A.1: Guinier and Porod fitting of free 10,000 poly(N,N-dimethylacrylamide) chains in DMF:EtOH 20:80 v/v at three polymer concentrations of 1, 3 and 5 wt.%.

Table A.1: Tabulation of R_g, P, and R_o for the fitting performed in Figure A.1. R_o was approximated assuming the freely jointed chain model with $\boldsymbol{R_o = \sqrt{6} R_g}$. The value for 1 wt% PDMA was used as a reference point because that polymer concentration is closest to the actual solution concentration used for micelle assembly.

	1wt% PDMA	3wt% PDMA	5wt% PDMA
R_g (A)	27.97	25.76	20.70
P	1.99	2.15	2.26
R_0(A)	68.51	63.10	50.70

Table A.2: Compilation of the raw PS-PDMA and iron oxide weights in solution and their conversion to the reported nanocrystal weight and volume fractions reported in the main text. Conversion from nanocrystal and polymer weight fractions to volume fractions was done assuming a bulk density of PS-PDMA of 1.1g/cm^3 and an average bulk density of 5.07g/cm^3 for iron oxide. An average density was used because the iron oxide nanocrystal synthesized are known to be a mixed phase material of Fe_2O_3 and Fe_3O_4.

PS-PDMA (mg)	Iron oxide (mg)	Nanocrystal weight fraction	Nanocrystal volume fraction
1	0.5	0.33	0.10

1	1.5	0.60	0.25
1	3	0.75	0.39
1	4	0.80	0.46

Table A.3: Compilation of the nanocrystal sizes obtained from fitting the nanocrystal form factor assuming a Gaussian size distribution. Fitting was done by varying three parameters of nanocrystal size, dispersity and sphere aspect ratio. The leftmost column is the abbreviated nanocrystal sized referenced in the main text while the second column contains the corresponding true nanocrystal sizes.

Nanocrystal size label (diameter) (nm)	Nanocrystal size (SAXS) (nm)	Nanocrystal size dispersity Gaussian Distribution Standard Deviation (SAXS) (nm)	Nanocrystal shape dispersity (SAXS)
3	3.41	0.42	1.7
4	4.49	0.56	1.54
5	4.60	0.25	1
7	7.14	0.65	1
8	7.76	0.46	1
9	9.15	0.68	1
12	11.71	0.66	1
14	14.28	0.82	1
16	15.85	0.72	1

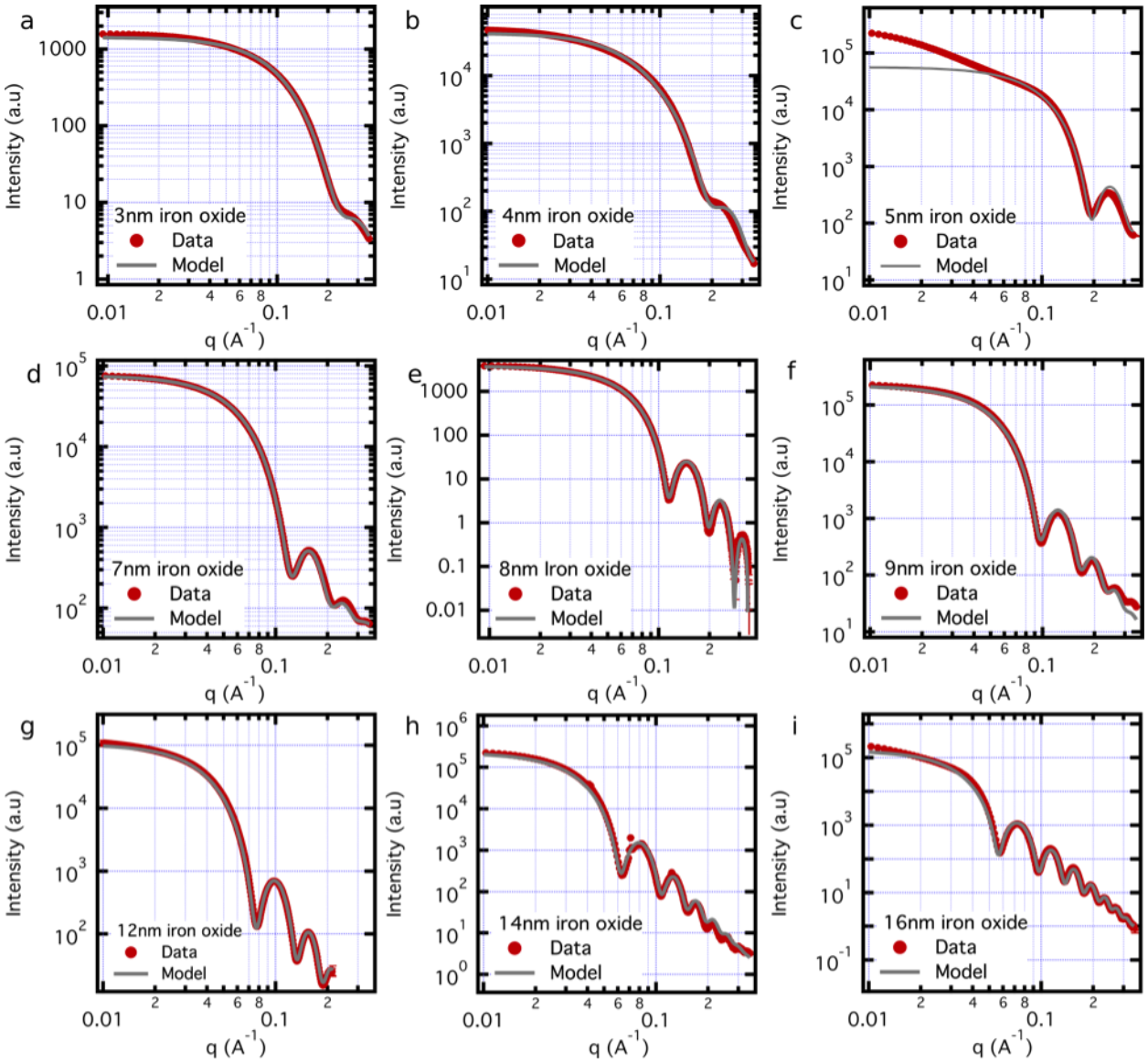

Figure A.2: Fitted nanocrystal form factors used to determine nanocrystal size, dispersity and circularity. For the 5nm spectra, light flocculation was observed which explains the low q deviation from the fitted model. Thus, specifically for that sample, fitting was performed using only high q data points from the form factor shoulder onward. The 12nm dataset was collected at a different detector distance so the data does not expand as far into the high q range, but the data is plotted with the same range as the other plots for ease of inspection.

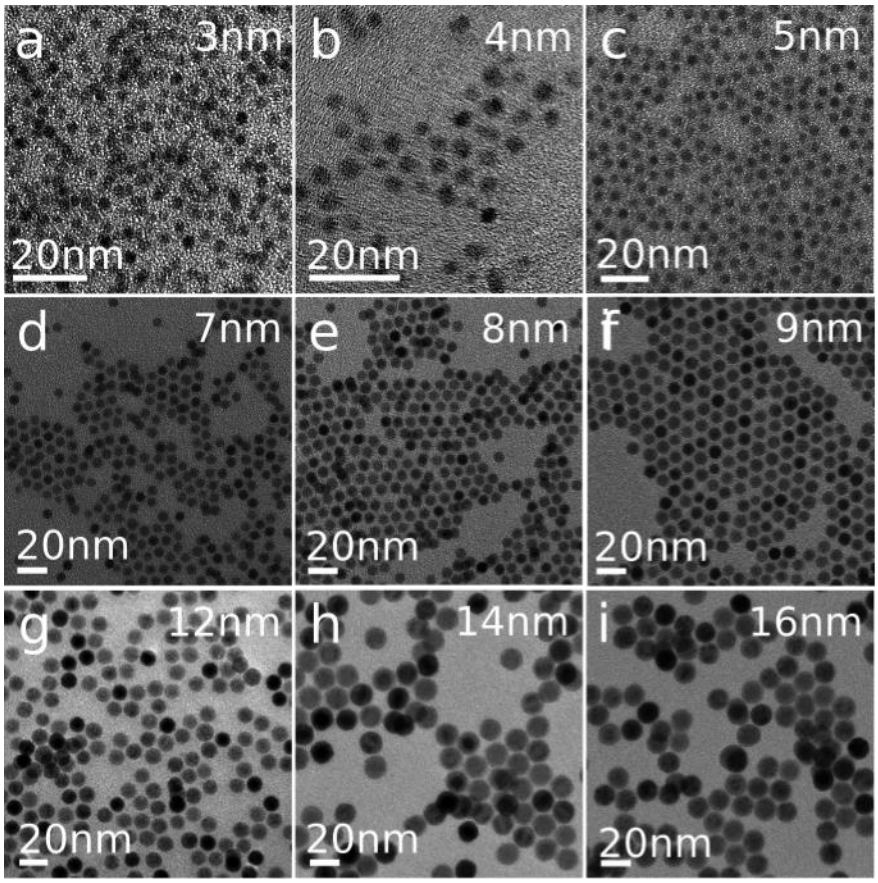

Figure A.3: TEM images of nanocrystal dispersions drop casted on ultrathin carbon TEM grids from toluene.

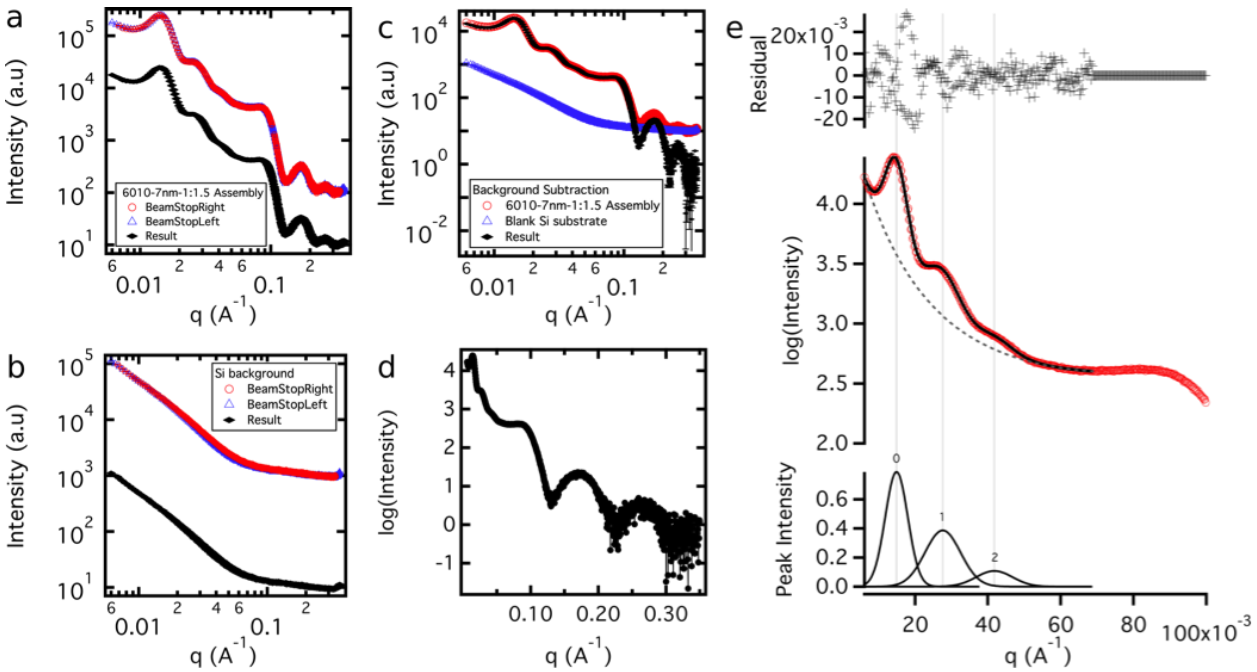

Figure A.4: Data treatment procedures to obtain peak heights of the low q peaks for peak height ratio analysis demonstrated using the 7nm 1:1.5 loading assembled dataset. Two halves of the area detector 1-D line-cut on each side of the beam stop is normalized by collection time and merged to remove gaps in the data for both the assembled film (a) and a blank Si substrate (b). (c) The intensity of the blank substrate is subtracted from the sample data. (d) The y-axis data is converted to log(intensity) and the data is redisplayed on linear scales. (e) Fitting was done using a log-cubic background and Gaussian peaks in the IgorPro multipeak-fitting module: red is the experimental data and black is the resultant fit. Peak height ratios are taken as the height of the first peak divided by the height of the zeroth peak.

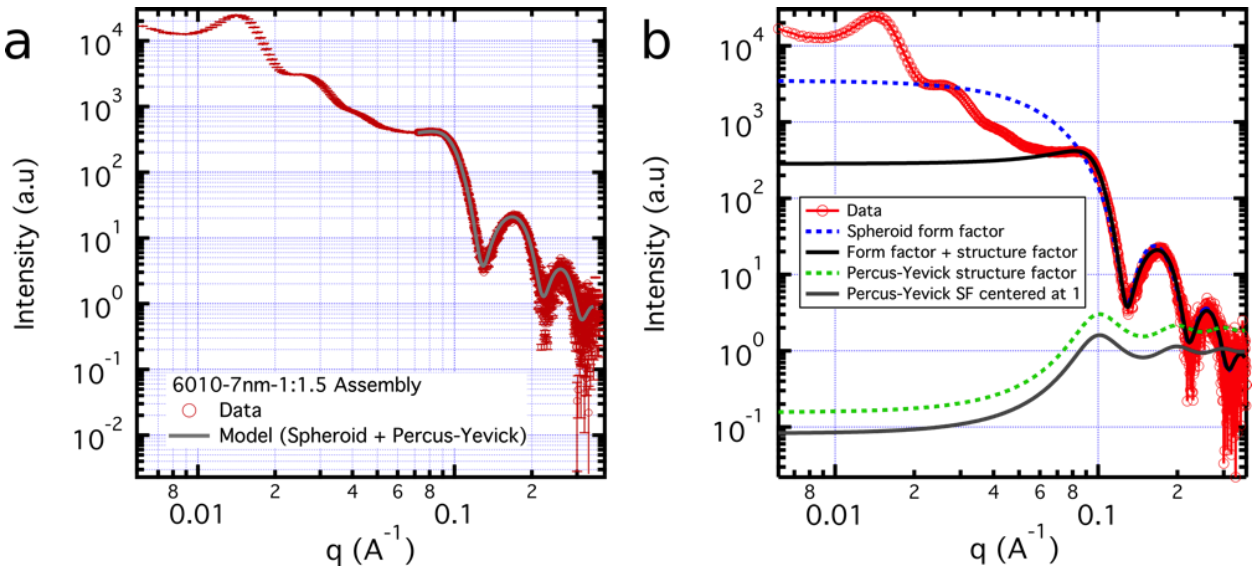

Figure A.5: a) Fitting of the higher q region of the data with a combination of a spheroid and Percus-Yevick structure factor. (b) The separate form factor and structure factor contributions to the model are

shown in blue and green while the data and corresponding fit is shown in red and black respectively. The structure factors presented in the main text were set to be centered around S(q)=1 under the assumption that the structure factor should converge to S(q)=1 for high q values.

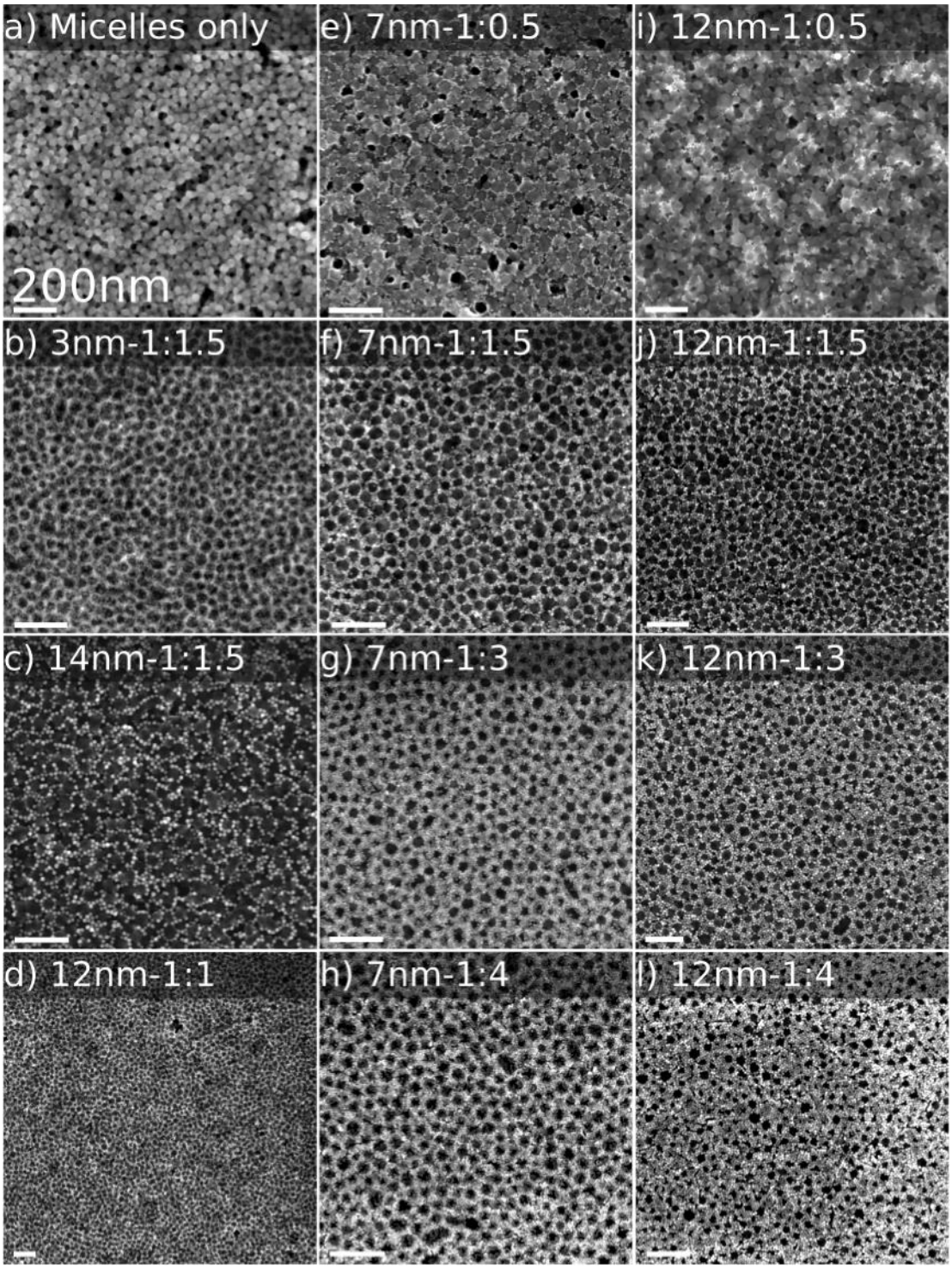

Figure A.6: SEM images of block copolymer micelle-nanocrystal assemblies at different nanocrystal size and nanocrystal loading. Image (d) is a larger area image of the same sample from which Fig 4 (a) was taken. All scale bars correspond to 200nm.

Appendix B

Supporting information to Chapter 3

B.1 Experimental supporting information

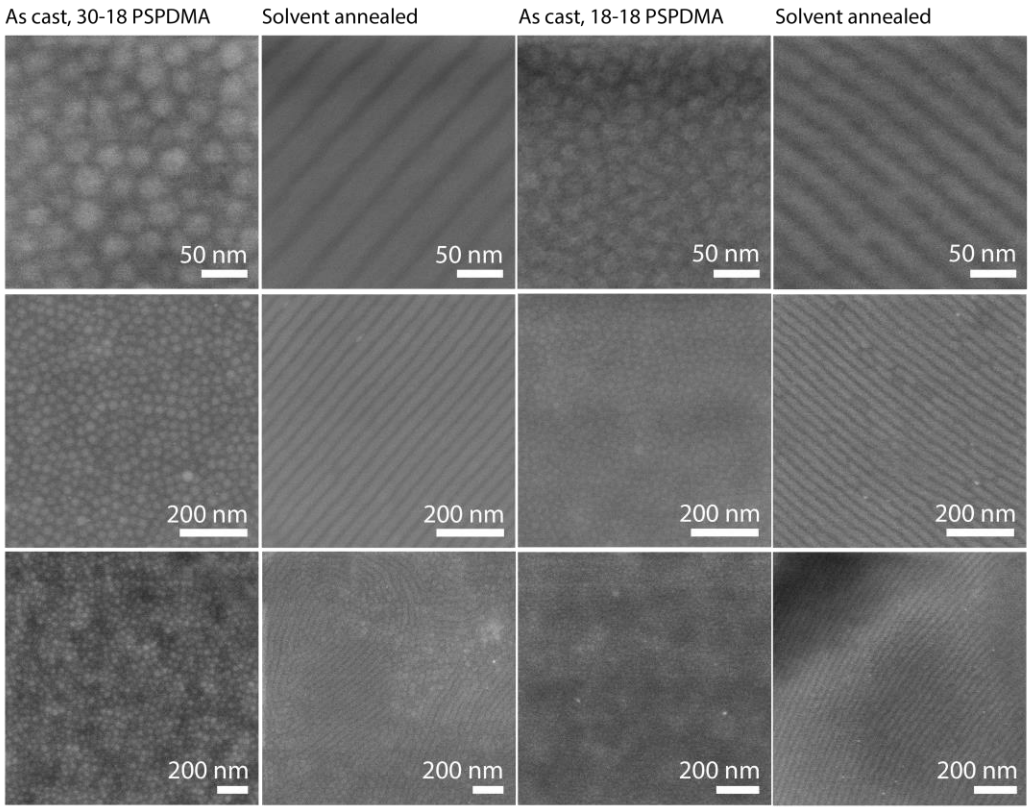

Figure B.1: Scanning electron microscopy images of 30k-18k PS-PDMA and 18k-18k PS-PDMA as cast and after solvent annealing at three magnifications.

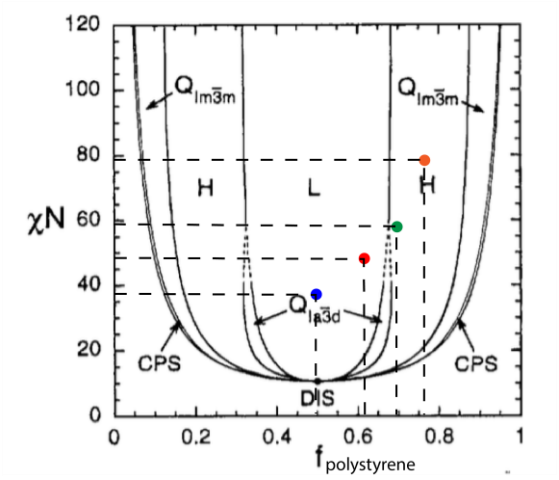

Figure B.2: Location of 18k – 18k Da PS-PDMA (blue), 30k – 18k PS-PDMA (red), 40k – 18k PS-PDMA (green), and 60k – 18k PS-PDMA (orange) on an idealized block copolymer phase diagram. Figure adapted from Matsen and Bates, *Macromolecules*, (1996), 29. Assuming that DMF preferentially swells PDMA relative to PS therefore reducing the effective volume fraction of PS in the system, we would expect a leftward shift in the phase diagram.

$$\chi = \frac{V_o}{RT}(\delta_{PS} - \delta_{PDMA})^2$$

Since we were not able to find a tabulated value for the solubility parameter for PDMA, we used the solubility parameter of DMF as an approximation arguing that since PDMA and DMF are structurally similar, the solubility parameter would also be similar. This is seen for instance in the case of benzene and polystyrene.

Table B.1: Values used to approximate χ *and* χN referred to in the main text

	δ ($MPa^{1/2}$)	V_o (cm^3)
PS	18.7	100
PDMA	-	105.8
Benzene	18.7	-
DMF	24.7	-
	Average:	102.9

MW (PS) (g/mol)	MW (PDMA) (g/mol)	χ
104.1	99	0.104

PS	PDMA	N (PS)	N(PDMA)	N total	χN	f (PS)
18000	18000	172.91	181.82	355	36.9	0.49
30000	18000	288.18	181.82	470	48.9	0.61
40000	18000	384.25	181.82	566	58.9	0.68
60000	18000	576.37	181.82	758	78.9	0.76

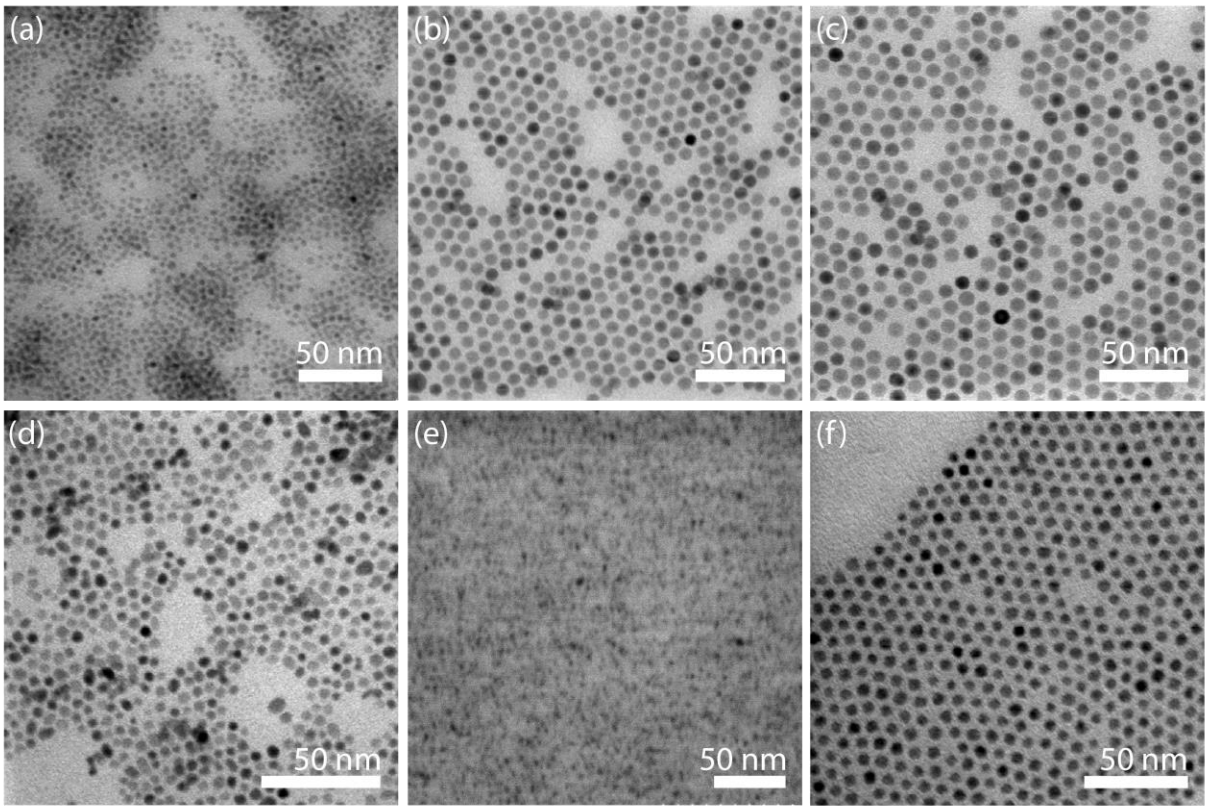

Figure B.3: Scanning transmission electron microscopy images of (a) 3 nm iron oxide, (b) 7 nm iron oxide, (c) 10 nm iron oxide, (d) 4 nm cerium oxide, (e) 2 nm Au, and (f) 5 nm CdSe-ZnS

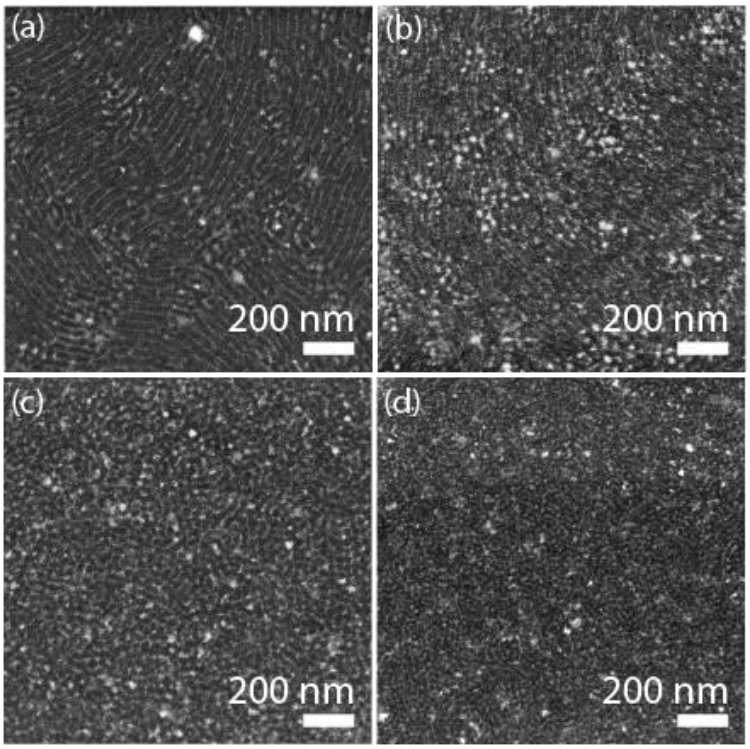

Figure B.4: (a) Solvent annealed 18k – 18k Da PS-PDMA with 5 vol% CeO_2, (b,c) after one day and one week of stirring prior to film casting and solvent annealing, and (d) with the standard solution procedure, but with the film heated to 120 °C to evaporate DMF prior to solvent annealing.

Appendix C

Supporting information to Chapter 5

C.1 Experimental supporting information

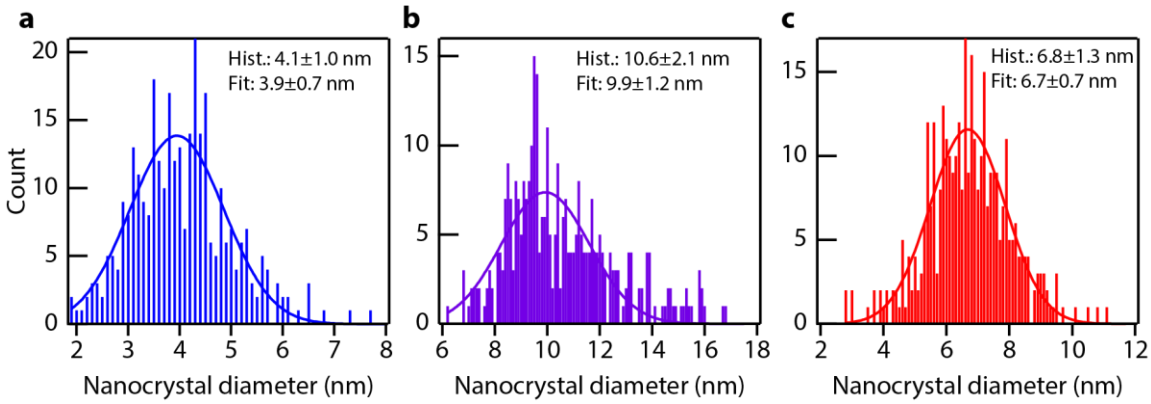

Figure C.1: Size distribution histograms for the nanocrystals used in this study. The average size and standard deviation is listed in each panel for both the histogram and the Gaussian fit to the histogram. a) 3.9 nm CeO_2. b) 9.9 nm CeO_2. c) 6.7 nm TiO_2.

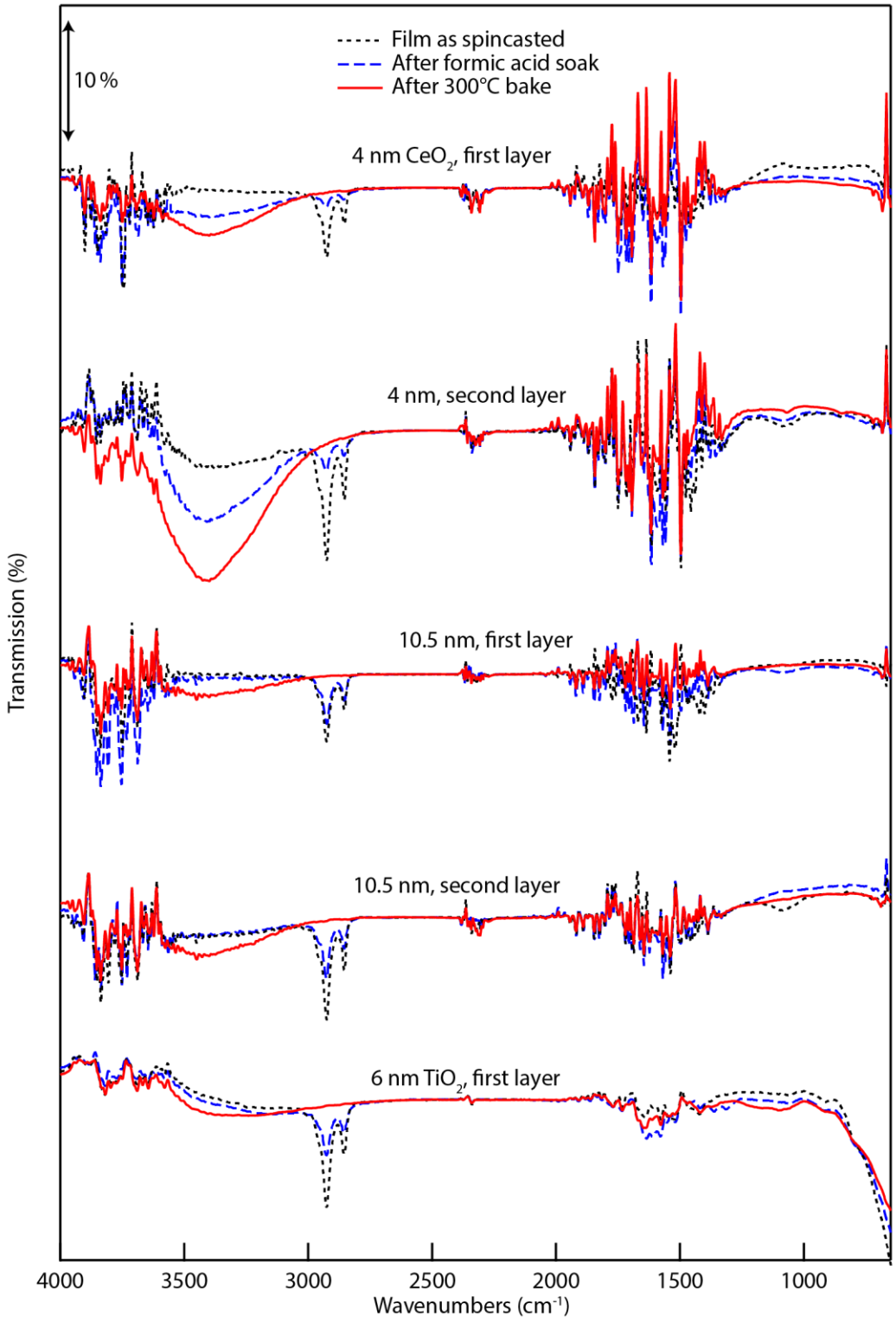

Figure C.2: FTIR spectra over the full spectral range tracking the ligand exchange and removal process for nanocrystal films on undoped silicon.

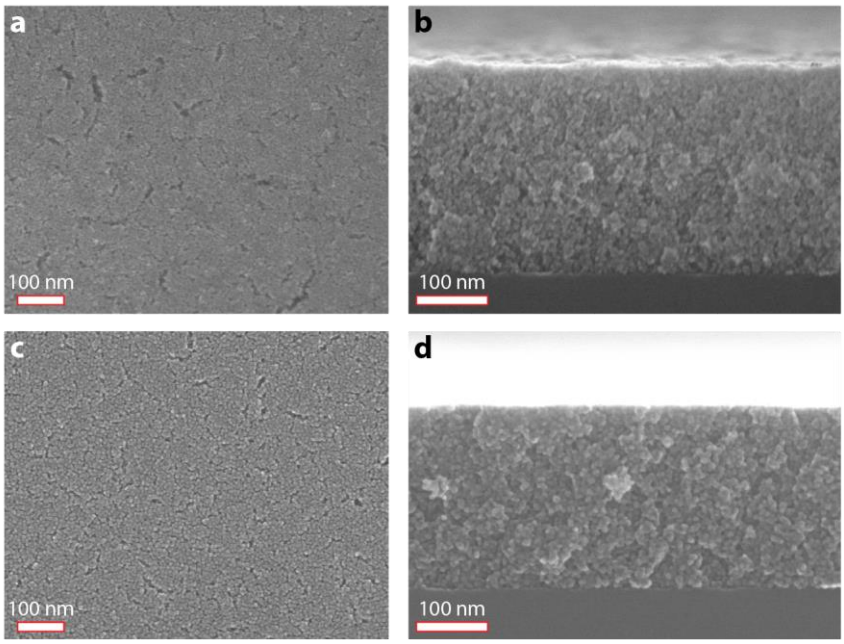

Figure C.3: Representative SEM images of nanocrystal films. a) Top-down micrograph of a film made from 3.9 nm CeO_2 nanocrystals. b) Cross-section of same film. c) Top-down micrograph of a film made from 6.7 nm TiO_2 nanocrystals. d) Cross-section of same film.

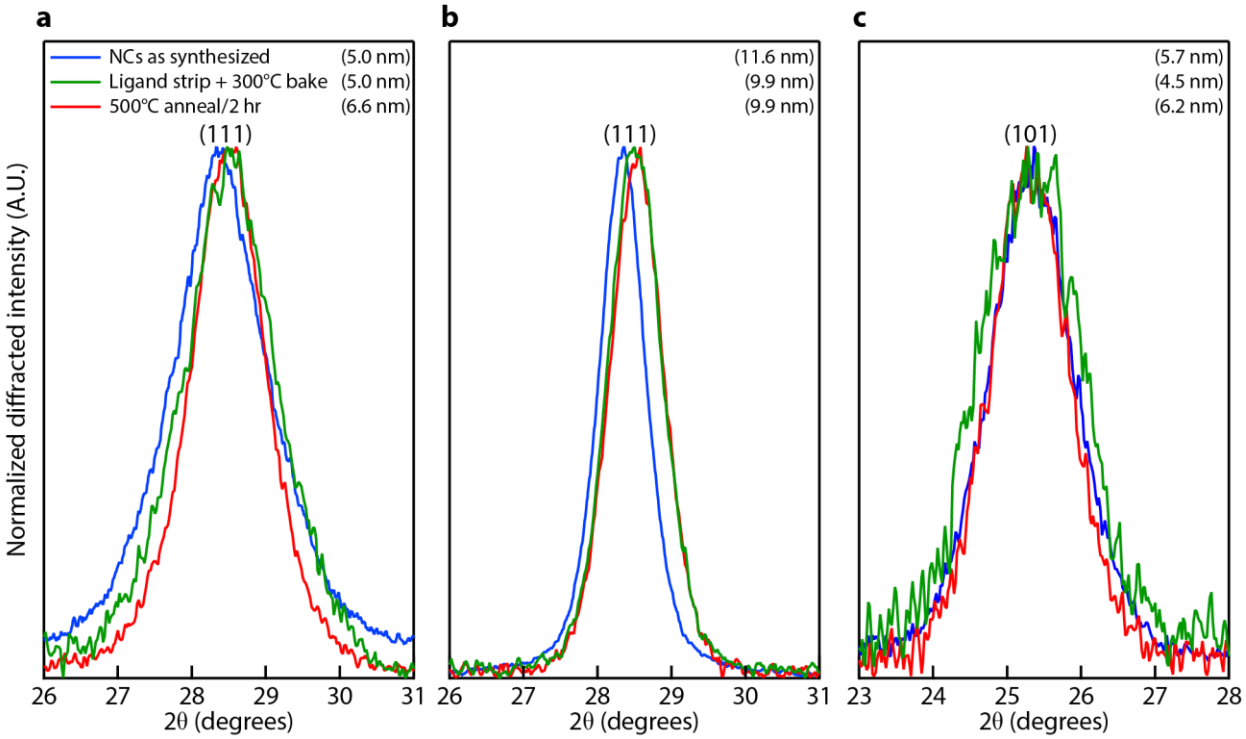

Figure C.4: Thin-film XRD patterns (θ-2θ scans) of nanocrystal films after annealing at 500°C for two hours under Ar. Scherrer grain size analysis was performed on the main diffraction peak (listed above the peak). The calculated grain size is listed in the upper right corner of each panel. a) 3.9 nm CeO_2. b) 9.9 nm CeO_2. c) 6.7 nm TiO_2.

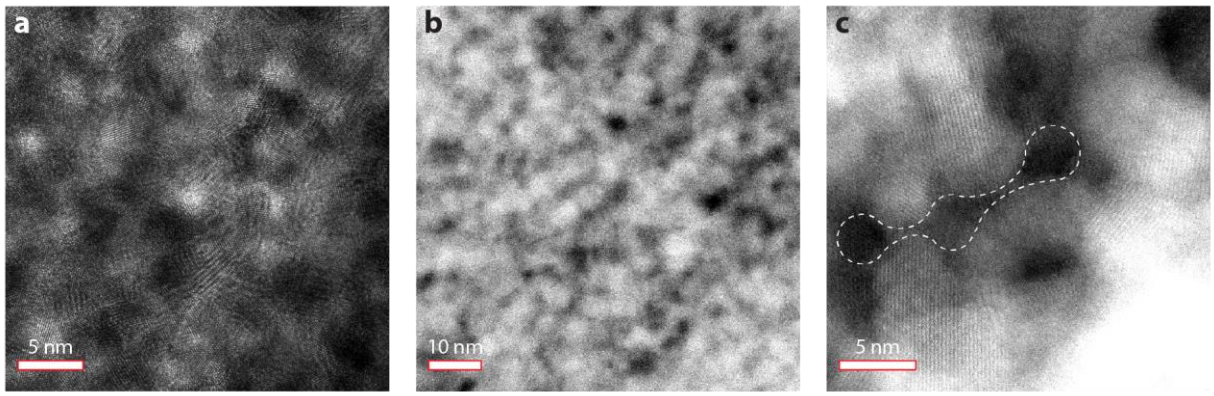

Figure C.5: a) Cross-sectional TEM micrograph of a 9.9 nm CeO_2 nanocrystal film, showing residual open porosity. b-c) Cross-sectional STEM micrographs of a 9.9 nm CeO_2 nanocrystal film, showing ink bottle geometry of the open porosity (example ink bottle geometry outlined in part c).

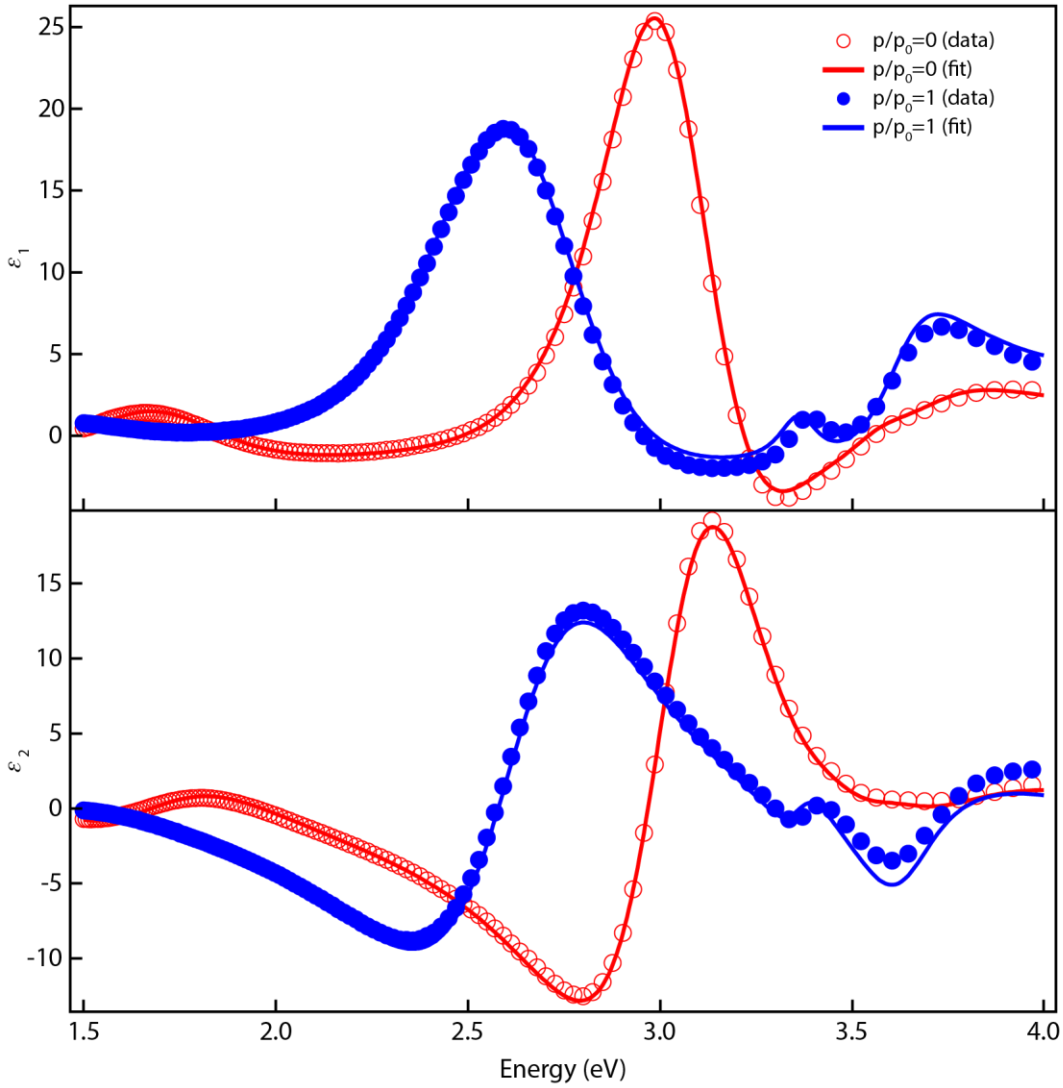

Figure C.6: Example ellipsometric porosimetry of a film of 9.9 nm CeO_2 nanocrystals. The ellipsometry data and the corresponding fits using the Semilab SEA software are displayed in terms of the real (ε_1, top panel) and imaginary (ε_2, bottom panel) dielectric functions of the material. Data and fits are shown for the two extremes in partial pressure of the toluene adsorbent: zero partial pressure (red), and saturation (blue).

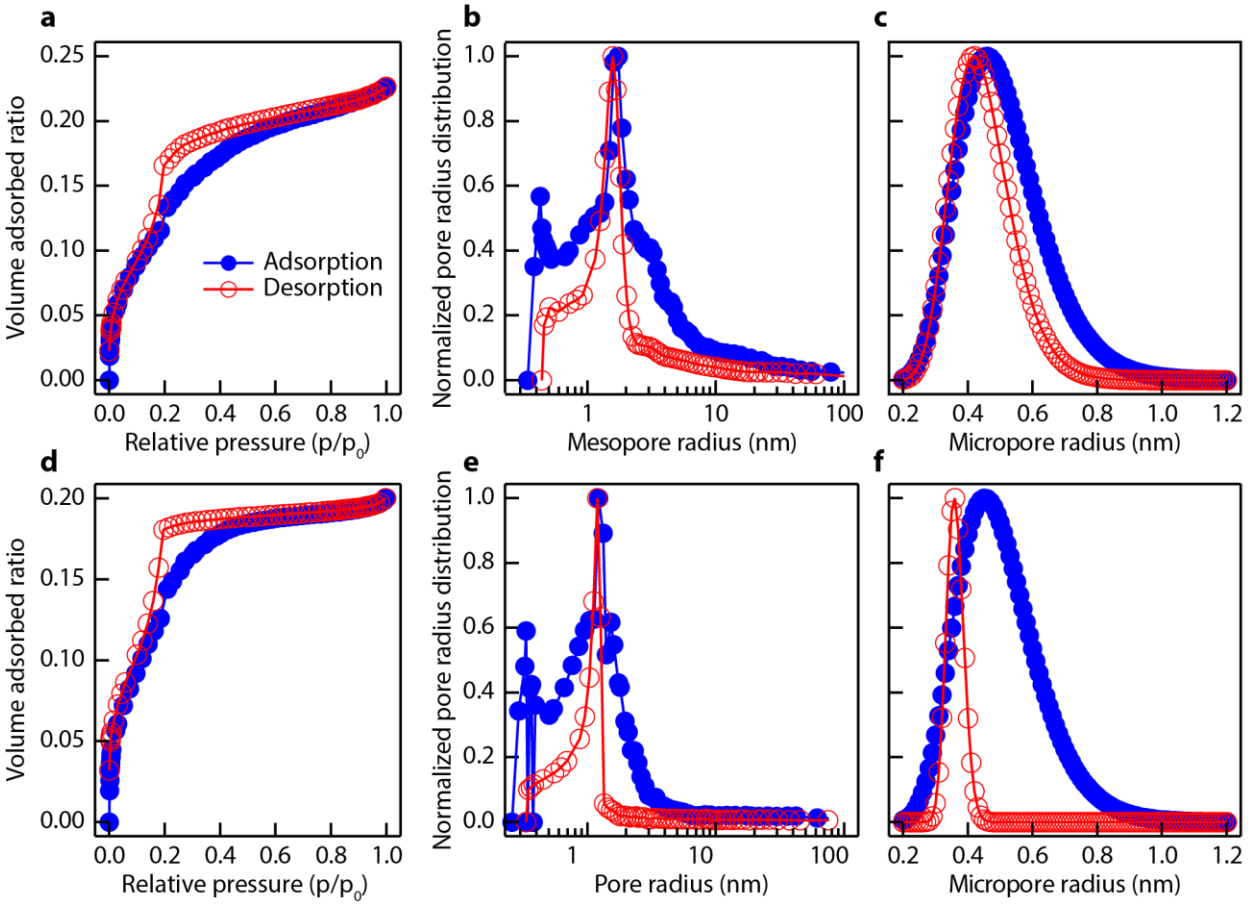

Figure C.7: Ellipsometric porosimetry data for nanocrystal films. a) Volume adsorption and desorption isotherm (for toluene) of a film made from 3.9 nm CeO_2 nanocrystals. b) Normalized mesopore radius distribution for the same film derived from EP. c) Derived micropore radius distribution for the same film. d) Volume adsorption and desorption isotherm of a film made from 6.7 nm TiO_2 nanocrystals. e) Normalized mesopore radius distribution for the same film. f) Derived micropore radius distribution for the same film.

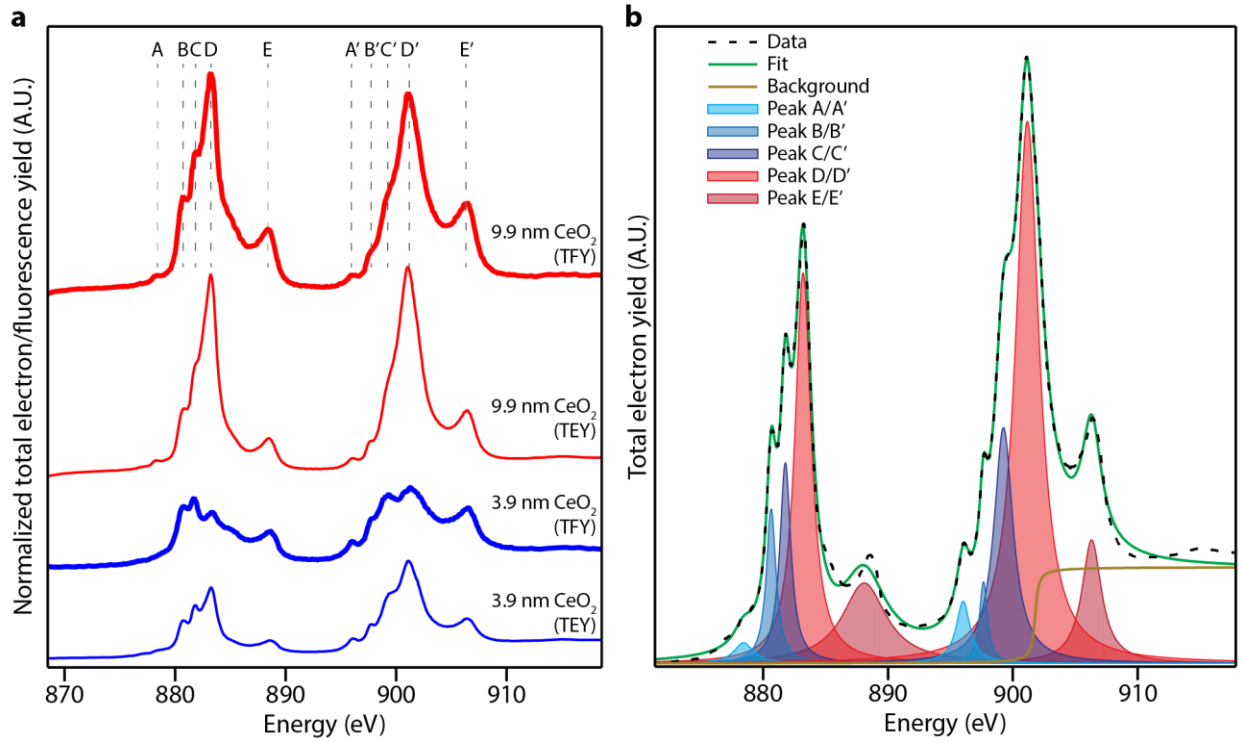

Figure C.8: X-ray absorption spectroscopy (XAS) of 3.9 nm and 9.9 nm CeO_2 nanocrystals at the Ce M4,5-edge. a) Normalized total electron yield (TEY) and total fluorescence yield (TFY) XAS spectra. The ten total M5 (A-E) and M4 (A'-E') peaks are annotated; peaks A/A', B/B', and C/C' are associated with Ce^{3+}, while peaks D/D' and E/E' are associated with Ce^{4+}. b) Example peak deconvolution for the TEY spectrum of 3.9 nm CeO_2 nanocrystals.

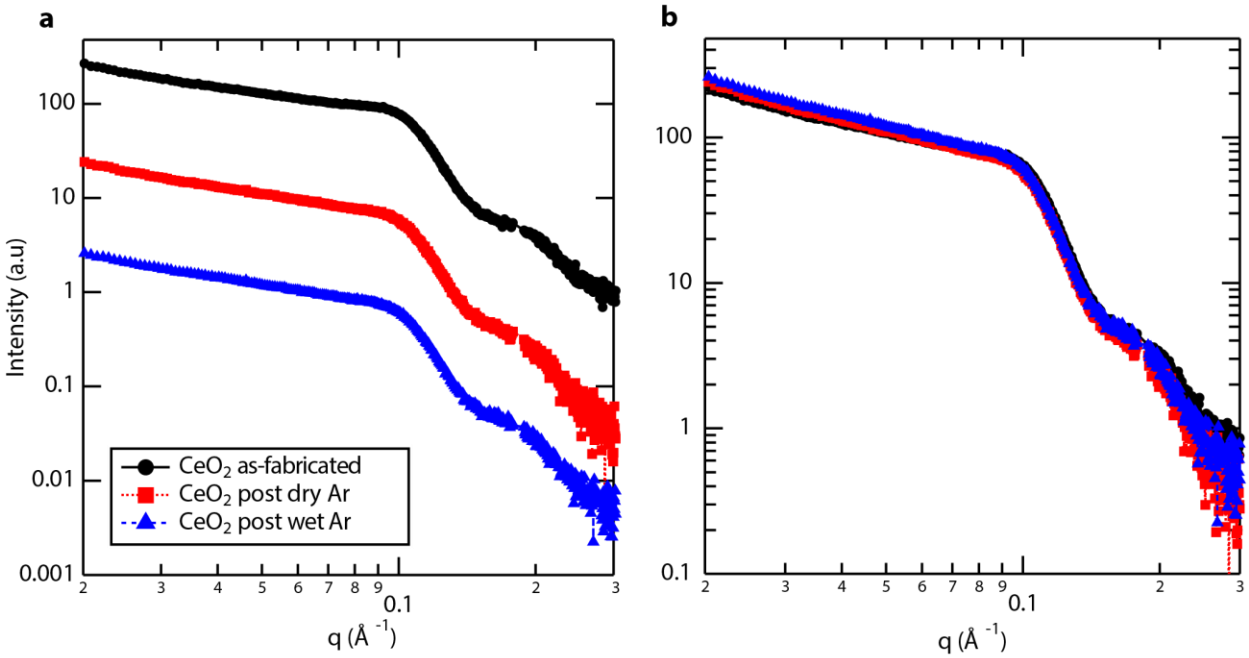

Figure C.9: Grazing incidence small angle X-ray scattering (GISAXS) patterns of a thin film made from 3.9 nm CeO_2 nanocrystals. a) GISAXS patterns from the thin film as-fabricated (top line), after

conductivity measurements in dry Ar (middle line), and after conductivity measurements in wet Ar (bottom line). b) Same GISAXS patterns overlaid. The nearly identical GISAXS patterns indicate no changes in nanocrystal size, porosity, or film microstructure during measurement.

The Dubinin-Radushkevich equation[120,121,176] describes the filling of micropores with solvent vapor and is written as:

$$\frac{V}{V_0} = \exp\left[-\left(\frac{1}{\beta E_0} RT \ln\left(\frac{p}{p_{\text{sat}}}\right)\right)^n\right]$$

where $\frac{V}{V_0}$ is the pore filling fraction, β is the affinity coefficient, E_0 is the reference adsorption energy, R is the gas constant, T is the temperature, p is the solvent vapor pressure, p_{sat} is the saturate solvent vapor pressure, and n is the exponent from the generalized Dubinin-Ashtakov isotherm ($n = 2$ in the Dubinin-Radushkevich equation). The Dubinin-Radushkevich equation was originally developed to describe solvent vapor adsorption into microporous carbons more accurately than the Kelvin equation, and equates adsorption potential ($A = RT \ln\left(\frac{p}{p_{\text{sat}}}\right)$) to the work required to bring a molecule from the gas phase to the pore surface.

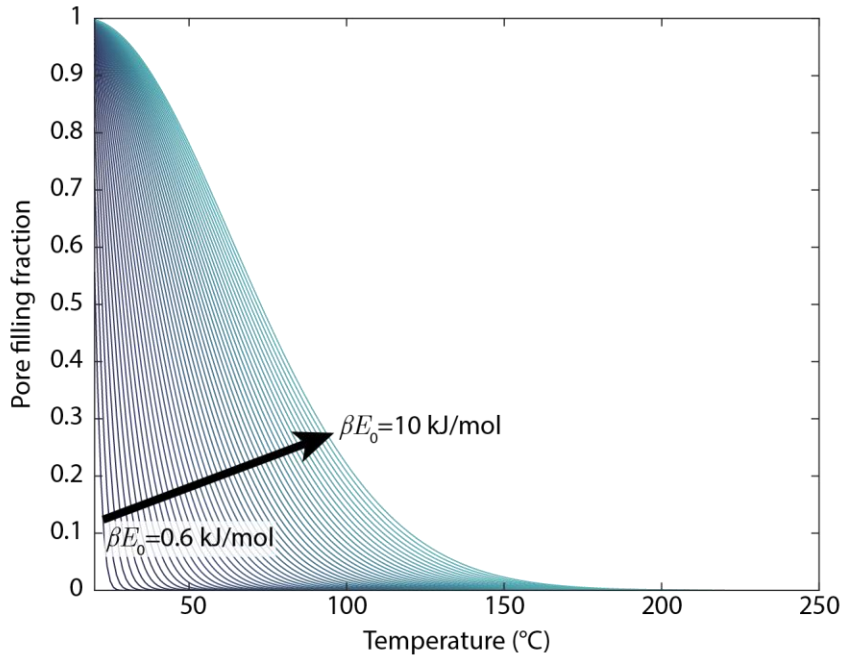

Figure C.10: Solution to the Dubinin-Radushkevich equation plotted for a range of values of absorption energy βE_0 (0.6 kJ/mol to 10 kJ/mol, in increments of 0.2 kJ/mol) between water and the ceria pore surface. This range was chosen as the water-ceria absorption energy likely falls within these two extremes—0.8 kJ is a low absorption energy, comparable to water-alumina[177], and 10 kJ is a high absorption energy, comparable to water-oxidized activated carbon[176].

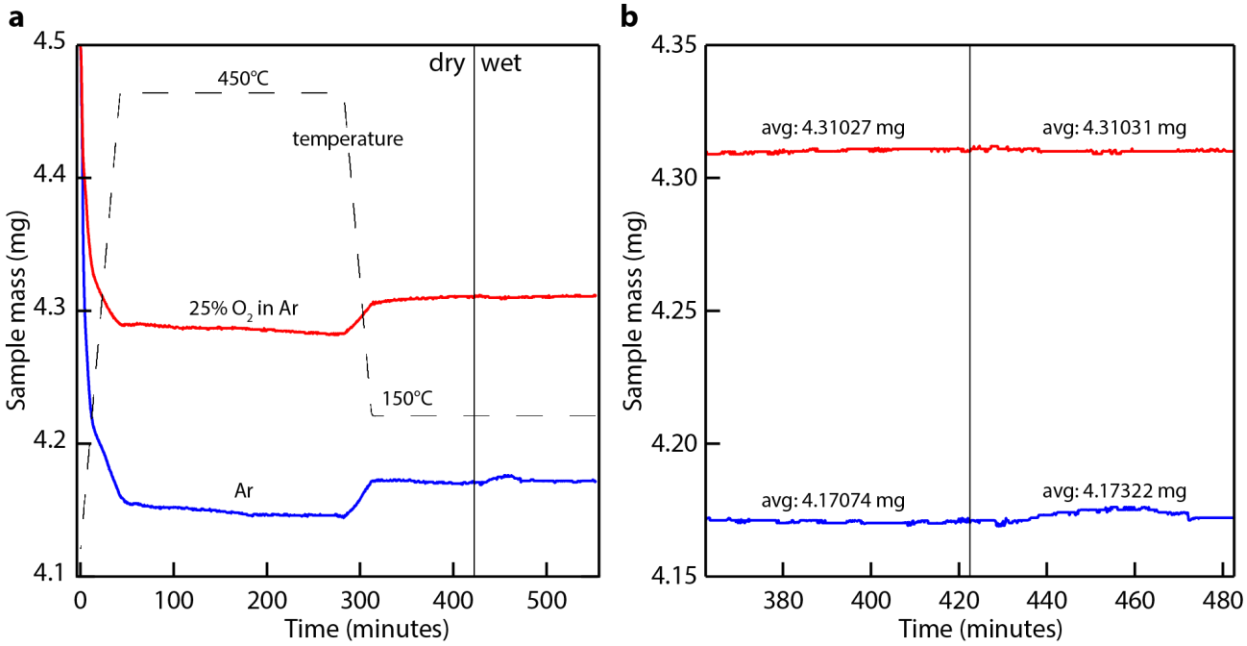

Figure C.11: Thermogravimmetric analysis (TGA) of 3.9 nm CeO_2 nanocrystal powder with surface ligands removed, in an Al_2O_3 crucible, after blank curve subtraction. a) Sample mass vs. time under both Ar atmosphere (blue line) and 25% O_2 atmosphere (red line) in both dry and wet (pO_2=20 mbar) conditions, with the switch from dry to wet conditions delineated by a vertical line. The temperature profile is shown as a dashed line. b) Zoomed-in display of the sample mass vs. time for one hour before and after switching (vertical line) from dry to wet conditions. The one-hour time averaged sample mass before and after the switch is listed above each curve.

Appendix D

Supporting information to Chapter 6

D.1 E.1 Experimental supporting information

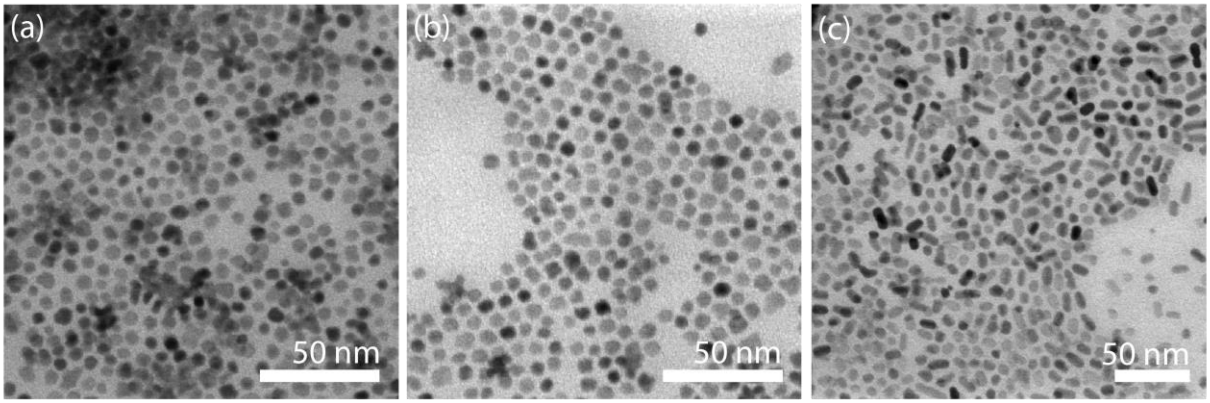

Figure D.1: Scanning transmission electron microscopy images of (a) 4 nm cerium oxide,(b) 4 nm Ga:CeO_2 and (c) 6 nm diameter titanium oxide.

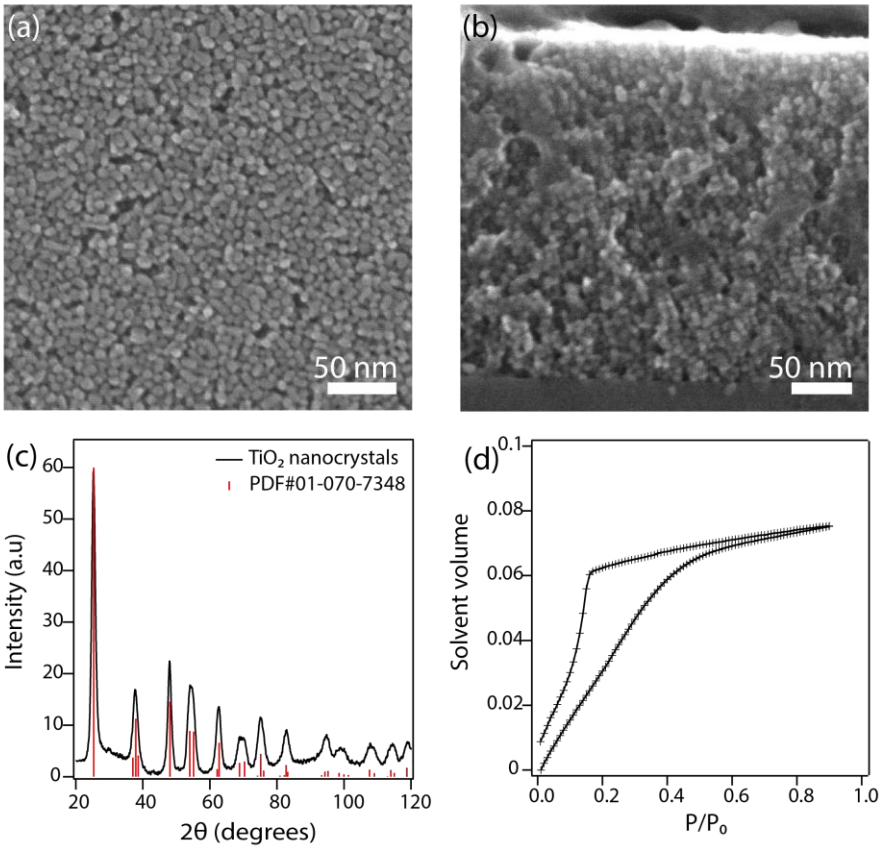

Figure D.2: (a,b) Top-down and cross-section SEM of a prototypical 300 nm titanium dioxide nanocrystal film used for transport measurements. (c,d) X-ray diffraction data mapped to PDF#01-070-7348 for titanium dioxide, and adsorption isotherm derived from ellipsometric porositmetry fitting for the same film.

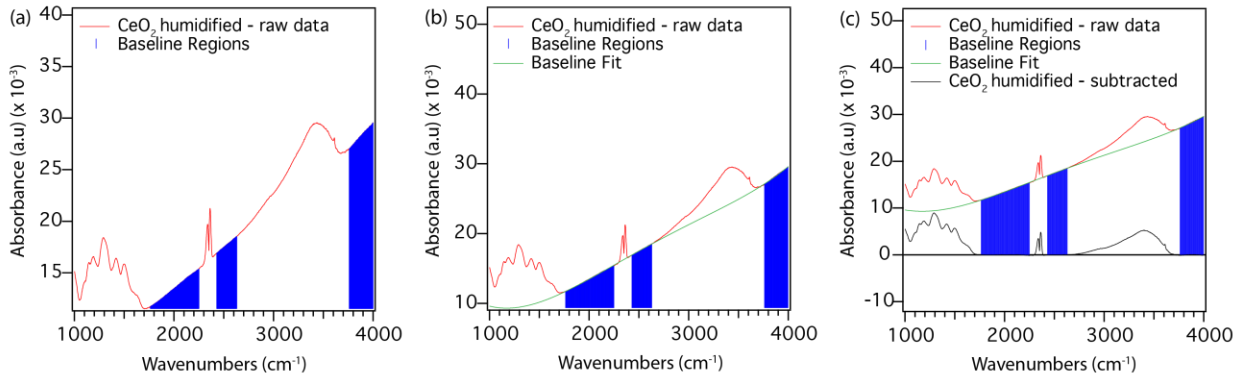

Figure D.3: (a) Selection of baseline regions for baseline fitting. (b) Baseline fitting with a fifth order polynomial for the hydroxyl region between 2400 – 3800 cm^{-1}. (c) Resultant curve after baseline fitting. Note, the spectra presented between 1000 – 1800 cm^{-1} was baseline subtracted separately using just a constant baseline to avoid distortions in the peak intensities.

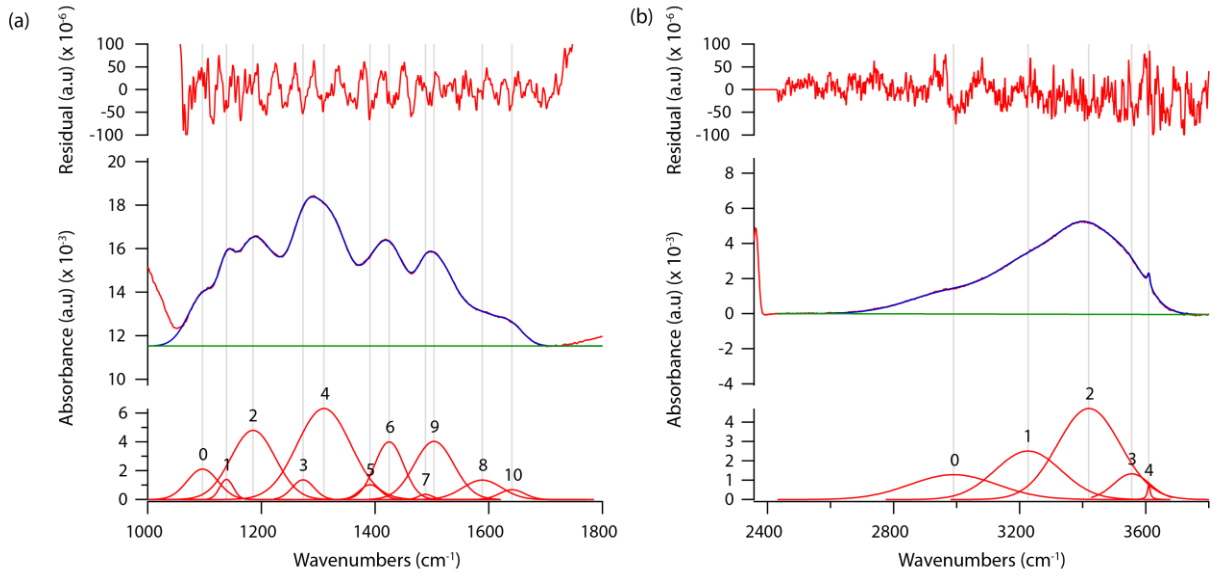

Figure D.4: (a) Gaussian peak fitting in the fingerprint region for the sample of cerium oxide after exposure to humidified Ar. (b) Gaussian and Lorentzian peak fitting in the hydroxyl region for the sample of cerium oxide after exposure to humidified Ar.

Table D.1: Fitting summary and assignment for the peak deconvolution for cerium oxide and titanium dioxide under dry Ar and humidified Ar conditions. References used to assign the water peak positions, and carbonate peak positions for CeO_2,[178] and TiO_2.[179–182] The notation for the assignment specifics for CeO_2 carbonate species were adapted from reference [178] where the authors calculated the actual carbonate coordinate on the CeO_2 cluster surface. The authors also neatly compiled all previous experimental assignment of carbonates and hydroxycarbonates on cerium oxide surfaces in their supporting information, and this compilation was used for peak assignment where assignments could not be done based upon their study.

Sample: Cerium Oxide - Dry Ar						
Type	Location	Amplitude	Area	FWHM	Assignment	Assignment specifics
Gauss	1343	3.16E-03	3.82E-01	1.14E+02	monodentate carbonate	experiment
Gauss	1530	5.18E-03	6.50E-01	1.18E+02	monodentate carbonate	1.31
Gauss	1564	1.70E-03	1.00E-01	5.53E+01	monodentate carbonate	1.3.1
Gauss	1640	2.04E-03	1.45E-01	6.68E+01	water	water bending
Gauss	2997	1.773E-03	7.651E-01	4.053E+02	ice-like water	-
Gauss	3232	4.072E-03	1.321E+00	3.047E+02	ice-like water	-
Gauss	3422	4.925E-03	1.187E+00	2.264E+02	liquid water	-
Gauss	3554	1.982E-03	3.162E-01	1.499E+02	liquid water	-
Lorentzian	3682	5.252E-04	2.757E-02	3.342E+01	surface hydroxyl	-
Sample: Cerium Oxide - Humidified Ar						

Type	Location	Amplitude	Area	FWHM	Assignment	Assignment specifics
Gauss	1096	2.11E-03	1.43E-01	6.38E+01	hydroxycarbonate /monodentate carbonate	experiment
Gauss	1139	1.40E-03	4.22E-02	2.84E+01	monodentate carbonate	1.30
Gauss	1185	4.80E-03	4.70E-01	9.19E+01	hydroxycarbonate /monodentate carbonate	12h,1.30
Gauss	1273	1.36E-03	6.57E-02	4.52E+01	monodentate carbonate	1.21
Gauss	1310	6.32E-03	7.47E-01	1.11E+02	hydroxycarbonate	12h
Gauss	1391	1.03E-03	4.67E-02	4.28E+01	monodentate carbonate	experiment
Gauss	1425	4.02E-03	2.55E-01	5.97E+01	hydroxycarbonate	1.2h
Gauss	1488	3.65E-04	1.10E-02	2.83E+01	monodentate carbonate	1.21
Gauss	1504	4.05E-03	3.52E-01	8.18E+01	monodentate carbonate	1.21
Gauss	1590	1.36E-03	1.17E-01	8.04E+01	hydroxycarbonate	1.2h
Gauss	1642	6.56E-04	3.52E-02	5.03E+01	water	water bending
Gauss	2987	1.27E-03	4.39E-01	3.25E+02	ice-like water	
Gauss	3224	2.49E-03	6.50E-01	2.45E+02	ice-like water	
Gauss	3418	4.69E-03	1.17E+00	2.34E+02	liquid water	
Gauss	3553	1.35E-03	1.94E-01	1.35E+02	liquid water	
Lorentz	3609	7.59E-04	1.54E-02	1.29E+01	hydroxycarbonate hydroxyl	12h, 1.2h
Sample: Titanium Oxide - Dry Ar						
Type	Location	Amplitude	Area	FWHM	Assignment	Assignment specifics
Gauss	1286	4.02E-04	2.25E-02	5.25E+01	bicarbonate	-
Gauss	1370	1.37E-03	1.67E-01	1.14E+02	monodentate carbonate	-
Gauss	1484	2.57E-04	1.39E-02	5.09E+01	bicarbonate	-
Gauss	1552	1.39E-03	2.68E-01	1.81E+02	bidentate carbonate	-
Lorentz	1638	2.13E-03	2.38E-01	7.11E+01	water	H2O bend
Gauss	3023	2.60E-03	1.23E+00	4.45E+02	ice-like water	
Gauss	3258	3.89E-03	1.32E+00	3.20E+02	ice-like water	
Gauss	3424	3.13E-03	6.80E-01	2.04E+02	liquid water	
Gauss	3555	1.41E-03	2.21E-01	1.47E+02	liquid water	
Gauss	3667	6.35E-04	3.35E-02	4.96E+01	surface-hydroxyl	

Sample: Titanium Oxide - Humidifed Ar						
Type	Location	Amplitude	Area	FWHM	Assignment	Assignment specifics
Gauss	1139	2.74E-04	5.58E-03	1.91E+01	unassigned	-
Gauss	1190	7.94E-04	4.52E-02	5.34E+01	unassigned	-
Gauss	1281	1.99E-03	3.59E-01	1.69E+02	bicarbonate	-
Gauss	1416	3.16E-03	2.78E-01	8.26E+01	bicarbonate	-
Gauss	1493	2.55E-03	1.67E-01	6.15E+01	bicarbonate	-
Gauss	1556	1.40E-03	1.01E-01	6.80E+01	bidentate carbonate	-
Gauss	1624	9.72E-04	8.16E-02	7.89E+01	water	H2O bend
Gauss	3001	1.23E-03	5.20E-01	3.96E+02	ice-like water	
Gauss	3247	1.97E-03	5.98E-01	2.85E+02	ice-like water	
Gauss	3427	2.41E-03	6.05E-01	2.36E+02	liquid water	
Gauss	3550	3.41E-04	4.80E-02	1.32E+02	liquid water	

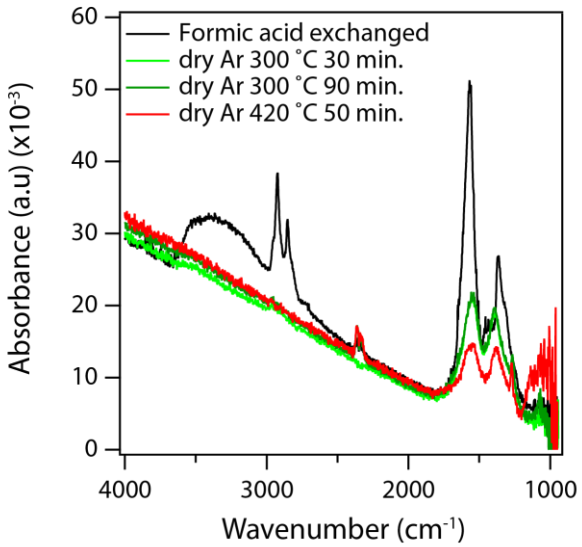

Figure D.5: *In-situ* FTIR of CeO_2 after formic acid exchange heating to 300 °C to desorb formate and then up to 420 °C.

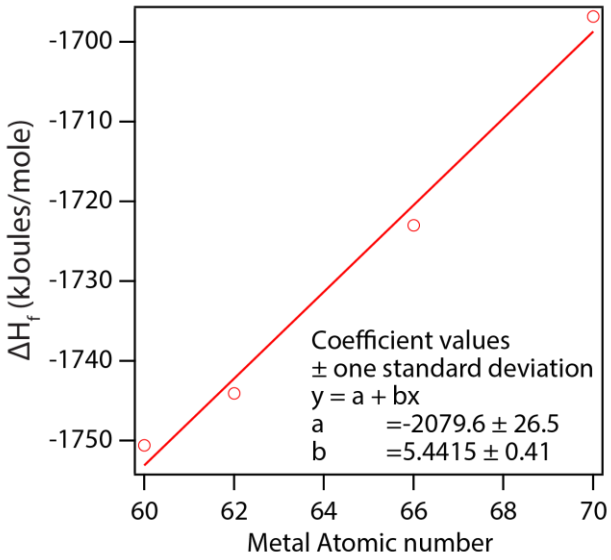

Figure D.6: Extrapolating the enthalpy of formation for $CeOHCO_3$ from published data of ΔH_f for $Nd(OH)CO_3$, $Sm(OH)CO_3$, $Dy(OH)CO_3$, and, $Yb(OH)CO_3$. The value for $CeOHCO_3$ is estimated at -1764 kJ/mol. Data obtained from *L. Merli, .Radiochimica Acta* **1996**, *74, 37-43*.[183]

Table D.2: Values used in the estimation of the stability threshold between cerium hydroxycarbonate and cerium oxide in the presence of water and carbon dioxide. The standard entropy for cerium hydroxycarbonate is approximated using the standard entropy for cerium hydroxide since there is no published value for cerium hydroxycarbonate.

Constants	Enthalpy of formation (kJ/mol)	Standard entropy (J/mol)	Source
Ce(s)	0	72	Handbook of Chemistry and Physics
Ce^{3+} (g)	3968.7	185.28	I.I. Diakonov et. al., Chemical Geology 151, 1998
OH	39	183.71	Handbook of Chemistry and Physics
OH^-	-137	172.47	dH from NIST Computational Chemistry Comparison and Benchmark Database, So from NIST Chemisty webbook
$Ce(OH)_3$	-1418.6	129.4	Navrotsky et. al., J. Chem. Thermodynamics, 88, 2015
O_2	0	205.138	Handbook of Chemistry and Physics
Ce_2O_3	-1796.2	150.6	Handbook of Chemistry and Physics
CeO_2	-1088.7	62.3	Handbook of Chemistry and Physics
H_2O (g)	-241.8	188.8	Handbook of Chemistry and Physics
CO_2	-393.5	213.8	Handbook of Chemistry and Physics

$Ce(OH)CO_3$	-1764.00	129.40	Extrapolated

Table D.3: Calculations to obtain the change in ΔG as a function of temperature for the two reactions involving CeO_2 and Ce_2O_3 with carbon dioxide and water vapor to form $Ce(OH)CO_3$. For the calculations of ΔG, since we are assuming a constant ΔS_o, we are implicitly assuming that entropy changes from the reactions are largely configurational and therefore not temperature dependent.

Reaction	$4\ CO_2\ (g) + 4\ CeO_2\ (s) + 2\ H_2O\ (g) = 4\ Ce(OH)CO_3\ (s) + O_2\ (g)$						
deltaH	=	-643.60	kJ/mol			Threshold temperature	
deltaS	=	-0.76	kJ/mol			Kelvin	°C
deltaG	=	-417.23	kJ/mol	, Temp(K) =	298.15	847.67	574.52
Reaction	$2\ CO_2\ (g) + Ce_2O_3\ (s) + H_2O\ (g) = 2\ Ce(OH)CO_3\ (s)$						
deltaH	=	-703.00	kJ/mol			Threshold temperature	
deltaS	=	-0.64	kJ/mol			Kelvin	°C
deltaG	=	-512.90	kJ/mol	, Temp(K) =	298.15	1102.57	829.42